HYPERSPECTRAL REMOTE SENSING AND FIELD MEASUREMENTS FOR FOREST CHARACTERISTICS

- A CASE STUDY IN THE HAINICH NATIONAL PARK, CENTRAL GERMANY

DISSERTATION

to attain the doctoral degree (Dr. forest.)
of the Faculty of Forest Sciences and Forest Ecology
Georg-August-Universität Göttingen

submitted by

Henning Aberle

born on the 21.11.1981 in Flensburg

GÖTTINGEN, MARCH 2017

1. Referee: Prof. Dr. Christoph Kleinn

2. Referee: Prof. Dr. Andrea Polle

Date of oral examination: 01.11.2016

ACKNOWLEDGEMENTS

First of all, I thank Prof. Dr. Christoph Kleinn and Dr. Hans Fuchs from the Chair of Forest Inventory and Remote Sensing for the research work opportunity and continuous support. I have been appreciating the time and atmosphere there. Moreover, I cordially thank the second referee Prof. Dr. Andrea Polle and Prof. Dr. Thomas Nauss as the third examiner.

Thanks to the people of the Department of Computational Landscape Ecology of the Helmholtz Centre for Environmental Research in Leipzig for providing the remotely sensed data and their efforts in the fieldwork.

I thank the Chair of Bioclimatology of the University of Göttingen for the support at the climate tower.

I would like to thank Manfred Großmann and the employees of the Hainich National Park and Dominik Hessenmöller as well as the DFG Biodiversity-Exploratories for the permission and data supply.

I thank all former and current colleagues and employees at the Chair of Forest Inventory and Remote Sensing. Cordial thanks to Yanti Sarodja, Lutz Fehrmann, Philip Beckschäfer, Dian Melati, Collins Kukunda, Ramón Trucios-Caciano, César Pérez-Crusado, Nils Nölke, Philip Mundhenk, Almut Niebuhr, Dengkui Mo, Xiaolu Tang, Paul Magdon, Axel Buschmann, Mauricio Vega-Araya, Lucia Morales, Silvia Wagner, Reinhard Schlote, Hendrik Heydecke and Ulrike Dockter. I also would like to thank Julia Obentheuer, Inka Lücke and Shaghayegh Shoeibi for working and helping in the framework of this study.

Thanks to the plenty of interesting people from around the world I have been granted to meet over time.

Finally, I am very grateful for my family and their constant support – dorför magg ick mi recht hartlik bedanken.

This research was mainly funded by the national aeronautics and space research center of the Federal Republic of Germany (DLR) with funds from the Federal Ministry of Economics and Technology (support code 50 EE1024). The study was conducted as part of a sub-project in the joint research project „ForestHype – Hyperspektraldaten zur Charakterisierung von Waldmerkmalen" within the framework of an EnMAP preparation program.

SUMMARY

Forests are dynamic and complex ecosystems that play important roles for economic, ecological and social aspects. Besides that, they house the largest share of terrestrial biodiversity. Forests function as carbon sinks, provide natural resources and become more and more valuable. Hence, comprehensive knowledge about forests and their status is crucial. Optical multispectral remote sensing is one appropriate instrument to observe and monitor larger areas. In recent years, hyperspectral sensors have been developed that offer much more spectral details. Besides remote sensing, surveys made in the field are essential for sensor calibration and training data.

This study captures both aspects of remote and ground observations using hyperspectral airborne and non-imaging field data covering a spectral range of 400-2500 nm. It consists of four sub-studies and was conducted in the Hainich national park in central Germany, a beech (*Fagus sylvatica*) dominated broadleaved forest with large old-growth stands. The study considers present issues and shows the capability of spectral high-resolution information.

In addition to spectral reflectances, selected broad- and narrowband vegetation indices (VI) are calculated and used to describe differences among the considered species. The leaf optical properties of the main tree species were examined including reflectance, transmittance and absorptance. Repeated measurements of reflectances were covering two subsequent growing seasons, allowing insights in the seasonal phenology. Overall, the optical properties depend highly on the date and measuring method. Examining species differences, clear rules for separation are not apparent. Especially in the shortwave infrared, a triplet grouping of species could be observed. Beech and hornbeam (*Carpinus betulus*) showed similar appearances in shortwave infrared, as well as maples (*Acer platanoides* and *Acer pseudoplatanus*), and Ash (*Fraxinus excelsior*) and Oak (*Quercus petraea*). However, general assumptions about the response pattern related to species are hard to communicate due to high variation and changes in the order of reflectance values. This study also revealed the complexity of spectroscopy in forests.

In a next step, in-situ leaf and crown reflectances were compared with remotely sensed values using airborne sensors. This study incorporates a unique data set of simultaneously gathered measurements. Compared to crowns, sampled leaves show much higher reflectances. Differences of the various levels could be described with simple linear and logarithmic model approaches. For further comparison, VI and red edge position metrics including Red Edge Position Index (REPI) and spectral derivatives were calculated for each level and species. Some of the in-situ leaf level values were more similar to the remotely sensed data than to the in-situ crowns.

Within an area of 2.25 ha, the canopy light interception and crown porousness was assessed. Different approaches were compared including digital cover and hemispherical photography in both visible and near infrared light. Additionally, hyperspectral irradiances were measured below

the canopy to retrieve the amount of intercepted light and corresponding extinction coefficients. Ground data was then compared to aerial hyperspectral imagery. From the calculated remotely sensed VI, the Photochemical Reflectance Index (PRI), followed by the Carotenoid Reflectance Index 1 (CRI1), showed the highest, albeit moderate, correlation with openness derived from hemispherical and near infrared cover photos. Fractional cover, derived from radiation measurements, was moderately correlated with Normalized Difference Lignin Index (NDLI) and Red Green Ratio Index (RGRI).

In the last sub-study, forest inventory data was combined with hyperspectral airborne data. Standard stand variables averaged per inventory plot were related to remotely sensed metrics. Basal area did not show any correlation with the derived spectral VI. Also in height, tree diameter at breast height (dbh) and stand density classes no clear trends could be observed. However, in near and shortwave infrared, there are tendencies of a relation between reflectance and dbh and density class. Comparing all calculated VI, the PRI had the highest, moderate, correlation with dbh and density classes as well as with mean tree height per plot. Again, the PRI showed promising results for future analyses.

ZUSAMMENFASSUNG

Wälder sind dynamische und komplexe Ökosysteme, die neben ökonomischen, ökologischen und sozialen Aspekten eine wichtige Rolle für die globale Biodiversität spielen. Sie funktionieren als Kohlenstoffspeicher, stellen natürliche Ressourcen zur Verfügung und werden immer wertvoller. Daher ist eine umfassende Kenntnis über die Wälder und deren Status immens wichtig. Optische multispektrale Fernerkundung ist ein geeignetes Instrument um größere Flächen zu beobachten und zu überwachen. In den letzten Jahren wurden hyperspektrale Sensoren entwickelt, die viel mehr spektrale Details liefern. Zusätzliche Feldaufnahmen sind essentiell für Sensorkalibrierung und die Sammlung von Trainingsdaten. Diese Untersuchung erfasst beide Gesichtspunkte von Fernerkundung und Beobachtungen am Boden, indem hyperspektrale Luftbilder und nicht-bildgebende Felddaten verwendet werden, die einen spektralen Bereich von 400-2500 nm abdecken. Die Arbeit besteht aus vier Teilstudien und wurde im Hainich Nationalpark inmitten Deutschlands durchgeführt, einem von Buche (*Fagus sylvatica*) dominierten Laubwald mit großen Altbeständen. Die Untersuchung befasst sich mit vorhandenen Problemen und zeigt die Leistungsfähigkeit von spektral hochaufgelösten Informationen auf.

Zusätzlich zu den spektralen Reflexionsgraden wurden ausgewählte Breit- und Schmalband Vegetationsindizes (VI) berechnet und für die Beschreibung von Unterschieden zwischen den berücksichtigten Baumarten verwendet. Daneben wurden die optischen Eigenschaften von Blättern der Hauptbaumarten untersucht, einschließlich Reflexion, Transmission und Absorption. Wiederholte Messungen von Reflektanzen decken zwei nachfolgende Vegetationsperioden ab, was Einblicke in die saisonale Phänologie ermöglicht. Insgesamt sind die optischen Blatteigenschaften abhängig vom Datum und der Messmethode. Bei der Untersuchung der Speziesunterschiede waren keine klaren Regeln zur Trennung erkennbar. Vor allem im kurzwelligen Infrarot wurden drei Gruppen zu je zwei Baumarten beobachtet: Buche und Hainbuche (*Carpinus betulus*) zeigten hier sehr ähnliche Werte, genau wie Ahorne (*Acer platanoides*, *Acer pseudoplatanus*), sowie Esche (*Fraxinus excelsior*) und Eiche (*Quercus petraea*). Allerdings sind generelle artbezogene Aussagen zu den Reflexionskurven eher schwierig zu treffen durch die hohe Streuung und Änderungen in der Reihenfolge bezüglich der Reflektanzwerte der Baumarten, die sich je nach Datensatz in unterschiedlichen Wellenlängenbereichen überschneiden können. Schließlich zeigt diese Arbeit auch die Komplexität von Spektroskopie in Wäldern auf.

Im nächsten Schritt wurden die Ebenen von Blatt zu Krone betrachtet. Dabei wurden in-situ Blatt- und Kronenreflektanzen mit fernerkundungsbasierten Werten von flugzeuggetragenen Sensoren verglichen. Diese Studie verwendete einen einzigartigen Datensatz aus simultan aufgenommenen Messungen. Im Vergleich zu den Kronen zeigten die Blätterproben viel höhere Reflektanzen auf. Die artspezifischen Unterschiede konnten herausgearbeitet werden. Unterschiede bzw. Zusammenhänge der verschiedenen Ebenen konnten mit einfachen linearen und logarithmischen

Modellen annähernd beschrieben werden. Für weitere Vergleiche wurden für jede Ebene und Baumart VI sowie Red edge-Positionsmetriken berechnet, inklusive dem Red Edge Position Index (REPI) und spektraler Ableitungen. Einige der in-situ Blattdaten zeigten dabei ähnlichere Werte zu den Fernerkundungsdaten als zu den in-situ Kronendaten

Auf einer 2,25 ha großen Fläche wurden alle Bäume aufgenommen und die Lichtinterzeption der Kronen sowie deren Porosität angesprochen. Verschiedene Ansätze wurden verglichen: digitale Standardfotos und hemisphärische Fotos, sowohl im sichtbaren als auch nahinfrarotem Bereich. Zusätzlich wurden hyperspektrale Globalstrahlungen unterhalb der Kronen gemessen, um die Menge an abgefangenem Licht und die entsprechenden Extinktionskoeffizienten zu ermitteln. Felddaten wurden mit hyperspektralen Luftbilddaten verglichen. Von den berechneten fernerkundungsbasierten VI zeigte der Photochemical Reflectance Index (PRI) gefolgt vom Carotenoid Reflectance Index 1 (CRI1) die höchsten, wenn auch moderaten, Korrelationen mit Kronenöffnungen aus sichtbaren hemisphärischen und den nahinfraroten Standardaufnahmen. Der Anteil an abgefangener photosynthetisch aktiver Strahlung, ermittelt aus den Strahlungsmessungen, zeigte eine moderate Korrelation mit dem Difference Lignin Index (NDLI) und dem Red Green Ratio Index (RGRI).

In der letzten Teilstudie wurden Waldinventurdaten mit flugzeuggetragenen Hyperspektraldaten auf größerer Fläche kombiniert. Standardmäßige Bestandesvariablen wurden pro Inventurplot gemittelt und den fernerkundungsbasierten Metriken gegenübergestellt. Die geschätzte Grundfläche pro Hektar zeigte keine Korrelation mit berechneten Vegetationsindizes. Auch konnten bei den Baumhöhen- und Durchmesserklassen (Brusthöhendurchmesser, BHD), sowie den Bestandesdichten keine klaren Trends beobachtet werden. Allerdings waren im nahen und kurzwelligen Infrarot Tendenzen eines Zusammenhangs zwischen Reflektanzen und Durchmesser und Dichteklassen erkennbar. Beim Vergleich aller VI hatte der PRI die höchste, moderate, Korrelation mit BHD- und Dichteklassen, sowie der mittleren Baumhöhe pro Plot. Wieder einmal zeigte der PRI vielversprechende Ergebnisse für zukünftige Analysen.

TABLE OF CONTENT

LIST OF FIGURES

LIST OF TABLES

ABBREVIATIONS

AISA	Airborne Imaging Spectrometer for Applications
ARD	Afforestation, Reforestation and Deforestation
ARI2	Anthocyanin Reflectance Index 2
ASD	Analytical Spectral Device
BMEL	Bundesministerium für Ernährung und Landwirtschaft
CH	Convex Hull
cm	centimeter
CO_2	Carbon dioxide
CRI1	Carotenoid Reflectance Index 1
CV	Coefficient of Variation
dbh	diameter at breast height
DCP	Digital Cover Photograph
DHP	Digital Hemispherical Photograph
DV	Derivative
EMR	Electromagnetic Radiation
EnMAP	Environmental Mapping and Analysis Programme
FAO	Food and Agriculture Organization of the United Nations
fAPAR	fraction of Absorbed Photosynthetically Active Radiation
fC	fractional Cover
FODIS	Fiber Optic Downwelling Irradiance Sensor
FWHM	Full Width Half Mean
GPP	Gross Primary Production
GSD	Ground Sampling Distance
ha	hectare
IPCC	Intergovernmental Panel on Climate Change
IUCN	International Union for Conservation of Nature
JRC	Joint Research Centre
k	extinction coefficient
LAI	Leaf Area Index
LDCM	Landsat Data Continuity Mission
LOP	Leaf Optical Properties
LUE	Light Use Efficiency
m	meter
n	number
NDVI	Normalized Difference Vegetation Index
NIR	Near Infrared
nm	nanometer
PAR	Photosynthetic Active Radiation
PRI	Photochemical Reflectance Index
r	Pearson correlation coefficient
R^2	Coefficient of determination
RAMI	Radiation Transfer Model Intercomparison
REDD	Reducing Emissions from Deforestation and forest Degradation
REIP	Red Edge Inflection Point
REP	Red Edge Position
REPI	Red Edge Position Index
RGRI	Red Green Ratio Index
RS	Remote Sensing
RUE	Radiation Use Efficiency
SIPI	Structure Intensive Pigment Index
SNR	Signal to Noise Ratio
SR	Simple Ratio
UNEP	United Nations Environment Programme
UNFF	United Nations Forum on Forests
VI	Vegetation Index
VIS	Visible part of the spectrum

Chapter 1

General introduction & study site

1 CHAPTER ONE – INTRODUCTION

1.1 BACKGROUND

In the last decades an increased change of the global landscapes and environments and a huge human impact have been come to pass. One main focus is on forests and their condition since they cover about one third of the Earth's surface as reported by the United Nations Environment Programme (UNEP et al., 2009). The area covered by forests in the country of Germany is about the same dimension and amounts to currently ca. 32 %, which are approximately 11.4 million ha (BMEL, 2015). These ecosystems are highly dynamic and very complex. They take up essential functions for local and global communities in social, ecological and economic aspects (Füssel et al., 2012; Thomas, 2012). Some of those functions represent the fundament of sustainability and have a higher impact than others have; some are maybe more evident on a closer inspection (Figure 1.1). One main role of forests is certainly the influence on the world's climate. They play an important role for water regulation. By the processes of evapotranspiration, respiration and photosynthesis they are consequently the main drivers in the terrestrial and atmospheric water, carbon and oxygen circles (Bonan, 2008). In addition, forests host a huge number of plant and animal species and contribute a big part to the overall biodiversity (FAO, 2010; Parrotta et al., 2012). Besides the relevance for global fauna and flora, there is also a big importance for the livelihood of local communities and international economies. Woodlands are essential for employment and livelihood of millions of people worldwide (Chao, 2012). The multipurpose character of forests makes mankind often facing with a balancing act between conservation and utilization.

Although some countries like Germany try to manage their forests in a way that the regrowth of trees is higher than or equals to the amount of felling (BMEL, 2015), a rising need for woody products, energy and especially land has been leading legally and illegally to deforestation and cultivation of large areas in many parts of the world. Besides an ongoing urbanization and expansion of infrastructure the loss of substantial ecosystems and forests has been intensified by grazing land for cattle and, more recently, for soy bean and oil palm plantations (Hansen et al., 2008; UNEP et al., 2009). Thus, the recent situation and markets have become challenging to researchers and decision makers world-wide and led to continuous reassessing and adapting these cross-linked processes. This holds especially for the debate about man-made climate change and future strategies (Franklin, 2001; Füssel et al., 2012; IPCC, 2013; Peng et al., 2011).

Figure 1.1: Services of forests cover ecological, economic and social aspects (Thomas, 2012, modified).

There are several international processes considering forest mitigation functions of forests by financial compensations. Among the most prominent in the last years is the UN-REDD program on reducing emissions from deforestation and forest degradation (FAO et al., 2011). More recently the UNEP started a collaboration with the International Union for Conservation of Nature (IUCN) bringing their REDD program and the Global Partnership on Forest and Landscape Restoration together with the goal of restoring forest landscapes (UNEP, 2014). The importance of forests for the climate is also based on the sequestration of carbon above ground and in the soil (Baccini et al., 2012; Pan et al., 2011; Saatchi et al., 2011). These carbon stocks are maybe not always an accumulating sink, for example, when forests are getting old and decay, but at least a storage of immense importance. Moreover, the global carbon cycle is affected not only by complete removal of forests but already by disturbances (McDowell et al., 2015; Seidl et al., 2014). However, we are coping loss of forests in some regions of the world (FAO & JRC, 2012; Sloan and Sayer, 2015), and because deforestation is the second largest source of anthropogenic CO_2 emission, it is crucial to have a sound monitoring to record changes over time (Kleinn et al., 2002; van der Werf et al., 2009; Wertz-Kanounnikoff, 2008).

Forest inventories are the primary sources of terrestrial data about wooded landscapes. On national level, the methods of inventory as well as the implementation of sampling techniques differ. However, mainly based on a systematic samples spread over a target area they record and report key variables like species composition, basal area, tree height, stem density and many other auxiliary data more. When surveying Earth's surface on local, regional and global scale another important measure is the utilization of remotely sensed data acquired from aircrafts or satellites (Belward and Skøien, 2014; Boyd and Danson, 2005; FAO & JRC, 2012; Franklin, 2001; Kleinn, 2002). It should be noted that usually only the land cover type can be derived rather than the kind of land use (Tuanmu and Jetz, 2014; Verburg et al., 2011). However, as additional information it

can be a helpful support for fieldwork and becomes more and more indispensable (Fridman et al., 2014; Gregoire et al., 2011; McRoberts and Tomppo, 2007). Selected ground targets or even whole landscapes are viewed from above and examined from a certain distance. The analysis of images and collected data takes place in a laboratory or workstation afterwards. Obtained information can then be shared and used for future decisions. Furthermore, changes in relation to a point in time as a base line can be registered using a standardized and operational monitoring system, which ideally includes a repeated survey at a meaningful temporal and spatial scale (Giri et al., 2013; Romijn et al., 2015). The exploitation of remotely sensed data is still continuing, and the techniques and methods can lead to information which is getting more interesting for forest management and planning purposes than it might be the case in the past (Holmgren and Thuresson, 1998). The challenging part is the derivation of useful and needed information. Nowadays there are plenty multispectral remote sensing (RS) platforms possibly related to observing and monitoring of forests (Boyd and Danson, 2005; Fagan and Defries, 2009), and the number of operating satellite systems is increasing since years (Figure 1.2).

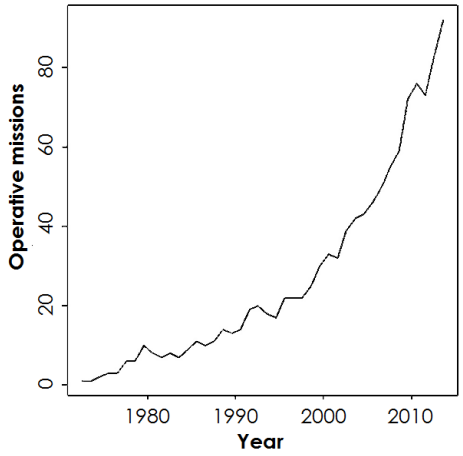

Figure 1.2: Number of near-polar orbiting, land imaging civilian satellite operational from 1972 to 2013 (Belward and Skøien, 2014, modified).

In the following, only some examples will be highlighted for a better assessment of the context and pointing to the international importance of remotely sensed monitoring. The European Earth observation program Copernicus, formerly called GMES (Global Monitoring for Environment and Security), started the Sentinel satellite series in 2014. It shall support in monitoring climate change, atmosphere, oceans and land (EC, 2015). Up to now, mainly Landsat satellites have been used for these kinds of large-area and often multi-temporal observations. Their newest replacement, the Landsat Data Continuity Mission (LDCM) or just Landsat 8, was launched in 2013. Also the Intergovernmental Panel on Climate Change (IPCC) is attempting to detect processes like afforestation, reforestation and deforestation (ARD) incorporating remote sensing for classification and monitoring purposes (IPCC, 2000). The global Forest Resource Assessment of the Food and Agriculture Organization of the United Nations (FAO) has implemented a special remote

sensing study to improve information about actual spatial distribution of forests and changes in time (FAO, 2010). Moreover, the FAO recently set up the global land cover database GLC-SHARE which incorporates and combines different data sources, from which the area of global tree cover amounts to 27.7 % (FAO, 2014). Latest publications and discussions about global forest mapping using remote sensing data show the importance and actuality of forest and vegetation mapping (Asner, 2014; Hansen et al., 2014, 2013; Lui and Coomes, 2015; Tropek et al., 2014). Finally, in the Global Climate Observing System (GCOS) there are 50 essential climate variables listed including land cover and vegetation type, leaf area index, above ground biomass and fraction of photosynthetically active radiation (GCOS, 2010). The World Meteorological Organization (WMO) supports this system as well as the Intergovernmental Oceanographic Commission (IOC) of UNESCO, the UNEP, and the International Council for Science (ICSU). Remote sensing technology is partly helping in deriving information about the target variables.

For observing large areas, multispectral data, having a moderate spectral resolution and only a few distinct broad bands, has already been widely used. Moreover, this type of RS has been actually the most preferable source of information when it comes to monitor forest cover changes over large areas and time intervals (Kim et al., 2014; Olander et al., 2008; Townshend and Justice, 1988). However, nowadays there is an increased appearance of *hyperspectral* sensors and their data exploitation – although the technology is already available since long (Goetz, 2009; Steiner and Gutermann, 1966; Treitz and Howarth, 1999). In contrast to the most often used multispectral sensors hyperspectral systems collect and provide data in numerous narrow channels resulting in rather contiguous signal responses. In this context it is often referred to as imaging spectroscopy or spectral imaging. Obviously, the high number of bands entails an enormously increased disk space. The spatial resolution is often lower than of comparable multispectral systems as a compromise for keeping the data size manageable (Burger and Gowen, 2011). Due to the higher dimensionality, its analysis is also much more complex. Furthermore, when designing such sensors it seems to be difficult to retain a good signal to noise ratio while decreasing the spatial resolution (Villafranca et al., 2012). In the last years the technology has enhanced due to better sensors and more powerful computers making data analyzable by new methods and accessible for more end users. However, hyperspectral data analysis has got a huge potential which yet has to be fully explored. All these circumstances and the yet low number of available systems are the reasons for that hyperspectral data analysis is still a rather young discipline. Even though the technology had been developed some time ago the analyses and scientific usage has become more interesting and promising for many different purposes (Arafat et al., 2013; Beck, 2003; Grosjean et al., 2014; Medina et al., 2011; Saldaña et al., 2013). Besides that, dealing with forests the recognition and mapping of tree species is a contemporary and ongoing issue in remote sensing (Clark and Roberts, 2012; Dalponte et al., 2013; Féret and Asner, 2013; Ghiyamat et al., 2013). Albeit there is a constant improvement of sensors and analysis methods, we must not disregard to use field observations as

training data for calibration and validation. The combination of these two approaches is a key challenge and should always be followed whenever possible. Besides RS systems there are also non-imaging hand-held sensors available for a range of different applications in mineralogy, geology, vegetation analyses. These field spectroradiometers can be used for calibrating sensors, measuring reflectance or the incoming radiation at sensor as well as at ground level. Furthermore it allows detailed examination of the optical properties of mineral soil or plant leaves, e.g. (Castro-Esau et al., 2006; Clark et al., 2005; Milton et al., 2009; Ramakrishnan et al., 2013).

Another way of plant-related imaging and non-imaging spectroscopy data exploitation is the calculation of vegetation indices. Broad-band indices such as the Normalized Difference Vegetation Index (NDVI) and Simple Ratio (SR) have been established in many studies (Bannari et al., 1995). Rather new hyperspectral vegetation indices offer complete new application possibilities and a more distinct and selective analysis of features (Thenkabail et al., 2000). Hence, hyperspectral data provide much more information and can be used for an improved vegetation analyses (Cole et al., 2014; Gitelson et al., 2003; Ustin et al., 2009) including the analysis of foliage biochemistry for deriving plant state and performance (Bartlett et al., 2011; Sims and Gamon, 2002). For these applications detailed hyperspectral data seem to be appropriate to investigate the processes related to plant physiology (Ghiyamat and Shafri, 2010). But recent argumentation reveals also to interpret the gained results such as nitrogen content in leaves and canopies with care. Observed relations in NIR and SWIR can have other reasons and often depend on leaf structure and water content. For that, it is important to distinguish between causality and correlation (Fisher, 2009; Knyazikhin et al., 2013a, 2013b; Ollinger et al., 2008; Townsend et al., 2013). Nonetheless, forest canopies can tell us a lot about the condition of forest stands. Therefore, many researchers link other field-observed data to remote sensing imagery. Since some characteristics of vegetation are influencing light absorption and hence the reflected radiation, the variable derivation can be done indirectly by optical measures. One popular variable is the leaf area index (LAI) which is related to growth and productivity (Pekin and Macfarlane, 2009; Soudani et al., 2006; Zheng and Moskal, 2009). In that context also the dimensionality and density of tree crowns plays a big role. Thus, canopy porosity and light interception are important factors for applications in forestry and ecology. One way for non-destructive estimations of LAI, openness or gap fraction is the use of digital hemispherical photography (Beckschäfer et al., 2013; Frazer et al., 1997; Jonckheere et al., 2004). Besides that, light detecting sensors, mainly the Licor LAI-2000 device, have been used (Gobron and Verstraete, 2009a; Nackaerts et al., 2000). However, one major drawback is the lack of spectral details measured about light interception and absorption. And only a few publications took this explicitly into account yet (Endler, 1993; Jordan, 1969; Wang et al., 2003). Beyond this and within the contexts of nature conservation and carbon-emission-trading systems it is crucial to generate comprehensive information about the existing forest. This includes knowledge about growing stocks and health condition of the plants. So, there is a demand for details on variables

describing the vegetation in general or rather the characterization of forests and trees in particular. Thus, the understanding of the impact of spatial arrangement of trees and species composition and of processes within these ecosystems such as physiology, seasonal phenology and optical properties of canopies is of central interest. Moreover, what is absolutely needed, besides remote sensing approaches, are detailed studies on leaf level (Homolová et al., 2013). That is what this study is taking up. It is carried out in a mixed temperate forest and shall consider present issues and show the capability of spectrally high resolved information in different applications with a focus on canopy light interception, tree species mapping and the modelling of important forest data such as diameter class and stand density.

1.2 OVERALL OBJECTIVES

In preparation of the upcoming German hyperspectral satellite mission EnMAP (Environmental Mapping and Analysis Program) several national and international research projects have been conducted. They cover a variety of applications like aquatic and urban research, geology and mineralogy, agriculture and forestry. Within the framework of that program also this study is carried out. Most parts of this study can be considered as basic research and methodological investigation. The focus is on the utilization and potentials of hyperspectral data within the framework of forestry and ecological research using regular inventory data and additional recorded information. Moreover, it shall give an overview in the applicability of the data and show some aspects and challenges occurring in the context of forest vegetation analysis and management planning on the example of a temperate forest. The study intends to help and improve understanding for the spectral-optical behavior of tree leaves and forest stands. It should further be investigated how sunlight is penetrating the canopy layer of a forest stand and which amount is being absorbed or scattered. Besides hyperspectral field data for radiation measurement on the ground also hyperspectral remotely sensed imagery is used which allows the linkage and comparison of data sets on different scales. As these campaigns are done simultaneously, this study has gathered very unique data sets. On leaf level the point of time is investigated which might emphasize the temporal development and the apparent interspecific differences in reflection. Another goal of this study is to investigate the potential of hyperspectral data for the discrimination of different tree species on different levels. Finally, aerial imagery is linked to permanent forest inventory plots to explore the relation of field data and remotely sensed hyperspectral information on a large area. In summary, the examples on the application of high spectral resolution sensors shall be shown in case studies conducted in a rather highly mixed forest of the Hainich, a German national park with a high number of unmanaged near-natural stands consisting of a variety of deciduous tree species.

1.3 THE STUDY SITE

This study was conducted in a part of the Hainich in Thuringia, a wooded ridge in the center of Germany, located at about N51.08° E10.45°. The terrain altitude ranges approximately between 200 and 500 m (Figure 1.3). The slope on the north-facing plateau area is about 1-4°, but can increase in some harsher cuts. The climate is sub-Atlantic with a sub-continental influence. Precipitation averages 750 mm annually, mean temperature is about 7.5° C. Mainly Triassic parent materials shell-limestones and loess from the Pleistocene are providing several different soil types like rendzina, luvisols, stagnosols and brown soils, having often a loamy texture (Fischer et al., 2010; Getzin et al., 2012; Knohl et al., 2003; Mölder et al., 2008). With a total area of 16,500 ha the surrounding Hainich is the largest coherent deciduous forest of Germany. In the year 1975, a part of 7,500 ha was declared as national park, of which about 5,000 ha is forest. The stands are commonly dominated by beech (*Fagus sylvatica*), followed by ash (*Fraxinus excelsior*), maples (*Acer spec.*), oaks (*Quercus spec.*), hornbeam (*Carpinus betulus*) and others. Only a few patches of coniferous trees exist, mostly composed of spruce (*Picea abies*). The species rich forest is listed as Subatlantic-Central European beech forest with *Lathyrus vernus*, *Hepatica nobilis* in the colline-submontane level (Bohn. et al., 2004). Several forest communities are present including *Galio-Fagetum*, *Hordelymo-Fagetum and Carpinum-Fagetum.*

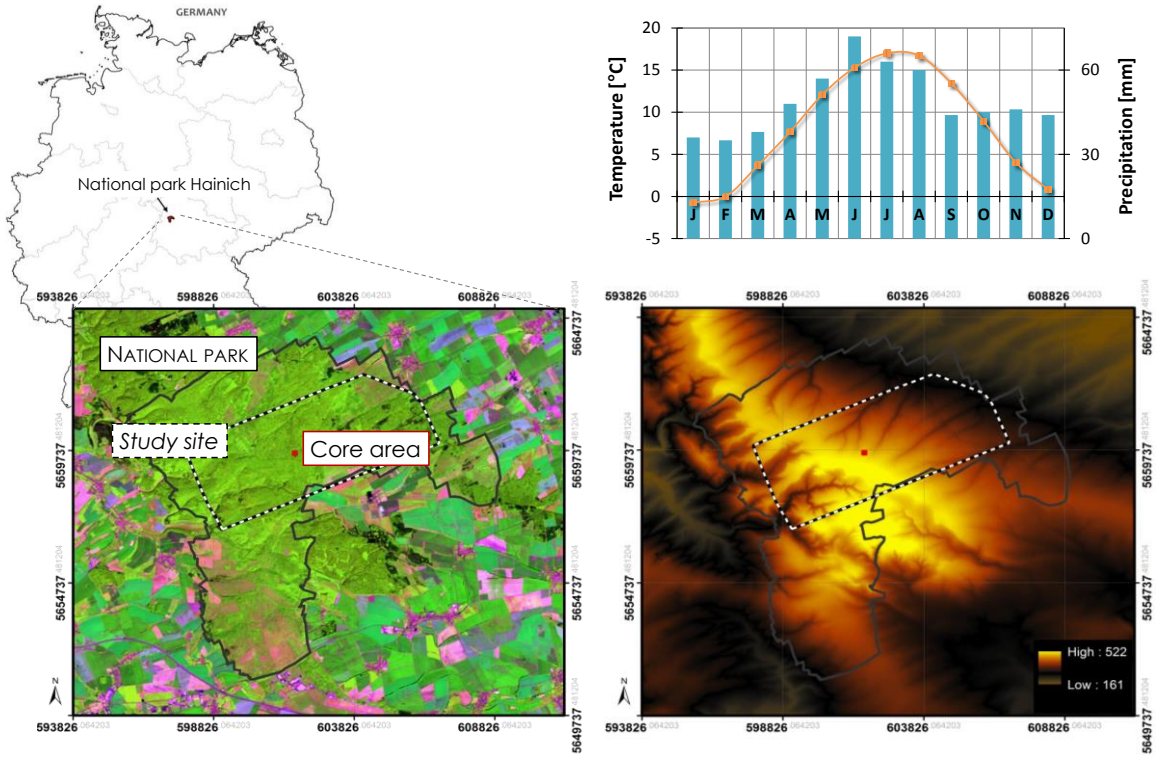

Figure 1.3: Location of the study site in central Germany within the National Park Hainich. Background images: Landsat 8, channel composite 6-5-4, date: 07.07.2013; digital elevation model: dtm20, 2010 (GeoBasisDE/TLVermGeo). UTM Zone: 32N, WGS84. Upper right: climate diagram for Mülverstedt (climate-data.org).

Due to the history and the recent protected status, many stands have not been managed for decades. Historically, these forests have been managed in a so-called coppice with standards system. Moreover, parts of the area were used as a military training ground between 1965 and 1997, so that near-natural forest stands have been evolved (Knohl et al., 2008, 2003; Kutsch et al., 2010; Mölder and Bernhardt-Römermann, 2009). Hence, many standing dead trees and lying wood debris can be found all over the area. The trees in the Hainich belong to very different age classes, and depending on the location it can reach up to more than 250 years. The highly mixed forest consists of a high variety of deciduous tree species and offers unique characteristics considering species compositions and diversity. Within this context these *Ancient Beech Forests of Germany* are listed as UNESCO World Heritage Site since 2011 together with the *Primeval Beech Forests of the Carpathians* (Nationalparkverwaltung-Hainich, 2012; UNESCO, 2014).

Figure 1.4: From left to right: Inside the study area in winter and summer; climate tower and canopy walk.

Nevertheless, the presence of trees of different species and ages makes it attractive and challenging for both terrestrial and remote sensing based studies. On account of the special conditions there, many long-time and recent studies from different fields of research have been conducted in the Hainich (Boch et al., 2013; Fischer et al., 2010; Guckland et al., 2009; Herold et al., 2014; Nölke et al., 2015). This also causes the presence of on-site research facilities. Within the study area a 45 m high climate tower is located (Figure 1.4), which is a part of the international FLUXNET network (Ershadi et al., 2014; Stoy et al., 2014). It is used, amongst others, for measuring carbon dioxide fluxes and solar radiation (Knohl et al., 2003; Pinty et al., 2011b). It allows one also to reach higher levels of nearby trees and canopies. Moreover, it shall provide the basis for a core area in which this study is carried out. A canopy walk nearby offers another way to access tree crowns and can be used for both touristic and scientific purposes.

1.4 THESIS STRUCTURE

A quick overview of the organization and content of this thesis shall be given in the following. This text is a monograph, but arranged in single sections which correspond to individual but closely

linked research sub-projects that may be the starting point for subsequent journal publications. The chapters are including subsequent content:

The next *chapter 2* is dealing with some basic and important principles of the physics of radiation and background information about the used technologies. Furthermore, the fundamentals of optical characteristics of vegetation are outlined here.

The subjects of *chapter 3* are the processing and analysis of in-situ collected spectral responses from different broadleaved trees. Further focus is on the species-wise leaf optical properties incorporating reflection, absorption and transmission as well as the derivation of phenology and seasonal trends in leaf reflectance.

Chapter 4 is picking up the reflectances of different Central European tree species with special regard to the levels of leaves, branches, crown and stand. Besides reflectances, specific vegetation indices are examined with a focus on the red edge position expecting varying results on the different scales.

In *chapter 5,* the topic is the analysis of forest canopies regarding canopy porousness and species composition. In an established core area the crown cover and light interception are obtained. Different techniques and technologies such as photography and radiation measurements are compared and examined. Furthermore, ground based data regarding canopy openness and light interception is connected with remotely sensed data. It is investigated whether there is a relationship between terrestrially measured and airborne derived data of high spectral resolution.

Chapter 6 deals with the linkage of hyperspectral remote sensing imagery and information acquired on the ground on a larger area. Data sets are forest management units and boundaries and forest inventory plots incorporating different target variables like tree species, basal area, height and diameter and stand density class. Plot data is opposed to spectral bands and vegetation indices.

The final *chapter 7* is the synopsis and concludes the single parts of this study and summarizes the work in the overall context. Additional ideas and analyses are presented that have not been examined further. After that follows a short outlook and future perspectives.

CHAPTER 2

THEORETICAL BACKGROUND & DATA MATERIAL

2 CHAPTER TWO – BACKGROUND

2.1 PRINCIPLES OF OPTICAL RADIATION

The basis for vision in general and optical remote sensing in particular is the detection, processing and interpretation of electromagnetic radiation (EMR). There are many natural and artificial sources of radiation: changes of energy levels of electrons, the acceleration of electrical charges, the decay of radioactive materials or the thermal motion of atoms and molecules. Actually, all matter with a temperature of more than the absolute zero point of ca. -273 °C emits EMR (Jones and Vaughn, 2010; Lillesand et al., 2008), but we are mainly talking about the radiation emitted by the sun in this context. First, it is important to have an idea about the rather complicated character of radiation. There are two models trying to explain the behavior of EMR: according to the first one, the flux of energy is moving in harmonic waves having a certain frequency in the magnetic and electric fields (Figure 2.1). The second model is seeing light as consisting of particles like photons and quanta. As EMR can show any of these properties, depending on the experimental design, both points of view have to be considered (Bolduc et al., 2014; Mather and Koch, 2011; Menzel et al., 2012).

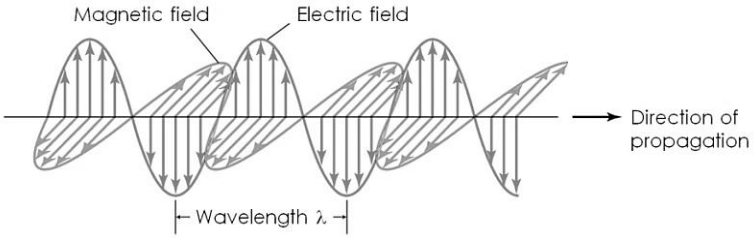

Figure 2.1: Concept of electromagnetic waves (UGA, 2013, modified).

All EMR disperse with the speed of light c of about 3.00×10^8 m/s. It is constant and independent from the wavelength λ. The relationship to the frequency f can then be expressed as:

$$c = \lambda f \quad \Rightarrow \lambda = c/f \qquad \text{(Eq. 2.1)}$$

Further, the energy of the photons Q is proportional to the frequency f:

$$Q = hf \qquad \text{(Eq. 2.2)}$$

where h is the Planck constant, which is 6.626×10^{-34} Js. If we include h in the formula for energy (Eq. 2.2), we can rewrite it as:

$$Q = hc/\lambda \qquad \text{(Eq. 2.3)}$$

Consequently the energy of photons is decreasing with increasing wavelength (Figure 2.2). In shorter wavelengths the ultraviolet are appearing, followed by x- and gamma-rays; the latter have

a very high content of energy. On the other end, towards low frequencies, micro- and radio waves come after the infrared region containing low energy.

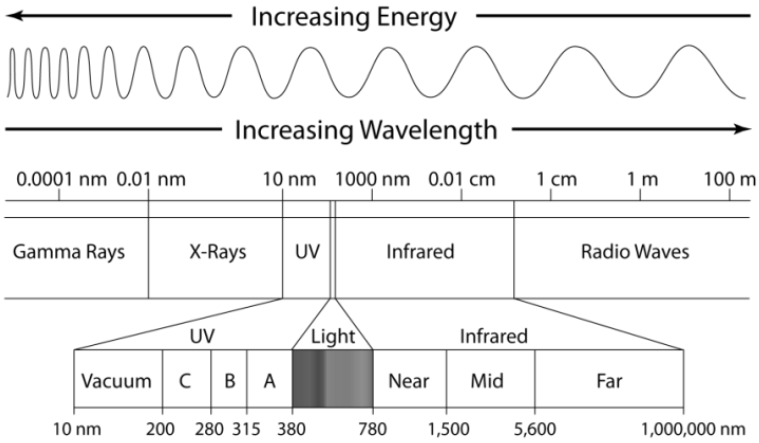

Figure 2.2: Electromagnetic spectrum (Lambert and Edwards, 2013).

What we can see with our eyes, is, generally speaking, a certain amount of light that is reflected or emitted by objects and matter. For us only the range of the spectrum about between 400 and 700 nm is visible with a maximal sensitivity at 550 nm (Mather and Koch, 2011). Inside the eye there are two types of receptors that are responsible for our color vision. The specialized cone cells are most sensitive to light at about 425, 530 and 560 nm, representing blue, green and red (Figure 2.3). Rod cells are more sensitive to light and hence important for the night vision. Their responsiveness peak is around 500 nm.

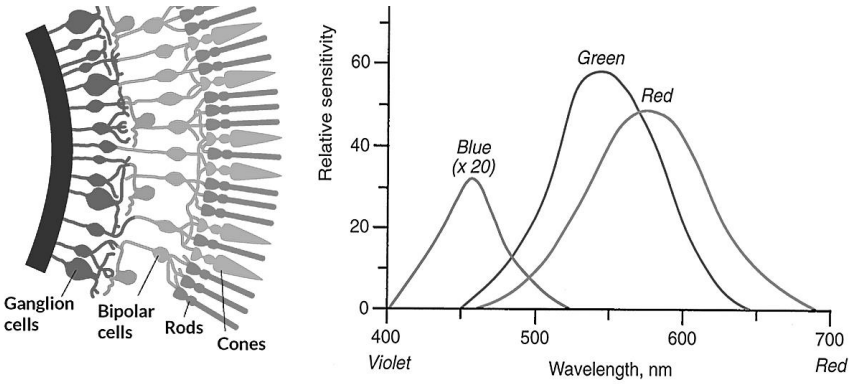

Figure 2.3: Left: Human eye's back part with receptor cells (SSP, 2015). Right: Response functions of the blue-, green- and red-sensitive cones in human eyes (Mather and Koch, 2011).

2.2 ILLUMINATION AND GEOMETRY

At this point it is useful for clarification to have an overview about terminology in hemispherical and directional radiation measurement (Table 2.1). The radiant energy is defined as the total energy that is radiated to or from all directions and usually noted in joule [J] which is newton

meter [N m] or watts multiplied by seconds [W s]. We can measure the incoming radiation or *irradiance* per time and area as radiant flux in watts per square meter [W m^{-2}]; while *radiance* considers a solid angle and not the complete hemisphere. It is usually noted in watts per square meter and steradian [W m^{-2} sr^{-1}].

Table 2.1: Selected terms and their definition used in radiation measurement (Jones and Vaughn, 2010; Lillesand et al., 2008).

Unit	Definition
Radiant energy (Q), [J] = [W s]	Total energy radiated in all directions
Radiant flux (F, Φ), [Js^{-1}] = [W]	Radiant energy emitted or absorbed per unit time
Irradiance (E), [W m^{-2}]	Radiant flux incident on unit area
Spectral irradiance (E_λ), [W m^{-2} nm^{-1}]	Radiant flux per wavelength incident on unit area
Radiance (L), [W m^{-2} sr^{-1}]	Radiant flux per unit area of surface per unit solid angle
Reflectance (R, ρ), [unit-less]	Ratio of incoming and reflected radiation

However, *reflection* is the central process and describes the amount of the incoming light that is thrown back from an object. One way to make data comparable and interpretable is to work with spectral reflectances derived from digital numbers or radiances, respectively (Eq. 2.4).

$$Reflectance = \frac{reflected\ radiation}{incoming\ radiation} \quad \text{(Eq. 2.4)}$$

The values range between 0 and 1 (0-100 %), as they define the ratio of reflected and incoming light – being more precisely the ratio of reflected radiant flux to incident radiant flux. Object surfaces can behave in very different ways. At a perfect specular object like a mirror the incident angle of incoming beams equals the exit angle. Diffuse or Lambertian materials are isotropic and reflect the incoming light equally to all directions (Figure 2.4). An example of a nearly diffuse object is the screen in cinemas. Here, up to a certain degree, the viewing position has not a big impact on the quality of the picture.

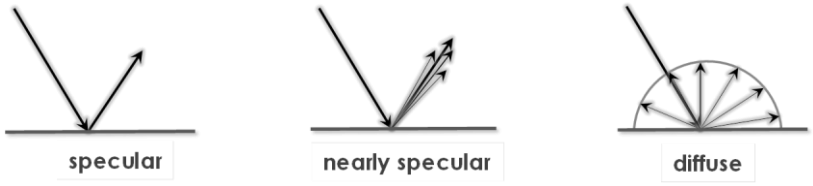

Figure 2.4: Different types of reflecting surfaces.

Hence, in reality surfaces are rather rough, often facing a mixture of these concepts and showing anisotropy. Especially when observing an object or a landscape consisting of several surfaces with different reflection behaviors from a distance. Another effect is apparent when the source of light

like the sun is in the same angle as the viewer. Here the reflected beams often create a hot spot in a specific region having the brightest values.

Not only the reflected radiation, but all kind of EMR is principally spreading to any direction and following the inverse square law. That means that the intensity, the energy per area, is depending on the angle and decreases with the distance to the light source: at a doubled distance the intensity (observed brightness) is four times lower. However, the theory of reflectance geometry is rather complex and not as trivial as it may appear at first glance. Of the nine geometries proposed by Nicodemus et al., 1977, only two are relevant for practical measurements. What we usually measure in the field 2or by remote sensors is in most cases hemispherical-conical reflectance (Figure 2.5). Strictly speaking, the frequently used term 'bidirectional' can in fact be seen as a rather theoretical concept than a measureable parameter.

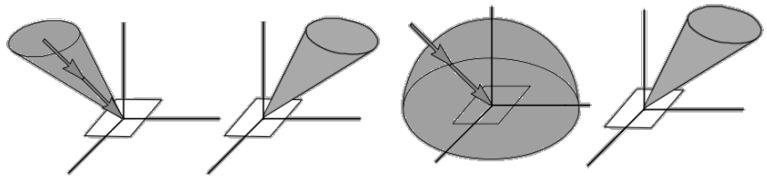

Figure 2.5: The conical (left) and hemispherical-conical (right) reflectances are normally measured (Nicodemus et al., 1977; Schaepman-Strub et al., 2006, modified).

The difference between reflectance and reflectance factor is sometimes not clearly emphasized; see Nicodemus et al. 1977 and Schaepman-Strub et al. 2006 for further readings. Nonetheless, the reflected signals are always depending on several variables like viewing and illumination angles in azimuthal and zenithal directions (Figure 2.6). The corresponding bidirectional reflectance factors (BRF) can be described by the viewing angles (Θ_v, Φ_v) and illumination angles (Θ_i, Φ_i) of incoming (I) and reflected radiation (R) (cf Nicodemus et al., 1977; Walter-Shea and Biehl, 1990).

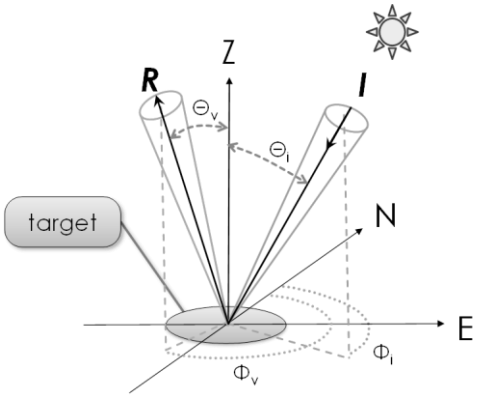

Figure 2.6: Reflection and illumination geometry. R=reflected radiation, I=incident radiation, Θ_v, Φ_v=viewing angles, Θ_i, Φ_i=illumination angles; N=north, E=east, Z=vertical zenith direction.

Furthermore, the Lambert's cosine law says that the incoming radiant intensity and reflected radiation L depends proportionally to the cosine angle between the incoming light and the surface of an ideal diffuse object ($L \sim cos(\theta_i)$):

$$E_\theta = E * cos(\theta) \Rightarrow E = E_0 * cos(\theta_i) \quad \text{(Eq. 2.5)}$$

where E_0 is the incoming radiant energy, E is the effective energy. Hence, it follows for a Lambertian object:

$$L = \frac{E_0}{\pi} cos(\theta_i) \quad \text{(Eq. 2.6)}$$

These are simplified and ideal assumptions for rather flat terrain. For sloped terrain, the effective incident angle i can be defined by (Smith et al., 1980):

$$cos(\theta_i) = cos(\theta_s) * cos(\theta_n) + sin(\theta_s) * sin(\theta_n) * cos(\phi_s - \phi_n) \quad \text{(Eq. 2.7)}$$

where θ_s is referring to the solar zenith angle and θ_n to the normal zenith angle or terrain slope, ϕ_s is the surface azimuth and ϕ_s is the solar azimuth.

2.3 IMPACT OF THE EARTH'S ATMOSPHERE

2.3.1 Scattering

Another important process which is influencing the optical appearance of objects and the photon's path through the air by redirecting is *scattering*. There are mainly three types of scattering (Landgrebe, 2003). Rayleigh scattering occurs when the atmospheric particles have a very small size in comparison to the wavelength of the radiation. On the optical range, the shortwave ultraviolet and blue light is scattered at first and the most, whereas towards the infrared this effect is decreasing. This is the reason why the sky appears blue. Due to this, the sky appears rather reddish during sunset as all blue light is scattered completely in the longer atmospheric path. Particles like dust, water droplets or smoke that have a similar size like the wavelength of the scattered rays are causing the Mie scattering. Its wavelength dependence is a bit more complex than in the Rayleigh scattering. The third type is the nonselective scattering. Here all wavelengths are scattered equally by large particles like water droplets or dust. Hence, scattering depends on the viewing and illumination angles. This has an impact on the appearance and reflection values within one scene. Figure 2.7 shows the effect of angle-dependency on both, scattering and reflectance. From that, it is clear that the reflection of the closed forest canopy is rather anisotropic. This is a proper example that the Lambertian assumption is not valid but only a rough approximation.

Figure 2.7: Extreme examples for backward scattering 'with' the sun (left) and forward scattering 'against' the sun (right) showing a beech forest canopy from the top of a tower in summer, own photos.

2.3.2 Sunlight and the atmosphere

Atmospheric *absorption* leads to the presence of so-called atmospheric windows. That means that the transmittance is wavelength dependent and EMR can penetrate the atmosphere only at certain portions of the spectrum. In other parts, the path of radiation is disturbed or blocked completely (Figure 2.8). This is crucial for channel selection of sensors detecting up- or down welling radiation, for in some wavelengths sensors are just 'blind'. Water vapor (H_2O) is responsible for the water bands at about 1400 and 1900 nm. They might be obsolete only under very dry conditions. The other main gases causing the absorption are carbon dioxide (CO_2), methane (CH_4), nitrous oxide (N_2O), oxygen (O_2) and ozone (O_3). Besides clouds, these gases are mainly responsible for the heating of the atmosphere, what we commonly name the greenhouse effect. Nevertheless the bigger part, almost 50 %, is being absorbed by the surface rather than by atmosphere (Trenberth et al., 2009). We can read the energy budget for the shortwave radiation as the sum of reflected, absorbed and transmitted radiation. About one third of the incoming sun light is reflected within the atmosphere and by the surface (Mather and Koch, 2011). For the sake of completeness, it should be noticed that the surface emits thermal radiation as heat. However, this study is not regarding this longwave emission. The focus is rather on the range of 400-2500 nm, which is also referring to the visible, near- and shortwave infrared regions in optical remote sensing. Corresponding solar radiation, the energy of the light emitted by the sun is about 1367 Wm^{-2} at Earth's top of atmosphere – similar to a 5800 K blackbody. It is striking that the shape of solar radiance is strongly depending on the selected units. When choosing radiant flux per wavelength the maximum is at about 500 nm, whereas it would be around 880 nm when the dependent variable is frequency instead. As this is a kind of a distribution function, one should not compare it with the functions of the sensitivity of our eyes. This is often misinterpreted and resulting in the conclusion that we are evolutionary optimally adapted to maximal solar output (Soffer and Lynch, 1999). At a more detailed level the spectral irradiance E_λ is the energy flux per wavelength unit, e.g. watts per square meter and micron. As described above, the irradiance at sea level differs from the sun light at the top of Earth's atmosphere. Absorption, reflection and scattering effects cause a

specific pattern and a lower intensity of the beams that reach the ground (Figure 2.8). Molecules like water and carbon dioxide induce furthermore the characteristic absorption bands, which imply that the insolation is extremely sensitive to atmospheric gases. Whereas the impact of clouds is not only fix for the water bands but rather affecting all the spectrum. Figure 2.9 depicts the decreasing effect of a thin cirrus-like layer on a rather sunny day. The graph is based on own measurements conducted in May at a latitude of about N 51°.

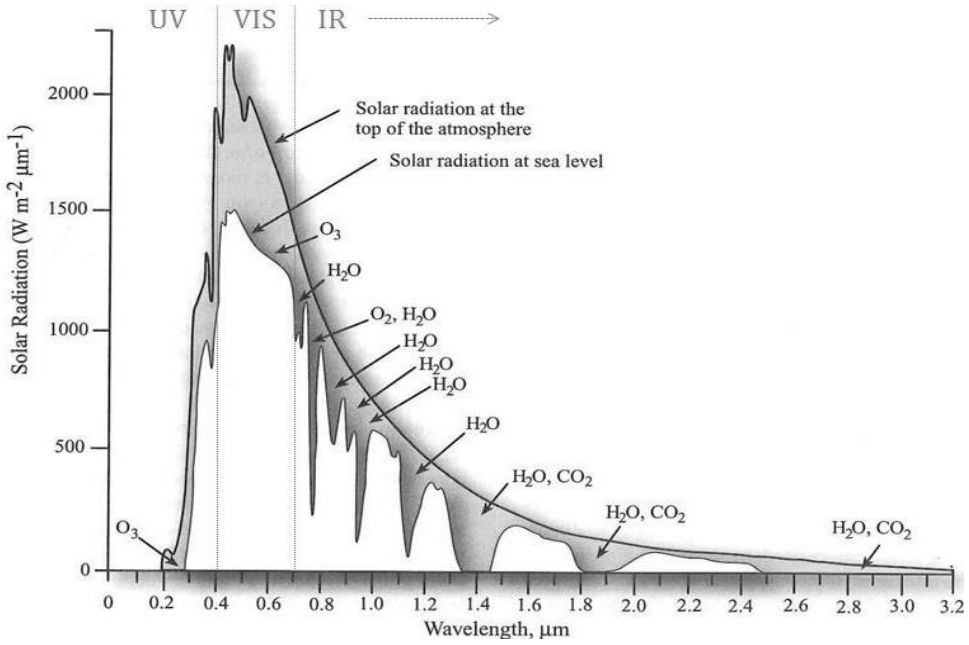

Figure 2.8: Solar radiation spectrum at Earth in the ultraviolet (UV), visible (VIS), near- and shortwave infrared (IR) spectral domain showing the absorption bands of ozone, oxygen and carbon dioxide (Jensen 2007, modified).

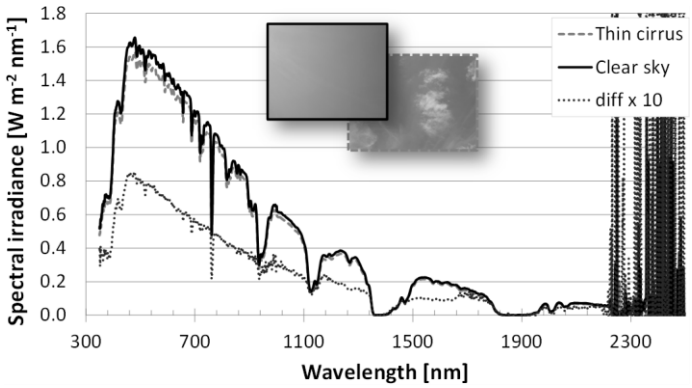

Figure 2.9 : Spectral irradiance at clear sky (solid line) and with cirrus and minor cloud cover (dashed gray line) and the difference (multiplied by 10) (dotted line); own measurements, date: 25.05.2012.

There is a clear and obvious relationship between the sensor-target angle and the energy content of the rays reaching Earth's surface. The irradiance quantity at surface level depends on the location on Earth, sun elevation angle, date and time. Commonly there are changes during the day with some stable conditions around the maximum at noon (Figure 2.10). This can be relevant when

planning a flight or field campaign and undertaking repeated and comparable measurements. As the global PAR radiation is highly correlated with the sun elevation angle, also other wavelengths show an increase with a peak around noon. Figure 2.11 depicts some measurements from shortly before 10:00 am until 01:00 pm, when the sun zenith is coinciding with the most powerful radiation. In absolute terms the changes in the shortwave infrared are apparently less than in the visible range. Again, at higher wavelengths over 2200 nm there is remarkable noise in the data induced by the sensor.

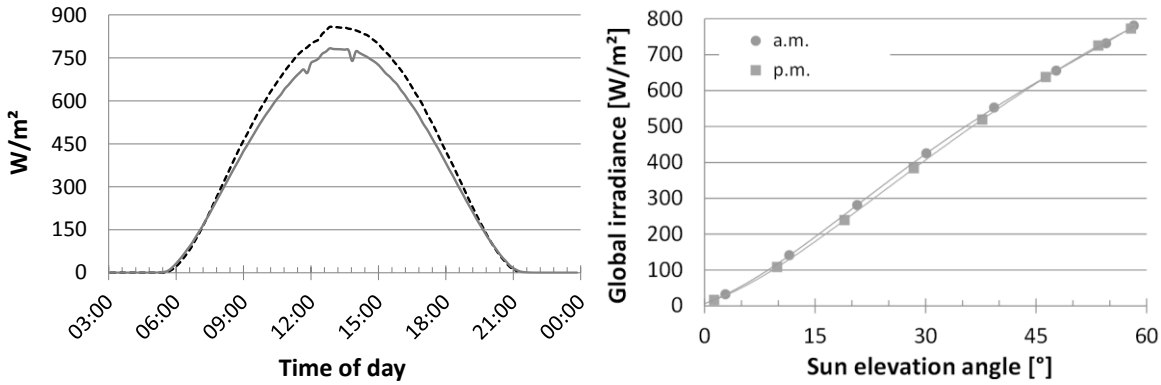

Figure 2.10: Left: Global PAR irradiance measured on towers at two sites in the Hainich national park on canopy walk (solid line), core area (dashed line). Right: Relationship between global irradiance at a canopy walk and sun elevation angle during 06:00-21:00, 24.07.2012.

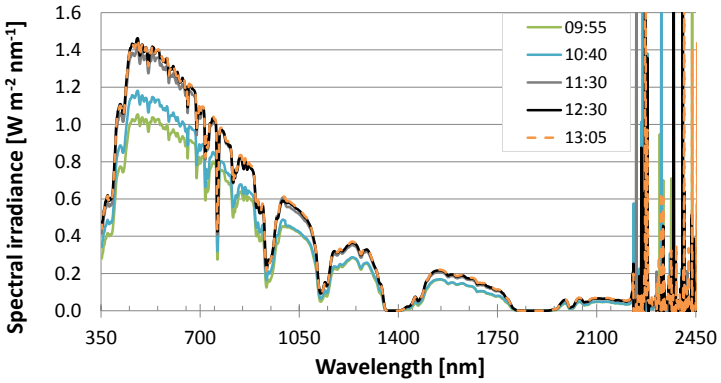

Figure 2.11: Spectral irradiance in dependence on the daytime, date: 20.08.2011, at about 51.1°N, 10.5°E.

2.4 REMOTE SENSING TECHNOLOGY

For a better understanding of the evolution and theory of remotely sensed imaging a short excursus shall be given now. There are mainly two types of platforms: airborne and spaceborne. The history of remote observation begun in the 19th century by using balloons and even cameras attached to pigeons. As often in the history, military purposes enforced the development of methods and technology. In the First World War, the air forces took pictures from zeppelins and planes mainly for reconnaissance, in the Second World War the success of bombing missions was

checked additionally by aerial photography (Baumann, 2014; Granshaw, 2015). In that time also infrared and radar measures had been incorporated starting a period of more elaborate utilization. One decade after successful launches of orbiting satellites in the 1960's a series of operational systems had been evolved with the Earth Resources Technology Satellite (ERTS-A), also known as Landsat-1 (Boyd and Danson, 2005; Campbell, 2006; Lillesand et al., 2008; Steiner and Gutermann, 1966).

The carried sensors or camera systems themselves can be split into groups of active sensors on one side and passive sensors on the other side. Active sensors emit or transmit, as the name implies, actively a certain range of the spectrum and receive and decode the returned signals. Mostly used examples are radio wave-based Radar (Radio detection and ranging) and laser-based Lidar (Light detection and ranging) technologies, commonly operating in a wavelength range of 1-100 cm. By contrast, passive sensors do not have their own source of energy or light which is usually the sun. Common photo cameras and most of the remote sensing sensors belong in this class as well as the instruments in this study. At all systems the path of incoming and reflected radiation is through at least a part of the atmosphere, and hence the signal is distorted by absorption and scattering. Additionally, adjacency effects by the neighboring areas of the focused target are influencing the signal. The common spectral range is 400-2500 nm.

There are four main resolutions that we should consider when dealing with remote sensing data: The *temporal* resolution defines the date and time of acquisition. This also incorporates monitoring aspects for repeated measurements of a specific area or landscape. The repetition time for a Landsat 8 satellite is 16 days, e.g. The *radiometric* resolution provides information about how the data is stored, or, better speaking, of how many grey values the image consists of. As it sets the contrast, it is hence also referred to sensitivity and usually determined in terms of bits, like 8-bit (=2^8) or 16-bit (=2^{16}). The *spectral* (optical) resolution is the covered wavelength range related to the number of spectral bands as it is linked to the bandwidth and is described by the full width half mean (FWHM). It is sometimes mixed up with the spectral sampling interval (Figure 2.12), which defines the steps of bands.

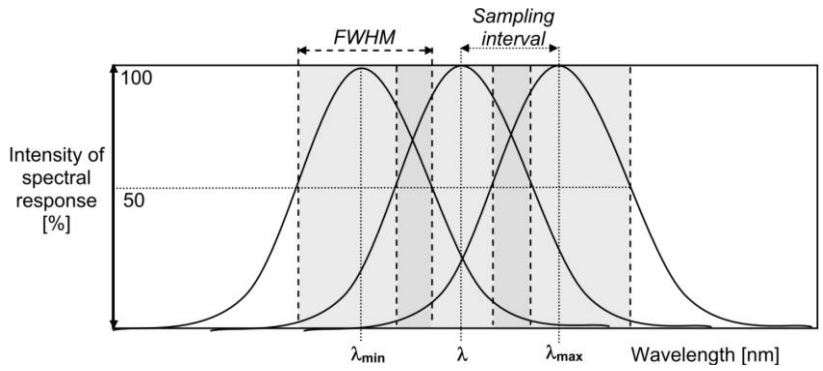

Figure 2.12: Concept of spectral resolution (FWHM) and sampling interval (Malenovský et al., 2007).

Finally, the *spatial* resolution is mainly about the pixel size. It is depending on the sensor's capability, size of the CCD array (charge-coupled device) and the viewing angles. Some important terms in remote sensing and its significance are: FOV=field of view, defines the swath width; IFOV=instantaneous field of view, defines the individual sensors' angle; GIFOV=ground instantaneous field of view, is the projected IFOV to the ground. The GSD=ground sample distance, (from GIFOV, detector size), defines finally the resulting pixel size (Figure 2.13). The spatial image resolution is crucial for detecting objects.

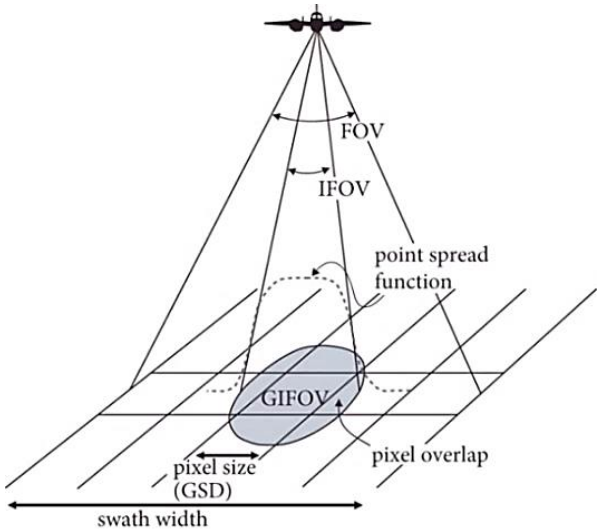

Figure 2.13: Illustration of some important key terms in remote sensing (Jones & Vaughn, 2010).

2.5 HYPERSPECTRAL SENSING

2.5.1 Non-imaging spectroscopy

When sunlight hits a surface, it depends on the material's properties and several processes like absorption how it appears and whether it is brighter or darker in specific wavelengths. By interpretation of reflected radiation, in relation to the incident radiation, we can draw conclusions about type and condition of the target matter. In many situations – not only in research – it is necessary to gain spectral information concerning the characteristics and composition of materials and objects on the ground. In order to emphasize the contrast of land cover types appearances Figure 2.14 depicts some targets with variable reflectances. The typical response patterns are apparent. Asphalt shows compared to gravel a rather low reflectance over the whole spectrum. Notice that grass shows a very typical vegetation reflectance curve with rather low values in the visible region and an increased signal in the near infrared.

Non-imaging field spectroscopy is a way to measure in situ radiation near the object or with direct contact using special hand-held instruments. With a spectroradiometer, it is possible to detect radiation in calibrated units like relative reflectances as a ratio of incoming and reflected rays, or

radiances and irradiances as flux per area. The user can record data in a high number of narrow bands over a rather wide range of the electromagnetic spectrum. However, according to the focus of the study in the following only the range of about 400-2500 nm is considered. The field spectroradiometer used in this study is an ASD FieldSpec 3 Hi-Res (Analytic Spectral Devices Inc., Boulder) which will be described in the next chapter in more detail.

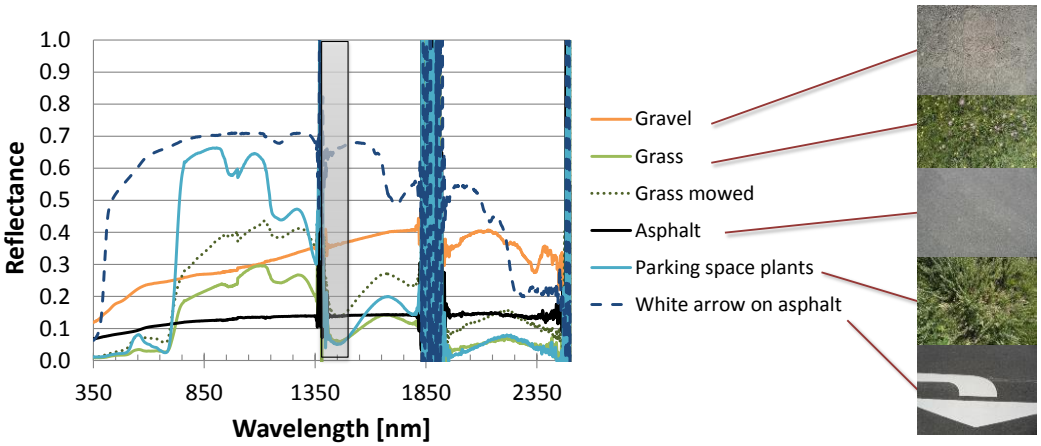

Figure 2.14: Ground raw reflectances derived with ASD FieldSpec 3; sensor-related jump at 1000 nm and the water bands at about 1400 and 1900 nm are recognizable as well as noisy signals at the end; own measurements.

As an accurate and rather sophisticated topic the field spectroscopy has been used in a variety of modern research questions (Milton et al., 2009). Measurements taken in the field can be linked to remote sensing directly (Groeneveld et al., 2006) or used for calibration purposes (Smith and Milton, 1999). However, several studies have been carried out on targets that are rather easy to access (Arafat et al., 2013; Ramakrishnan et al., 2013; Schmidt and Skidmore, 2003), but when dealing with non-imaging spectroscopy in forests the circumstances are obviously entirely different. The most self-evident challenge is the tree height of about 20-40 m in temperate forest stands, which makes it difficult to reach the top of the crowns for measuring. There are several ways for harvesting leaves and branches to get samples without felling trees: some inventive methods use helicopters (Milton et al., 1994) and towers (Leuning et al., 2006), catapults (Omar, 2010) or slingshots, pole pruner, canopy crane (Castro-Esau et al., 2006) and even shotguns (Clark et al., 2005; Clark and Roberts, 2012; Ollinger et al., 2008). Besides the height issue, the surfaces of canopies are rather uneven and complex creating differences in reflection. Holes and gaps caused by the crown structure create a rough pattern and generate shadowed and sunlit parts having different spectral responses which highly depend on the scale. Additionally, trees of uneven age and growth have a variable appearance. On the level of leaves as crown compartments, these differences might be completely altered or even interspecific absent. Hence, the discrimination of species is another complex topic.

2.5.2 Imaging Spectroscopy

2.5.2.1 Background

In opposite to the low-band-number systems emerging hyperspectral sensors offer a completely new point of view to our world. The data consist not only of a few but rather of hundreds of bands – for comparison: 8 broad bands of multispectral Landsat 7 ETM+ and 220 spectral bands of hyperspectral Hyperion. Figure 2.15 shows the distinct response functions representing the sensor's sensitivity of each channel of four common multispectral satellites as implemented in the R-package *hsdar* (Lehnert et al., 2015). For comparison, a continuous hyperspectral leaf reflectance curve is also plotted.

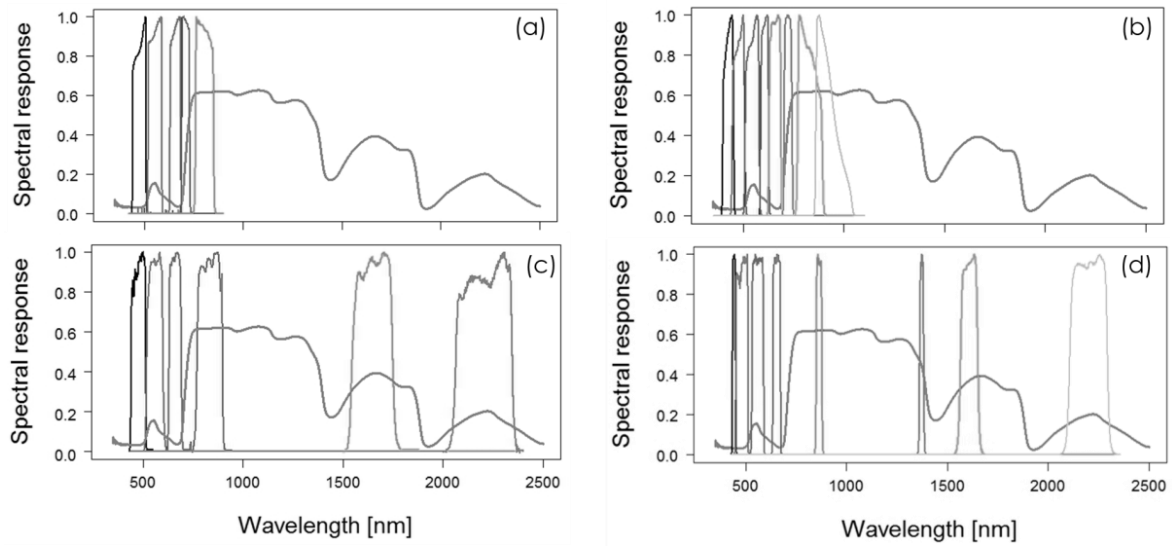

Figure 2.15: Examples of sensor sensitivity as relative response functions for (a) RapidEye, (b) Worldview2 (c) Landsat 7 and (d) Landsat 8. For comparison, a hyperspectral reflectance curve of a beech leaf derived from field spectroradiometer based on own measurement is shown.

For the definition and characteristics the presence of narrow and contiguous bands is more important than just the number of channels alone (Qi et al., 2012). Hence, the term *hyperspectral* does not have a direct physical meaning but is rather referring to the large number of channels. In this context we can translate *hyper*, which means 'beyond', actually with 'too much'. This is also because many neighboring bands are containing redundant information and are partly highly correlated, so that they have to be filtered according to the intention and target information. Moreover, some bands might not contain any useful information at all due to absorption and noise. The high spectral resolution can cause classification problems. The Hughes' phenomenon describes for example the curse of dimensionality and says that the higher the number of dimensions the higher the estimation error and the poorer the performance of classification can be (Hughes, 1968; Shahshahani and Landgrebe, 1994). That can easily occur when using hyperspectral data having much more bands than training samples. Hence often data reduction techniques like principal

component analysis (PCA), minimum noise fraction transformation (MNF) and discriminant analyses (Chang, 2013; Kalacska et al., 2007; Pu, 2009) or other more appropriate methods are applied. Another reason for reducing the amount of information is to create data sets, which are easier to handle.

Hyperspectral RS is also referred to imaging spectrometry or imaging spectroscopy (Goetz et al., 1985; Green et al., 1998). In imaging spectroscopy, besides the two spatial axes of an image, there is a third axis representing the hyperspectral bands. That is why data can be represented as a three-dimensional data cube (Figure 2.16). Each picture element contains information for every channel leading to a specific vector of values. Plotting them yields a continuous graph which some authors call spectral signature. But this implies that targets are constantly distinctive and unique. However, the reflection of Earth's land cover surfaces is rather ambiguous and varies with the condition and time. Users should be aware that there is not the one and only signature for a specific category – apart from pure material often analyzed under laboratory conditions. Hence, we should talk rather about spectral curves or spectral response patterns than about spectral signatures.

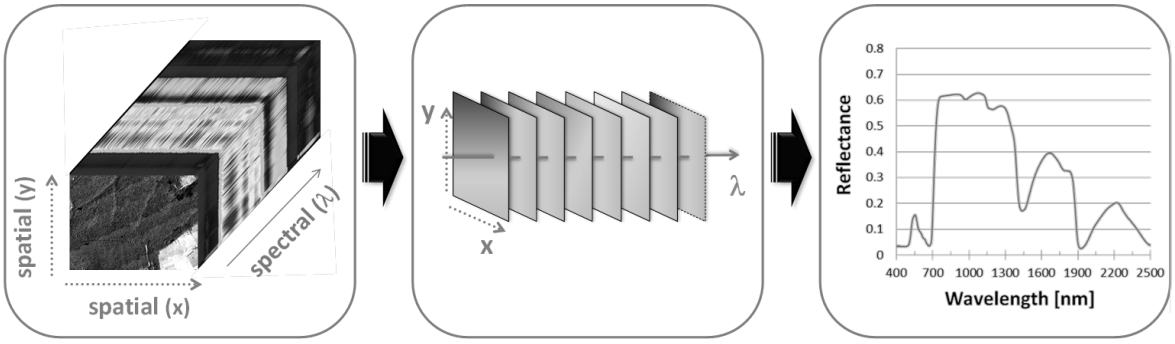

Figure 2.16: Relationship between hyperspectral image cube (left), picture element (middle) and spectral response curve (right) (Aberle, 2014, modified).

Imaging technology with a very high number of bands has been used in the investigation of lake sediments (Grosjean et al., 2014), human biomedicine (Medina et al., 2011) and also food quality (Gowen et al., 2007; Huang et al., 2014; Saldaña et al., 2013). However, one big issue is the observation of objects from a larger distance by remote sensing. Just as the non-imaging spectroscopy hyperspectral remote sensing is incorporating many possible applications like marine research (Vahtmäe et al., 2006), urban information and planning (Cilia et al., 2015; Heiden et al., 2012; van der Linden and Hostert, 2009), mineralogy and geology (Crouvi et al., 2006) and agriculture (Arafat et al., 2013; Thenkabail et al., 2000).

2.5.2.2 Image radiance and ground irradiance

The following paragraph shall give an example of how measured irradiances can be used for direct image corrections. When operating hyperspectral imaging sensors such as AISA (Airborne imaging spectrometer for applications) EAGLE and HAWK (SPECIM, SPECTRAL IMAGING LTD., Finland), spectral irradiance is measured by default at the aircraft using the diffuse fiber optic down welling irradiance sensor (FODIS). In this case, additional to the airplane's sensor irradiance, also ground irradiance was measured close to the forest by a cosine receptor attached to an ASD FieldSpec 3 – in next chapters referred to as above-canopy irradiance. Using this we can rather simply derive a reflectance image (Figure 2.18 b) by:

$$R = \left(\frac{L}{E}\right) * \pi \qquad \text{(Eq. 2.8)}$$

where R is representing the reflectance value, L the image radiance and E the spectral irradiance. After spectral smoothing with a Savitzky-Golay filter (Savitzky and Golay, 1964; Schafer, 2011) the result is at first glance similar to atmospherically corrected reflectance AISA EAGLE/HAWK imagery used in this study (Figure 2.18 c). Note that no explicit atmospheric correction was done using additional software tools. However, it is rather noisy and the water bands are apparent.

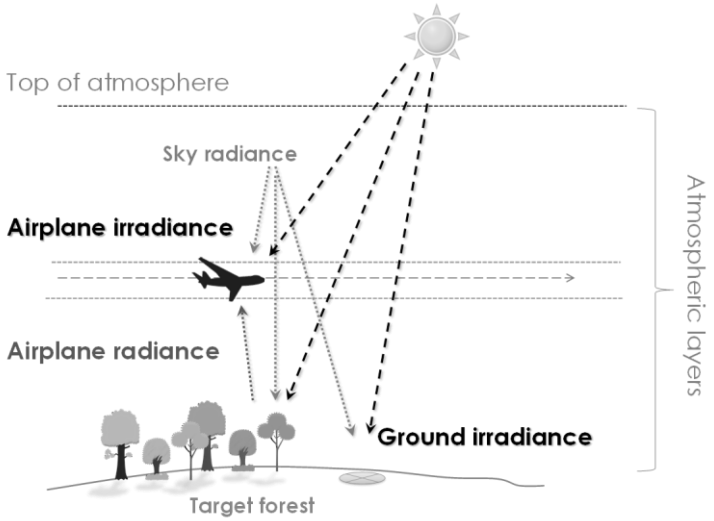

Figure 2.17: Scheme of measuring radiances and irradiances at the airplane's and the ground sensor.

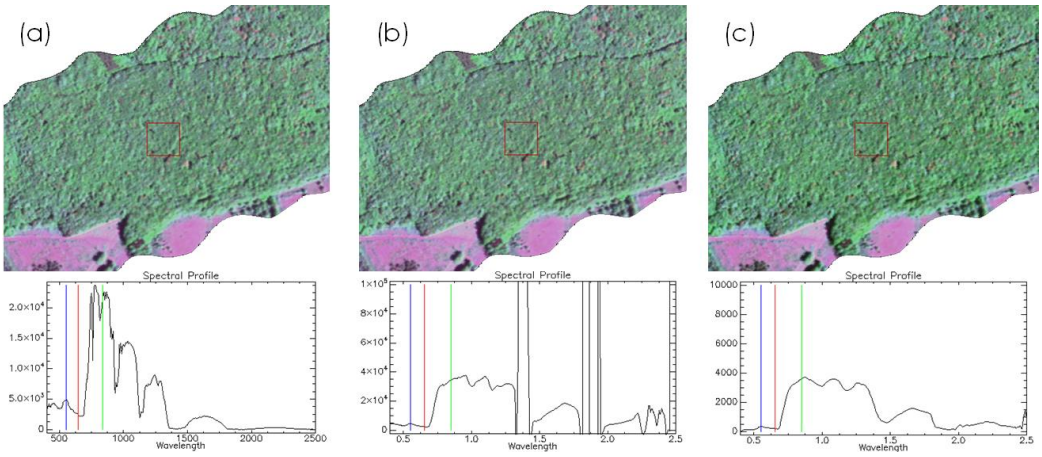

Figure 2.18: Spatial subset (RGB: ~650-870-550 nm) from hyperspectral AISA EAGLE/HAWK flight stripe and the corresponding spectral profiles of the central pixel. (a) Original radiance image without atmospheric correction. (b) Own reflectance image as ratio of image radiance to ground irradiance multiplied by π with an additional application of a 2-5-5 Savitzky-Golay filter. (c) Delivered reflectance product for comparison.

2.5.2.3 Hyperspectral imaging sensors

Several countries are operating hyperspectral-imaging sensors in remote sensing. The following passage will present some examples of recent and future missions (see also Staenz and Held, 2012; Vorovencii, 2009), as there is an ongoing development and constant release of new sensors. Obviously, for technical and practical reasons, there are more aerial platforms than space-based. Some selected hyperspectral earth observation satellites that should be mentioned in this context are NASA's FTHSI (on MightySat II), Hyperion (on EO-1) and HICO (on International Space Station ISS), ESA's Chris (on PROBA-1), and China's HJ-1A. For the upcoming years there are also some new space-based missions planned: HyspIRI (USA), PRISMA (Italy) and HISUI (ALOS-3) (Japan), see Table 2.2. The German-led hyperspectral satellite mission EnMAP (Environmental Mapping and Analysis Program) has to be highlighted here, as this study had been conducted within the framework of preliminary investigations in a national research program. EnMAP shall offer 244 bands over the range of 420-2450 nm at a GSD of 30 m (Kaufmann et al., 2014). Its postponed launch is scheduled for 2018 (Guanter et al., 2015) (May 2015, enmap.org). The most prominent airborne systems are AVIRIS, HyMap, HySpex, Hydice, CASI, series of AISA and DAIS, EPS-H, PROBE-1 and APEX. Usually mounted on aircrafts they deliver a GSD depending on their IFOV and the distance above the ground. Flight height is normally ranging between 1000-2000 m. Typical applications are rather experimental tests and still small-area investigations. In this study the combined AISA (Airborne Imaging Spectrometer for Applications) sensors EAGLE and HAWK are used, an along-track scanning system.

Table 2.2: Overview of selected former, current and planned space- and airborne hyperspectral sensors.

Type	Sensor	Spectral range	Bands	GSD
Spaceborne	MODIS	405-14385 nm	36	250-1000 m
	HICO (ISS)	380-960 nm	100	90 m
	Hyperion (EO-1)	400-2500 nm	220	30 m
	Chris (PROBA 1)	415-1050 nm	<150	17-34 m
	FTHSI (MightySat II)	400-1050 nm	142	30 m
	HJ-1A	450-950 nm	115	100 m
	HISUI	400-2500 nm	185	30 m
	PRISMA	400-2500 nm	250	20-30 m
	HyspIRI	380-2500 nm	210	60 m
	EnMAP	420-2450 nm	244	30 m
Airborne	AVIRIS	380-2500 nm	224	depends on IFOV and flight height
	HyMap	400-2500 nm	128	
	HySpex Odin	400-2500 nm	427	
	Hydice	400-2500 nm	210	
	itres CASI	380-1050 nm	288	
	APEX	400-2500 nm	300	
	PROBE-1	400-2500 nm	128	
	DAIS	430-12300 nm	76	
	EPS-H	430-2500 nm	152	
	AISA EAGLE	400-970 nm	122	
	AISA HAWK	970-2500 nm	254	

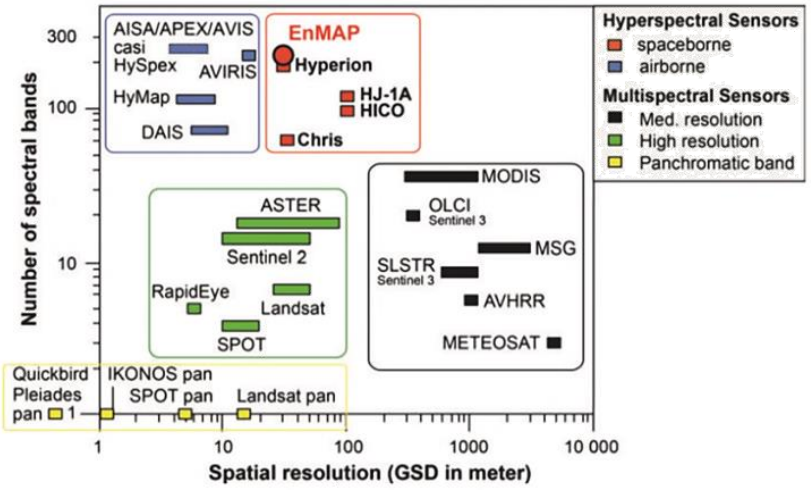

Figure 2.19: Overview of resolutions of some important earth observation sensors (Kaufmann et al., 2012).

2.6 PLANTS AND SUN LIGHT

2.6.1 Photosynthesis and absorption

As mentioned, every type of matter has a different reflection behavior depending not only on the external but also on internal conditions such as the chemical composition. The variability in reflectance of vegetation is furthermore determined by biochemical constituents and their concentrations (Bartlett et al., 2011; Blackburn and Ferwerda, 2008; Ollinger et al., 2008; Ustin et al., 2009). However, plant-related field spectroscopy is nearly always about green vegetation having chloroplasts and doing photosynthesis. The useable range of the spectrum is the photosynthetic active radiation (PAR) and equals almost the visible spectrum (400-700 nm). Since photosynthesis is one of the main drivers in foliage reflectance, it is crucial to know more about the procedures behind. As a central part of the global carbon cycle the energy-storing process of photosynthesis converts water and carbon dioxide to oxygen and carbohydrates (sugar) under the usage of solar light energy ($h\nu$). Thus, it is inducing the accumulation of biomass. The simplified net reaction equation can be written as:

$$6\,CO_2 + 6\,H_2O \xrightarrow{h\nu} C_6H_{12}O_6 + 6\,O_2 \qquad \text{(Eq. 2.9)}$$

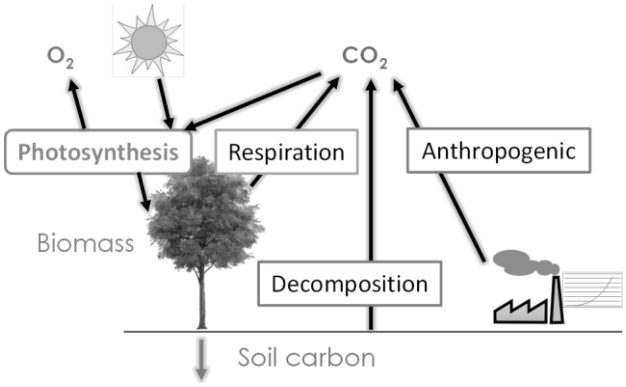

Figure 2.20: Simplified role of photosynthesis as part of the terrestrial carbon cycle – not including oceans.

It is noteworthy but obvious as well that plants do not exploit all of the incoming sunlight properly for growth and metabolism. From an energetic point of view, the whole process of photosynthesis is not very efficient as there is a certain amount of unused energy. About half of the visible light is not usable for the photosynthetic pigments. In addition, the structures of plants or leaves that are not well oriented to the sun are contributing to a loss of energy. Finally, only 5 % is de facto being stored as chemical energy in carbohydrates. This makes it also understandable why a good knowledge about these processes is necessary, as the CO_2 concentration in the atmosphere is increasing and the future effect on the photosynthesis of plants remains partially unclear (Sadava et al., 2011). Chlorophylls and pigments like anthocyanins, carotenes and xanthophylls mainly dominate absorption within healthy leaves. The peaks in chlorophyll-driven absorption (Figure

2.21) at the so-called *Soret* bands are clearly apparent in the blue region of the spectrum as well as the *Q* bands for the red region (Lichtenthaler and Buschmann, 2001; Zigmantas et al., 2002). Compared to reflectances of leaves the extracted chlorophyll shows absorption peaks that are shifted towards the shorter wavelengths about 20 nm (Rühle and Wild, 1979). Additionally, the maxima of the absorption are dependent on the solvent; chlorophyll is not water-soluble. Due to the presence of other accessory and non-photosynthetic pigments the identification of single pigments from a plant leaf can be quite challenging (Buschmann et al., 1994; Ustin et al., 2009). Apart from the absorption caused by photosynthesis there are other interactions occurring as parts of the overall radiation system. Plant leaves emit only small amounts as heat or fluorescence, but reflect and let pass a certain amount of the incident visible and infrared light (Figure 2.22). Absorption, reflection, scattering and therefore transmission are the central processes for the light interception of canopies and wavelength dependent.

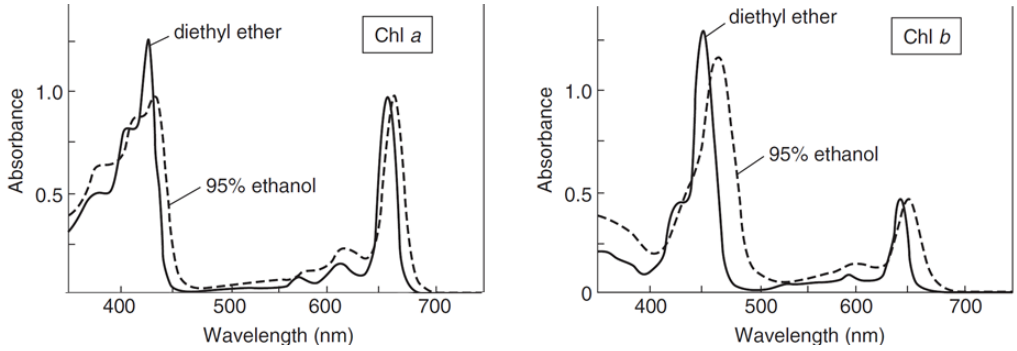

Figure 2.21: Differences in absorption of chlorophyll a and b in diethyl ether and the more polar solvent 95 % ethanol, where a shift of the (smaller) maxima to longer wavelengths is observed; red maxima were set to the same values (Lichtenthaler and Buschmann, 2001, modified).

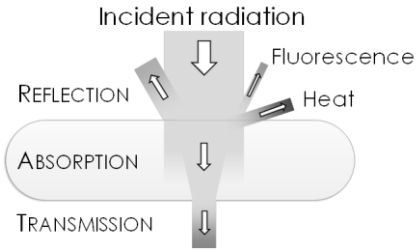

Figure 2.22: Simplified scheme of radiative interactions between incoming sun light and a healthy green leaf.

That leads to the characteristics in leaf reflection, as already touched previously. Due to absorbing processes as described above leaves and needles appear greenish to the human's eyes. This is also evident in the low reflectances in the blue and red range of the spectrum and a small peak at about 550 nm. Very typical for green vegetation is the harsh increase in reflectance in the region at 700-750 nm, called red edge, followed by a high plateau in the near infrared (Figure 2.23). When leaves mature and start withering spectral response curves of vegetation show a completely different

pattern. Besides an obvious change in the visible and red edge area the strongest impact is in the near infrared due to destruction of cell structures and decreased water content. Figure 2.23 shows typical reflectances of a healthy green and a withered leaf, representing photosynthetically active and non-photosynthetically active vegetation, respectively.

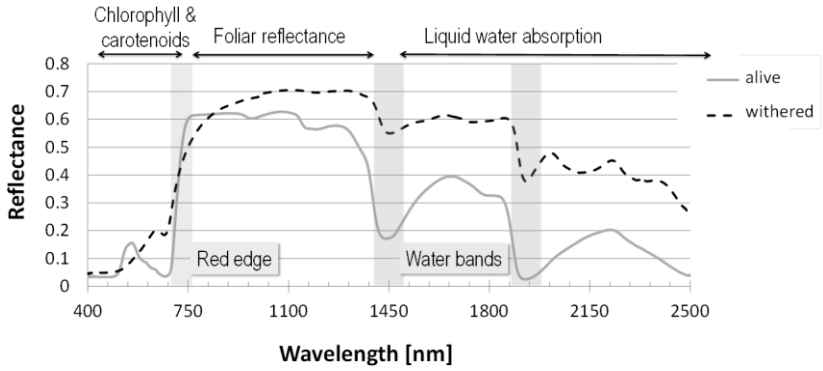

Figure 2.23: Example of spectral response patterns of a living and a withered leaf of Boston ivy vine (*Parthenocissus tricuspidata*); besides the photosynthetic absorption, the red edge and two water absorption bands are the most prominent features; own measurements.

While the chloroplasts in the palisade mesophyll are mainly responsible for reflectance in the VIS region, the spongy mesophyll plays a bigger role in the NIR reflection by multiple scattering. In the shortwave infrared, the reflectance values are normally lower with extreme minima at about 1400 and 1900 nm, which is mainly caused by leaf water. Additionally, the reflection is heavily influenced by cell structure, lignin and cellulose and other biochemicals (Fourty et al., 1996; Jones and Vaughn, 2010). Differences in reflectance are more striking when comparing broadleaf deciduous and evergreen coniferous tree species groups. In the PAR region of the spectrum, we can observe a similar pattern, but especially in the near and shortwave infrared reflection is lower for conifers. This is mainly due to the texture and inner structure of needles having a rather undifferentiated palisade and spongy mesophyll (Figure 2.24). Furthermore, unlike leaves, they usually do not have a distinct upper and lower side and hence show a different reflection behavior.

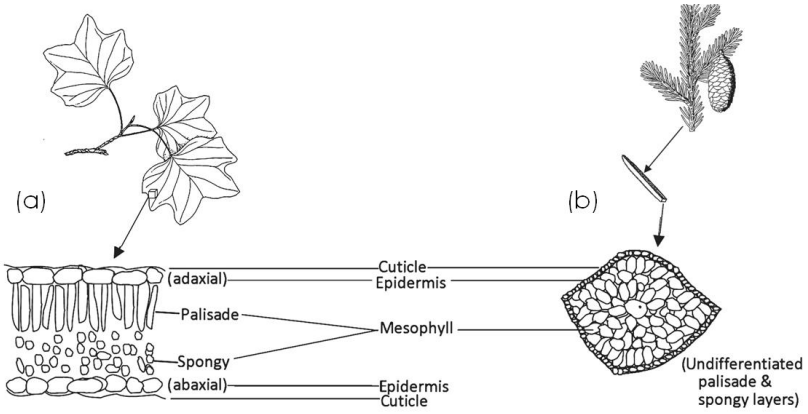

Figure 2.24: Schematic cross section of typical leaves (a) (here: *Liriodendron tulipifera*) and needles (b) (here: *Picea rubens*). Compared to the leaf the coniferous needle shows a more packed structure (USDA Natural Resources Service, 2010, in: Ollinger, 2011, modified).

2.6.2 Spectral indices for vegetation analysis

In both imaging and non-imaging systems, the reflection pattern of plants allows the utilization of special metrics by calculating ratios, differences or other algebraic combinations of reflectance values at specific wavelengths. These vegetation indices (VI) can be brought in relation to a variety of target variables (Bannari et al., 1995; Glenn et al., 2008). By using VI researchers try to get information about the general health condition (Lausch et al., 2013a) but also to derivate biophysical variables (Thenkabail et al., 2000) such as leaf and canopy water content (Colombo et al., 2008) or concentration of chlorophyll (Carter and Knapp, 2001; Wu et al., 2008). In addition, it may help in estimations of leaf area index (Gong et al., 2003; Haboudane et al., 2004) and biomass (Das and Singh, 2012; Van Der Meer et al., 2001). Furthermore, different species, vegetation types and landscapes can be compared and monitored. VI often base upon a normalized difference or a band ratio, like the two most prominent:

- Normalized difference vegetation index (NDVI) (Rouse et al., 1974)

$$NDVI = \frac{\rho_{NIR} - \rho_{RED}}{\rho_{NIR} + \rho_{RED}} \quad \text{(Eq. 2.10)}$$

- Simple ratio (SR) (Tucker, 1979)

$$SR = \frac{\rho_{NIR}}{\rho_{RED}} \quad \text{(Eq. 2.11)}$$

where ρ_{RED} and ρ_{NIR} represent the reflectance in the red and the near infrared region of the electromagnetic spectrum. They exploit the optical properties of healthy vegetation which shows high absorption in red and a high reflection in the NIR. The values for NDVI range between -1 and +1. Healthy green and dense vegetation has a NDVI of 0.6-0.9. Both NDVI and SR tend to saturate in dense stands with high leaf area index and biomass (Huete et al., 2002; Sellers, 1985). They belong to the group of broadband VI and are derived by incorporating a specific but rather wide range of the electromagnetic spectrum. They are commonly calculated for large-area and global applications using multispectral sensors (Huete et al., 2002, 1997). In contrast, hyperspectral data allow the calculation of narrow-band indices using distinct bands of a single wavelength. Due to the high number of bands there are much more possibilities for hyperspectral normalized-difference and ratio indices (Agapiou et al., 2012; Pacheco-Labrador et al., 2014; Schlerf et al., 2005; Zarco-Tejada et al., 2005). Since VI are usually directly linked to the characteristics of green plants and leaves, one can obtain a clear relation to the development stage during a growing season (Figure 2.25) (Cole et al., 2014; Gonsamo et al., 2012).

Le Maire et al. (2004) examined in a comprehensive study all VI published from 1973 to 2002 that are sensitive to chlorophyll. A more recent and thorough overview of all common VI can be found in an online database, in which researchers gathered information about imaging sensor-dependent indices and their possible applications (Henrich et al., 2012). It should be noted that VI values can

differ with the relative response function of each remote sensing system affecting a direct comparison (Cundill et al., 2015; Trishchenko et al., 2002). However, besides the desired factors also other issues such as sensor-sun-geometry, illumination and background soil conditions can affect the apparent reflectance (Liang, 2004).

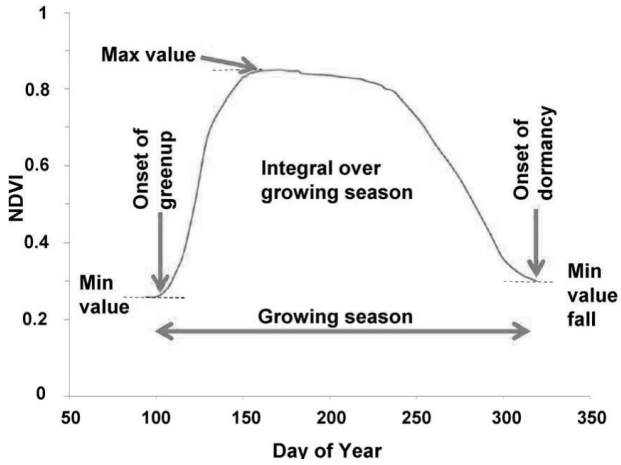

Figure 2.25: Example of a seasonal course of NDVI with key phenology moments (Nilson et al., 2012)

2.7 HYPERSPECTRAL DATA SET

2.7.1 Field spectroscopy

The field spectroradiometer used in this study is an ASD FieldSpec 3 Hi-Res (ANALYTIC SPECTRAL DEVICES INC.) – one of the most popular sensors, which has been recently used in different studies (Bartlett et al., 2011; Ferreira et al., 2013; Manakos et al., 2010; Mansour et al., 2012). The device covers a wide wavelength range by two detectors: one photodiode-array for the visible and near infrared (350-1000 nm) and two photodiode-arrays for the short wave infrared (1000-2500 nm). The spectral sampling is 1.4 nm and 2 nm, respectively. ASD specifies the spectral resolution with 3 and 10nm. It is defined by the full-width-half-maximum. By internal interpolation, it offers finally 2150 single channels and band widths of 1 nm, storing data in 16 bit. Scanning time is 100 ms. Users can obtain wavelength, reflectance, transmittance, radiance and irradiance after calibration. To the input fiber optic cable, having a field of view (FOV) of 25°, several foreoptics can be attached including narrower FOV, a diffuse cosine receptor or contact probe and a clip for direct measurements. It weighs about 5.2 kg, is carried in a backpack and controlled wirelessly by laptop.

Figure 2.26: ASD FieldSpec 3 Hi-Res field spectroradiometer.

2.7.2 Imaging spectroscopy

In contrast to multispectral systems, hyperspectral sensors acquire hundreds of bands. In this study the combined AISA (Airborne imaging spectrometer for applications) push broom line scanners EAGLE and HAWK (SPECIM, SPECTRAL IMAGING LTD., Finland) are used mounted on an aircraft. The sampling interval values are about 4.6 nm (EAGLE) and 6.3 nm (HAWK) (Figure 2.27). The 368 narrow bands cover a spectral range of 400-970 nm and 970-2500 nm, respectively.

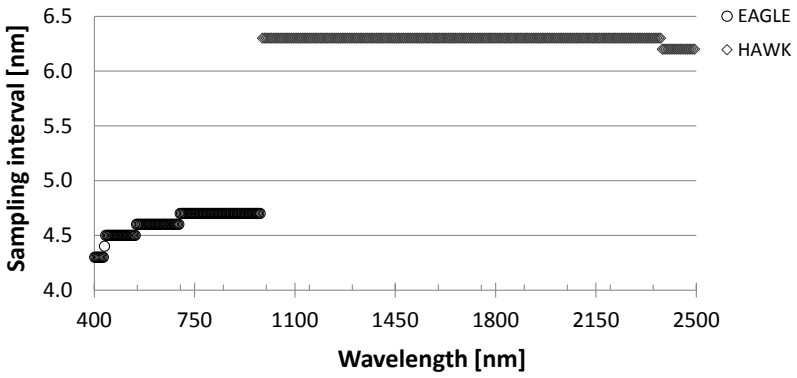

Figure 2.27: Sampling intervals of the delivered reflectance imagery of AISA EAGLE (VIS-NIR) and HAWK (NIR-SWIR).

The sensors detect reflected radiation from the surface and store the signal as radiances. These can be converted to unit-less reflectance by building the ratio to the spectral irradiance measured simultaneously skywards. The flight was conducted on 24.07.2012 at perfect conditions after several attempts and waiting for stable and sunny weather. The planning of the flight campaign was done in consultations with the Department of Computational Landscape Ecology of the Helmholtz Centre for Environmental Research UFZ in Leipzig, which also performed the acquisition and preprocessing including following steps:

- Radiometric and geometric correction using the ENVI module CaliGeo (SPECIM)
- Correction of some sensor-dependent striping effects (Figure 2.30) using the ROME method (Reduction of Miscalibration Effects (Helmholtz Center Potsdam, GFZ German Research Center for Geosciences)
- Atmospheric correction using ATCOR 4, (Atmospheric and Topographic Corrections, RESE)
- Spectral smoothing by a Savitzky-Golay filter incorporating 6 neighboring bands

Resampled pixel size (GSD) is 2.0 m. The delivered product was finally referenced using additional data like aerial images and basemap imagery in ESRI's ArcMap. Every airborne survey has to consider that the aircraft is never completely steady, though the pilots are countering. Besides the forward moving there are the three principal axes in which an airplane can rotate or move (Figure 2.28). *Pitch* defines the up and down movement of the nose. *Roll* is the rotation around the longitudinal axis. *Yaw* describes the movement and heading lo left and right. All these unavoidable

issues have to be corrected and are affecting location and size of picture elements before the final image is ready for analyzing (Figure 2.29). Precise GPS positions are crucial for the geometric correction. The original raw image is rather rectangular, consisting of lines (rows) and samples (lines); the sensor's FOV defines the image width. The corrected image does not have straight borderlines anymore. The influence of the airplane's movement is clearly apparent in the new arrangement and curvy image borders. The planned eight flight lines and the footprints of the finally realized stripes are shown in Figure 2.31. The discrepancy of planning and realization is apparent, as there are a few small gaps between some images. However, the image stripes have a width of about 500-700 m each, a length of about 9-11 km and cover a large area of the northern Hainich national park.

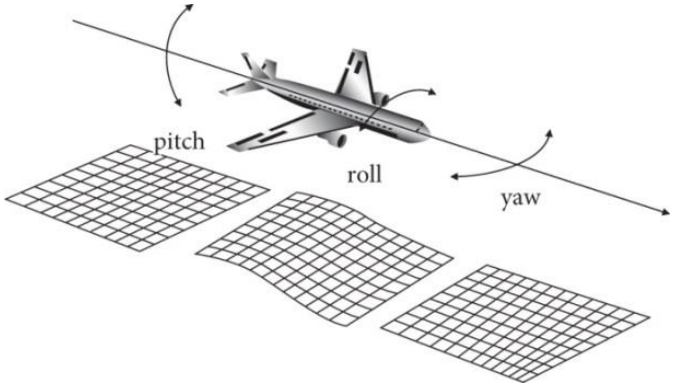

Figure 2.28: Illustration of the effects of aircraft instability due to rotations in three directions: pitch, roll and yaw affect the geometry of single pixels and the whole image (Jones and Vaughn, 2010).

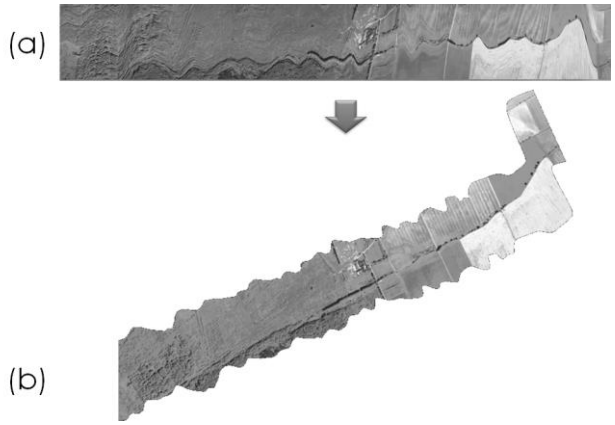

Figure 2.29: Subset of flight stripe number six as raw (a) and final referenced image (b); the influence of aircraft instability is clearly apparent.

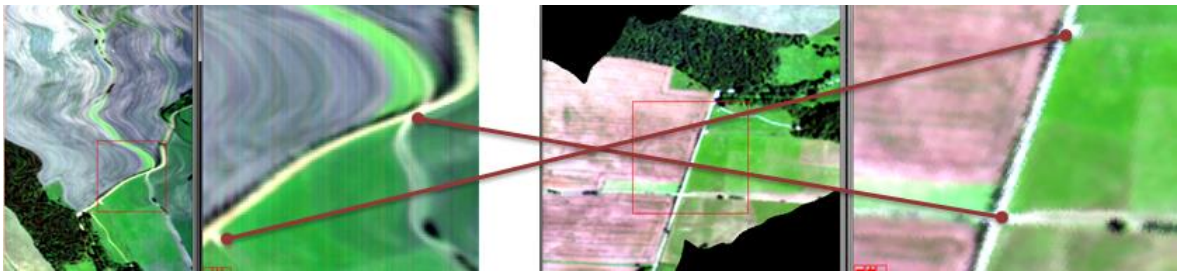

Figure 2.30: Thin stripes are apparent in the raw images (left) and almost completely removed after the processing (right).

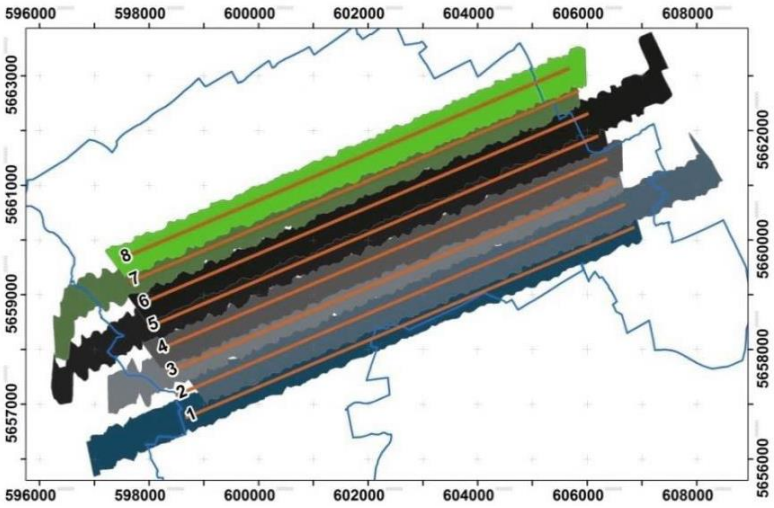

Figure 2.31: Planned flight lines 1-8 (straight lines) and final covered flight stripes (filled areas) within the national park area (outer polygon).

The geometric correction was more challenging because the imagery includes mainly forested area what makes it difficult to find prominent points like cross roads or house corners. Thus, final image matching and georeferencing was done manually by using exposed trees with a prominent crown checking aerial imagery and topographic maps. Additionally, the first and last bands are not included due to noisy signals; the spectral range is adjusted from 0.4019-2.5009 µm to 0.4404-2.3886 µm (Figure 2.32).

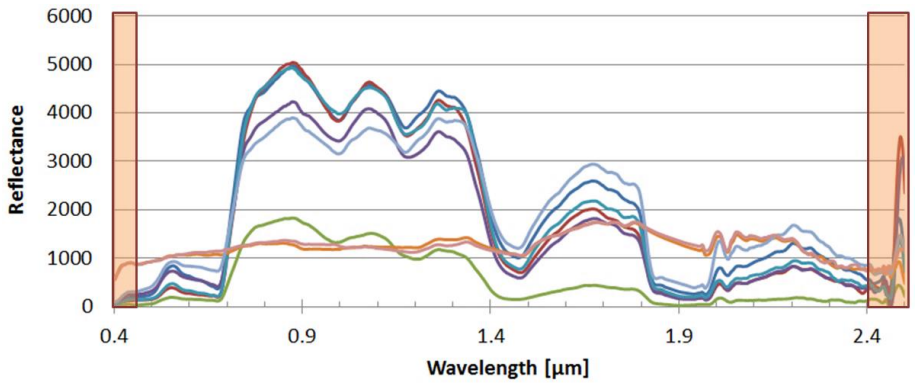

Figure 2.32: Final spectral range after cutting the first and last bands – apparent reflectances using the example of seven arbitrarily chosen pixels.

For better data handling and analysis the eight flight strips need to be aligned and put together to a single file. Loading all tiles simultaneously for mosaicking did not lead to satisfying results due to anisotropic effects and differences in reflectances at the image borders. Instead, this process was done in the software ENVI using a step-by-step approach merging the files consecutively. As mentioned in the first chapter, depending on the resolutions and data type hyperspectral imagery can be quite large in terms of data size. In this case the final mosaic stored as a band-interleaved .dat-file (ENVI standard) occupies disc space of almost 18 GB. For comparison: an uncompressed Landsat 8 scene (Geotiff, Level 1T) has a data size of just about 2 GB, but covers an area of ca. 170 x 183 km, which is roughly thousand times larger than the study site here.

2.8 FOREST DATA SET

2.8.1 Inventory plots

2.8.1.1 Sampling and plot design

The sampling design describes how the sample points are selected and how many of them (Kleinn, 2015). Here the data basis is a subset of a systematic sampling forest inventory. Available data (Nationalparkverwaltung-Hainich, 2011) were used to cover an area of ca. 5x8 km. On a grid of 200 by 200 m, 606 plots (Figure 2.33) including more than 14,000 sampled trees have been considered for this study. The plots are part of permanent control sampling gathered in 2009-2011.

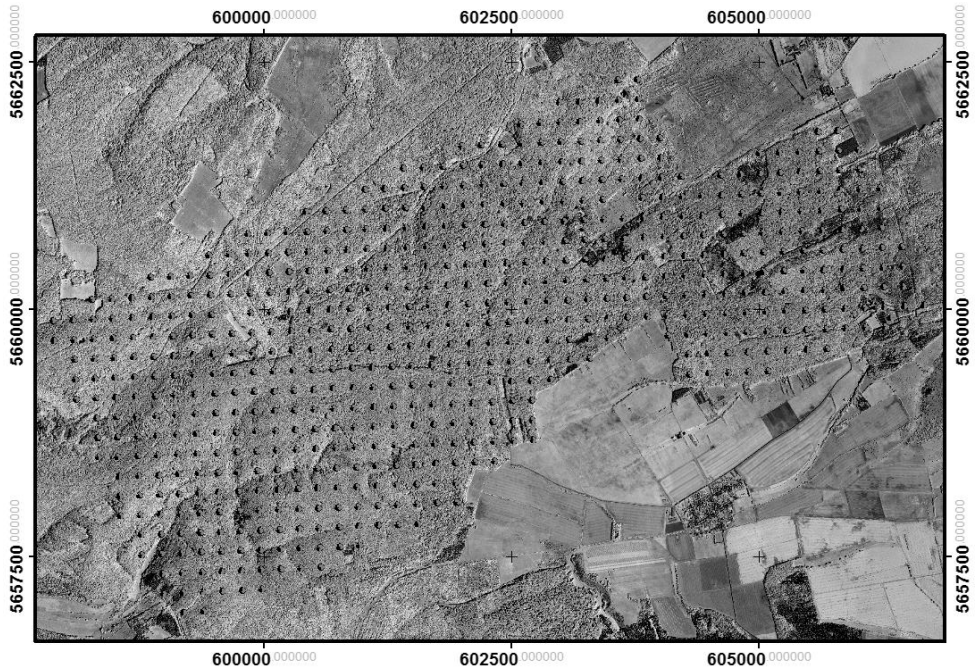

Figure 2.33: Spatial distribution of the inventory plots in a 200 x 200 m grid covering the whole study area.

The plot or response design is a nested plot consisting of three circular plots of 200, 500 and 1000 m^2 around each plot center (Figure 2.34). Trees are sampled depending on their diameter at breast height (dbh) measured at 1.3 m. Within the innermost circle (radius, r = 7.98 m) only trees with a dbh of 7.0-24.9 cm are recorded; on the second circle (r = 12.62 m) trees with a dbh of 25.0-49.9 cm, on the biggest circle (r = 17.84 m) all trees with dbh larger than 50.0 cm, respectively.

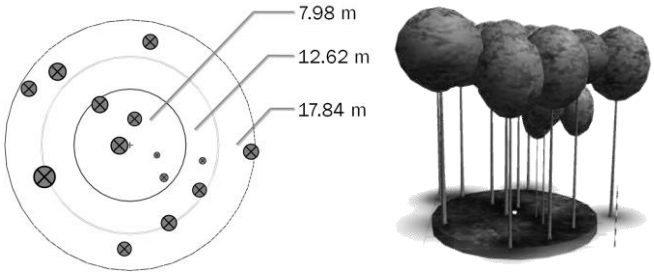

Figure 2.34: Nested plot design of the permanent forest inventory (left). The three horizontal radii of the circles are 7.98 m, 12.62 m and 17.84 m. Green spots show sampled trees according to their dbh. Same plot modelled in the Waldplaner software (Hansen and Nagel, 2014) (right).

As every plot has the same radii on an even surface, the diameter differs in rugged terrain and has to be corrected concerning the slope. A proper slope correction needs accurate determination of the slope in the field. However, depending on the terrain adjusted plot diameters differ only within some centimeters from the original values for map plane. The frequencies of corrected field plot diameters are plotted in Figure 2.35. It can be shown that there are some slopes in the study area. However, the majority of adjustments is rather small and amounts some centimeters.

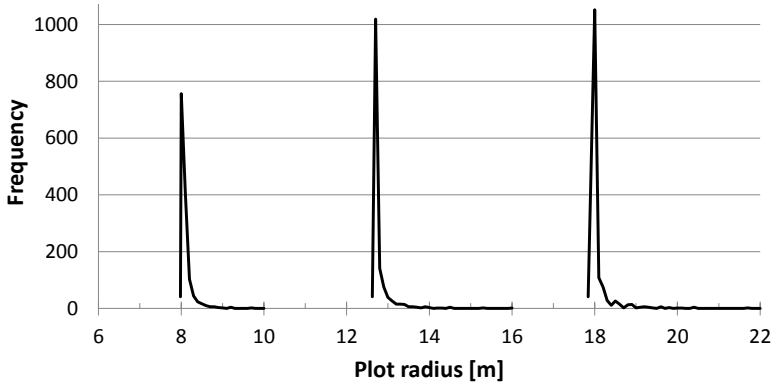

Figure 2.35: Frequencies of adjusted plot diameters for the nested inventory plots, consisting of three circles of 7.98, 12.62 and 17.84 m at map plane.

2.8.1.2 Tree attributes

Since it is rather laborious to measure the height of all trees of a sample plot in a forest inventory, it is common not to measure all heights. Then, missing values can be derived by a height-diameter model. Here the curve model after Petterson (Eq. 2) (Nagel, 2009; Petterson, 1955; Schmidt, 1968) is used:

$$Height = 1.3 + \left(\frac{dbh}{a + b * dbh}\right)^{3.0} \quad \text{(Eq. 2.13)}$$

where dbh is the trunk diameter measured at 1.3 m height, a and b are model coefficients. Since tree species vary in growth behavior, the model was applied separately for ash, beech, maples, hornbeam, oaks, spruce and other broad-leaved and coniferous species. Model fitting was done in the statistical software R (R Core Team, 2012) using the nonlinear least squares *nls* function and the *nlstools* package (Baty et al., 2015). A similar procedure was done for the crown base heights. Missing values were also derived from the model. Expansion factors (EF) according to the plot size have to be considered to get estimates for one hectare, representing 10.000 m^2.

$$EF_r = \frac{10000}{\pi * r^2} \quad \text{(Eq. 2.14)}$$

where EF_r is the expansion factor according to the sample plot radius r. The EFs here are 50, 20 and 10 for the 200, 500 and 1000 m^2 plots, respectively. Similarly, for the derivation of plot-wise data such as the average dbh, the smaller plots of 200 and 500 m^2 need to be adjusted to the biggest of 1000 m^2. Figure 2.36 depicts clearly the diameter distribution as derived from the inventory data before and after incorporating the corrected number of trees by the expansion factors. The histogram is typical for a natural forest having a unimodal shape with the majority in smaller dbh classes. The bigger the trees are the smaller is their occurrence.

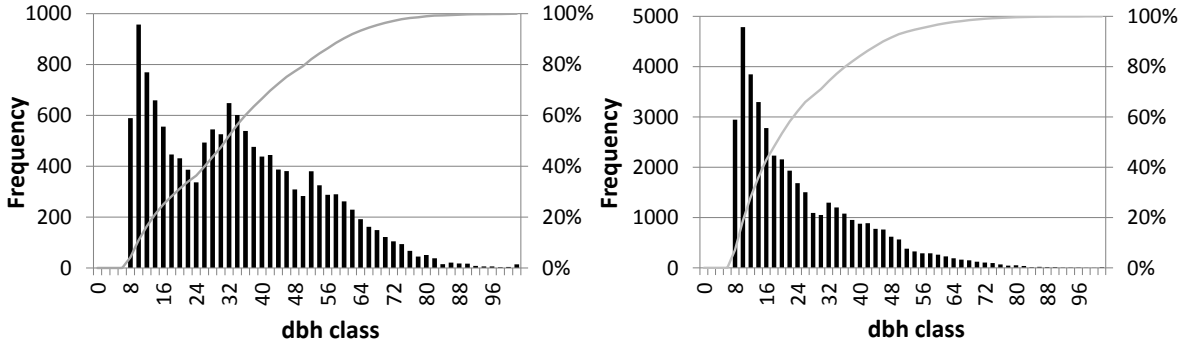

Figure 2.36: Histograms of the dbh classes before (left) and after applying the expansion factors (right).

Furthermore, for each tree the following attributes were modelled: basal area [m^2/ha/tree], trunk below crown [m], circular crown width [m] and crown radius [m]. All tree-wise variables can be averaged per inventory plot and/or species-wise using the arithmetic mean:

$$\bar{y} = \left(\sum_{i=1}^{n} y_i\right)/n \quad \text{(Eq. 2.15)}$$

where $\bar{y}$ is the mean, y_i is the observation and n is the number of samples. The standard deviation s is a measure of the average variation of the data from the mean and is calculated for simple random sampling as the square root of the variance:

$$s = \sqrt{\frac{\sum_{i=1}^{n}(y_i - \bar{y})^2}{n-1}} \qquad \text{(Eq. 2.16)}$$

For all plots the distribution of the averaged tree heights, including modelled values for trees without measured height, shows two maxima at 26 and 29 m (Figure 2.37). Generally, the majority of plot mean heights is larger than 20 m. The mean is 25.21 m, with a standard deviation of 5.13 m.

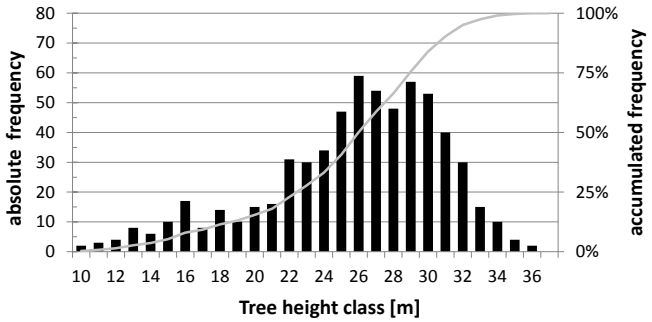

Figure 2.37: Distribution of tree height classes as plot-wise means.

2.8.1.3 Tree species composition

Overall, 29 tree species have been observed in the inventory data set. The whole area is dominated by broadleaf deciduous tree species. The following nine species classes are built: beech (*Fagus sylvatica*), ash (*Fraxinus excelsior*), hornbeam (*Carpinus betulus*), oaks (*Quercus spec.*), Sycamore maple (*Acer pseudoplatanus*), other broadleaves, spruce (*Picea abies*), Scotts pine (*Pinus sylvestris*), other coniferous. It is clear that the proportions of species depend on the variable used as reference, so that the calculated species fraction is depending on the analysis of the data. In Figure 2.38 are additionally the classes Linden (*Tilia spec.*) and Norway maple (*Acer platanoides*) incorporated. So, considering the basal area, as a more meaningful variable than the number of stems, beech has a lesser portion, but is still by far dominant (Aberle, 2014).

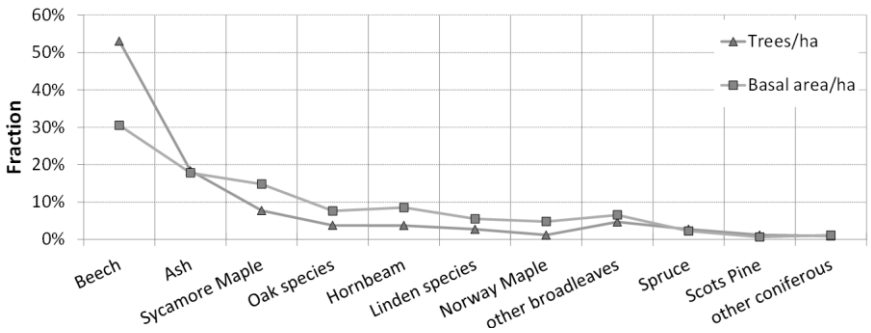

Figure 2.38: Main tree species (groups) fractions derived from nested forest inventory plots within the study area.

By building sub-classes, we can compare the values with class values derived from the German national forest inventory (Figure 2.39). In this study area beech is the most frequent species (m^2/ha: 31 %, n/ha: 53 %), whereas on national level it is spruce (m^2/ha: 32.0 %, n/ha: 29 %). Generally, the study area is rather special, as the proportion of coniferous species is low. However, the proportion of oak species is quite similar to the nationwide average.

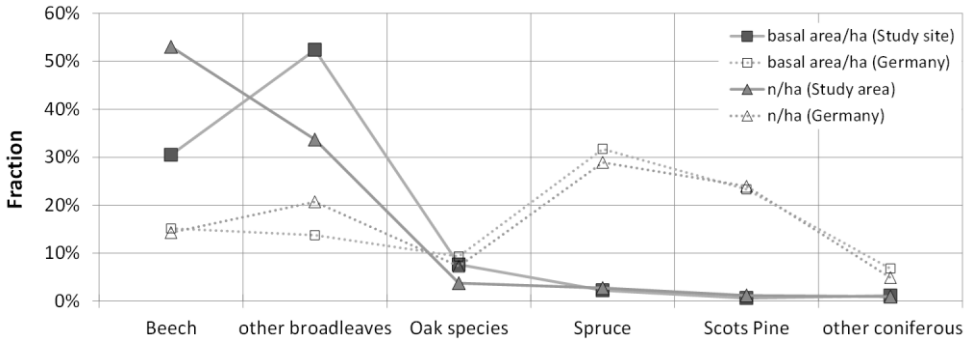

Figure 2.39: Tree species fraction in the study area compared to the national average derived from the 3rd national forest inventory in Germany (BMEL, 2015).

2.8.2 The core area

2.8.2.1 Collecting forest stand data

For the second data set a 2.25 ha large full census plot was established which will be addressed now. Inside this core area, 25 core plots of 30 by 30 m were established. All trees with a dbh greater than or equal to 15 cm were recorded in spring 2012. The dbh was measured crosswise at larger trees. Smaller trees were omitted, as there were only a few in the understorey and considered as negligible. All in all 416 trees were surveyed recording the spatial position using compass and an ultrasonic HAGLÖF Vertex IV. Accurate coordinates of one of the tower's corner, which were measured on the top using longtime GPS logging, served as a reference point. Tree diameters were measured with caliper and diameter tape for bigger trees, respectively. Additionally, dbh-related circular crown dimensions were modeled for each species including crown width using formulas from empirical growth models (Nagel, 2009). For practical reasons we measured tree top heights plus live crown heights not on every tree. Height values of 99 individuals were measured using the Vertex. The remaining height values were estimated using the height-dbh curve model after Petterson (1955) derived from the measured heights:

$$Height = 1.3 + \left(\frac{dbh}{a + b * dbh}\right)^{3.0} \quad \text{(Eq. 2.17)}$$

where dbh is the trunk diameter measured at 1.3 m height, a and b are model parameters. The model was applied separately for ash, beech and other species. A similar procedure was done for

the crown base heights. Missing values were also derived from the model. The following statistics were calculated for the fitted model: the root mean square error $RMSE$ (Eq. 7) and pseudo-coefficient of determination R^2 or adjusted coefficient of determination R^2_{adj} (Eq. 8).

$$RMSE = \sqrt{\frac{\sum_{i=1}^{n}(y_i - \hat{y}_i)^2}{n - p}} \quad \text{(Eq. 2.18)}$$

$$R^2 = r^2_{y_i\hat{y}_i} \; ; \; R^2_{adj} = 1 - \left(\frac{\sum_{i=1}^{n}(y_i - \hat{y}_i)^2}{\sum_{i=1}^{n}(y_i - \bar{y})^2}\right)\left(\frac{n-1}{n-p}\right) \quad \text{(Eq. 2.19)}$$

where n is the sample size, p is the number of parameters to be estimated, $\bar{y}$ is the mean value of the dependent variable (tree height), $\hat{y}$ is the predicted value, and $r^2_{y_i\hat{y}_i}$ is the correlation coefficient for a linear regression between the observed and the predicted values of the dependent variable (tree diameter) (Ryan, 1997). Residuals e (Eq. 2.20) are defined as the deviance of the observed data to the model. The standardized residual for each pair e_{iSTD} is the residual divided by the square root of the residual variance s (Eq. 2.21):

$$e_i = y_i - \hat{y}_i \quad \text{(Eq. 2.20)}$$

$$e_{iSTD} = \frac{e_i}{s} \quad \text{(Eq. 2.21)}$$

2.8.2.2 Species composition and spatial distribution

Typical for that area is that the by far dominating species are beech (*Fagus sylvatica*) and ash (*Fraxinus excelsior*). Beech outnumbers ash with about 66 % versus 23 % when just counting the number of stems. Considering each tree's basal area instead these differences are still present, but less: 55 % and 35 %, respectively (Figure 2.40). The third most frequent is Sycamore Maple (*Acer pseudoplatanus*) with about 7 %. The other tree species play minor roles.

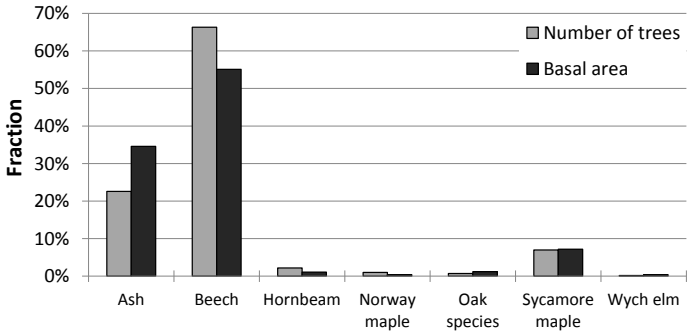

Figure 2.40: Proportions of the recorded tree species within the core area considering number and basal area.

The spatial distribution of the trees does not show any clear pattern (Figure 2.41). However, it should be noted, that the climate tower is located close to the center and a small path is heading to it from the corner of the plot in the south-east, by what the arrangement is influenced. Another bigger gap is located in the north-east and close to the tower. For the purpose of visualizing, the entire single-tree-value table was converted to xml format and read into the growth model software BWINPRO7 (Nagel, 2009). A three dimensional view of the recorded trees can be produced then (Figure 2.43). Aerial CIR imagery was used for checking if the trees are mapped spatially correctly. In some parts of the core area there are several mismatches (Figure 2.42). In contrast to coniferous species such as spruce (*Picea abies*) or Douglas fir (*Pseudotsuga menziesii*) broadleaf trees do not have a straight and vertical stem and grow often leaning sidewards causing discrepancies in located tree base and tree crown top.

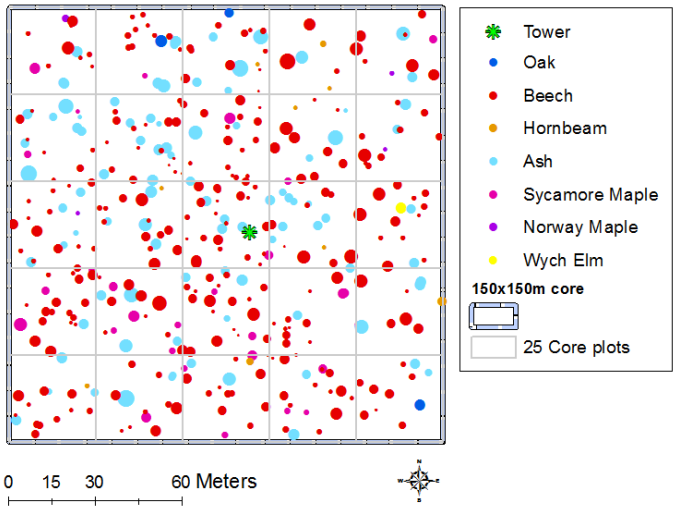

Figure 2.41: Sampled trees inside the core zone. Point sizes are relative to measured dbh.

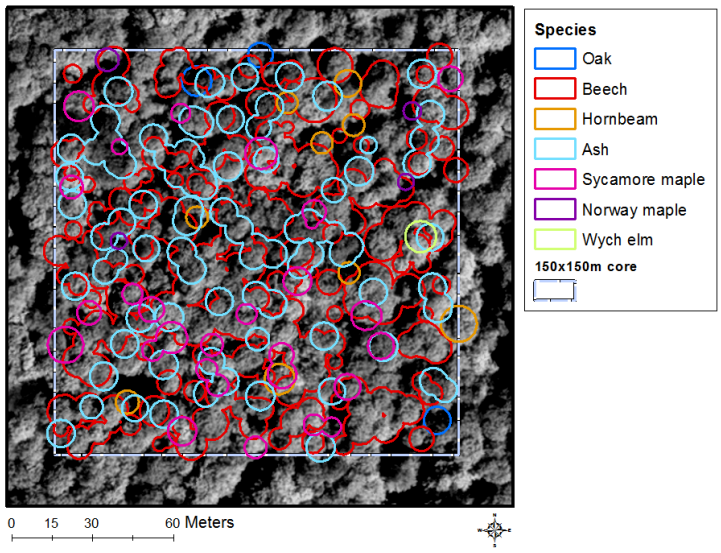

Figure 2.42: Modelled tree crowns in comparison with an aerial near infrared image (Biodiversity Exploratories, acquisition date: 05.06.2010). The crown areas are dissolved for each species for better visualization.

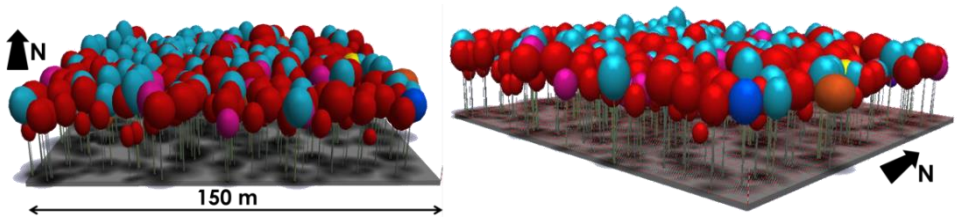

Figure 2.43: Three-dimensional model of the forest stand generated with ForestSimulator of BwinPro7 (Hansen and Nagel, 2014). Dominant species: red=beech (*Fagus sylvatica*), light-blue=ash (*Fraxinus excelsior*).

2.8.2.3 Tree height and diameter

For the prediction of missing tree top heights Petterson's (1955) height model was used. The model curves for ash and beech are displayed in the following scatterplots (Figure 2.44). The dependent variable is height, the independent variable the measured dbh values. The corresponding model coefficients and statistics are listed in Table 2.3. For beech the pseudo R^2 is higher (0.62) than for ash (0.37), which is also related to the higher number of trees. However, for other species it is slightly larger (0.64). The $RMSE$ are rather similar and ranging between 2.95 and 3.58 m. The associated residuals are distributed rather equally (Figure 2.45), which is indicating a good model fit to the acquired data.

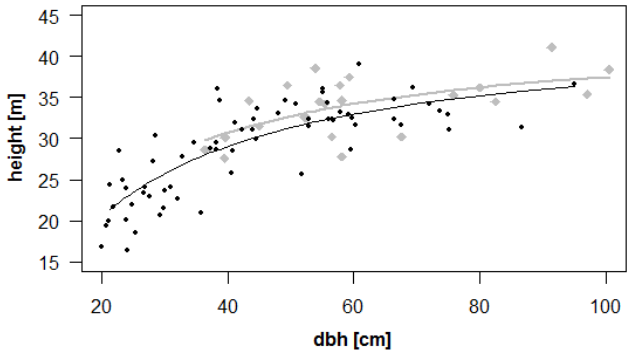

Figure 2.44: Petterson's height-dbh curves used for modelling missing tree heights of ash (grey) and beech (black).

Table 2.3: Adjusted-, pseudo-R^2, root mean square error (RMSE) and coefficients of the Petterson's height model for the three species (-groups).

Species (group)	Model coefficient		Statistics of fitted model		
	a	b	Adjusted R^2	Pseudo R^2	RMSE [m]
Ash	1.4442	0.2879	0.3353	0.3656	2.95
Beech	1.7162	0.2874	0.6176	0.6241	3.21
others	2.1529	0.2868	0.5955	0.6415	3.58

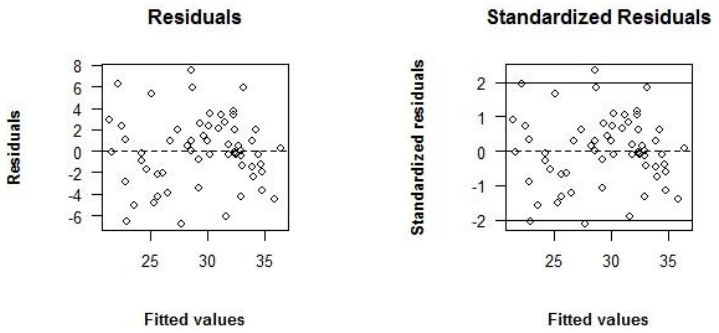

Figure 2.45: Residual plots of the height-dbh curve model for beech.

The spatially limited stand shows a relatively homogeneous canopy height and diameter distribution (Figure 2.46). This is as expected due to the rather small extent of the stand and the little variation in close-by neighborhoods due to autocorrelation. The mean measured tree top height is 30.00 m (standard deviation, sd: 5.53 m) – after applying the Petterson model for missing values the final mean height is 29.31 m (sd: 4.9 m). Measured dbh averages out at 46.1 cm (sd: 17.86 cm). However, differences in height and diameter are becoming more evident on species level. Plotting the histograms of tree height classes for each species there is a certain pattern to identify (Figure 2.48). The majority of the ash trees are the highest, followed by the dominant beech. Furthermore, the occupation of different niches within the forest canopy is apparent at several heights at around 22 m, at 28-30 m and above 36 m.

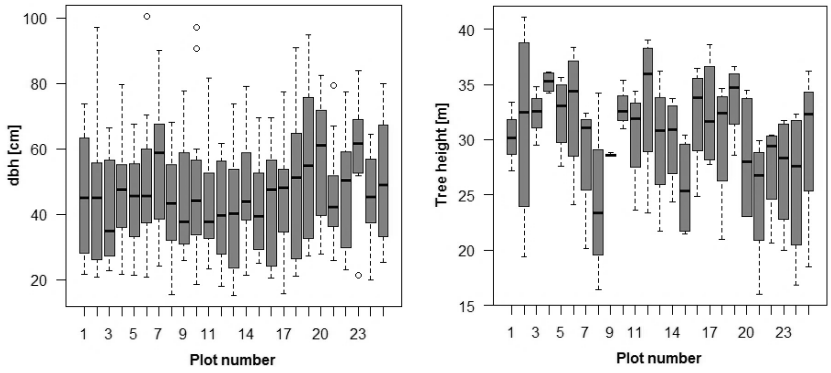

Figure 2.46: Left: Measured dbh values per core plot. Right: Modelled and measured tree heights.

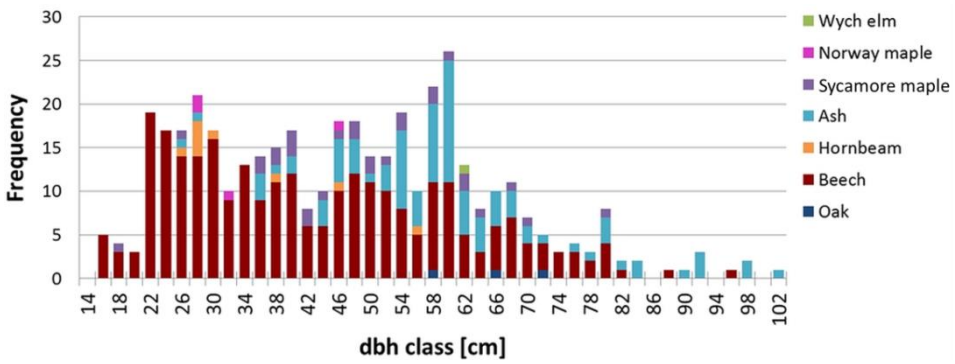

Figure 2.47: Histogram of diameter classes per species.

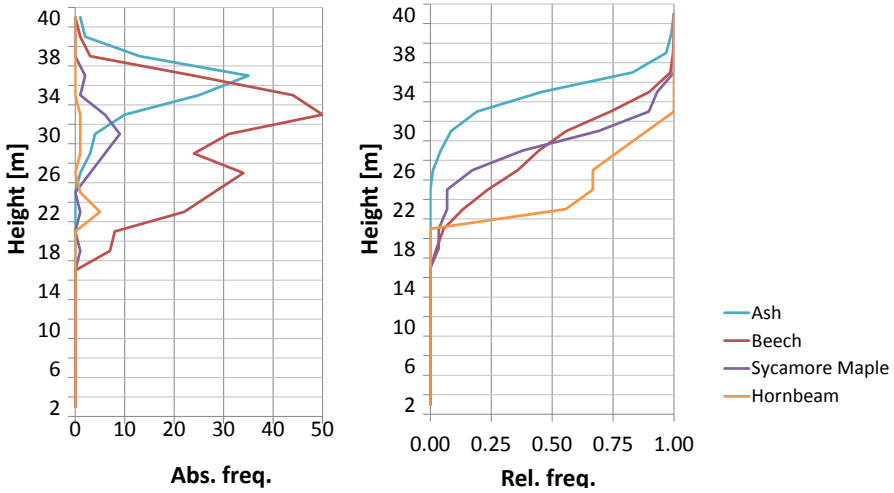

Figure 2.48: Tree top heights as absolute and accumulated relative frequencies of the four most frequent species Ash (*Fraxinus excelsior*), Beech (*Fagus sylvatica*), Sycamore Maple (*Acer Pseudoplatanus*) and Hornbeam (*Carpinus betulus*) within the core area. The majority of Ash trees are higher than the dominant Beech.

Table 2.4: Surveyed trees and their corresponding basal area per core plot

Plot	Tree stems	Sum of tree basal area [m²]	Basal area [m²/ha]
1	13	2.49	27.67
2	19	3.77	41.89
3	20	2.87	31.89
4	21	3.86	42.89
5	16	2.70	30.00
6	13	2.90	32.22
7	18	4.65	51.67
8	26	3.99	44.33
9	16	2.71	30.11
10	18	3.68	40.89
11	19	3.02	33.56
12	26	4.22	46.89
13	25	4.52	50.22
14	17	3.13	34.78
15	19	2.95	32.78
16	14	2.08	23.11
17	22	4.18	46.44
18	14	3.24	36.00
19	6	1.82	20.22
20	11	3.03	33.67
21	12	2.15	23.89
22	15	3.21	35.67
23	9	2.86	31.78
24	12	2.11	23.44
25	17	3.77	41.89

CHAPTER 3

LEAF OPTICAL PROPERTIES OF EUROPEAN BROADLEAVED SPECIES

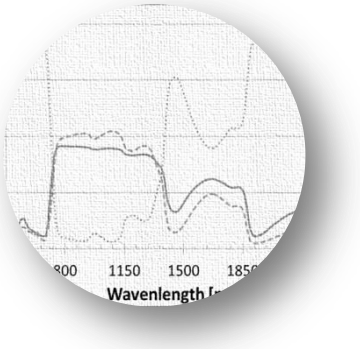

3 CHAPTER THREE - LEAF OPTICAL PROPERTIES AND PHENOLOGY

3.1 INTRODUCTION

Shape and size, that is how we can generally describe a leaf of a deciduous tree. Besides that, the color is the most striking feature. Spectral reflection, absorption and transmission of light are the main processes that specify the leaf optical properties (LOP). Those characteristics of the spectral behavior can depend on several factors such as species (Castro-Esau et al., 2006), the stage of development and the age of leaf and tree (Roberts et al., 1998; Wilson et al., 2001). The location within a tree crown plays an important role as sun and shade leaves typically differ in e.g. leaf area, thickness and chlorophyll content (Gausman, 1984; Legner et al., 2013; Lichtenthaler et al., 2007). Furthermore, other leaf structural characteristics like cuticular thickness and intercellular air spaces may also influence the appearance (Slaton et al., 2001). For us, healthy tree leaves usually appear in a variation of green due to very high absorption in blue and red induced by plant pigments and a relative higher reflection in green. Beyond the visual range of the electromagnetic spectrum the near infrared (NIR) and shortwave infrared (SWIR) are of central interest, as leaves show there a higher reflection. In contrast to coniferous needles, which typically have a lower NIR reflection, the leaves of broadleaf trees have two sides that are more distinct: the top adaxial side, which is mainly apparent from above, and the lower abaxial side, which tend to be brighter for many species. In most cases these have different functions and hence diverging reflectance behaviors due to construction, cuticular hairs etc. However, there is some confusion in the literature as some authors state that cuticular wax is influencing the reflectance (Clark and Lister, 1975; Lu, 2013; Sims and Gamon, 2002) while others say it is almost not affecting due to its transparency (Knipling, 1970; Ollinger, 2011). In any case, after the shooting leaves pass through a certain development during a growing season, which we might call seasonal phenology, and in which LOP alter over time due to changes in structure, biochemical composition and photosynthesis rate (Wilson et al., 2001). Although recent studies show that photosynthesis is rather related to the day length than to temperature (Bauerle et al., 2012), the explanation of seasonal patterns in canopy photosynthesis is still complicated, as many factors such as leaf area index also vary (Groenendijk et al., 2011; Stoy et al., 2014). Vegetation indices (VI) can be used to detect the best point in time for species discrimination or the condition assessment of vegetation (Cole et al., 2014). Hence, the calculation of VI also help in emphasizing specific optical features that are related to biophysical factors (Dillen et al., 2012). Since VI are linked to the characteristics and development stage of green plants and leaves, it should be further checked if there are evident changes of VI values on leaf level over a growing season. Hence, it is important to gather comprehensive information for comparison, monitoring and the understanding of responses on weather or even climatic changes (Botta et al., 2000; White et al., 2009). For this purpose, remote

sensing can be applicable covering large areas (Glenn et al., 2008; Gonsamo et al., 2012). The number of forest vegetation studies incorporating remote sensing is increasing (Boyd and Danson, 2005; Fagan and Defries, 2009). Although some studies examined leaf trait data in relation to leaf reflectance, including chlorophyll and leaf pigments (Gitelson et al., 2003; Le Maire et al., 2004), nitrogen content (Dillen et al., 2012; Pacheco-Labrador et al., 2014) and leaf metabolism (Serbin et al., 2012), still detailed studies on leaf level are often disregarded and actually highly needed (Homolová et al., 2013).

Detailed leaf level data about spectral reflection, absorption and transmission are also indispensable inputs for simulations and the application of radiative transfer models and their inversion, respectively. These models allow the examination of leaf optical properties under different conditions incorporating varying contents of water, chlorophyll and pigments or leaf angle distribution (Féret and Asner, 2011; Féret et al., 2008; Jacquemoud et al., 2009). They are further important for coping and analyzing scaling effects between data gained at different levels: in-situ, at laboratory or by remote sensing. Hence, they can improve the establishment of ties between information at the levels of (i) leaves, (ii) tree crowns, (iii) forest stands and (iv) forested landscapes and ecosystems. Model data usually bases on generated look-up tables incorporating several scenarios and settings (Richter et al., 2011). Because broadleaf trees show a changing spectral behavior throughout a season after foliation, it is crucial to cover a variety of input data incorporating detailed species-related information and the temporal component. Overall, we can state that detailed LOP case studies for different tree species are still lacking. Moreover, the literature reveals that what is furthermore missing is recent investigation in respect to deciduous broadleaf tree species in old growth temperate forest. That is what this case study is taking up. Here, the examined LOP include hyperspectral reflectances assessed from leaf surface and transmittances as the result of on-leaf reflectance and within-leaf actions such absorption and scattering. The amount of absorption as the main effect of photosynthesis is determined subsequently. The focus is on beech (*Fagus sylvatica*) as this is the dominant tree species at the study site. In addition, the other main tree species oak (*Quercus petraea*), ash (*Fraxinus excelsior*) and Sycamore maple (*Acer pseudoplatanus*) are incorporated as well as Small-leaved linden (*Tilia cordata*), hornbeam (*Carpinus betulus*) and Norway maple (*Acer platanoides*). Besides that, both the upper and the lower sides of leaves are examined incorporating an additional data set in order to see if there are species-dependent differences in adaxial and abaxial reflectances. All measurements are done by using a new high-resolution field spectroradiometer, also to test its capabilities. Finally, following central questions shall be answered:

- What are the optical properties of main Central European broadleaved tree species?
- Do shade-tolerant species like beech, Small-leaved linden and Sycamore maple have similar leaf optical properties?

- ¬ What is the proportion of each spectral response for reflectance, transmittance and absorbance and how do they differ?
- ¬ How stable are LOP and VI over the time of a growing season?
- ¬ What are the consequences for radiative transfer model inputs on leaf-level?

3.2 MATERIAL AND METHODS

3.2.1 Study location and data collection

The study area is located at about N 51.08° E 10.45° in a forest ridge within the Hainich National Park, Thuringia in central Germany. See chapter 3 for a more detailed description of the site. Measurements gathered in this study were executed utilizing the tree canopy walk of the National Park and the 45 m high climate tower within the forest. Hence, even higher situated sun-leaves and upper crown parts could be reached for sampling. Tree height is about 30 m; the age is estimated to be around 200 years. Data collection was conducted on sunny days in 2012 (25.05., 19.07., 24.07.) and 2011 (02.08., 16.08., 23.08.) during the growing season to ensure equal conditions in tree physiology and minimize differences in daily leaf chemistry, which may lead to different spectral responses. Corresponding daily weather data is shown in Figure 3.1. Additional reflectances from upper and lower side of leaves as auxiliary data were collected at a canopy walk close to the forestry campus in Göttingen, located in a younger mixed broad-leaf stand at about N 51.56° E 09.96°. Reflectance measurements of both sites of leaves were done in July 2011 and May 2012, whereas transmittances could only be obtained for three species at three points in time.

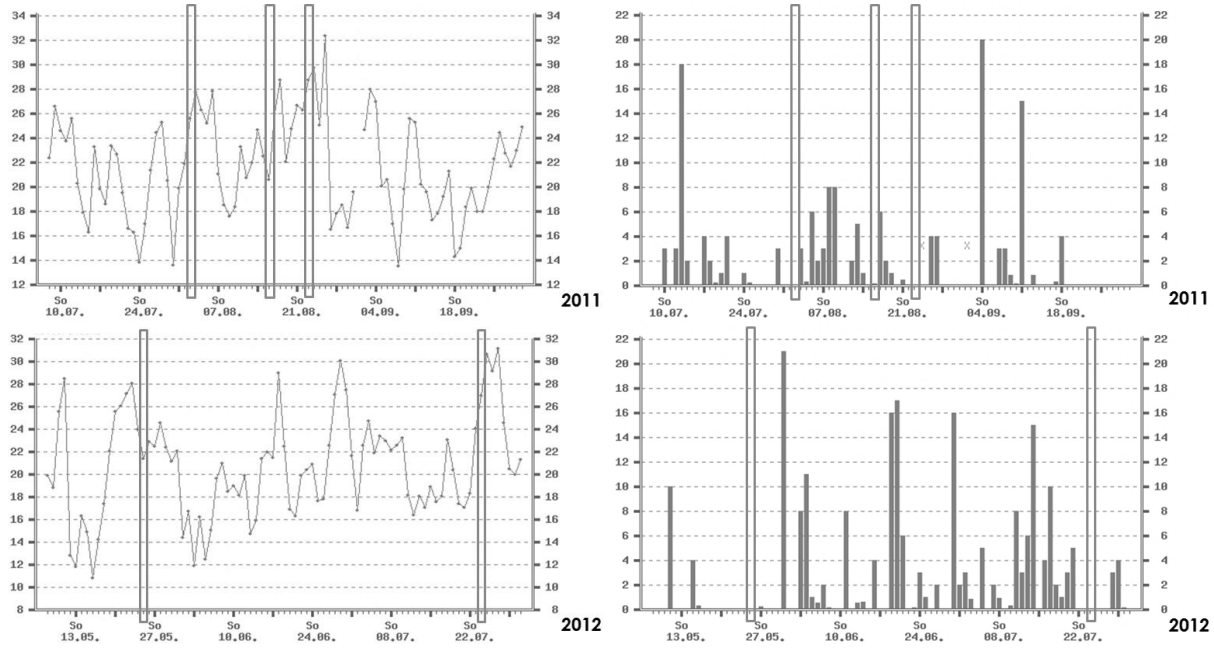

Figure 3.1: Daily maximum air temperature [°C] and daily precipitation [mm] for the days of measurement (marked) acquired at a weather station in close-by Eisenach (source: WetterOnline.de).

As the term leaf reflectance is often used, it should be noted that the upper side as well as the lower side of the leaves were considered in some of the measurements, which is very important to incorporate for a complete analysis (Cordón and Lagorio, 2007; Hughes et al., 2008). A field spectroradiometer ASD FieldSpec 3 (ASD Inc., Boulder, USA) was used for the in situ data collection. The device has a spectral resolution of 350-2500 nm and a spectral sampling of 1.4-2.0 nm. By using internal interpolations, which produce bandwidths of 1 nm, it offers 2150 single channels. At the FieldSpec's fiber optic a contact probe (2011) and a leaf clip (2012), respectively, was attached for direct measurements to minimize the influence of air between sensor and leaf (Figure 3.2).

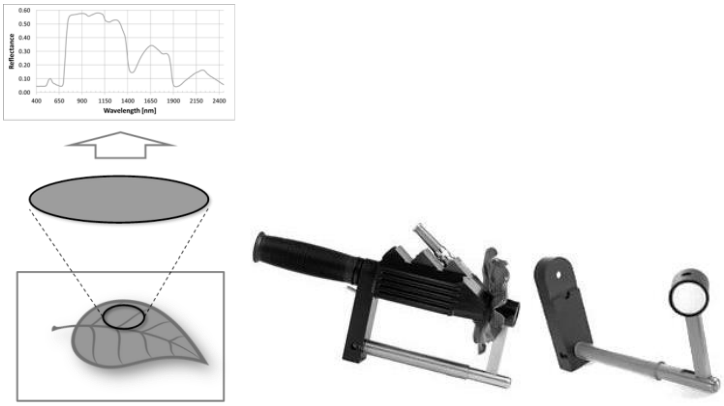

Figure 3.2: Schematic derivation of leaf reflectance (left); ASD leaf clip in action (middle) and its white reference (right) (ASDI, 2012).

This setting allows measuring reflectances of the upper (adaxial) and the lower side (abaxial) of a leaf as well as transmittance and the subsequent calculation of absorptance. Measurements were done quickly to prevent damages on the leaves by the bulb's heat. In order to avoid mistakes and minimize measurement errors during the sampling every recording consist of a minimum of four repeated readings. Overall, more than 200 leaves comprising over 900 single values were sampled (Table 3.1). For the supplementary acquisition of adaxial and abaxial reflectances, 77 measurements are recorded additionally.

Table 3.1: Sampled leaves and amount of single measurements per tree species.

Common name	Scientific name	Measurements	Leaves
Ash	*Fraxinus excelsior*	214	51
Beech	*Fagus sylvatica*	220	52
Hornbeam	*Carpinus betulus*	165	42
Norway maple	*Acer platanoides*	38	9
Oak	*Quercus petraea*	102	24
Small-leaved linden	*Tilia cordata*	111	25
Sycamore maple	*Acer pseudoplatanus*	77	19

3.2.2 Data processing

3.2.2.1 General remarks

Before the data analysis, the raw spectral responses have to be checked for consistency, errors and outliers occurring while measuring. Data processing was mainly done using following software: ASD ViewSpecPro v. 6.0 (ASDI, 2008), Excel 2010 (Microsoft, 2010), the free software RStudio v. 0.9ff. (RStudio Team, 2015) together with R v. 3 (R Core Team, 2012) and SAMS (Spectral Analysis and Management System) (CSTR, 2005). Overall, there are many steps incorporated in the whole analysis. Figure 3.3 depicts the basic workflow including corrections and filtering as described in the following.

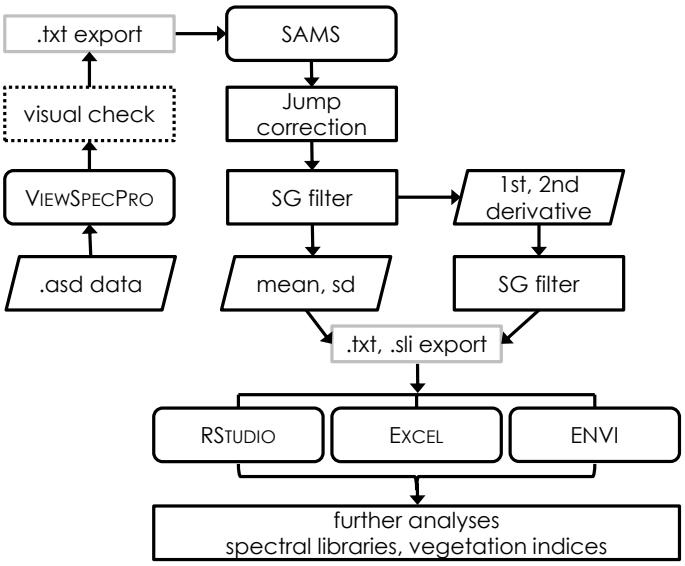

Figure 3.3: Workflow for the spectral data collected with the ASD FieldSpec.

3.2.2.2 Sensor jump correction

The spectroradiometer ASD FieldSpec 3 consists actually of three sensors in the VIS-NIR (350-1000 nm), NIR-SWIR1 (1000-1800 nm) and SWIR2 (1800-2500 nm) region of the spectrum. At the transitions at 1000 and 1800 nm, sometimes harsh jumps or steps are apparent in the signal. Since it was observed that the jumps could go in both positive or negative direction and being sometimes larger or smaller, the raw responses have to be corrected in order to guarantee continuous signal and comparability. Here, an additive jump correction for each of the corresponding wavelength is applied as implemented in SAMS (Rueda and Wrona, 2003). The result is an adjusted curve without those breaks but with different values (Figure 3.4). Jump-corrected data can then be used in further processing steps.

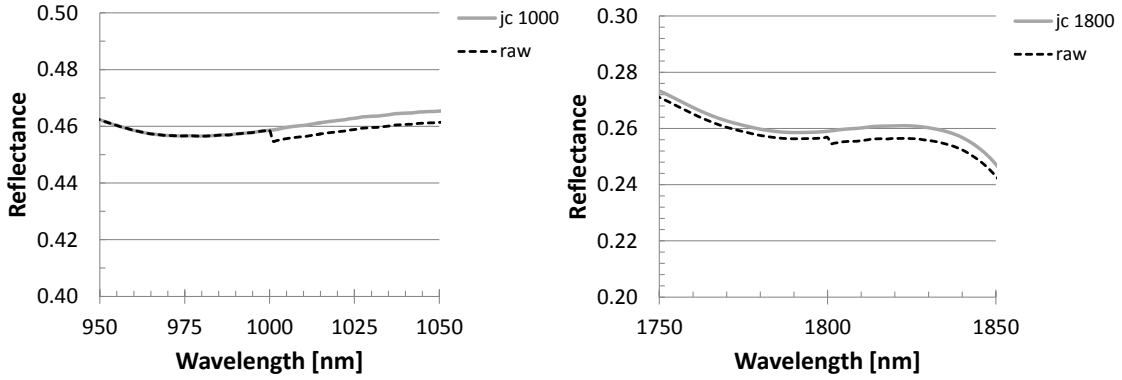

Figure 3.4: Example of correcting the sensor signal jump at 1000 nm (left) and 1800 nm (right), dashed line: raw data, solid line: corrected data.

3.2.2.3 Signal filtering

Depending on the sensor, the collected and unprocessed spectroradiometer signals are often relatively noisy and can show a rather rough curve. Hence, they have to be smoothed by specific filters incorporating the surrounding data for creating a new updated value. Implementing such filters make signals easier to interpret and a bit more comparable. There are several functions which can possibly be applied such as moving mean or median filter, splines or wavelets (Ghiyamat and Shafri, 2010; Goyal et al., 2013; Schmidt and Skidmore, 2003). However, users should do this with care, keeping the main characteristics of the signals without losing too much information. Here, a 2-5-5 Savitzky-Golay (SG) filter was applied (Savitzky and Golay, 1964; Schafer, 2011; Vaiphasa, 2006), a second order least-squares polynomial for smoothing the signal incorporating the 5 previous and the 5 following bands. The applied filter produces a curve which is less noisy (Figure 3.5).

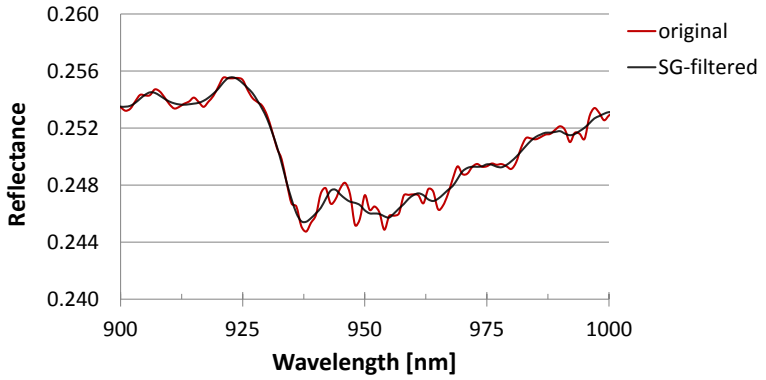

Figure 3.5: Example for applying a 2-5-5 Savitzky-Golay smoothing filter (black) to raw reflectance (red) of a beech crown part.

3.2.2.4 Vegetation indices

Hyperspectral data allows the calculation of both broadband and narrow-band vegetation indices. This can be done for remotely sensed imagery as well as for direct leaf data (Kumar et al., 2010;

Thenkabail et al., 2000; Zarco-Tejada et al., 2005). Here, seven VI are analyzed comprising greenness, leaf pigments and light use efficiency (Table 3.2). The two broadband indices NDVI (Normalized Difference Vegetation Index) (Rouse et al., 1974) and SR (Simple Ratio) (Tucker, 1979) are a measure of greenness and hence of healthy, green vegetation. Both incorporate the relation of green leaf reflection in near infrared and the absorption of chlorophyll in red and are suitable to estimate the absorption by carotenoids like xanthophyll and the uptake of carbon dioxide. Just as SR, NDVI can saturate in dense vegetation conditions when LAI becomes high. Both indices CRI1 (Carotenoid Reflectance Index 1) (Gitelson et al., 2002) and ARI2 (Anthocyanin Reflectance Index 2) (Gitelson et al., 2001) are related to leaf pigments apart from chlorophyll. Carotenoids are involved in the light absorption processes of vegetation and protect plants from too much light which could have even negative effects. Higher index values imply a greater carotenoid concentration relative to chlorophyll. Anthocyanins are present in both suffering senescence and newly grown leaves. Since weakening vegetation usually contains higher concentrations of both carotenoid and anthocyanin, CRI1 and ARI2I are measures of stressed vegetation. The three further indices are more associated with the light use efficiency. Broadband RGRI (Red Green Ratio Index) (Gamon and Surfus, 1999; Sims and Gamon, 2002) highlights the relation of leaf redness caused by anthocyanin and chlorophyll incorporating reflectance in the red and green spectrum. The SIPI (Structure Insensitive Pigment Index) (Peñuelas et al., 1995) is an indicator of leaf pigment concentrations maximizing the sensitivity to the ratio of chlorophyll to carotenoids. Finally, the PRI (Photochemical Reflectance Index) (Gamon et al., 1992; Gamon and Surfus, 1999; Garbulsky et al., 2011) is sensitive to changes in pigments, especially xanthophylls, that are indicative of photosynthetic light use efficiency or the rate of carbon dioxide uptake by the leaves. All indices are also indicators for foliage stress (Exelis, 2012).

In order to enhance comparability, the calculated vegetation indices are standardized to each other in a next step by a ranking per VI over all species leading to normalized index VI_{Nj}. The result of this normalization is that the new values range between zero and one:

$$VI_{Nji} = \left(\frac{VI_{ji} - minVI_{ji}}{maxVI_{ji} - minVI_{ji}} \right) \qquad \text{(Eq. 3.1)}$$

where VI_{ji} is the original record for the j-th VI, $maxVI_{ji}$ and $minVI_{ji}$ represent the maximum and minimum of the corresponding recorded VI over all species i.

Table 3.2: Overview about the calculated vegetation indices in this study.

Objective	Index	Formula	Reference
Greenness	Normalized Difference Vegetation Index (NDVI)	$NDVI = \frac{\rho_{NIR} - \rho_{RED}}{\rho_{NIR} + \rho_{RED}}$	(Rouse et al., 1974)
	Simple Ratio (SR)	$SR = \frac{\rho_{NIR}}{\rho_{RED}}$	(Tucker, 1979)
Leaf pigments	Carotenoid Reflectance Index 1 (CRI1)	$CRI1 = \frac{1}{\rho_{510}} - \frac{1}{\rho_{550}}$	(Gitelson et al., 2002)
	Anthocyanin Reflectance Index 2 (ARI2)	$ARI2 = \rho_{800} * \left(\frac{1}{\rho_{510}} - \frac{1}{\rho_{700}}\right)$	(Gitelson et al., 2001)
Light use efficiency	Red Green Ratio Index (RGRI)	$RGRI = \frac{\rho_{RED}}{\rho_{GREEN}}$	(Gamon and Surfus, 1999)
	Structure Insensitive Pigment Index (SIPI)	$SIPI = \frac{\rho_{800} - \rho_{445}}{\rho_{800} - \rho_{680}}$	(Peñuelas et al., 1995)
	Photochemical Reflectance Index (PRI)	$PRI = \frac{\rho_{531} - \rho_{570}}{\rho_{531} + \rho_{570}}$	(Gamon et al., 1992)

3.2.2.5 Statistics

All measured spectral responses are averaged by the arithmetic mean:

$$\mu = \frac{\sum_{i=1}^{n} y_i}{N} \quad \text{(Eq. 3.2)}$$

where y_i are the observed values of all N elements. The parametric standard deviation sd of the mean is calculated as the square root of the variance:

$$sd = \sigma = \sqrt{\frac{\sum_{i=1}^{N} (y_i - \mu)^2}{N}} \quad \text{(Eq. 3.3)}$$

The unitless coefficient of variation CV then calculated by dividing the standard deviation σ by the mean μ for each date of measurement. Furthermore, Pearson's correlation coefficient r is derived as a measure for the relationship of two variables:

$$r = \frac{\sum_{i=1}^{n} (x - \bar{x})(y - \bar{y})}{\sqrt{\sum_{i=1}^{n} (x - \bar{x})^2 (y - \bar{y})^2}} \quad \text{(Eq. 3.4)}$$

Additionally, the non-parametric Spearman rank correlation coefficient r_s is used for grouped and interval scaled variables, respectively.

3.3 RESULTS

3.3.1 Leaf optical properties of different tree species

3.3.1.1 Adaxial and abaxial reflectances

The additional measurements were conducted at a canopy walk close to the forestry campus in Göttingen on 12.07.2011. Reflectance measurements from both sides of leaves of ash, hornbeam, Norway maple, field maple, Sycamore maple and Small-leaved linden are shown in Figure 3.6. Oak and beech are not present in this site. Differences between ad- and abaxial reflectances are apparent especially in the VIS and SWIR2 region of the spectrum. Generally, all trees show higher abaxial values in the VIS meaning a brighter backside of the leaves, where Sycamore maple reflects the most. Comparing the sampled species it can be shown that only for ash also the abaxial NIR reflectance is higher, all others have lower or similar values. Ash, hornbeam, Field- and Norway maple show a lower adaxial reflection in the SWIR2, whereas at Sycamore maple and linden the difference between upper and lower leaf side is far less.

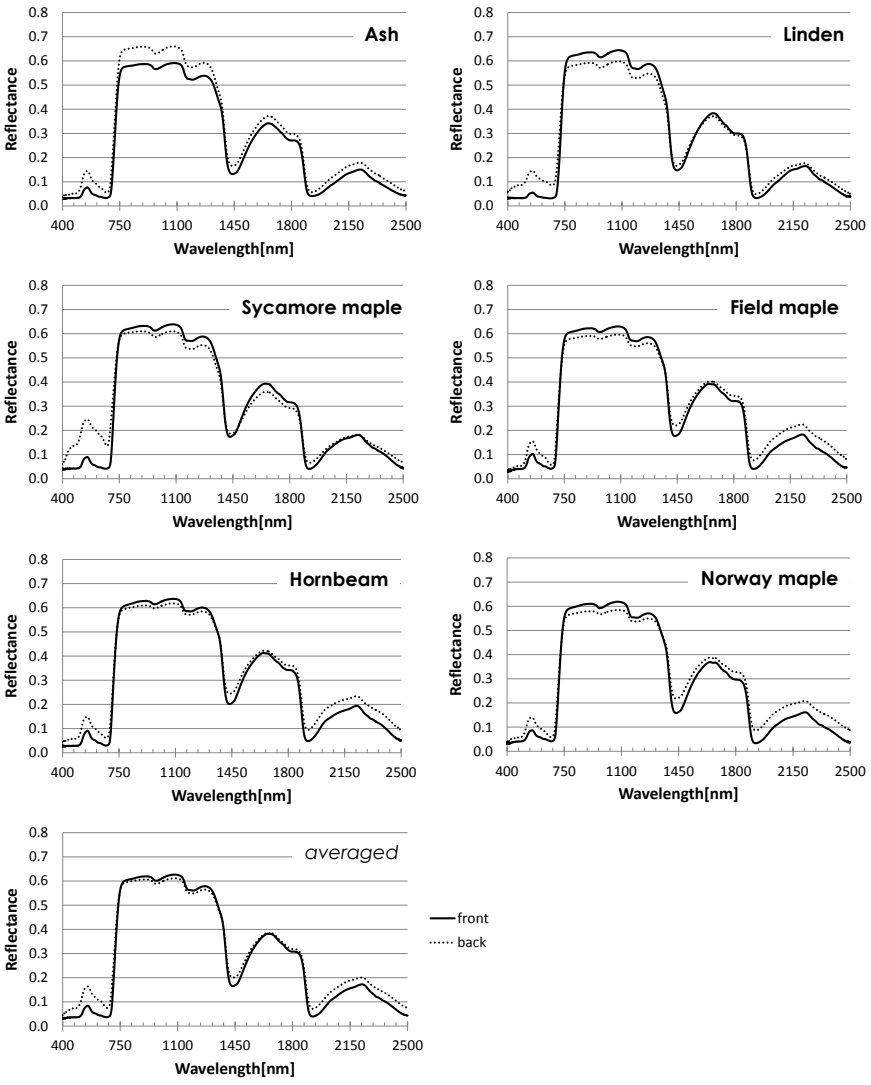

Figure 3.6: Mean upper adaxial (solid line) and lower abaxial (dotted line) leaf reflectances, date of measurement: 12.07.2012.

3.3.1.2 Leaf level reflection, absorption and transmission

When doing repeated measurements, a certain deviation occurs depending on the development age, water content and condition of single leaves. At the first glance, all sampled species show the typical response pattern of green healthy vegetation. This is not only valid for trees but can also be observed in leaves of Dog's mercury (*Mercurialis perennis*), an herbaceous plant growing frequently underneath the trees in the study site. The two local minima at about 1400 and 1900 nm are induced by water content in the leaves, equivalent to the water bands in the atmosphere.

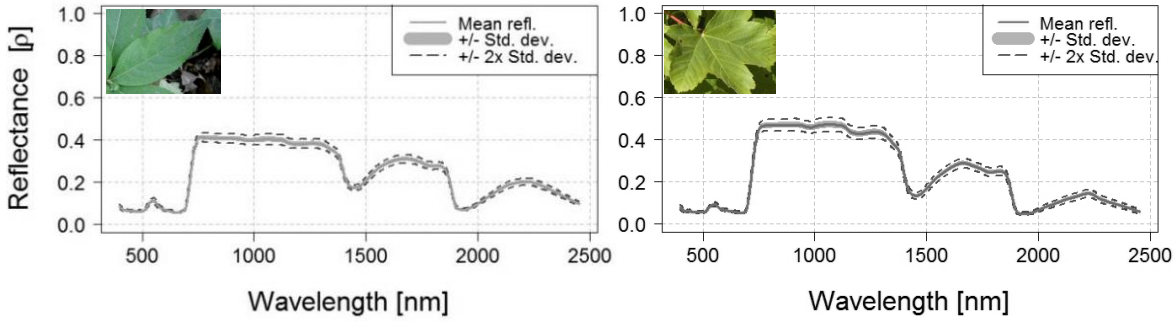

Figure 3.7: Examples of mean reflectances (± standard deviations) of sampled leaves of Dog's mercury (*Mercurialis perennis*) and Sycamore maple (*Acer pseudoplatanus*), date of measurement: 19.07.

On the one hand, the circumstance that plant leaves have typical and similar response curves leads to the fact that the curves of different species overlap in many regions of the spectrum. On the other hand, mean reflectance of a species can cross the curve of another (Figure 3.8). For example, hornbeam shows on average higher values in the near infrared as beech, whose reflectance is higher in shortwave infrared. In contrast, oak reflects least in SWIR1 and SWIR2 but has a medium reflectance in NIR. When considering the difference between the maximum and minimum values over all species, it can give a first indication which wavelengths may play an important role for differentiation. Biggest differences are apparent in the green and SWIR2 and around three inflections points (i) the red edge region (~717 nm), (ii) between NIR and SWIR1 (~1420 nm) and (iii) between SWIR1 and SWIR2 (~1870 nm). Besides the leaf surface reflectance (R) also transmittance (T) and absorptance (A) were acquired. The proportion and shape of transmittance is similar to leaf reflectance. According to the physical rules of radiation, the sum of these three fractions equals one (=100 %).

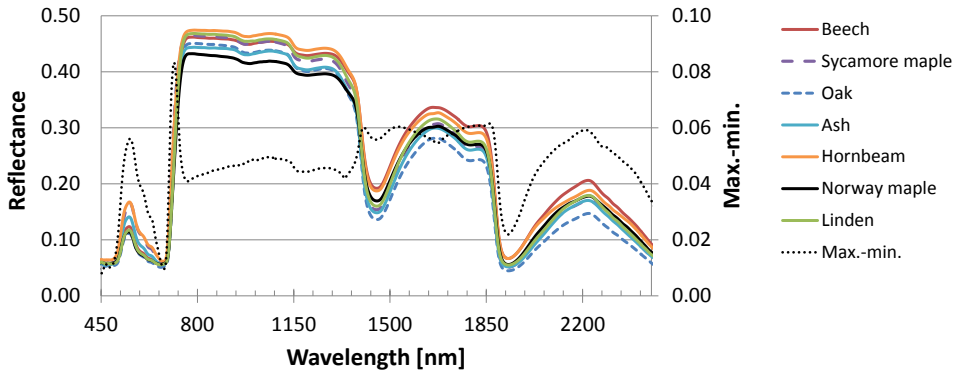

Figure 3.8: Mean reflectances of sampled leaves and the corresponding differences of maximum and minimum (dashed line), date of measurement: 25.05.2012.

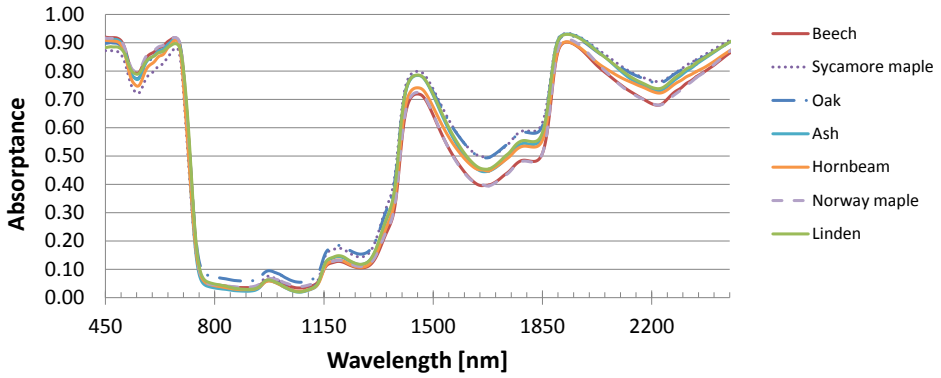

Figure 3.9: Mean absorptance of sampled leaves, date of measurement: 25.05.2012. Highest absorption occurs in the visible blue and red and in the water absorption bands.

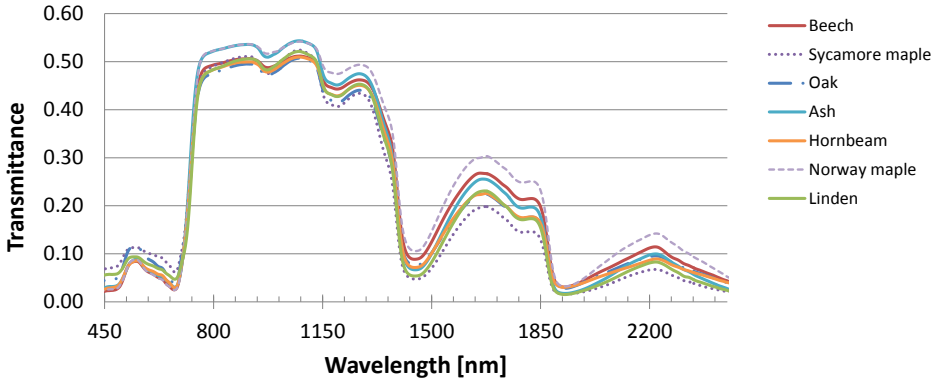

Figure 3.10: Mean transmittance of sampled leaves, date of measurement: 25.05.2012. The curves show patterns comparable to reflectance data.

Tree leaves mainly absorb the sun light in the visible and shortwave infrared region of the electromagnetic spectrum. As the high reflection already induces, absorption is least in the near infrared. Moreover, the curves for reflectance and transmittance have similar patterns. The latter shows however a bigger impact of the water absorption features near to 970 and 1190 nm and lower values in SWIR. All reflectance curves have a similar shape following the typical response of

green vegetation. However, there are more interspecific differences apparent in the transmission and absorption. The curves in Figure 3.11 are presented in relation to beech as a reference for better visualization. Both maple species, Sycamore m. and Norway m., differ from each other, whereas the latter is showing a pattern, which is most similar to beech. Nonetheless, note that the deviations are rather small, but can reach up to 12 % within the spectral range of 450-2450 nm. Larger differences appear in smaller wavelengths due to sensor noise. Especially in absorptance, beech shows most often higher values than the other species. Here Norway maple deviates by far least from beech, whereas Sycamore maple and oak have a very similar pattern primarily in SWIR. Generally, the biggest differences are apparent in the inclination points at the red edge, at about 720 nm, and at the first water band at about 1400 nm.

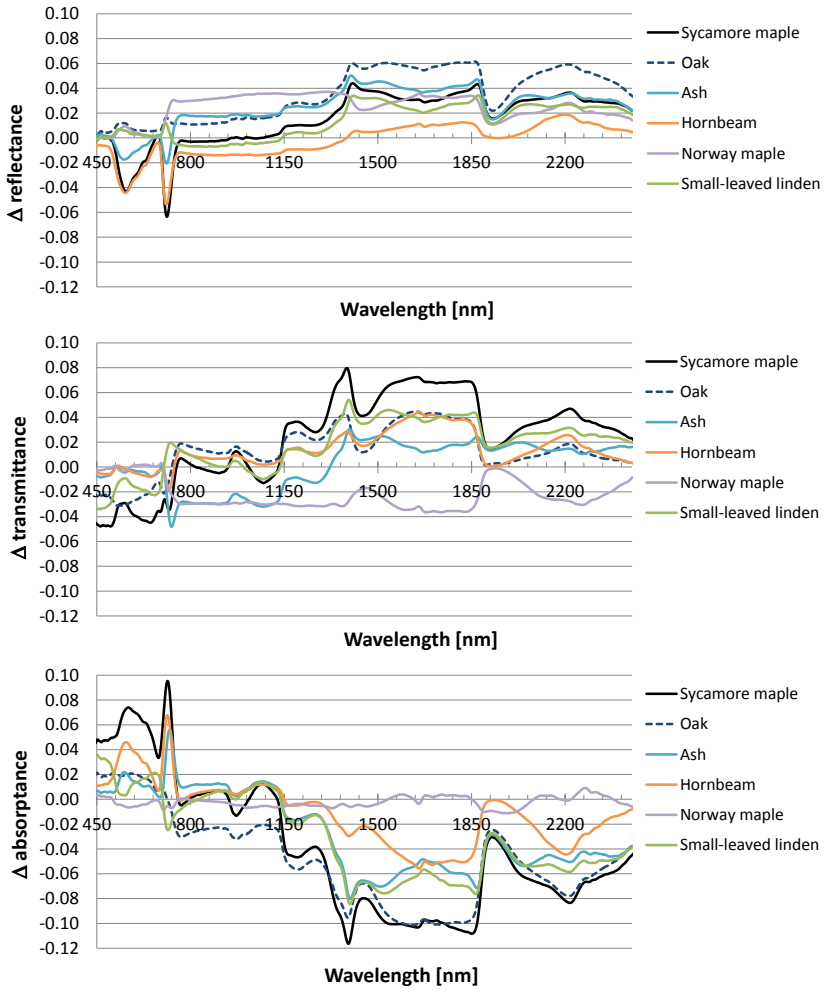

Figure 3.11: Deviations in leaf reflectance, transmittance and absorptance in relation to beech (zero) as the reference spectrum.

By building the average over all bands and over the PAR region only, one can observe distinct deviations between the species. These become clear when the species value are put in relation to beech. Hornbeam shows reflectance and absorptance values that are most similar to beech over the complete spectrum, oak deviates the most. All species absorb more than beech, whereas ash

has a similar transmittance, and only Norway maple transmits less. However, averaged values seem to be not very meaningful for a detailed inspection, as the PAR region makes clear. Here we can see completely different pattern than in the NIR and SWIR (Figure 3.12).

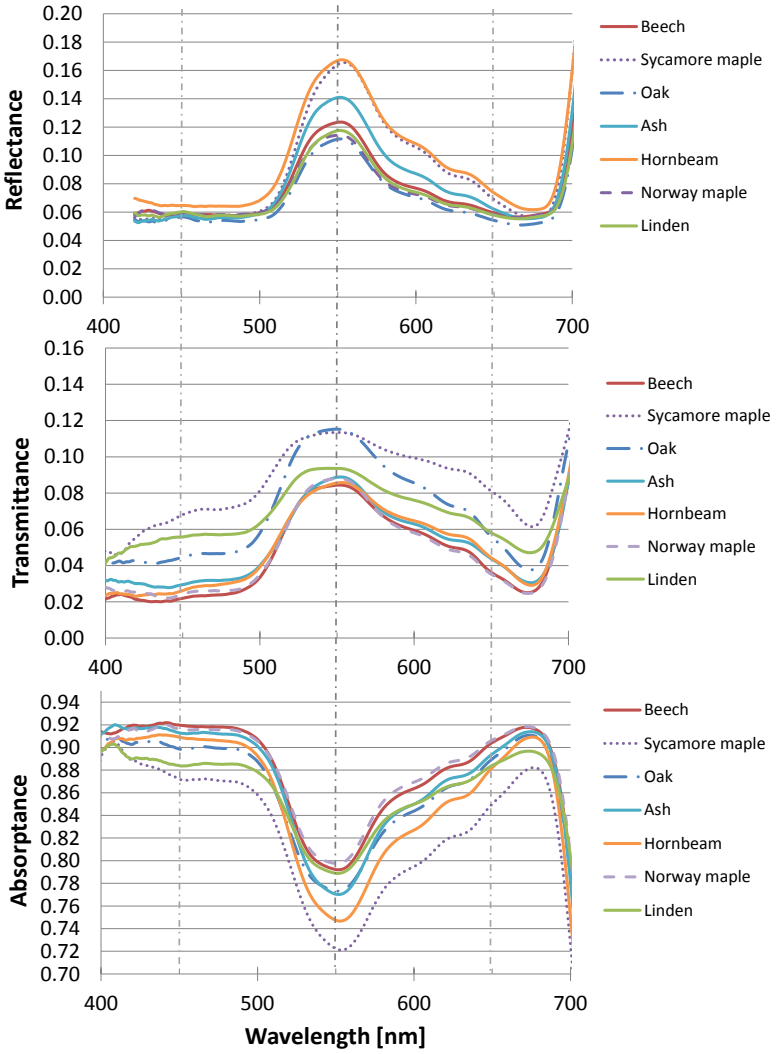

Figure 3.12: Average spectral leaf reflectance, transmittance and absorptance in the PAR region.

Hornbeam and Sycamore maple reflect the most, oak and Norway maple least. *T* curves show a similar pattern as the reflectances, except for Sycamore maple, oak and linden, which transmit more especially towards the blue and red. Similarly, Sycamore maple and hornbeam show the lowest *A*, Norway maple and beech the highest indicating higher concentrations of absorbing pigments such as chlorophyll a and b. Besides the main absorption in the blue below 500 nm and red regions of the spectrum with a minimum at about 680 nm, some features are especially apparent at the wavelengths 580 and 627 nm as well as at about 619 and 634 nm. They actually deviate from the input bands used for the calculated vegetation indices.

The following graphs show the relationships between leaf reflectance, absorptance and transmittance averaged over all sampled tree species – in May, approximately the first month of

the growing season (Figure 3.13). The dependencies on the wavelength becomes clear after the separation of five main spectral regions: 420-700 nm (VIS≈PAR), 760-1100 nm (NIR), 1150-1450 nm (SWIR1a), 1500-1800 nm (SWIR1b) and 1900-2450 nm (SWIR2). *R*, *T*, and *A* show the weakest changes in the NIR region. Generally, reflectance values are positively related to transmittance and slightly lesser to absorptance. Absorptance decreases highly when transmittance is increasing nearly over all wavelengths.

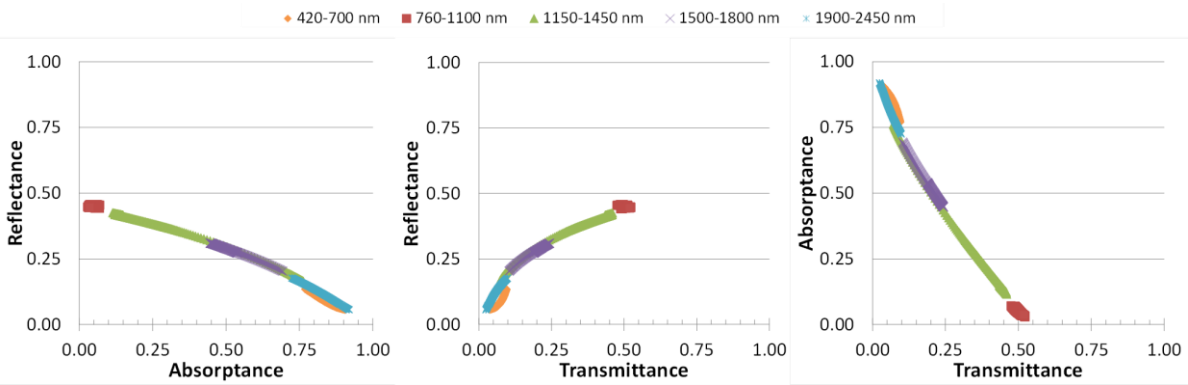

Figure 3.13: Relationships between reflectance, absorptance and transmittance as averaged over all tree species sampled in May.

3.3.2 Multitemporal measurements

3.3.2.1 Leaf spectral transmittance

As a main aspect in this study is to demonstrate and analyze the growing-seasonal trend in the appearance of deciduous leaves, multitemporal measurements were conducted during two growing seasons in 2011 and 2012. One important parameter is the leaf transmission as an indicator of photosynthetic activities and rate of absorption and reflection. Spectral transmittances at two points of time (25.05.2012, 19.07.2012) were obtained for ash, beech and Sycamore maple. The measurements are revealing a quite peculiar behavior. At the second beech transmittance response pattern there is only a distinct decrease around 800 nm, the remaining curve is almost identical with the first, but shifted minimally. The transmittance of Sycamore maple, in contrast, has a stronger decrease over the whole NIR plateau and minor increase in the PAR region. However, the curves of ash do not show at all any similarities to each other (Figure 3.14). Transmittance in the PAR range is for beech lower than for the other species, whereas, compared to the others, there is a higher transmittance in NIR and SWIR, where the leaf water content is mainly responsible for the spectral behavior. Furthermore, the differences between the May and July values are less for beech implying almost full development of the leaves in early growing season. All three species transmit less at NIR and SWIR in July.

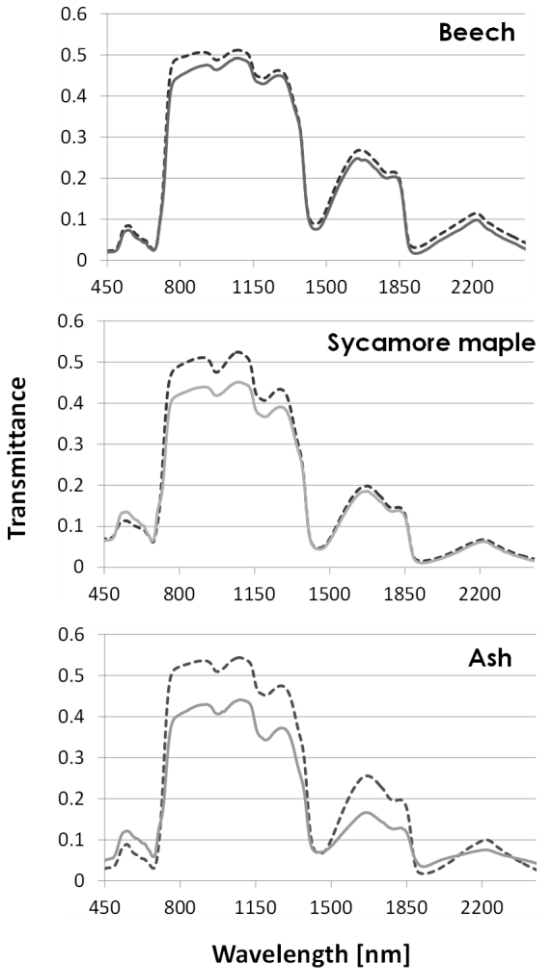

Figure 3.14: Transmittances on leaf level for beech, Sycamore maple and ash as sampled in May (dashed line) and July (solid line).

3.3.2.2 Leaf spectral reflectance

In Figure 3.15, the mean spectral response patterns of sampled tree species leaves from several dates are plotted. Again, all species have the typical shape of the curves in common. The 2011 data is showing much higher values in NIR and SWIR due to the different way of measurement using contact probe and 2-leaf-stack. However, when looking at the different acquiring dates, it is striking that there is a specific trend for every tree species from May until August. In the visible range of the electromagnetic spectrum (ca. 400-700 nm) values tend to decrease, caused primarily by the increasing amount of chlorophylls, which absorb mainly in the blue and red range (400-500 and 600-700 nm).

In contrast, there is a distinct shift upwards in the near infrared and the first part of the shortwave infrared. Considering these shifts over time, it can be deduced which tree species start shooting leaves and greening first. Therefore, hornbeam shows a bit delayed leave maturing, while ash reached higher reflectances in the near infrared earlier. While all species show similar NIR reflectances in the August measurements, hornbeam and especially oak have lower values on the

02.08.2011. The same applies for the SWIR1, where only beech shows higher values at that day compared to the other dates.

Generally, beech reflects more in SWIR1 and SWIR2 than the second most frequent species ash. Moreover, the three rather shade-tolerant species beech, linden and hornbeam reflect on average in SWIR1 the most, followed by maples. Nonetheless, at all species both minima of the water bands at about 1400 and 1900 nm are rather constant over all measurements. Having a look on the region of the photosynthetic active radiation, the reflectance curves of May-July 2012 follow a clear decreasing trend over all bands with a higher absorption in red and blue. The three measurements within August 2011 are more or less equal to each other and do not show any huge development in time. However, the pattern is similar in all data sets.

In VIS, there are fewer influences by the measurement method of the two years apparent. This is evident when zooming in to a range of 400-700 nm (Figure 3.17). Except for oak, the reflectances are the highest in May 2012, whereas in July 2012 especially linden and hornbeam show the lowest values. Even at the measurements within three weeks in August, there are distinct differences for single species like oak and Sycamore maple. By contrast, ash and mainly hornbeam are rather constant. Furthermore, there is a certain pattern in the responses for the species, and one can see specific shapes of the curves. Norway maple and linden have a narrower peak at the green wavelengths, whereas hornbeam and Sycamore maple this peak is wider and with a more gentle slope particularly towards the red. Hence, the shadow-tolerant species beech, linden and hornbeam do not show explicitly different reflectance curves compared to intolerant oak and ash.

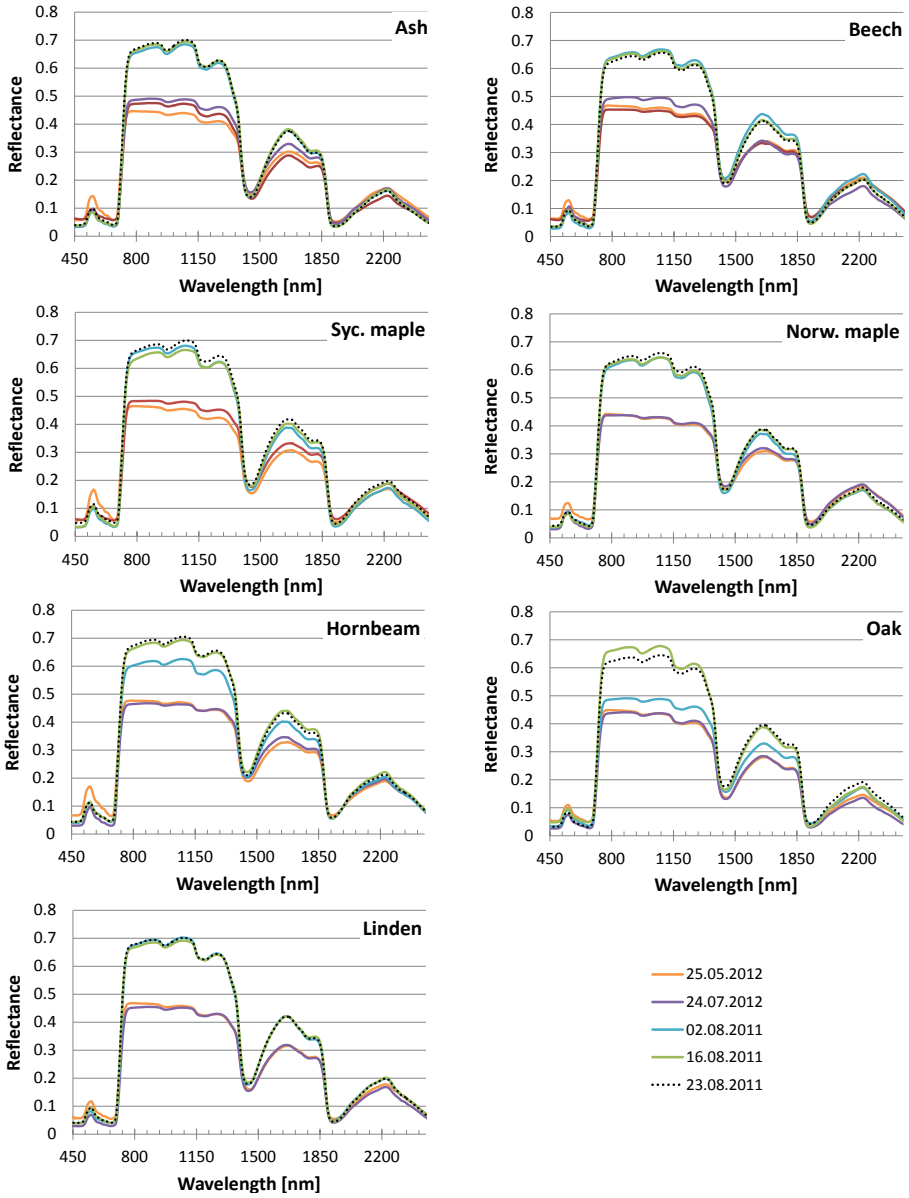

Figure 3.15: Phenologies of leaf reflectances of the compared seven tree species. Early measurements show higher chlorophyll absorption but lower reflectance in infrared.

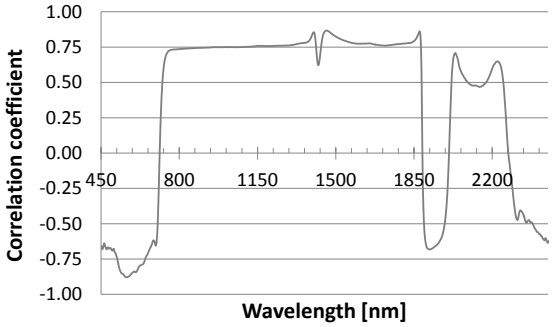

Figure 3.16: Pearson's correlation coefficient between mean reflectance and day of the year over all species.

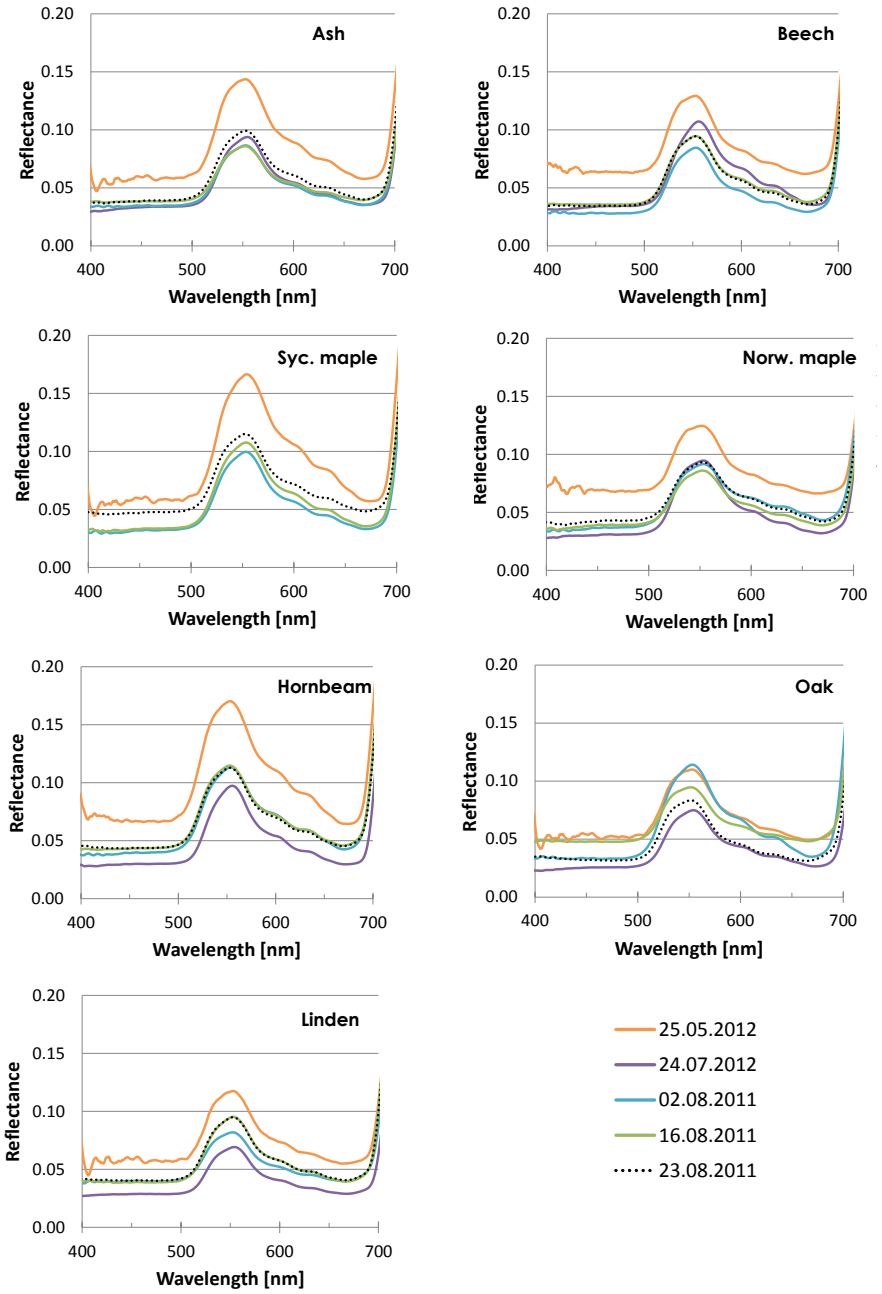

Figure 3.17: Leaf reflectances in PAR region, note that for Sycamore maple there is no value for July.

The overall mean reflectances for each tree species for both years are showing perfectly the typical and rather smooth patterns of a high-resolution measurement on leaf level. Yet some species are partially very similar, and there is a sort of grouping in the responses. This is especially obvious in the SWIR2 region, where three clusters are (i) beech and hornbeam, (ii) Norway maple, Sycamore maple and linden and (iii) oak and ash.

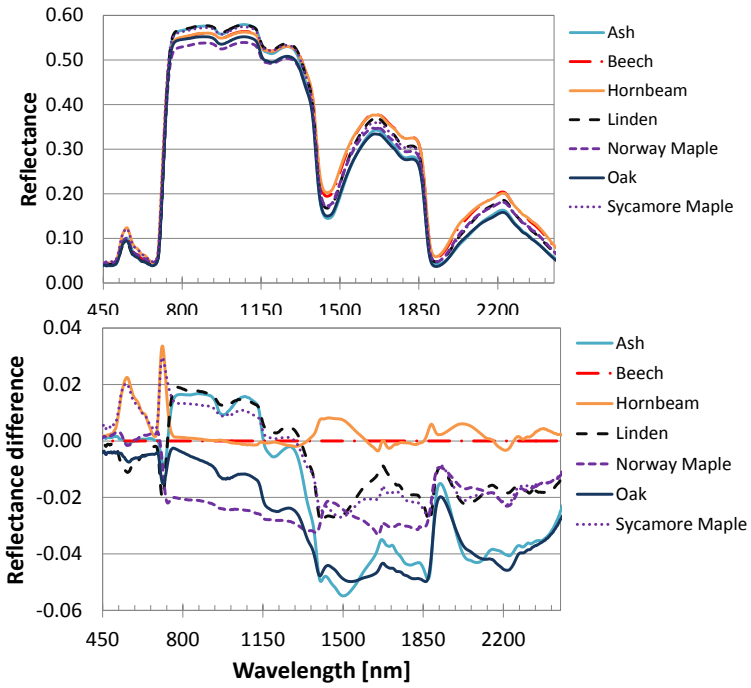

Figure 3.18: Overall means (2011-2012) of the leaf level reflectances (top) and the corresponding differences to beech as reference (bottom).

Within the visible section between 450 and 650 nm, we can see similarities between hornbeam and Sycamore maple showing the highest values and amongst ash, beech and Norway maple (Figure 3.19a). Oak and linden (lime) reflect the least. Whereas in NIR we can separate two groups at about 800-1120 nm: (i) Lime, ash and Sycamore maple and (ii) beech and hornbeam (Figure 3.19b). Oak and Norway maple have the lowest values. In SWIR1 (Figure 3.19c) again beech and hornbeam and SWIR2 (Figure 3.19d) are objectively quite similar. However, especially in SWIR2 the grouping of species is most striking. Here, oak and ash show similar pattern.

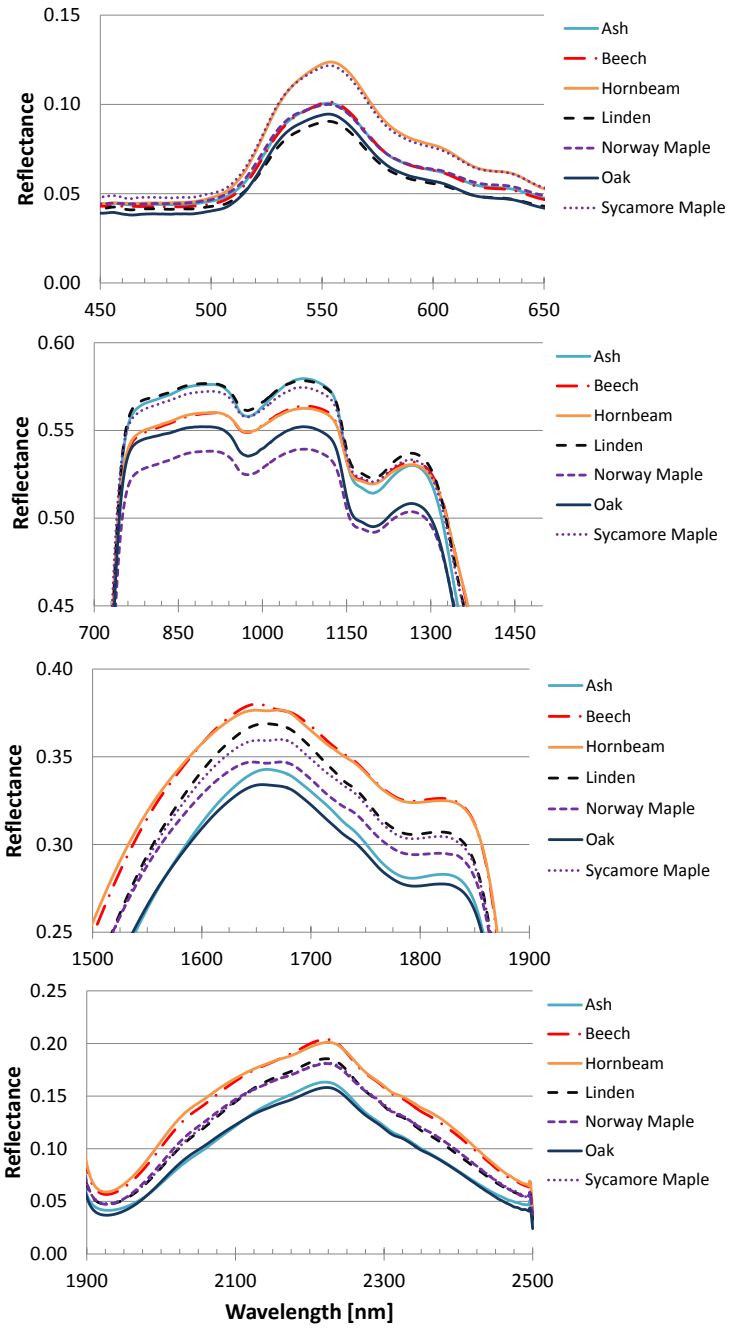

Figure 3.19: Leaf reflectances of the sampled tree species magnified for VIS, NIR, SWIR1 and SWIR 2 (top to bottom). At each spectral region, some sort of species grouping is apparent.

Standard deviations over all species by acquisition date are shown in Figure 3.20a. Furthermore, the corresponding Pearson's correlation coefficients of reflectance value and day of the year are plotted against the wavelength showing highest trends in NIR. Biggest deviations are at the red edge position in end of May and July and for 23rd of August at about 1080 nm. By contrast, the other dates in July and August show high deviations at both inclination points around the water absorption band at 1450 nm. Since standard deviations are not comparable here, we have to consider the coefficients (CV) of variation for each data set. CVs are giving different and more meaningful results in terms of comparability for the wavelengths with the most variation (Figure

3.20b). The NIR plateau shows with less than ca. 5 % the lowest variations. The highest dispersions are apparent in the VIS at about 550-600 nm, where the CV is 10-17 %, followed by a peak before the red edge region at 700 nm, and close to the water absorption bands at 1450 and 1975 nm. Here it reaches up to 21 %. Highest positive correlations between CV and day of the year are present in blue, red, the beginning of the NIR plateau and the second water band, negative correlations in green, at the red edge and moderately in SWIR1.

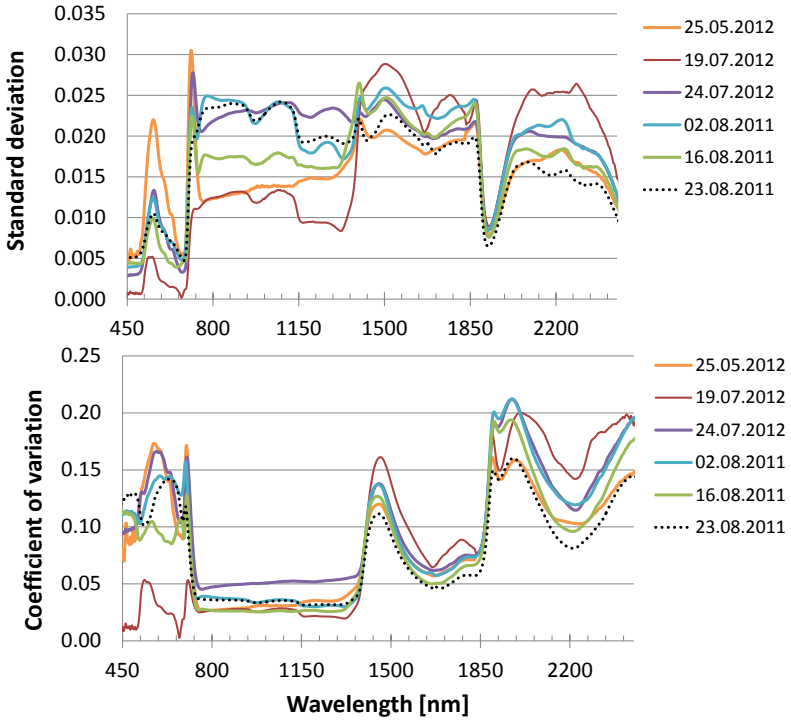

Figure 3.20: Top: Standard deviations over all mean species for each measurement date. Bottom: Corresponding coefficients of variation (CV).

Considering only the VIS spectrum, we can see the local maxima on the right hand side of the "green hump" at 550 nm, which seems to shift with the date towards the red wavelengths (Figure 3.21). However, the exceptions are in the data of the 16.08. and the 19.07. Below 500 nm, there is some fluctuation in the CV, which is induced by lower sensor stability in shorter wavelengths.

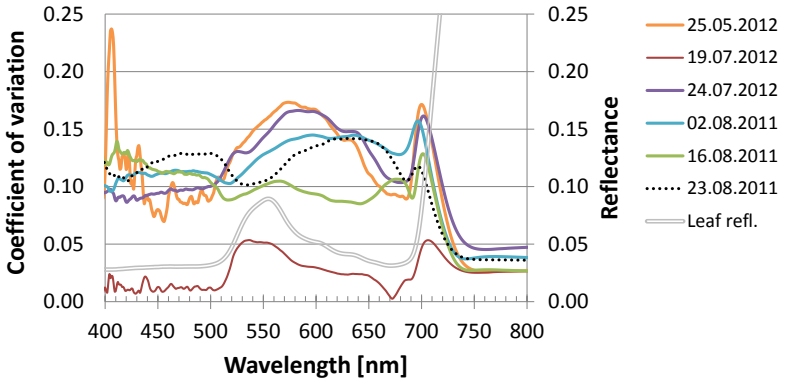

Figure 3.21: Magnified plot of the coefficients of variation in the visible and red edge spectral region. For comparison, a typical leaf reflectance is plotted.

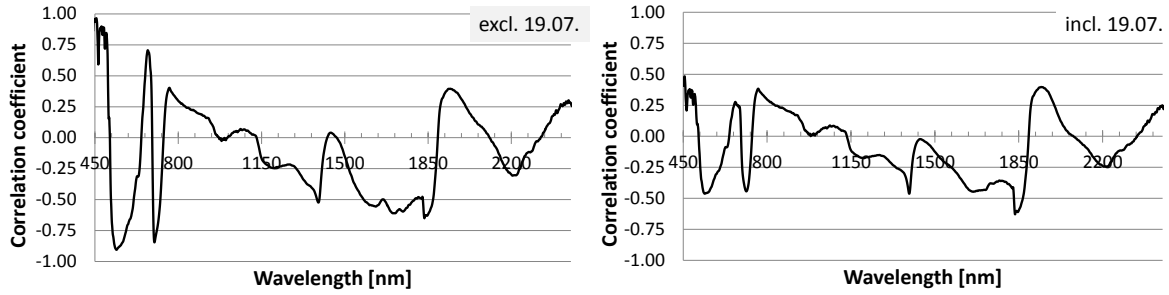

Figure 3.22: Band wise Pearson's correlation coefficients between CV and day of the year incl. and excl. 19th of July data.

3.3.2.3 Vegetation indices

The derived vegetation indices NDVI, SR, PRI, SIPI, RGRI, CRI1 and ARI2 change more or less over time, according to the input reflectances (Figure 3.23). Combining both years 2011 and 2012 to one growing season data set, there is a slight increase apparent in NDVI and SR, whereas the indices CRI1, ARI2 show a decrease. The CRI1 values of Norway maple are quite similar but lower to hornbeam and by far smaller than of beech. RGRI and SIPI do not change much from July to August, except the Norway maple and hornbeam series. Here we can state a maximum in beginning of August. PRI is only rather stable over the time for some species. However, higher PRI deviations are present for hornbeam and mainly beech end of July, as well as an increase for oak. As the range of data values is different for each VI, e.g. about 0-20 for ARI2 and -0.1-0.06 for PRI, the applied normalization (Eq. 1) helps in displaying and intercomparison (Figure 3.24). While beech and oak show considerable changes, linden and ash are somewhat constant in relation to the others.

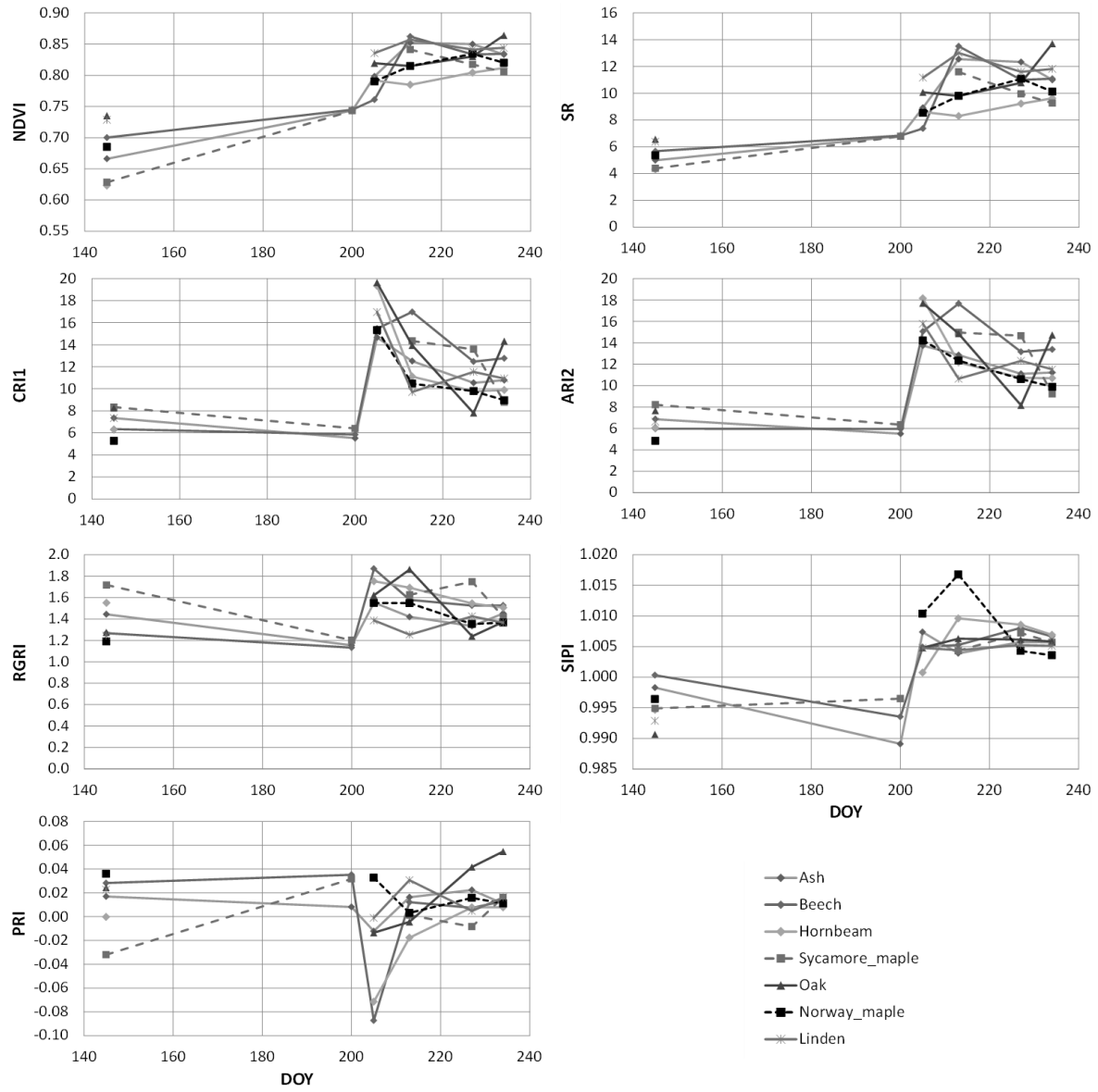

Figure 3.23: Changes in the calculated mean VI over the growing season May-August.

When checking the overall mean values for all tree species (Figure 3.25), it is striking that almost all species follow similar trends. Nonetheless, VI values and the corresponding ranking are crossing each other, so that there is often no clear ranking in species. One can see that a higher NDVI leads by trend to a larger CRI1 due to a higher content of Chlorophyll. The VI of the beech data set are rather constantly in the mid-range and are the largest for CRI1 and ARI2 together with oak. Another group is including hornbeam, linden ash and Sycamore maple. By contrast, all species are separated from each other more evenly in NDVI and SR. The overall trend of VI is also including some discrepancies like the SIPI data of oak, which is on average quite stable, but also relatively high compared to the other species. However, these means neglect the larger SIPI of Norway maple in July/August. The biggest variation in terms of standard deviation is noted in RGRI followed by SIPI and PRI, the lowest in ARI2 and CRI1.

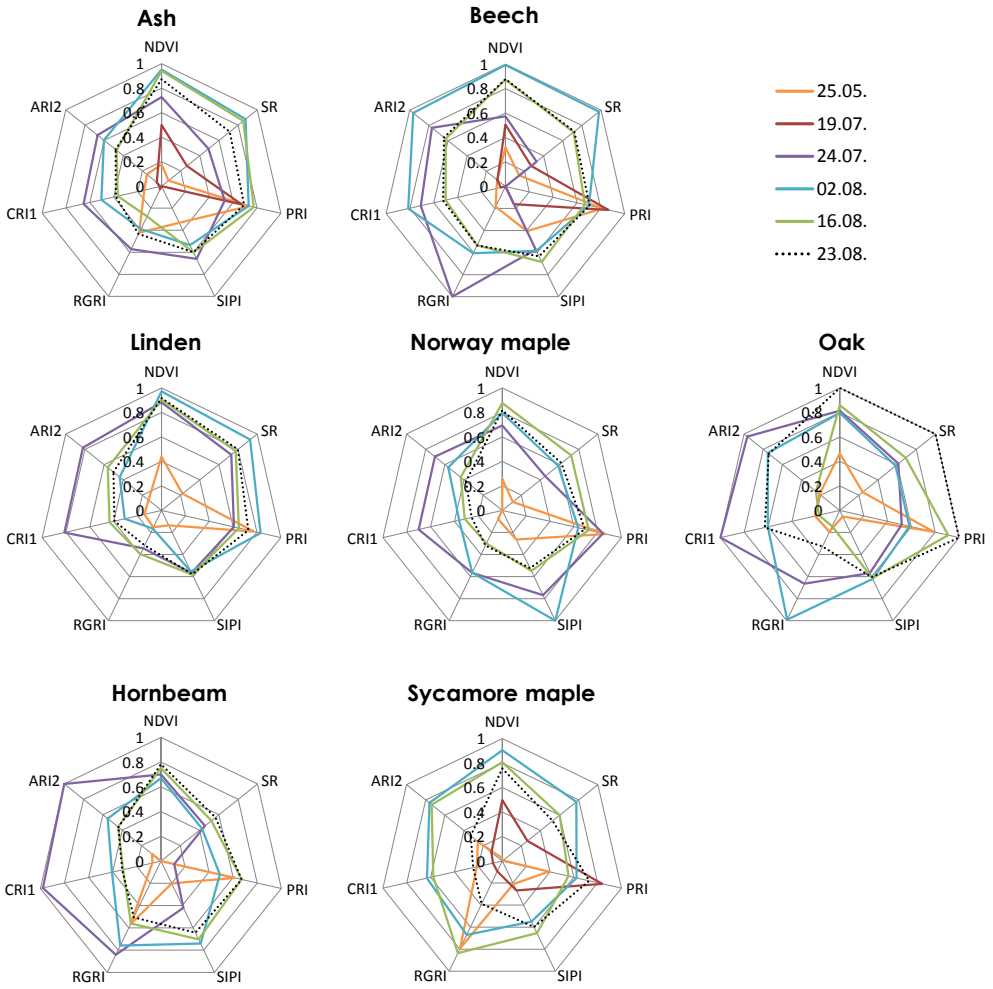

Figure 3.24: Selected VI over time for all sampled tree species. Data is normalized to 0-1 (min. to max.) for each VI by a ranking over all species.

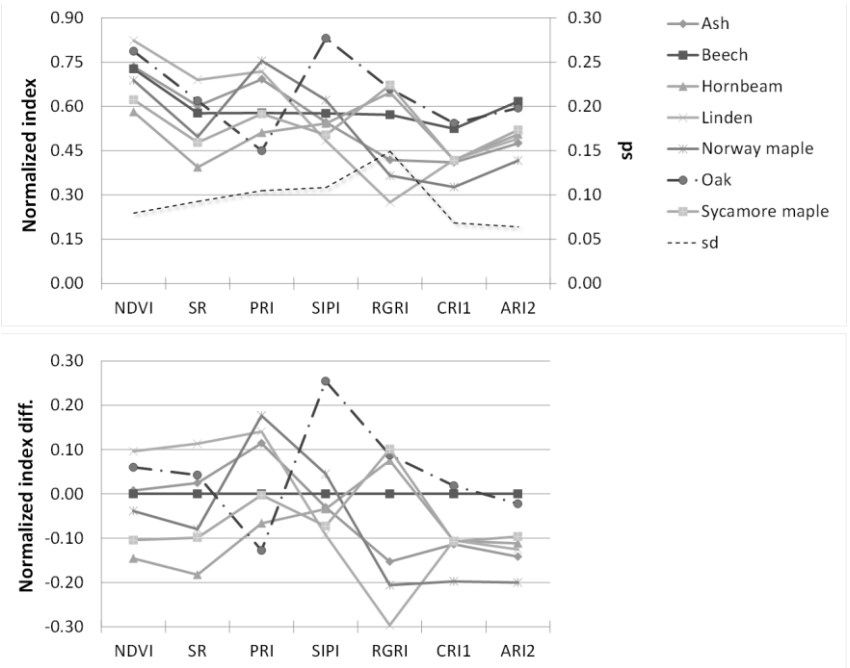

Figure 3.25: Normalized VI over all measurements in time for each species incl. standard deviation (sd) (top) and as differences from beech as reference (bottom), excl. data from 19th of July.

3.4 DISCUSSION AND CONCLUSIONS

Many field spectroscopy studies have been conducted on minerals or agricultural crops dealing in fact with targets which allow rather easy ground measurements (Arafat et al., 2013; Ramakrishnan et al., 2013; Schmidt and Skidmore, 2003). It is clear that the conditions are quite different and rather complex when dealing with spectroscopy and forests. As a general remark one can say that the utilization of a field spectroradiometer is not as trivial as it might look like at first sight. Even after some training users should be aware of the radiation physics and the measurement technology and handle it with care to avoid mistakes leading to unusable data. A crucial point is the way of sampling as there is no established method yet for collecting leaf spectra in trees. However, in this study we only gained data from leaves that were healthy, intact and typical for the individual tree crown. Because the study was done in a national park, it was not possible to harvest the leaves. Hence, the number of samples per species could maybe higher in future research to ensure an adequate sampling. Since we could not use any marking tapes or tags, it might be that not always the same branches of the sample trees were recovered. Another restriction within the framework of data acquisition is the limited time slot per measurement day. It emerged that is was rather time consuming to collect several recordings within one day around noon. Certainly, direct measurements using leaf clip or contact probe are not as weather-dependent as imaging spectroscopy. However, we tried to conduct measurements only during sunny weather to ensure (i) correct device calibration by white reference panel and (ii) similar biochemical conditions within leaves for better comparison between days and further remote sensing data acquisition.

In both years of measurements, two different fore-optical devices were used: in 2011, a contact probe for measuring two stacked leaves, in 2012, a leaf clip for one leaf each time. Indeed, the amount of leaves in a stack is influencing the reflectance and transmittance values especially in the NIR region, which matches perfectly with other studies (Bartlett et al., 2011; Lillesaeter, 1982; Woolley, 1971). This is important for the comparison of data at different scales like remote sensing and in-situ measurements and gives insights for the derivation and estimation of forest canopy light interception. However, because all species were treated similarly, it is assumed that those factors can be disregarded for analyses based on averages. Moreover, the vegetation indices data sets do not show tremendous deviations, but rather complement to one other. Measurements from different dates such as the transmittances of beech are fitting very well to each other and do support that the work was done quite accurately. Moreover, the identified relationships between reflectance, transmittance and absorptance do match particularly with the results of prior studies (Bauerle et al., 2004; Panferov et al., 2001). This also underscores that the measurements were done correctly.

There is possibly a concern about the method of smoothing original reflectance data. The used Savitzky-Golay filter, like any other filtering technique, can polish too much and may destroy

important features, but also introduce artefacts. However, since the obtained data is in very high resolution without noteworthy noise – except the first and last couple of bands – and the processing steps were observed with care, this risk can be neglected.

We could see that the derivation of tree leaf reflectances is a non-trivial and complex topic. Talking about reflectances, on the one hand, there are discrepancies between the leaves within each crown. However, here only most upper sun leaves were considered and not the general differences in leaf optical properties (LOP) of sun and shade leaves. On the other hand, there are differences within and between species in leaf structure and composition like epidermal hairs or cuticular differences such as waxy layers, which can influence the surface reflectance tremendously. Hence, it is also important to incorporate both sides of the leaves (Cordón and Lagorio, 2007; Hughes et al., 2008). In this study, all species showed a higher VIS-reflectance at the abaxial than at the adaxial top side. Especially ash trees (*Fraxinus excelsior*) tend to turn their leaves easily already at slower wind speeds and show the lower bright sides upwards. This is also a reason why they can appear lighter than beech (*Fagus sylvatica*), e.g., in (near infrared) aerial or satellite imagery of mixed temperate stands. At least for tropical species the thickness of leaves seems to be another key factor for leaf reflectance (Castro-Esau et al., 2006; Knapp and Carter, 1998), which was not possible to analyze in this study, but might be incorporated for the temperate species in further research.

The portions of measured reflectance (R) and transmittance (T) and derived absorptance (A) are as expected and show typical curves of healthy green vegetation. Transmission shows similar pattern to reflection, but it is clear that it is impossible just to infer transmittance and absorptance from reflectance values without an explicit measurement. However, at least in the scatterplot for May we can see rather clearly an approximated relation between R, T and A. Generally, transmittance tends to be higher than reflectance only in NIR but lower in VIS and both SWIR regions. Absorptance behaves accordingly to that and rather reciprocally having minimal values in NIR. Corresponding to the absorption by chlorophyll and water, the local minima in transmission are at about 460 and 680 nm and at 1450 and 1920 nm, respectively.

If we compare species, the transmittances showed for beech lower values in the visible range the electromagnetic spectrum than for the other species, but a higher transmission in the infrared. This could be related to the shade tolerance of beech and its ability of (i) utilizing the high energy radiation better and (ii) shading other plants creating a milieu in which it has an advantage over competitors. This result is also supported by high absorptance values in blue and red of beech, which is in fact similar to Norway maple. By contrast, Sycamore maple, also known as shadow-tolerant mainly in younger ages, however shows higher transmission in the VIS region. Moreover, beech and linden do not show any special pattern that differs on the first sight from the other less shade-tolerant species ash and oak. Further detailed analysis need to follow up.

The seasonality was demonstrated well in this study, as there are clear trends in reflectances during the growing season. In addition, the spectral behavior differs between tree species. This is related to a variety of reasons such as leaf thickness, leaf surface and internal structure as well as pigment and water content, that have to be taken into account. The variation in the standard deviations of reflectances over all species and time underline the implication of the date of measurement. For some reasons the few reflectance values derived on 19th of July do not seem to fit in the sequence of values and should be not included in further analysis. Considering the coefficients of variation as a first measure of dispersion, we can see that the highest variations appear in the visible region around 580 and 700 nm as well as close to the water absorption bands in SWIR. This is especially interesting for a comparison with remote sensing sensors, which are usually blind or affected by the noise in the signal induced by water vapor within the atmosphere. Rather surprising was the low dispersion in the NIR plateau. However, that matches with similar results found by researchers on species level (C. Zhang et al., 2014).

As the reflectances change, seasonality is consequently also apparent in the calculated vegetation indices. It could be shown that during the summer the conditions start to stabilize. However, for the CRI1 (Carotenoid Reflectance Index 1) and similar for ARI2 (Anthocyanin reflectance index 2) there seems to be a decrease from July to August for all sampled species, with exception of oak. PRI (Photochemical Reflectance Index) tends to respond in a wider range within short time changes in illumination conditions (Soudani et al., 2014). During the growing season, there were only a few days of constant weather conditions, which could have an immediate effect on the tree biophysiology. This might be supported by the findings in this study, as the measurements for July and August indicate where the values differ highly from the others. LOP derived in past and future could be set into relation with local weather conditions such as temperature, precipitation or drought stress.

Another possible application for the utilization of leaf level spectra are radiative transfer models like PROSAIL (PROSPECT and SAILH) (Jacquemoud et al., 2009; Schlerf and Atzberger, 2006) or the DART model (Gastellu-Etchegorry et al., 2004). Gathered LOP can be used as basis input and validation for modelling tissue layers and canopies and hence whole forest stands under different conditions. Here we can also state that the point of time of a simulation should be chosen meaningfully according to the date the spectral input data was collected. However, since details about the relation of the sequestration of carbon (C) and the light-use efficiency (LUE) or photosynthesis rate, respectively, remain partly obscure (Garbulsky et al., 2011; Wong and Gamon, 2015), additional information about the actual radiation use efficiency (RUE) over the full spectrum and the assimilation of C may finally be connected to growth and carbon uptake models (Anderson et al., 2000; Stoy et al., 2014).

One key feature in reflectance is the red edge position (REP) at about 720 nm besides the inclination points of the water bands, which differ both in time and interspecifically. There is a link of REP to health and senescence status and the concentration of chlorophyll, carotenoids and anthocyanin. A shift of the red edge position towards shorter wavelengths is induced by pigment degradation and vice versa (Gitelson et al., 2003; Vogelmann et al., 1993). Hence, the derivation of leaf pigments from samples might be another meaningful task to implement in forthcoming investigations. In order to complete the image of foliage characteristics, the estimation of leaf water content as a main driver for absorption in SWIR (Ceccato et al., 2001). That and the determination of non-pigment constitutes incl. cellulose and lignin, which are mainly responsible for the appearance in NIR and SWIR (Clark and Roberts, 2012; Dawson et al., 1999), could help to enhance the knowledge about spectral pattern and physiological traits.

The utilization of hyperspectral field data can be a powerful tool for detailed spectral analyzes. However, the user should be aware of the large amount of data that can arise and a proper way to analyze it. Furthermore, it should be considered, whether there is a benefit at all, if we consider the increased labors and rather higher costs in using this technology. A scientifically interesting and important approach the combination of spectra measured on the ground and remotely sensed data. However, reflectances are more similar on leaf level than on the scale of crown or stands. Hence, it is crucial to have knowledge about the trends and changes in leaf reflectances during a growing season. Depending on the point of time the measurements are conducted, the spectral response patterns can lead to completely different conclusions and result. It was successfully shown that there are species-specific differences in phenological reflectances. The appearances and reflectances of tree leaves do highly change during growing season, especially in the for human eyes invisible infrared, so that foliage is more than just greenish. All in all, detailed data about leaf optical properties are very crucial for a variety of research applications and still highly needed (Homolová et al., 2013). The derived results contribute hence to understand the optical properties and leaf traits of temperate broadleaved tree species. Certainly, the discrimination of tree species on different scales like leaf and crown is a main focus. Next steps within the framework of this study are the linkage to remotely sensed information and the comparison of tree crown reflectances.

CHAPTER 4

SPECTRAL TRAITS OF TREES AT DIFFERENT SCALES

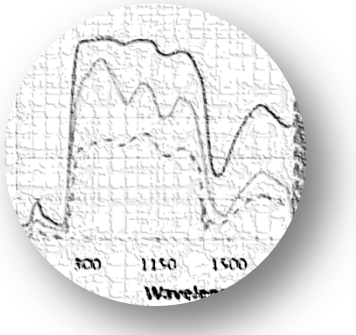

4 CHAPTER FOUR – SPECTRAL TRAITS OF BROADLEAVED TREE SPECIES AT DIFFERENT SCALES

4.1 INTRODUCTION

Knowledge about the spatial extent of forested land and particularly its status is essential for planning and conservation (Lui and Coomes, 2015; O'Connor et al., 2015; Turner et al., 2015). A standard way in Earth observation is the utilization of optical airborne and satellite systems detached from the ground. Imaging and non-imaging hyperspectral sensors offer contiguous information covering commonly the electromagnetic spectrum between visible violet and shortwave infrared. For a meaningful operation, the link between ground information and the signal reaching the sensor is crucial. In-situ field observations or measurements are used as reference for remotely sensed data and for sensor calibration (Pfitzner et al., 2006). Obtained data can be used for a variety of applications. Some studies are conducted on minerals, agricultural crops or on other targets that are rather easy to reach (Arafat et al., 2013; Ramakrishnan et al., 2013; Schmidt and Skidmore, 2003). However, when dealing with spectroscopy and forests the circumstances are obviously quite different. Here, the appearance of trees and their traits are of central interest. The heterogeneous canopy surface and variations in type, height, stand density and development stage influence the reflection behavior (Barbier et al., 2012; Nilson and Peterson, 1994). Other drivers are biophysical and chemical components within the foliage (Curran, 1989). As shown in previous chapters, leaf optical properties are species- and time dependent and show typical response patterns. Distinct spectral features are mainly caused by absorption at certain wavelengths. Detecting those characteristics is pertinent to describing plant type and condition.

A rather important feature of vegetation reflectance curves is the red edge position (REP) (Cho et al., 2008b; Dawson and Curran, 1998), also referred to as red edge inflection point (REIP) (Schlerf et al., 2005; Ustin et al., 2009). It marks the maximum slope of the reflection between the red and near infrared region at about 700-720 nm. Furthermore, the REP is associated with chlorophyll content and hence with plant vigor (Filella and Peñuelas, 1994). Since precise determination of the REP requires a continuous spectrum of narrow bands, hyperspectral data is predestined for this. There are mainly two groups of approaches to define the REP (Li et al., 2005). The first one is using a curve fitting method (Baranoski and Rokne, 2005; Guyot et al., 1992), the second group is based on the calculation of derivates (Tsai and Philpot, 1998; Zarco-Tejada et al., 2003). Derivatives of spectral reflectances allow the separation of background signal and are relatively insensitive to illumination issues (Demetriades-Shah et al., 1990; Tsai and Philpot, 1998). A first derivative for instance should have a local maximum at the red edge inflection point of the original response curve. However, it varies with the content of chlorophyll in the leaves and can show one or even

two peaks at the red edge region (Cho and Skidmore, 2006; Le Maire et al., 2004). In this study, first and second derivatives are calculated and checked for a bimodal red edge hump. Derivatives have been proven their potential mostly in laboratory and in-situ spectroscopy data (Panigrahy et al., 2012), but there are still uncertainties in scaling and airborne hyperspectral remote sensing using real data (Lausch et al., 2013b; Zhang et al., 2006).

The mapping of tree species and the recognition of differences are contemporary and ongoing issues in remote sensing (Clark and Roberts, 2012; Dalponte et al., 2013; Féret and Asner, 2013). Information about the REP might be helpful in distinguishing species (Ghiyamat and Shafri, 2010), but it is by nature depending on the scale, such as leaf and crown (Cho et al., 2008b; Dillen et al., 2012). Spectral derivatives are tested for species discrimination, where they could not always convince to be an appropriate tool (Kumar et al., 2010; Zhang et al., 2006). Moreover, they showed better results when the discrimination is less challenging (Ghiyamat et al., 2013). On the other hand, researchers found significant differences in species (Cho et al., 2008b). However, some studies found that the important wavelength regions for species discrimination are not always clear or the same: VIS and NIR (Ferreira et al., 2013) or NIR and SWIR, e.g. (Clark and Roberts, 2012). Vegetation indices (VI) are further appropriate measures to stress spectral features (Huete et al., 1997; Schlerf et al., 2005). Hyperspectral sensors offer a high number of possible VI by using ratios, normalized differences or further equations incorporating any of their bands (Bannari et al., 1995; Prospere et al., 2014). The capability for estimations of leaf area and chlorophyll content is shown (Brantley et al., 2011; Gitelson et al., 2003). However, similar to the detection of the REP, the values of VI are affected by the resolution of the data. Overall, there are still big scaling issues between leaf, canopy and stand level (Kumar et al., 2010; Malenovský et al., 2007; Schaepman, 2009), and the relationships are yet to be fully understood.

Here, I attempted to describe the relationship between leaf and crown level using simple linear and nonlinear modelling approaches. Moreover, besides the spatial scale, also the temporal dimension for in-situ data is analyzed by incorporating two subsequent growing seasons. This study bases on unique data sets of field and remote sensing data as ground measurements were conducted simultaneously to a hyperspectral airborne survey. Hence, it shall be examined how the spectral responses of broadleaved tree species, selected spectral features and indices change with the level of acquisition and if we can draw conclusions from one scale to another. On the basis of red edge position metrics potential differences will be assessed.

4.2 MATERIALS AND METHODS

4.2.1 Study site

The area is located in the Hainich, a beech (*Fagus sylvatica*) dominated ridge at N51.08° E10.45° and with an elevation of about 440 m a.s.l. Data is collected within the national park. See chapter 3 for a detailed description about the study site. The broadleaved trees have a height of about 25-30 m and an approximate age of 100-120 years. Exact stand information was not available since the stands are unmanaged since decades (Knohl et al., 2003; Mund et al., 2010).

4.2.2 Remotely sensed and in-situ data

The combined airborne hyperspectral sensors AISA EAGLE and HAWK (SPECTRAL IMAGING LTD., Finland) build the remote sensing data part in this study. The cameras record a spectral range of 400-2500 nm split in 368 bands resulting in a spectral sampling of 4-6 nm. The spatial resolution or ground sampling distance (GSD) of the imagery is 2.0 m. It was resampled to 0.25 m pixel size using a nearest neighbor approach in order to achieve a spatially more accurate extraction of pixel values. This procedure allows quasi-subpixel crown delineation while maintaining original pixel values. Because the original resolution is often not sufficient, aerial color infrared photography, Google Earth (GOOGLE INC.) and the basemap in ArcMap (ArcGIS Desktop 10, ESRI) were used as auxiliary data for delineating the tree crowns. Spectral responses of seven broadleaved tree species on the ground are collected by an ASD FieldSpec 3 Hi-Res field spectroradiometer (ANALYTICAL SPECTRAL DEVICES INC.) in the growing seasons of 2011 and 2012 using ASD contact probe and leaf clip, respectively. Also, see chapter 2 for the details. The general study setup is shown in Figure 4.1.

Overall, 18 individual trees were sampled at the canopy walkway within the forest allowing reaching crowns from above (Figure 4.2). Sampled tree species are ash (*Fraxinus excelsior*), beech (*Fagus sylvatica*) hornbeam (*Carpinus betulus*), Norway maple (*Acer platanoides*), Sessile oak (*Quercus petraea*), Sycamore maple (*Acer pseudoplatanus*) and Small-leaved linden (*Tilia cordata*). It is presumed that leaves of shade tolerate species such as beech and hornbeam are more similar to each other, and it is expected that they are different from the other tree species. The second data set consists of reflectance measurements of tree crown parts to get a more direct link to remote sensing imagery. The distance from sensor to crown ranges from about 1 m, only in a few cases the spacing was up to 5 m. Thus, using a fore optic with an IFOV of 25° the resulting footprints have an average diameter of about 0.5 m, what would correspond to four resampled AISA pixels. The spectral response patterns of the corresponding tree crown part can be extracted from the hyperspectral images.

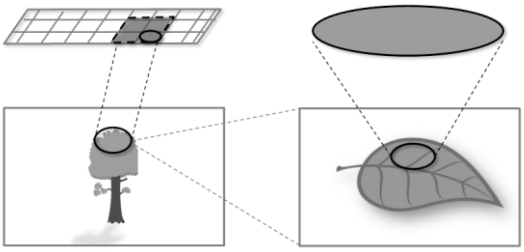

Figure 4.1: Sketch of the general study setup: Extraction of spectral responses on crown level and single leaf level.

Table 4.1: Number of sampled leaves, amount of single measurements and pixels per tree species.

	Measurements		Pixels $_{0.25m}$
Species	**Leaf ASD**	**Crown ASD**	**Crown AISA**
Fraxinus excelsior	214	22	1200
Fagus sylvatica	220	51	2448
Carpinus betulus	165	54	1578
Acer platanoides	38	24	383
Quercus petraea	102	10	1573
Tilia cordata	111	55	770
Acer pseudoplatanus	77	8	-

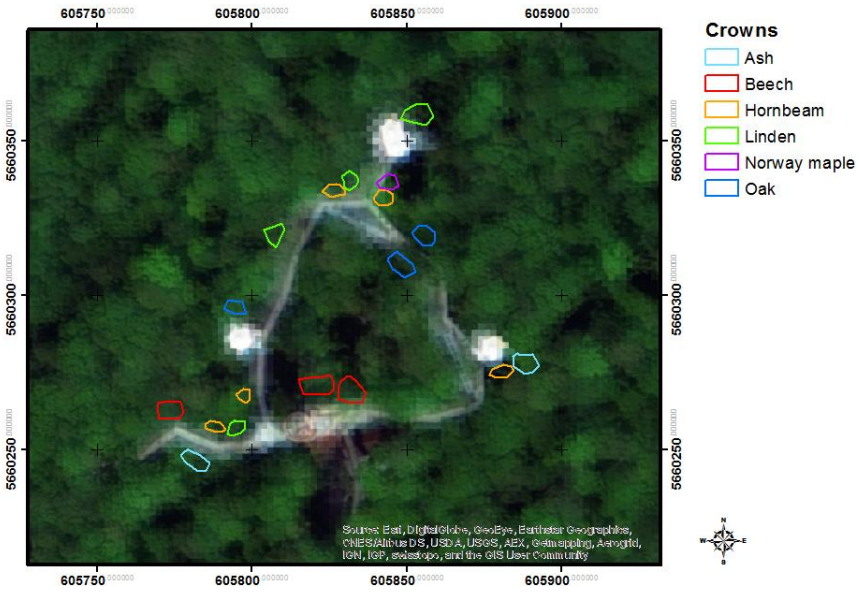

Figure 4.2: Locations of to the sampled trees at the canopy walk. Imagery: AISA EAGLE/HAWK true color composite, overlaid with 33 % transparency to a ArcGIS basemap. Projection: UTM zone 32N, WGS84.

4.2.3 Spectral derivatives

Derivatives (DV) of spectra give an indication of the slope of the original curve as a rate of change. As an approximation, following approach for the first derivative (DV_1) can be used by calculating the slope of a focal line:

$$DV_1 = \frac{\Delta_\rho}{\Delta_\lambda} = \frac{\rho_{i+1} - \rho_i}{\lambda_{i+1} - \lambda_i} \quad \text{(Eq. 4.1)}$$

where ρ represents the reflectance value of the single entry i at the wavelength λ. An increasing reflectance means a positive first derivative, a decreasing reflectance result in a negative first derivative. The second spectral derivative (DV_2), which is a derivation of the first derivative, can be useful for the determination of features such as absorption bands and the red edge inflection point. Furthermore, special vegetation indices can be constructed using the derivatives instead of the original response (White et al., 2008). In spectroscopy, derivatives of even up to the 4th degree are usable, where peaks are more related to absorption. However, as signal noise is being emphasized, too, in this study the calculated first and second derivatives are smoothed again by a Savitzky-Golay filter (Savitzky and Golay, 1964). This frequently used filter applies here a second order polynomial including the five previous and five next positions of the focal value for smoothing.

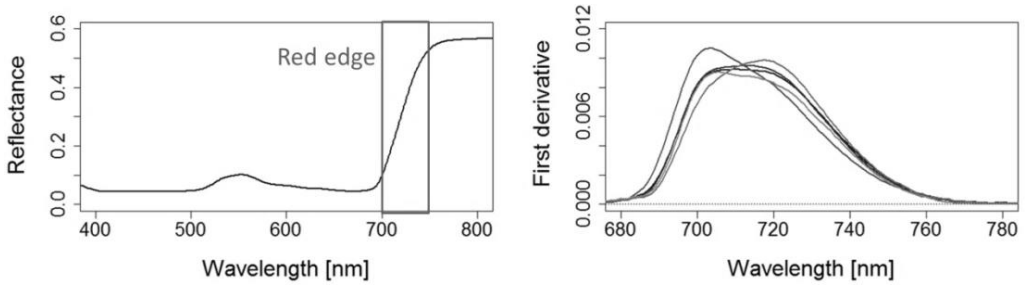

Figure 4.3: Left: Example leaf reflectance with indicated red edge region. Right: Examples for demonstration of first derivative reflectances on leaf level of different species. Peak maxima determine the red edge position. Graphs show own data.

4.2.4 Vegetation indices

Here, the broadband Normalized Difference Vegetation Index (NDVI) and the narrowband indices Photochemical Reflectance Index (PRI), Carotenoid Reflectance Index 1 (CRI1) and Anthocyanin Reflectance Index 2 (ARI2) are calculated to investigate their changes on varying scales. They are common indices and have been the subject in research studies (Cho et al., 2008b; Clark and Roberts, 2012; Prospere et al., 2014).

Table 4.2: Overview of the calculated vegetation indices. ρ represents the specific reflectance.

Objective	Index	Formula	Reference
Greenness	Normalized Difference Vegetation Index	$NDVI = \frac{\rho_{NIR} - \rho_{RED}}{\rho_{NIR} + \rho_{RED}}$	(Rouse et al., 1974)
Leaf pigments	Carotenoid Reflectance Index 1	$CRI1 = \frac{1}{\rho_{510}} - \frac{1}{\rho_{550}}$	(Gitelson et al., 2002)
	Anthocyanin Reflectance Index 2	$ARI2 = \rho_{800} * \left(\frac{1}{\rho_{510}} - \frac{1}{\rho_{700}}\right)$	(Gitelson et al., 2001)
Light use efficiency	Photochemical Reflectance Index	$PRI = \frac{\rho_{531} - \rho_{570}}{\rho_{531} + \rho_{570}}$	(Gamon et al., 1992)

Additionally, for defining the red edge position, the Red Edge Position Index (REPI) was calculated following Guyot et al. (1988) (cf. Baranoski and Rokne, 2005; Cho and Skidmore, 2006; Dawson and Curran, 1998) using a linear four-point interpolation method:

$$\rho_{re} = \frac{\rho_{670} + \rho_{780}}{2} \quad \text{(Eq. 4.2)}$$

$$REPI = 700 + 40\left(\frac{\rho_{re} - \rho_{700}}{\rho_{740} - \rho_{700}}\right) \quad \text{(Eq. 4.3)}$$

where ρ is the reflectance at the corresponding wavelength, ρ_{re} is the inclination point reflectance. $REPI$ represents the red edge position expressed by the wavelength. For the calculation, it uses the reflectance values of two bands in red (670 and 700 nm) and in near infrared (740 and 780 nm), respectively (Figure 4.4). The idea behind this interpolation, is to assume a straight line between low values due the chlorophyll absorption and high values in the NIR plateau in order to determine the red edge position at about the center of this line (Cho et al., 2008a; Cho and Skidmore, 2006).

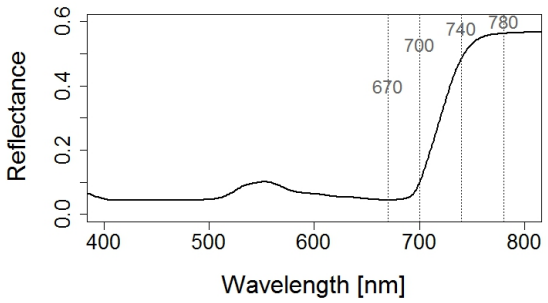

Figure 4.4: Wavelengths used for the four-point interpolation method for determine the red edge position. Leaf reflectance is shown as example, based on own data.

4.2.5 Inter-level comparison and regression

A priori, data from different scales for each species are opposed to each other in scatterplots, by what the correlations become visible. In order to estimate approximately relations and

dependencies several approaches can be applied. A simple linear model regression describes a line through data points which minimizes the average deviation from the mean value:

$$y = a * x + b \quad \text{(Eq. 4.4)}$$

Another approach is to use a logarithmic model when data tend to saturate on specific values:

$$y = a * ln(x) + b \quad \text{(Eq. 4.5)}$$

where x is the original reflectance, y is the synthetic; a and b are the model parameters in each case. For the modelling, the in-situ data gathered by the field spectroradiometer is resampled to the spectral sampling interval of the AISA EAGLE/HAWK imagery.

4.3 RESULTS

4.3.1 Leaf level

4.3.1.1 ASD leaf level - reflectances

In the following, only the spectral responses of tree leaves gathered on 24.07.2012, the day the remote sensing flight was conducted, are presented. The reflectances were obtained from the upper, usually sunlit side of the leaves and show the typical pattern of healthy green vegetation, as already demonstrated in the previous chapter. Furthermore, their shape is rather similar on average (Figure 4.5). On a closer look at four spectral regions VIS, NIR, SWIR1 and SWIR2 some pattern and grouping of the species is apparent.

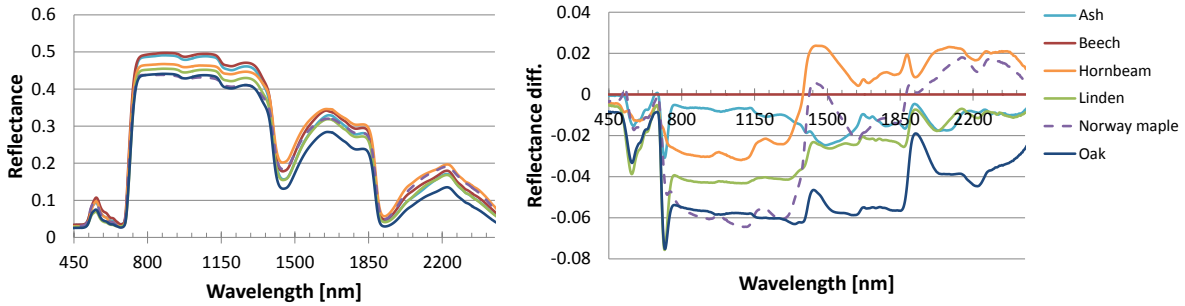

Figure 4.5: Left: Spectral response pattern of the leaves, averaged over the measurements from 24.07.2012. Right: Differences to beech as reference.

4.3.1.2 ASD leaf level - spectral derivatives

The first derivative DV_1 are rather similar over all species (Figure 4.6). They show a major peak at the red edge inflection point and two big negative peaks at the inclinations of the water absorption bands in SWIR. In the second derivatives DV_2, the amplified noise in the curves becomes more visible especially in the shorter wavelengths. DV_2 values of zero mark local maxima of DV_1 and inflections in the original reflectance curve. Overall, the differences between the sampled species

are small. For defining the exact REP, the spectral derivatives are showing their characteristics at the red edge region. The first derivative is always unimodal on leaf level, leading to rather distinct values. The REP can be deduced visually directly from such graphics, either at the peaks of DV_1 or at the intersections of DV_2 and the abscissa where the values are equal to zero (Figure 7). Beech and hornbeam have similar values, having a lower REP. By contrast, the similar responses of linden and oak feature higher REP, indicating higher chlorophyll content.

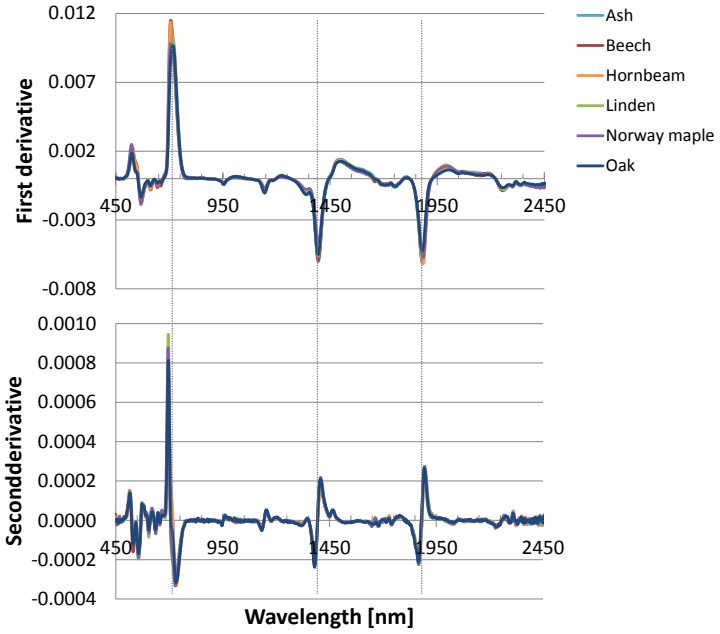

Figure 4.6: First (top) and second (bottom) derivative of averaged spectral responses of the sampled tree species. Inflection points at the red edge area and the two main water absorption bands are highlighted.

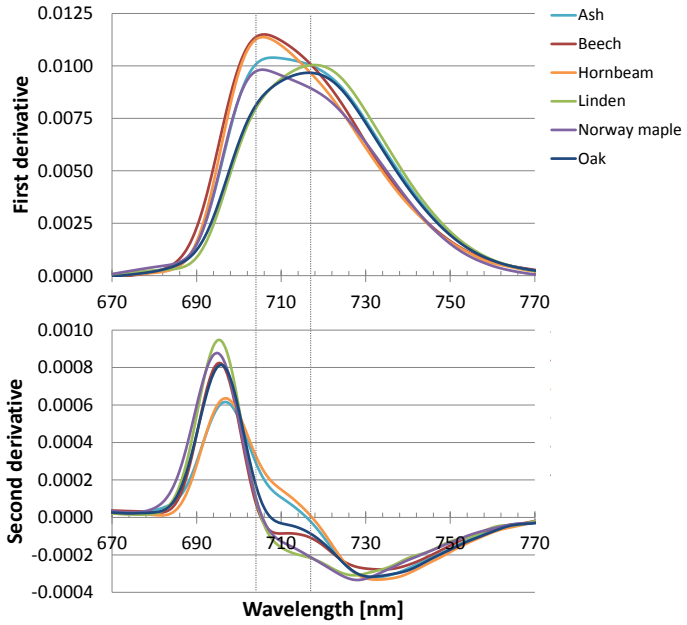

Figure 4.7: Top: First derivative of the leaf spectra between 670 and 770 nm at the red edge region. Peak maxima mark the REP. Bottom: Second derivative of the leaf spectra. Intersections of the curves and zero around 700-720 nm are marking inflections and hence the REP.

4.3.2 Crown level

4.3.2.1 ASD crown level - reflectances

The presented in-situ crown reflectances consist of two data sets acquired with the ASD field spectroradiometer in the growing seasons of 2011 and 2012, containing seven and six species, respectively. Similar to the leaf level data there are also big differences in the crown reflectance values (Figure 4.8). The two main water absorption bands are clearly visible by the sensor noise at about 1450 and 1900 nm. The second data set from 2012, however, appears less influenced by the water vapor or humidity, as the first water band is not as obvious. Additionally, especially in VIS the reflectances are very low. The data sets reveal that there are no clear trends in species reflectances in terms of comparative relation to each other. Neither in absolute nor in relative sense the species are following a ranking. Nevertheless, for a better comparison with the simultaneously acquired remote sensing data the focus shall be on the data gathered in 2012 in the forthcoming paragraphs.

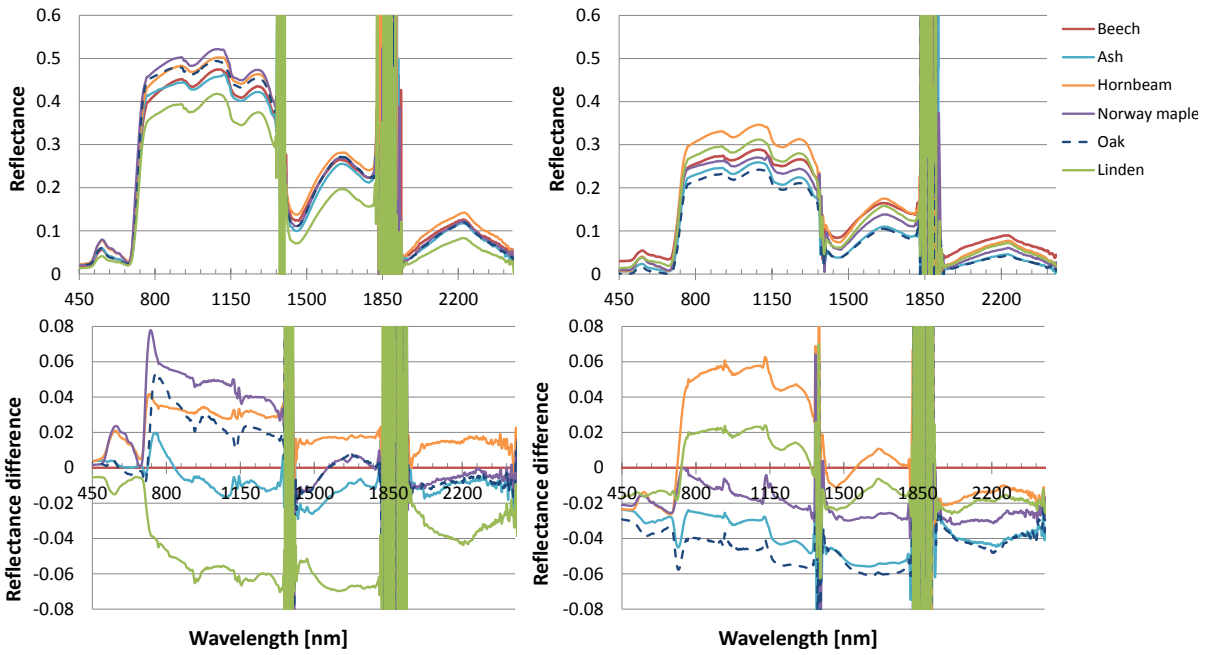

Figure 4.8: Crown level field reflectances and the deviations from beech as reference in 2011 (left column) and 2012 (right column).

4.3.2.2 ASD crown level - spectral derivatives

The DV values of 2012 are much lower than the campaign of 2011, and compared to the leaf level data the patterns are more influenced by noise (Figure 4.9, a, d). At the hump at the red edge of the first derivative, the unimodality is less distinct than in the leaf data. Moreover, a double peak is rather apparent. There are modes at about 701 nm and 725 nm for all species followed by a local maximum at about 718 nm (Figure 4.9, b, e). However, seemingly there is a similar tendency of a blue-shift of REP by which maples and hornbeam have their maximum of DV_1 towards shorter

wavelengths. Whereas there is apparently a red-shift for beech, ash, oak and linden. This should be proven further in section about the finding of the red edge inclination point. Consequently, a graphical reading of the REP from the second derivative is rather difficult as there are multiple points where the values equal zero intersecting the abscissa (Figure 4.9c, f). Here the determination is chosen in such way, that the values be read at the last intersections before becoming negative.

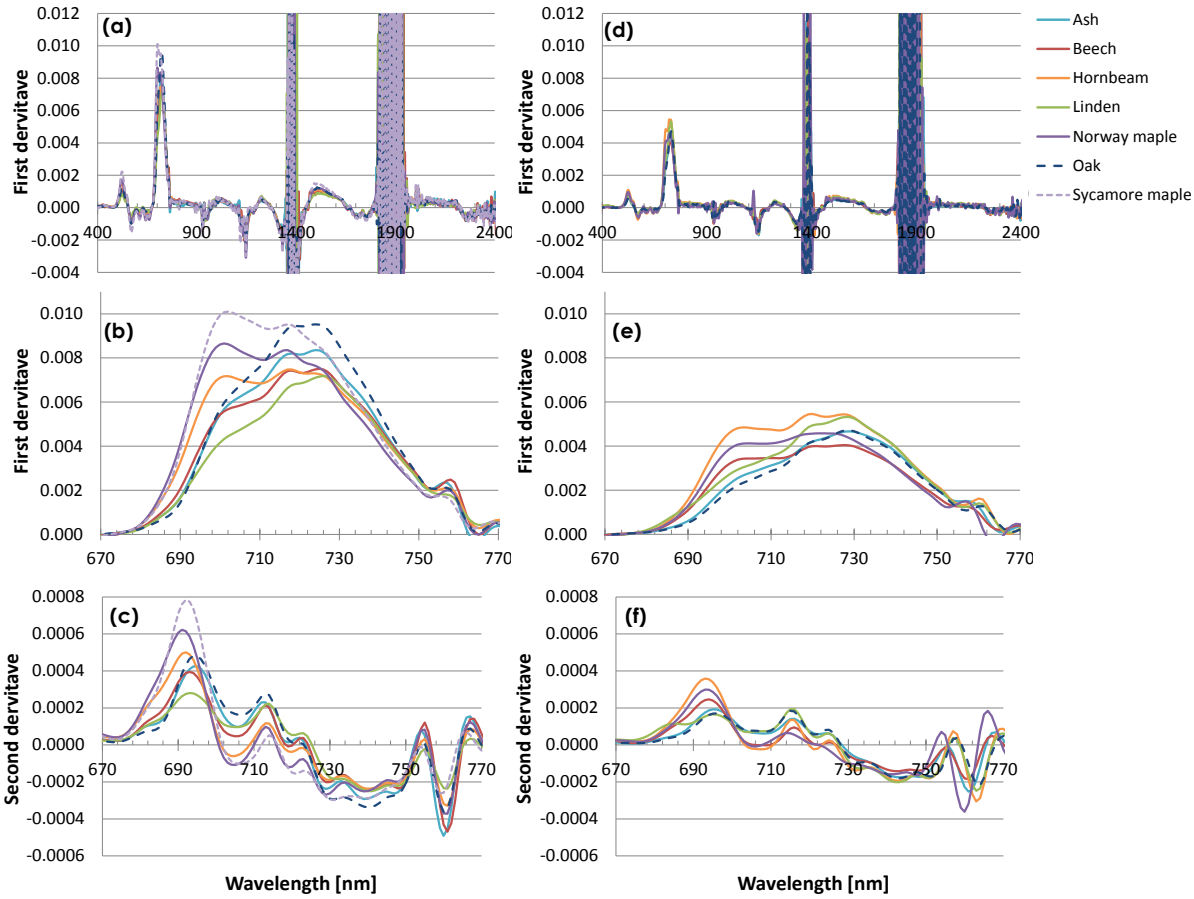

Figure 4.9: First spectral derivatives of in-situ crown reflectances as acquired in 2011 (a) and 2012 (d). Spectral subsets of the red edge region of the first (b, e) and second derivatives (c, f). The 2012 data is not including Sycamore maple.

In contrast to the leaf level signatures and the remotely sensed spectra, there are small peaks present in the in-situ crown data at about 760 nm, which is known as the O_2-A absorption band (Raychaudhuri, 2012). This correlates actually with the sun-induced chlorophyll fluorescence and can be used for further monitoring purposes such as plant status and photosynthetic efficiency (Meroni et al., 2009; Yang et al., 2015).

4.3.2.3 AISA crown level - reflectances

In contrast to the very high-resolution field spectroradiometer measurements, the images have a coarser spectral sampling interval of 4.3-4.7 nm (EAGLE) and 6.2-6.3 nm (HAWK). The at-sensor

reflectance is displayed in Figure 4.10. Mean NIR values range about 0.3-0.4, are on average between both leaf- and crown level ASD sets. Especially the response pattern of ash differs from the other species and is much higher in NIR. One striking circumstance is that due to the pre-processing and interpolation procedures the two main water absorption bands, which usually cause noise, are not anymore present in the data. Furthermore, the small absorption features in the NIR plateau at about 995 and 1175 nm are more distinct than at the two other examined data sets gathered with the field spectroradiometer. The deviations from beech are mainly positive for most of the species. Only oak and ash show in SWIR1 and SWIR2 lower values than beech, which is similar to the ASD crown data.

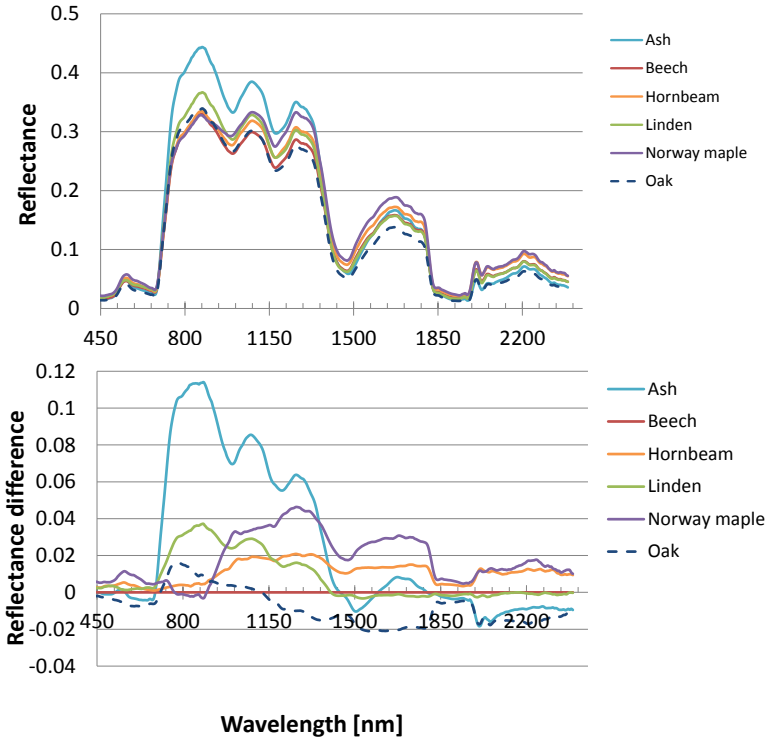

Figure 4.10: Mean crown reflectances (top) for the sampled trees as derived from AISA EAGLE and HAWK and corresponding differences from beech as reference (bottom).

4.3.2.4 AISA crown level - spectral derivatives

The extracted pixel values of the imagery can be handled for the derivative analysis just like the field spectroradiometer data. The typical pattern of DV_1 is also recognizable here. However, the red edge region shows a weak double peak and the maximum is less clear to define. Moreover, the curves of DV_2 pass consequently through zero at nearly the same position at about 709 nm (Figure 4.11).

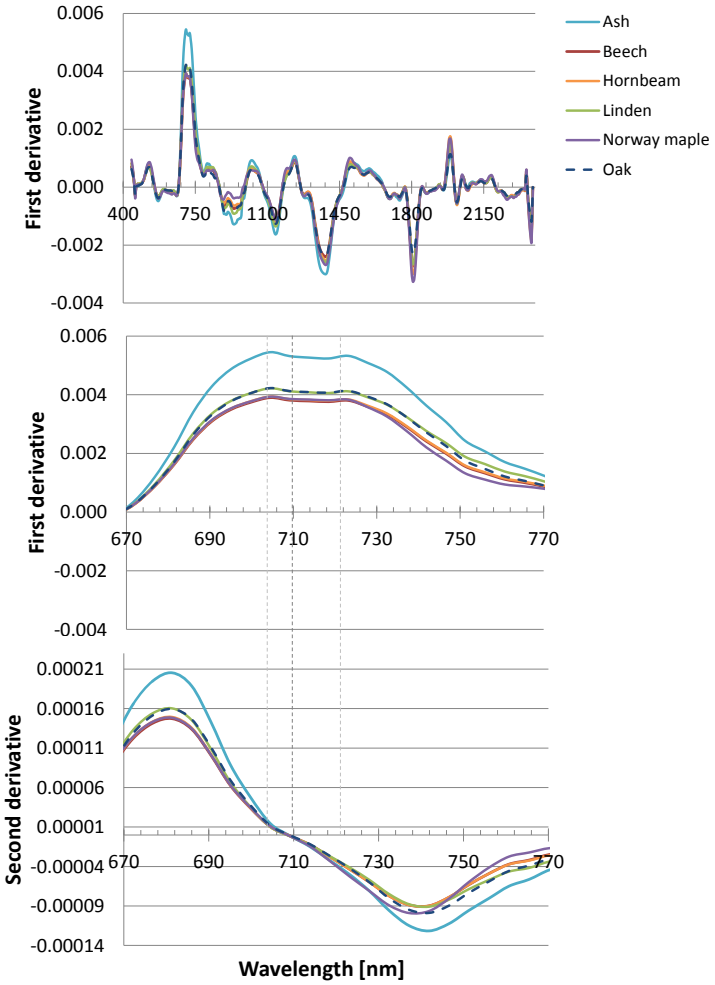

Figure 4.11: First derivatives of AISA EAGLE/HAWK spectra and their course between 670 and 770 nm at the red edge region. Bottom: Corresponding second derivative.

4.3.3 Level comparison - reflectance

The direct comparison per individual tree of in-situ and remote sensing data as sampled on 24.07.2012 reveals the differences for the levels of measurement. Leaf data has highest reflectances, ASD crown data the lowest. Apart from that, there is almost no clear pattern or grouping apparent in the species reflectances on varying levels. However, oak reflectances are the lowest nearly in every wavelength. Whereas beech, linden and hornbeam belong to the species with highest values (Figure 4.12).

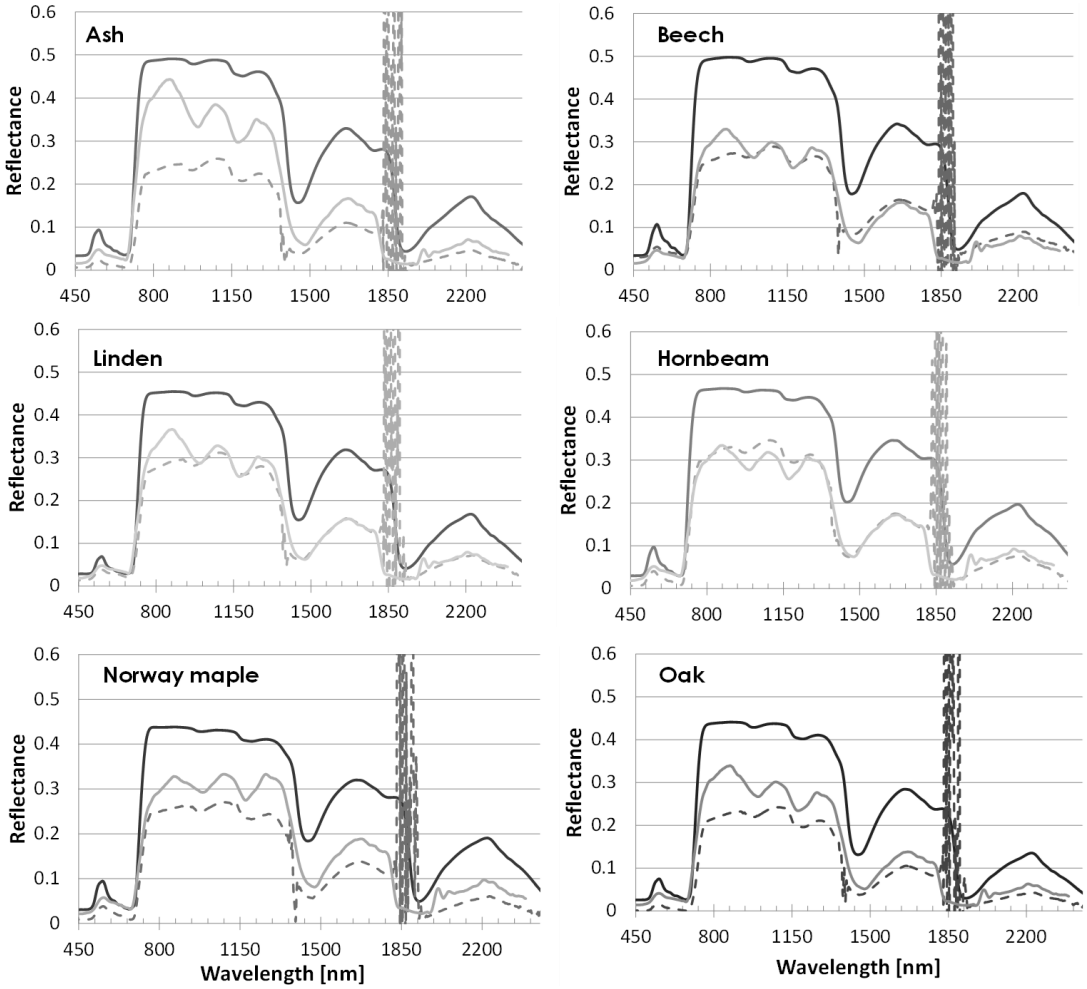

Figure 4.12: Mean reflectances for sampled species on three levels: (i) ASD leaf (darker solid line), (ii) ASD crown (dashed line) and (iii) AISA crown (light solid line). Date of measurement: 24.07.2012

By opposing the data from different scales for each species, the correlations become better observable. While the relationship between ASD-crown and AISA-crown data seems to be linear, it is different between ASD-leaf and AISA-crown data (Figure 4.13). Hence, a simple linear model could be applied to the in-situ crown data in order to approximately describe the AISA pixel values. For modelling of leaf reflectance, as the dependent variable, from the AISA data, the logarithmic approach is chosen. However, since an automatic fit did not lead to satisfying results, the model parameters a and b are forced to the final values afterwards (Table 4.3) by visual interpretation of the modelled curves. The coefficients of determinations (R^2) are ranging about 0.8-0.97. Figure 4.14 presents the resulting synthetic reflectance curves on the examples of ash and hornbeam. Bigger deviations are apparent especially in the near infrared and in the water absorption bands. The latter are somewhat negligible for remote sensing sensors and exist only because of preprocessing and interpolation. However, the modelled curves are seemingly a fair approximation.

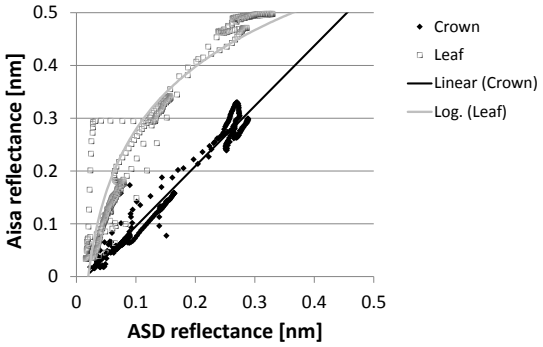

Figure 4.13: Relationships between AISA EAGLE/HAWK crown and in-situ ASD reflectances on crown and leaf level over all wavelengths using the example of beech.

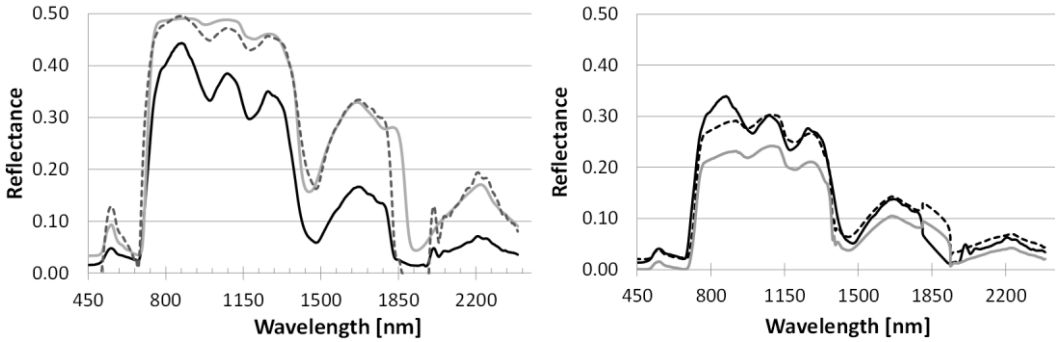

Figure 4.14: Left: Ash reflectances as derived of crowns from AISA EAGLE/HAWK (dark solid line) and leaves by ASD (brighter solid line) in comparison to modelled leaf reflectances (dashed line). Right: Oak crown reflectances from AISA (dark solid line), ASD crown (brighter solid line) and modelled AISA (dashed line).

Table 4.3: Model parameters of each species for transforming crown (ASD) to crown (AISA) and from crown (AISA) to leaf (ASD).

	ASD-crown -> AISA $y = a * x + b$			**AISA -> ASD-leaf** $y = a * ln(x) + b$		
Species	***a***	***b***	**RMSE**	***a***	***b***	**RMSE**
Ash	1.50	0.005	0.028	0.165	0.63	0.056
Beech	1.10	0.015	0.018	0.174	0.65	0.062
Hornbeam	0.90	0.020	0.014	0.185	0.66	0.059
Linden	1.00	0.008	0.023	0.179	0.64	0.062
Norway maple	1.15	0.020	0.016	0.171	0.60	0.054
Oak	1.17	0.020	0.020	0.155	0.59	0.055

4.3.4 Level comparison - vegetation indices and red edge position

The vegetation indices obtained for the three levels reveal several issues (Figure 4.15). All NDVI range between 0.71 and 0.95, and differences between the levels are considerable. However, leaf data and remote sensing values show values that are more similar. This holds especially for beech and oak. The in-situ crown NDVI data shows a bit different pattern. Most of the PRI values are

negative between -0.11 and 0.03. By contrast, here are both crown data sets more similar. Except for beech, the ranking of PRI is more pronounced than for NDVI: first ASD leaves, followed by ASD crowns and AISA crowns. Narrowband vegetation indices CRI1 and ARI2 usually tend to have rather similar pattern. However, we can see that on crown level, there are some serious deviations depending on the scale. Nevertheless, the general trend is similar for each level. The in-situ crown data differ strongly and show furthermore extremely high values for both indices – inexplicably and primarily for the oak data. Overall, indices calculated on leaf level are most stable and show least variation between species. The red edge inflection points were obtained separately using spectral derivatives and the Red Edge Position Index (REPI). Here, the first presented in-situ leaf and crown level also contain values from two growing seasons for comparison with an averaged and more stable data set. We can see for the leaves a clearer trend in the REP over the species with Ash and Linden having the highest REP, Beech, Sycamore maple and Hornbeam the least. Similarly, this is apparent in the field crown data (Figure 4.16).

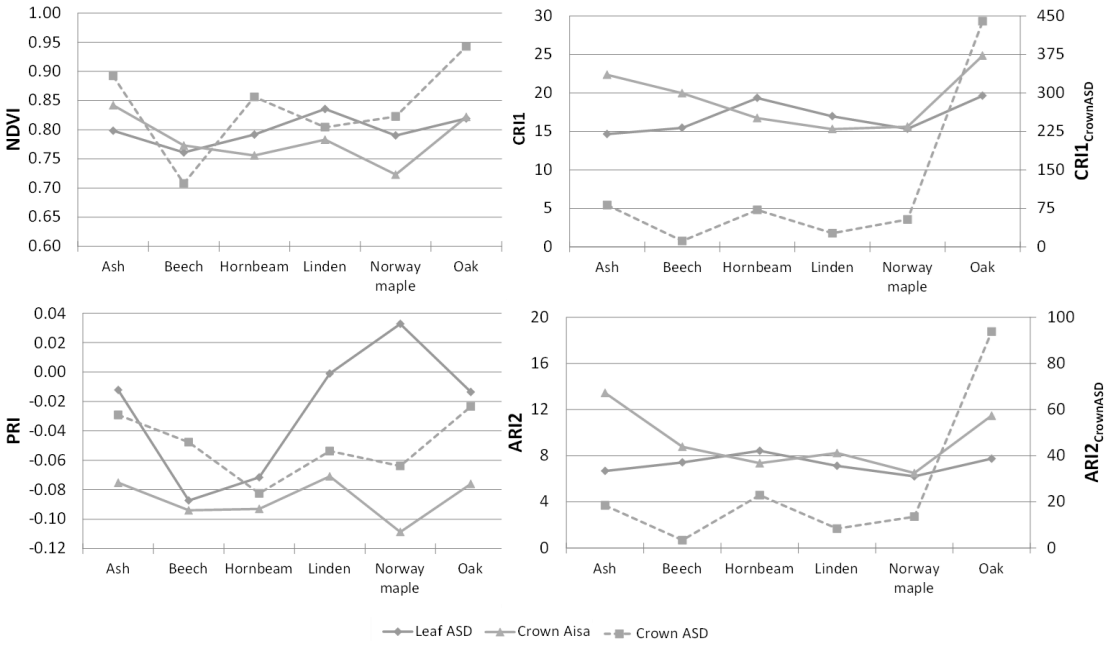

Figure 4.15: Mean NDVI and PRI values for the different tree species at different scales and sensors. Only data from 24.07.2012 are considered. CRI1 at ASD crown level deviates and is scaled separately.

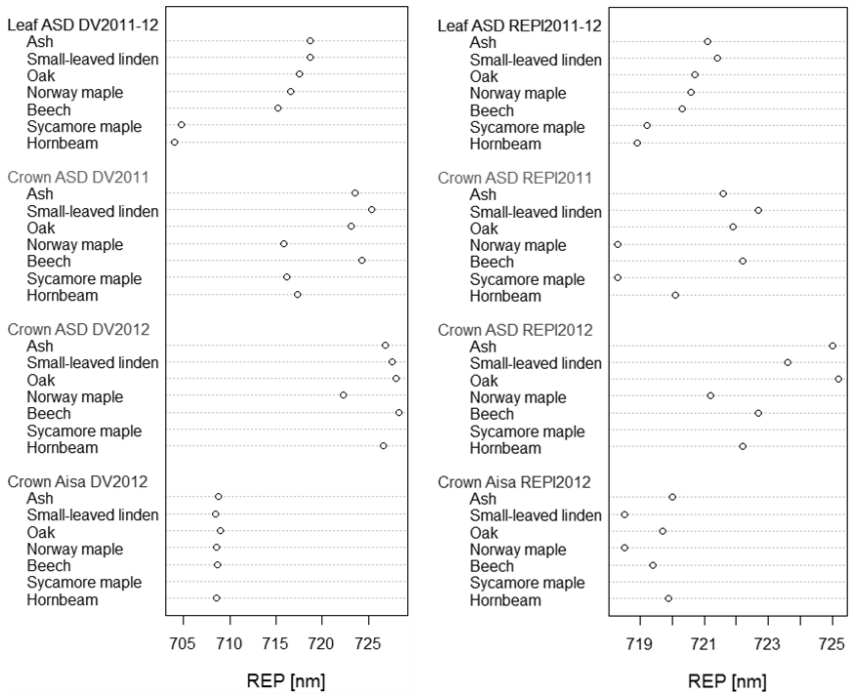

Figure 4.16: Graphical comparison of the red edge inflection points from 2011-2012 data at different levels. Left column: REP from derivatives, right column: REP from REPI. Notice the different scales.

There are clear variations in the collected data, and discrepancies between the REPs derived by the different methods are obvious even within one species. REP from second order derivatives (REP_{DV}) show a far higher variation than the index-based (REP_{REPI}) (Figure 4.17). The latter stays on relative constant level of about 720-725 nm, whereas REP_{DV} values go down to 705 nm. In any case, the REPs from AISA imagery have the nethermost values on average. The overall trend over all measurements indicates a certain ranking in REP: ash, linden and oak have higher REP than beech, followed by hornbeam and Norway maple. A similar pattern in the REP is recognizable plotting the data over all species (Figure 4.18).

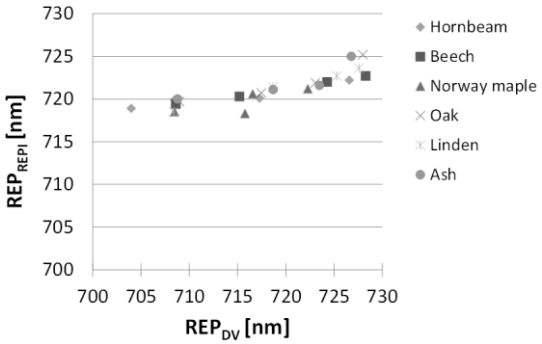

Figure 4.17: Pairwise comparison of red edge positions (REP) for the sampled trees at the three scales in-situ leaf, in-situ crown and remotely sensed crown as derived by red edge position index (REPI) and spectral derivative (DV).

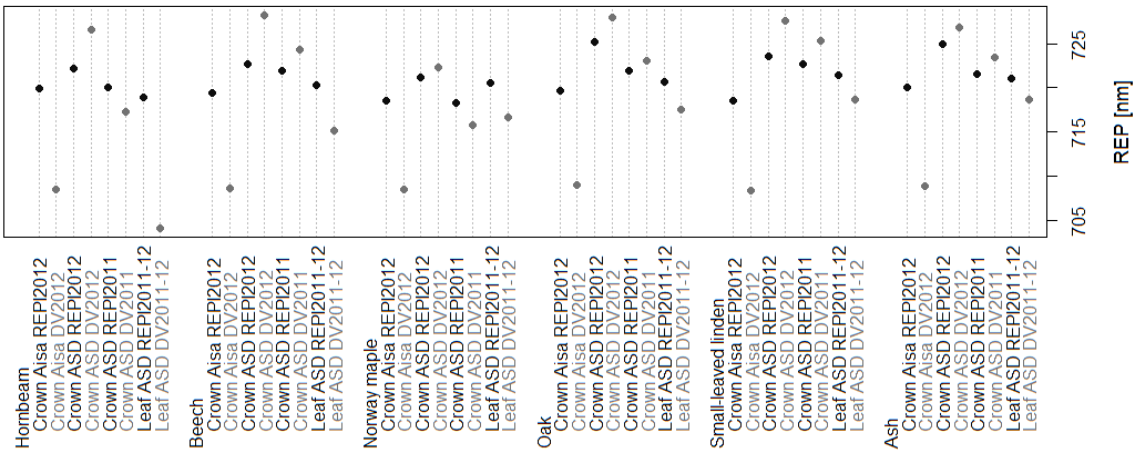

Figure 4.18: Graphical comparison of the red edge inflection points from 2011-2012 data at different levels for each species, without Sycamore maple.

Considering only the day when the data was gathered simultaneously, the values are slightly different compared to the full data set from two growing seasons. Again, on crown level the REP from AISA images are lower than the in-situ ones from the ASD device. However, in contrast to the other scales the remote sensing-based REP are similar and range around 709 nm, so that they are actually the same for all species. The leaf level derivatives yield the lowest values for Norway maple, Hornbeam and Beech (Figure 4.19). The red edge positions derived from in-situ leaf level data and from imagery are generally more similar to each other than the one from in-situ crown reflectances. On the other hand, both crown REP_{DV} and REP_{REPI} from ASD measurements are more consistent in terms of values and show the smallest differences (Figure 4.20).

The scale-dependency is also apparent when checking the relationship between red edge position values and vegetation indices. Obtained R^2 values (Leaf/AISA image) would range for NDVI~REP_{REPI} at about 0.87/0.43 and about 0.18/0.76 for PRI~REP_{REPI}, respectively. By contrast, the correlations are much less or even not apparent at all when using the derivative approach: 0.01/0.55 (NDVI~REP_{DV}) and 0.41/0.14 (PRI~REP_{DV}). However, as these are gained only from six species mean values, those relations cannot be seen as ultimate but rather show the unsteady behavior and a potential ambivalence in the interpretation of results.

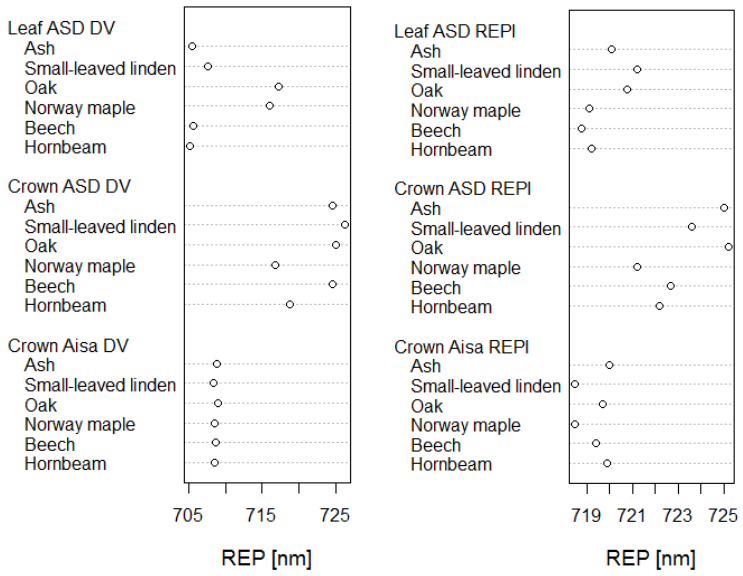

Figure 4.19: Red edge positions (REP) for the sampled tree species as derived from simultaneous measurements by second order spectral derivatives (DV, left) and by red edge position index (REPI, right).

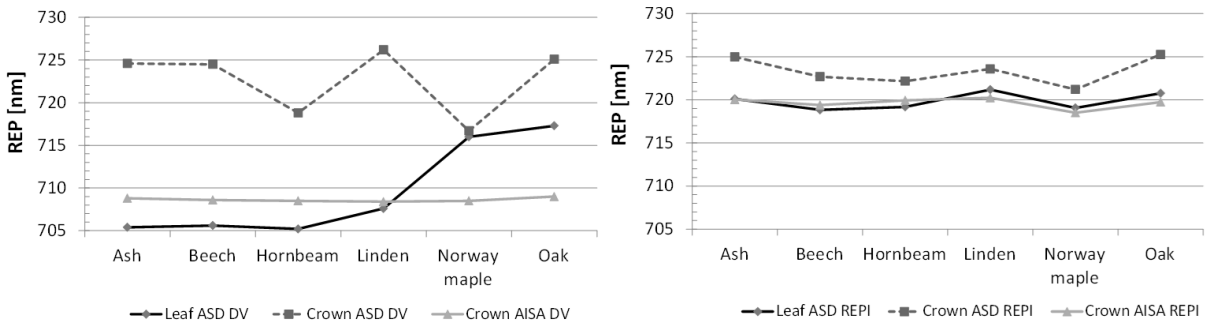

Figure 4.20: Red edge positions (REP) for the sampled tree species as derived from simultaneous measurements by second-order spectral derivatives (DV, left) and by the red edge position index (REPI, right).

4.4 DISCUSSION

In this study, the considered leaf level data was all sampled on the day of the flight over, which yields to an extraordinary and unique data set. The scale-dependency of tree reflectances from single leaves to crowns could be successfully demonstrated for the spatial, temporal and spectral resolution. It could be observed that reflectance measurements of vegetation is a rather dynamic and inconstant business. Inner and outer conditions influence the spectral appearance of tree leaves and crowns. These variations can be immediate responses or the result of a longer treatment. In this study, there were considerable differences in crown reflectances of the two considered years. The data from 2011 show much larger values than the 2012 data. This can have several reasons such as different weather conditions during the growing season or a higher leaf water content causing higher reflection in NIR and SWIR. Another factor might be the used field

spectroradiometers and their calibration. Here, small operational mistakes and carelessness can lead to false results. The same holds for the processing of the data. The final explanation for the discrepancy remains open.

Obtained reflectances of leaves and crowns show common range and shape of green vegetation. Here, leaves reflect more in NIR and SWIR than crowns or crown parts, respectively. This was also found in some investigations (Cho et al., 2008b) and is in contrast to other studies (Clark et al., 2005). Explanation can be in the stacking of leaves causing a higher reflectance in longer wavelengths of NIR and SWIR. However, stronger observed absorption features, which are mainly present in NIR of the remotely sensed data, are also reported by Clark et al. (2005) and support the correctness of this study. Additionally, the responses obtained on both leaf and crown level sometimes show in some spectral regions nearly identical values for different species.

Calculated narrowband vegetation indices CRI1 and ARI2 were most stable on leaf level. Variations on crown level are indicating an influence by canopy structure and background, respectively. The other levels showed more inconsistence variations. Another approach considered here is the calculation of first and second order derivatives for finding important bands and distinctive features like the red edge position. REPI as derived by the linear interpolation technique tends to have higher red edge position values than other methods (Dawson and Curran, 1998). This could partly be observed here as well. In theory, a higher REP is related to both a higher concentration of nitrogen (Cho and Skidmore, 2006) and a higher chlorophyll content (Le Maire et al., 2004). Incorporating modelled spectra, a jump of the REP could be observed by Le Maire et al., (2004) when chlorophyll content exceeds 45 $\mu g/cm^2$. Although the first derivatives did not show strong bimodal appearance at the red-edge region as found in other studies (Cho and Skidmore, 2006; Miller et al., 1991), the slight bimodal DV_1 found in this study are related to medium-high chlorophyll content. Assuming the information found in the literature, we could say that the sampled leaves of beech and hornbeam have a lower chlorophyll content than for instance oak and linden. While the data is relatively unambiguous for leaf level data, the interpretation of the near- and far-remote derivatives is somewhat more complex, especially for the data set of 2012. In-situ ASD crown data measurements as well as the AISA data tend to have a double peak, which are less distinct in the pixel spectra. Beech and hornbeam showed occasionally rather different traits. The presumed assumption of similar characteristics cannot hold finally. Moreover, there is almost no obvious trend regarding species and level of data acquisition, what makes it rather difficult to deduce clear statements. Moreover, there are differences in chlorophyll and carotenoid concentration or in leaf water contents over the time, due to the development during the growing season, which is also species-specific.

Differences in the REP obtained from derivatives are also depending on the grade of smoothing. The more neighboring values are included in the filter function the smoother gets the graph.

Generally, it should be noticed that each smoothing can even have a negative influence on the results (Vaiphasa, 2006), depending on the intentional task, when important features are polished away unseen. Here, a Savitzky-Golay filter was applied for each derivation smoothing the five previous and subsequent neighboring values. Smoothing is also part of the pre-processing of the remote sensing data. Additionally, it should be kept in mind that the airborne images were acquired from a height above ground of almost 2000 m. Even though the distance between sensor and surface is rather small, there is still an influence of the atmosphere comprehending absorption and scattering processes due to water vapor, molecules and particles. Hence, the pixel values are just the result of a long processing chain.

The definition of the correct REP is rather challenging (Baranoski and Rokne, 2005). Contrary to often stated that red edge parameters should be, at least, less sensitive to changes in canopy structure, leaf optical properties, background reflection, illumination angles and irradiance than VI (Curran et al., 1995; Ghiyamat and Shafri, 2010), it could be shown however that it depends highly on the data resolution as well as on the approach. The assignment of the red edge position by graphical interpretation of the second derivative should theoretically lead safely to the true REP. Moreover, we are assuming commonly that there is only one rather distinct REP per spectrum. In this study, the curves of DV_2 of the in-situ crown reflectances are intersecting the abscissa more than once in some cases (species). This finding is somewhat comparable to prior studies (Cho and Skidmore, 2006). On one hand, it supports the correctness of the measurements. On the other hand, it evinces the dilemma of a correct reading. For the AISA imagery, the utilization of the derivatives is not constructive in this case as the values are too similar.

A further issue is that maybe there are not the same conditions at the canopy walk as at other locations within the forest. Because the relative new construction, built in 2008-2009, may have still an impact on the soil density or water supply. However, since all trees undergo the same condition, we could neglect this issue. For modelling correct AISA and leaf data the information about the full width half mean (FWHM) of EAGLE and HAWK was not on hand for this study. Instead, the spectral sampling interval was used. Since in this case the correct spectral response function is not considered, the results might be affected by the resampled data. The sampling of tree leaves itself is always an awkward issue which is usually never really addressed in the literature. A standard protocol might help in documentation and further comparisons.

As already mentioned, stacking leaves for measurement can have a massive impact on the reflectance and hence on the resulting REP and calculated VI (Vogelmann et al., 1993). Sampled leaves show rather high reflectances in NIR and SWIR especially after stacking like in year 2011. Since crowns and canopies also consist of multiple tissue layers, one might expect similar behavior on that scale. However, this study demonstrates that this assumption is too simple and does not hold. Canopies cannot just be seen as stacked leaves. There is multiple scattering within the rather

rough surface of a forest canopy. Moreover, it consists of gaps and shaded parts, bark and epiphytes, twigs and branches. Another driver is surely the background like other trees, shrubs, grass or bare ground. Depending on the site, the understory can influence the spectral behavior even of upper tree parts (Eriksson et al., 2006; Ollinger, 2011). That means also consequently that for upscaling towards coarser resolutions of remote sensing sensors is quite complex, and, there is no general scaling approach being the best (Wu and Li, 2009). Even on a single leaf, there are areas of different reflection performance such as leaf veins or spots of varying pigmentation. Hence, what we obtain is always a compounded signal of a more or less heterogeneous surface.

4.5 CONCLUSIONS AND OUTLOOK

Conducted measurements and derived results are highly dependent on the level of acquisition. The link between leaf level data and canopies and hence to forests and landscapes is a crucial point for understanding of photosynthetic efficiency and productivity (Gamon, 2015). Specific vegetation indices such as the PRI can help to clarify those relationships between spectral appearance and carbon fluxes (Garbulsky et al., 2011). Red edge position information can be used as an indicator for the chlorophyll content, which is essential for the photosynthesis. I compared the REP on different scales from leaves to crowns with different approaches using (i) spectral derivatives and (ii) calculating a red edge position index (REPI). It reveals that there are rather big deviations in the derived REP. The values differ with the two methods and with the level of acquisition. Interestingly, REPI values from leaves and from the images are more similar to each other than to the in-situ crown data. However, the presented relations between leaf and crown responses base on a rather rough and simple but promising approach that should be analyzed further. Specific models for different ranges of wavelengths might help to improve minimizing the deviations from model and target variable. Another possible approach would be to use radiative transfer models to obtain more controllable input and results (Gastellu-Etchegorry et al., 2004; Jacquemoud et al., 2009). The up- and downscaling of vegetation responses over a variety of levels incorporating field and remote sensing are important subjects and ongoing topics (Colombo et al., 2008; Lausch et al., 2013b; Schaepman et al., 2010). Spectral unmixing techniques (Keshava, 2003) could be incorporated for data with coarser spatial resolution. Observed differences in REP at different scales demonstrate to interpret results with care as they can imply erroneous deductions about chlorophyll content and productivity status. Upcoming research should include hyperspectral vegetation indices to examine the scaling effects also in relation to biophysiological traits. Another possible aspect would be considering the leaf water content and drought stress. Certainly, more research is needed on the REP and a possible incorporation to species discrimination (Ghiyamat and Shafri, 2010).

Looking at the field of imaging spectroscopy, we are facing challenges and opportunities in using data from different sensors with different spatial and spectral resolutions. On one side, there are hyperspectral airborne platforms like the used AISA system or the HyMap sensor (Schlerf et al., 2005) with variable GSD. On the other side, there are satellites such as Hyperion and upcoming EnMAP (Segl et al., 2015, 2012). New hyperspectral spaceborne sensors will surely be in the future focus to improve Earth observation and mapping. Further analysis steps are resampling to band characteristics of other imaging systems and the comparison of sensors. Since this study used rather high spatial resolution data, resampling using relative spectral response functions of sensors directly is only meaningful to other aerial sensors like multispectral frame cameras or to satellite sensors such as RapidEye, Worldview 2 and 3, Sentinel 2, SPOT or Quickbird (Forestier et al., 2013). For coping both the spatial and the spectral scale successfully, a simulation and evaluation framework is needed for modelling larger pixels like from Landsat 8 or Hyperion and EnMAP. However, the key for the future is the utilization of multiple sources of information and its adequate distribution, and hence we need intercomparable data with standardized pre-processing. For a better understanding of ecosystem functions, multi-scale research studies on forests are still needed and important for comparison, interpretation and drawing conclusions. For all this, not only spectrally but also spatially coordinated sensor products are required.

APPENDIX

Table 4.4: Mean red edge positions (REP) for the different tree species at different scales and sensors. DV=second derivative from 2011 and 2012, respectively and the corresponding Red edge position index (REPI) in brackets.

		REP [nm]			
		Leaf	**Crown**		
Species		**ASD $DV_{2011-12}$ ($REPI_{2011-12}$)**	**ASD DV_{2011} ($REPI_{2011}$)**	**ASD DV_{2012} ($REPI_{2012}$)**	**AISA DV_{2012} ($REPI_{2012}$)**
Hornbeam	*Carpinus betulus*	704.0 (718.9)	717.3 (720.1)	726.6 (722.2)	708.5 (719.9)
Sycamore maple	*Acer pseudoplatanus*	704.7 (719.2)	716.1 (718.3)	- (-)	- (-)
Beech	*Fagus sylvatica*	715.2 (720.3)	724.3 (722.0)	728.3 (722.7)	708.6 (719.4)
Norway maple	*Acer platanoides*	716.6 (720.6)	715.8 (718.3)	722.3 (721.2)	708.5 (718.5)
Oak	*Quercus spec.*	717.5 (720.7)	723.1 (721.9)	728.0 (725.2)	709.0 (719.7)
Small-leaved linden	*Tilia cordata*	718.7 (721.4)	725.3 (722.7)	727.6 (723.6)	708.4 (718.5)
Ash	*Fraxinus excelsior*	718.7 (721.1)	723.5 (721.6)	726.8 (725.0)	708.8 (720.0)

Table 4.5: Mean NDVI values for the different tree species at different scales and sensors. Only crown data from 2012 considered.

		NDVI		
Species		**Leaf ASD**	**Crown ASD**	**Crown AISA**
Hornbeam	*Carpinus betulus*	0.754	0.856	0.756
Sycamore maple	*Acer pseudoplatanus*	0.763	-	-
Beech	*Fagus sylvatica*	0.794	0.708	0.773
Norway maple	*Acer platanoides*	0.785	0.823	0.723
Oak	*Quercus spec.*	0.811	0.943	0.822
Small-leaved linden	*Tilia cordata*	0.822	0.804	0.783
Ash	*Fraxinus excelsior*	0.800	0.892	0.842

Table 4.6: Mean PRI values for the different tree species at different scales and sensors. Only crown data from 2012 considered.

		PRI		
Species		**Leaf ASD**	**Crown ASD**	**Crown AISA**
Hornbeam	*Carpinus betulus*	-0.0164	-0.1528	-0.0930
Sycamore maple	*Acer pseudoplatanus*	-0.0022	-	-
Beech	*Fagus sylvatica*	0.0019	-0.0633	-0.0940
Norway maple	*Acer platanoides*	0.0229	-0.1067	-0.1087
Oak	*Quercus spec.*	0.0198	-0.0481	-0.0760
Small-leaved linden	*Tilia cordata*	0.0188	-0.0929	-0.0709
Ash	*Fraxinus excelsior*	0.0107	-0.0485	-0.0752

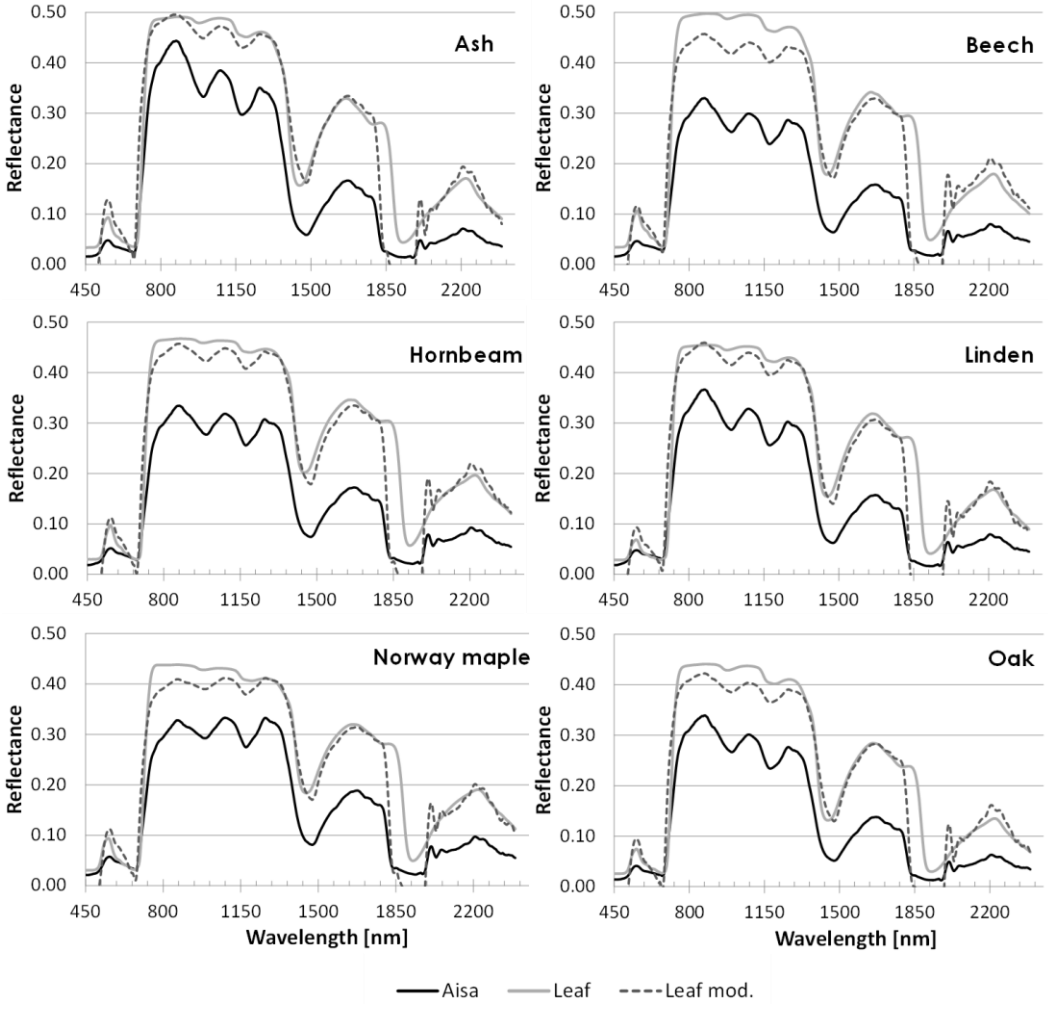

Figure 4.21: AISA EAGLE/HAWK crown reflectances and corresponding ASD measured and modelled leaf reflectances.

Chapter 5

Describing light interception in an old-growth forest

5 CHAPTER FIVE – CANOPY LIGHT INTERCEPTION IN AN OLD-GROWTH BROADLEAVED FOREST STAND

5.1 INTRODUCTION

The sun, billions of years old, is emitting its energy to us from a distance of more than 1.5×10^8 km. This "starlight" is essential for most of Earth's life. It is crucial for growth and vitality of higher plants and the main driver for the photosynthesis, that process, in which simply spoken water and carbon dioxide are converted to oxygen and sugar with the usage of solar energy. Depending on site and climate, the efficiency of this light use is linked to the gross primary production and finally the sequestration of biomass and hence carbon (Anderson et al., 2000; Keith et al., 2009; Luyssaert et al., 2008). Within this context the radiation utilization efficiency describes the assimilation of biomass in relation to total incoming radiation (Garbulsky et al., 2011). The quantification of sunlight going through tree crowns and the intercepted amount is an important issue. As light availability is relevant for many processes within the complex forest ecosystems, it is crucial to have knowledge about its distribution within forest stands. Moreover, since light regime within and below canopies as well as the optimal exploitation of sunlight play key roles in supporting or constraining species in the understory, the understanding of the processes is finally important for silviculture and forest management. Furthermore, within forest crowns the availability of light influences tree species competition, what in turn is influencing the light distribution. Besides the composition of plant species it is affecting also the behavior and abundancies of animals by variations in visibility and temperature (Endler, 1993; Lehnert et al., 2013).

As shown in chapter 3, the transmission through leaves depends on the species, health condition and season of the year. Hence, the light reaching the lower layers and its composition is affected by the entire crown including woody parts. The estimation of the proportion of ground area, which is covered by canopy, or more precisely by tree canopy, is a central part of national and international forest definitions (FAO, 2012; Gschwantner et al., 2009; Pulla et al., 2013). Within this context of acquisition readers are often confronted with the terms canopy density, canopy closure, canopy cover, crown cover and crown closure. According to the definitions of IPCC (Intergovernmental Panel on Climate Change) and FAO (Food and Agriculture Organization of the United Nations) *canopy cover* and *crown cover* are the same as *crown closure* (FAO, 2012; IPCC, 2003). Now and then there are still misunderstanding and confusion about the terminology which need to be standardized (Gonsamo et al., 2013; Korhonen et al., 2006). However, the concept of canopy cover and canopy closure (Figure 5.1) has already been carried out in several studies (Jennings et al., 1999; Korhonen et al., 2006; Paletto and Tosi, 2009; Rautiainen et al., 2005), and some compared methods and devices (Jonckheere et al., 2004; Thimonier et al., 2010).

Figure 5.1: The concepts of canopy closure (left) incorporating viewing angles and canopy cover (right) following Jennings et al. (1999) and Korhonen et al. (2006).

Many terrestrial methods of measuring the porousness of forest canopies have been developed and proposed using different devices such as hemispherical densiometer, vertical densitometer, cajanus tube or photography (Goodenough and Goodenough, 2012; Korhonen et al., 2006; Marchi and Paletto, 2010; Paletto and Tosi, 2009; Rautiainen et al., 2005). Especially hemispherical photos have been widely used for the description of canopy structure and light regime as well as for the estimation of the leaf area index (LAI) (Beckschäfer et al., 2014; Hale and Edwards, 2002; Russell et al., 1989; Wagner, 1998; Wang et al., 1992). A common way of analyzing photos is a binarization in order to group the pixels into plant and non-plant, which is actually the sky background (Rich, 1990). One major drawback in applying photographically derived parameters is the neglecting of occlusion of branches and overlapping leaves within the tree canopy strata and hence the occurrence of clumping effects. That often leads to underestimated values compared to the real leaf area derived from destructive methods (Fassnacht et al., 1994; Van Gardingen et al., 1999; Walter et al., 2003). That is one reason why the geometry of viewing angle and rays are taken into account to reduce these effects (Walter et al., 2003). Nevertheless, the results are often not sufficiently explainable (Gonsamo and Pellikka, 2009) and the direct link to real leaf area is not guaranteed. Hence, only gap fraction or openness of binarized photographs can be considered as the most traceable metric we can simply derive. Similar to photographs, devices often used in studies as reference such as the LI-COR LAI-2000 (Gong et al., 2003; Gower and Normann, 1991; Morisette et al., 2006) are assuming foliage as black and usually do not consider light transmitted through leaves.

Certainly, there are several research studies about light transmission through canopies (Black et al., 1991; Canham et al., 1993; Endler, 1993; Hardy et al., 2004; Jordan, 1969). But as commonly only green leaves are capable of making photosynthesis a more detailed exploration should be done. Moreover, an explicit spectral information about the transmitted or absorbed light has only been barely considered (Huang et al., 2007). Further example studies were conducted in conifer stands (Wang et al., 2003) or in tropical forests (De Castro, 2000). Hence, analyses for old-growth temperate forest stands are still lacking.

The processes behind incoming sunlight that is transmitted through foliage and canopy and scattered within the tree crowns are quite complex and follow the principle of energy conversation. As light absorption is highly related to plant state and productivity, the quantification of the intercepted incoming sunlight is a vital issue. Again, the determination of absorption by green vegetation gives information about the plant's status and condition (Gobron et al., 2006). In that context the fraction of absorbed photosynthetically active radiation (fAPAR, fPAR) within the spectral range of 400-700 nm is labeled as an essential climate variable (Gobron and Verstraete, 2009b), which is linked to chlorophyll content (Gitelson et al., 2003) and the assimilation of CO_2 (Sellers et al., 1992). However, there is still some confusion and disagreement about the estimation of fAPAR (Gobron and Verstraete, 2009b), what might be also concerned with the rather complicated estimation of the absorbed PAR. If a forest canopy is dense and has green leaves, APAR can be approximated by the IPAR. That is the amount of PAR intercepted by all parts of the vegetation, not only by leaves, which reflect less PAR when healthy and green (Daughtry and Ranson, 1986; Eklundh et al., 2011; Serrano et al., 2000).

Besides in-situ ground-based measurements, the derivation of closure and cover estimations can also be achieved by using remotely sensed data as an auxiliary tool for regionalization and mapping larger areas (Pu and Gong, 2004). Operational fAPAR products might be derived on a rather coarse scale by satellites like MERIS (Medium Resolution Imaging Spectrometer), MODIS (Moderate Resolution Imaging Spectroradiometer) and MISR (Multi-angle Imaging Spectroradiometer) (D'Odorico et al., 2014; Gobron and Verstraete, 2009b; Pinty et al., 2011a). The utilization of hyperspectral sensors having numerous bands to measure the reflected radiation by remote sensing and below the canopy to estimate the amount of intercepted light is a suitable approach. This can be fostered by incorporating broad- and narrowband vegetation indices (VI) to highlight specific features (Huete et al., 1997; Jackson and Huete, 1991; Schlerf et al., 2005). Especially in hyperspectral remote sensing the number of possible VI incorporating band ratios, normalized differences or other equations using any channel combination is enormous (Agapiou et al., 2012; Bannari et al., 1995; Prospere et al., 2014). Several vegetation indices showed already their capability for remote estimations such as of LAI and chlorophyll content (Brantley et al., 2011; Gitelson et al., 2003). Here, besides others, the photochemical reflectance index (PRI) is in the main focus (Garbulsky et al., 2011; Wu et al., 2015). PRI is found to be sensitive to leaf area index (Barton and North, 2001) and seems to have an inverse relation with light use efficiency (LUE) (Peñuelas et al., 2013; Soudani et al., 2014). However, literature reveals also that there are still ambiguities and uncertainties about this relationship and the role of canopy structure (Garbulsky et al., 2011; Wu et al., 2015).

This study takes up the needs and findings of prior studies and tries additionally to address canopy light absorption using common but also newest sensors in a rather simple manner. The study is

conducted in a mature deciduous forest stand which is part of global carbon flux research networks. In order to encompass the view from above, high-resolution hyperspectral remote sensing data is used. Moreover, a unique set of ground radiation measurements and simultaneous remote sensing imagery acquisition are the basis this work. Below-canopy spectral irradiances shall give precise insights on transmitted light composition. One objective is the derivation of local light extinction coefficients for the old-growth broadleaved stand, which describe the transmission/absorption rate of the radiation through the canopy. Another question to be answered is which parts of the electromagnetic spectrum are most affected by the attenuation and what are the possible consequences. The data set is completed by digital cover photography (DCP) and digital hemispherical photography (DHP) in order to address canopy structure and porousness. Therefor a device is introduced which is combining two cameras incorporating visible and near infrared light. On the remote sensing side, besides several commonly used vegetation indices, here the focus is on the PRI. It shall be examined if the remotely sensed PRI can be used for establishing estimations of within-canopy light interceptions. By using rather simple methods this research case study compares different approaches, which describe canopy structure and light interception. It shall furthermore contribute to a better understanding of the behavior of the involved processes.

5.2 MATERIALS AND METHODS

5.2.1 Study site

The study area is located at N51.08° E10.45° and an elevation of about 440 m a.s.l. in the Hainich, a beech (*Fagus sylvatica)* dominated primeval forest. The site belongs to the FLUXNET network (Ershadi et al., 2014), is a CarboEurope verification site (Mund et al., 2010) and since 2011 part of a UNESCO World Heritage site (UNESCO, 2014). Tree age can reach 250 years. The old-growth stand is unmanaged since over 60 years (Knohl et al., 2003). For the area a maximum leaf area index of about 5.0-5.5 is reported (Anthoni et al., 2004; Knohl et al., 2003; Kutsch et al., 2008; Pinty et al., 2011b).

Surrounding a climate tower a squared core area of 150x150 m (2.25 ha) was established and additionally split into 25 plots for spatially more comprehensive analysis, consecutively named core plots. Each plot has a size of 30x30 m, which corresponds to the pixel size of Landsat and Hyperion satellites as well as to the upcoming EnMAP sensor. On the core area 416 trees having a diameter at breast height (dbh) measured at 1.30 m of minimum 15 cm were recorded noting position, diameter, species and some heights (Figure 5.2). Positions are subsequently confirmed with a canopy height model derived from airborne laser scanner. See chapter 3 for a detailed description about the tree survey methods and the study site. Highest individuals are ash trees

(*Fraxinus excelsior*) representing the second most frequent species. Further present species are Sycamore maple (*Acer pseudoplatanus*), Hornbeam (*Carpinus betulus*), Norway maple (*Acer platanoides*), Oak (*Quercus petraea*) and Wych elm (*Ulmus glabra*).

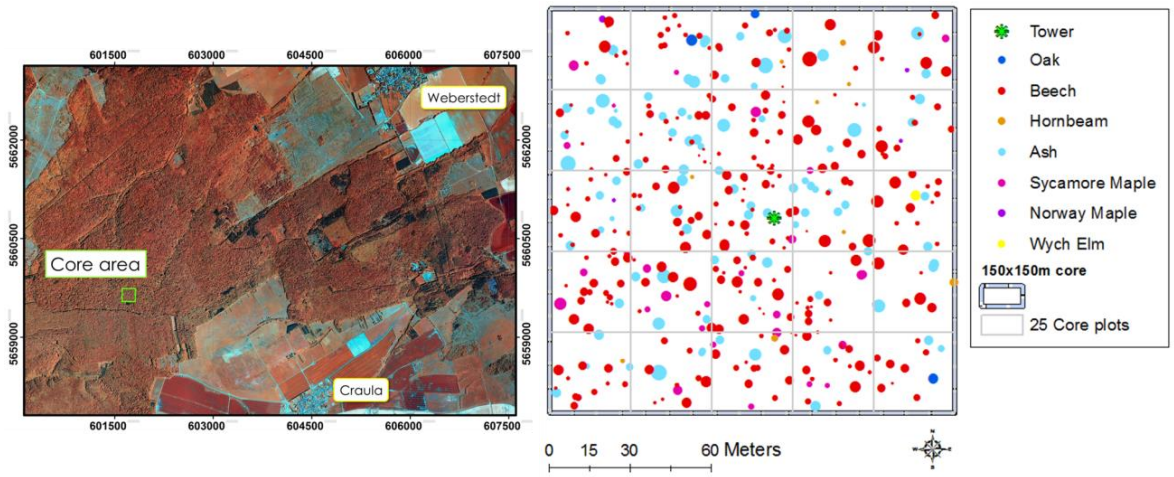

Figure 5.2: Left: Location of the core area; aerial false color photograph, composite: NIR-G-B. Right: Recorded trees within the core area. Point size is relative to the diameter at breast height

Table 5.1: Core area characteristics (tree dbh ≥ 15 cm).

Species	Percentage of total stems	Mean dbh [cm]	Mean height [m]
Beech (*Fagus sylvatica*)	66.3	41.7	28.1
Ash (*Fraxinus excelsior*)	22.6	62.8	33.7
Sycamore maple (*Acer pseudoplatanus*)	7.0	59.3	28.4
Hornbeam (*Carpinus betulus*)	2.2	33.5	24.1
Norway maple(*Acer platanoides*)	1.0	32.4	22.2
Oak (*Quercus petraea*)	0.7	64.1	30.2
Wych elm (*Ulmus glabra*)	0.2	62.8	30.4

5.2.2 General study setup

For the detection of reflected radiation of the forest canopy remotely sensed hyperspectral data is used. The incident above and below canopy radiation within the forest stand were measured using a high resolution field spectroradiometer. This spectral global irradiance is depending on wavelength, stand density, canopy gap distribution and species composition. Besides that also different digital crown photographs were conducted for detailed intercomparison purposes. The following figures show the general scheme and setup (Figure 5.4, Figure 5.4). Finally, acquired point data can be interpolated.

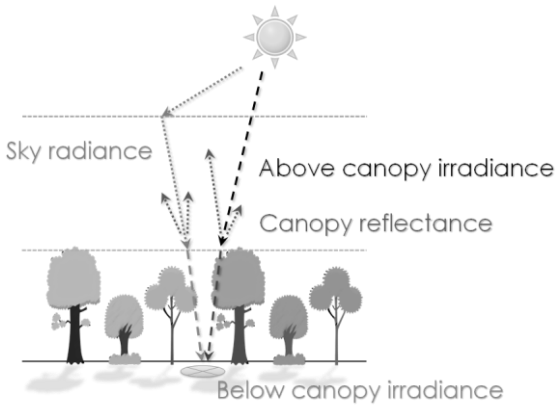

Figure 5.3: Simplified scheme of radiation measurements.

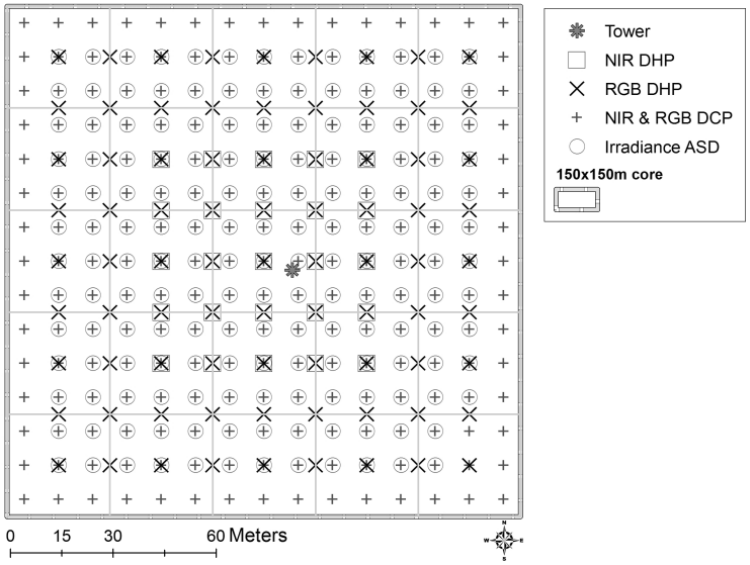

Figure 5.4: Core area and spatial arrangement of measuring positions.

5.2.3 Remotely sensed data

The remote sensing imagery used in this study was acquired on 24.07.2012 by the AISA cameras EAGLE and HAWK (SPECTRAL IMAGING LTD.). These hyperspectral sensors are sensitive for a spectrum of 400-2500 nm. Pixel size is 2 m corresponding to the flight height above ground. Acquisition and preprocessing was performed by the Department of Computational Landscape Ecology of the Helmholtz Centre for Environmental Research UFZ Leipzig. The delivered product was finally georeferenced using additional data like aerial imagery and basemap images in ArcMap (ArcGIS Desktop 10, ESRI). Besides the direct utilization of reflectance values broad- and narrow-band vegetation indices can be calculated. In this study the following vegetation indices are analyzed as they are calculated in the software ENVI (v. 4.8, ITT VIS) (Table 5.2). They represent the most important aspects and they have been used in several studies (Clark and Roberts, 2012; Gitelson et al., 2002).

Table 5.2: Vegetation indices used in this study and the according formulas. ρ is the reflectance at specific wavelengths.

Objective	Index	Formula	Reference
Greenness	Normalized Difference Vegetation Index	$\mathrm{NDVI} = \frac{\rho_{\mathrm{NIR}} - \rho_{\mathrm{RED}}}{\rho_{\mathrm{NIR}} + \rho_{\mathrm{RED}}}$	(Rouse et al., 1974)
	Simple Ratio	$\mathrm{SR} = \frac{\rho_{\mathrm{NIR}}}{\rho_{\mathrm{RED}}}$	(Tucker, 1979)
Leaf pigments	Carotenoid Reflectance Index 1	$\mathrm{CRI1} = \frac{1}{\rho_{510}} - \frac{1}{\rho_{550}}$	(Gitelson et al., 2002)
	Anthocyanin Reflectance Index 2	$\mathrm{ARI2} = \rho_{800} * \left(\frac{1}{\rho_{510}} - \frac{1}{\rho_{700}}\right)$	(Gitelson et al., 2001)
Carbon	Normalized Difference Lignin Index	$\mathrm{NDLI} = \frac{\log\left(\frac{1}{\rho_{1754}}\right) - \log\left(\frac{1}{\rho_{1680}}\right)}{\log\left(\frac{1}{\rho_{1754}}\right) + \log\left(\frac{1}{\rho_{1680}}\right)}$	(Fourty et al., 1996)
Light use efficiency	Red Green Ratio Index	$\mathrm{RGRI} = \frac{\rho_{\mathrm{RED}}}{\rho_{\mathrm{GREEN}}}$	(Gamon and Surfus, 1999)
	Structure Insensitive Pigment Index	$\mathrm{SIPI} = \frac{\rho_{800} - \rho_{445}}{\rho_{800} - \rho_{680}}$	(Peñuelas et al., 1995)
	Photochemical Reflectance Index	$\mathrm{PRI} = \frac{\rho_{531} - \rho_{570}}{\rho_{531} + \rho_{570}}$	(Gamon et al., 1992)

5.2.4 In-situ data

5.2.4.1 Photography

Digital cover photos were taken on the same 10 m wide grid as the irradiance measurements. This campaign was conducted begin of September 2012. During the acquisition all photos were shot around noon but avoiding direct sunlight. For normal RGB (VIS) photos a 6 megapixel NIKON D70 digital single-lens reflex (DSLR) camera, for the near infrared (NIR) an almost identical D70s was used. It is modified and is operating without an internal filter, so that the camera is sensitive for infrared light. Both cameras are equipped with a standard 17-35 mm 1:2.8-4 lens, a TAMRON SP AF Aspherical DI LD-IF objective. Since infrared light contains less energy the exposure time needed to be adjusted to 1/100 sec. and +5 steps, aperture was set to f/4.

For the DCP acquisition a custom-built device designed by the author combines one VIS and one NIR camera (Figure 5.5). It is using a dielectric cold mirror (EDMUNDOPTICS NT43-962) which is set to an incidence angle of 45° reflecting the visible light, but letting through near infrared. The average NIR transmission at 800-1200 nm is >85 %, average VIS reflection at 425-650 nm is >90 %. With the cameras aligned to each other this arrangement allows simultaneous photo shooting using a remote control. This copes moving of leaves and branches by wind and changes of the objects within the scene by shifting the tripod. Due to the settings of the construction and the dimensions of the cold mirror, the camera objectives have to set to high zoom. This leads to images that are covering a smaller area.

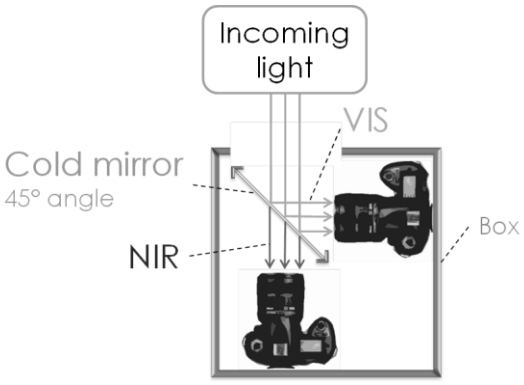

Figure 5.5: Schematic setting of the MultiCam D70 using two DSLR cameras, vertically arranged pointing towards sky.

Additionally, wide angle photographs were collected on a subset of plots using a simple WALIMEX fisheye converter lens shortening the focal length by factor of 0.25 and offering viewing angle of about 165° which is subsequently termed digital hemispherical photos (DHP). 81 hemispherical VIS (DHP_{VIS}) were recorded on a regular grid with a spacing of 15 m. Exposure time was set to 1/160 sec., aperture to f/8. In addition, a set of 25 hemispherical near infrared photos (DHP_{NIR}) were shot on the same grid around the center of the core area, mainly for test purposes. All images of this study were taken 1.3 m above ground on a tripod, leveled and aligned to magnetic north.

Table 5.3: Overview of the below-canopy measurements in this study. The ASD measurements contain a continuous spectrum of 400-2500 nm.

Method	Spectrum	Records
ASD Irradiance	VIS-SWIR2	167
DCP	VIS	225
	NIR	225
DHP	VIS	81
	NIR	25

While some authors suggest only to use the blue channel (Gonsamo and Pellikka, 2009; Pekin and Macfarlane, 2009; Zhang et al., 2005), here I followed Jonckheere et al., 2005, incorporating all three RGB bands. After visual inspection the photographs were analyzed using batch processing in the free software ImageJ (Rasband, 2014). This includes the conversion of the original photos to 8-bit greyscale images. For binarization the Intermodes algorithm (Prewitt and Mendelsohn, 1966) was applied for setting the threshold. Only for one photograph the produced binary image was deficient. The instead applied Huang algorithm (Huang and Wang, 1995) led to the subjectively best result in that case. Finally, for all image data sets describing parameters such as arithmetic mean, median and standard deviation of the relative gap proportions were calculated. This is the amount of sky pixels of an image in relation to non-sky pixels. Since gap fraction, or openness, is

related with the natural logarithm of the LAI, it is possible to derive an estimation of the leaf area index from hemispherical photography (Lang and Xiang, 1986; Leblanc et al., 2005).

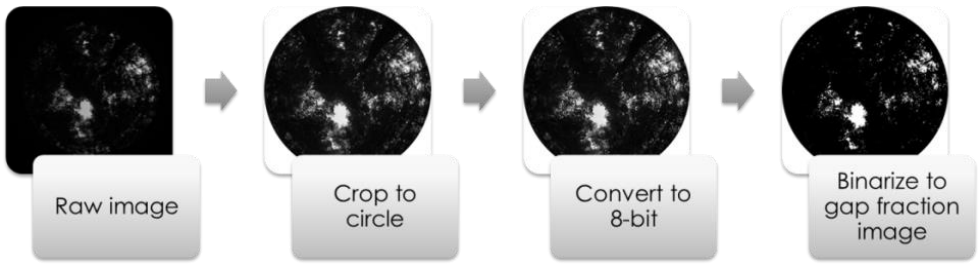

Figure 5.6: Workflow for the hemispherical photograph processing.

5.2.4.2 Spectral irradiance

What we commonly call sunlight is the visible part of the electromagnetic spectrum rayed by the sun. The maximum energy is in the visible range of the spectrum from 400 to 700 nm reaching the surface during noon when sun zenith is largest. Figure 5.7 illustrates the sun geometric angles during a summer day at the Hainich.

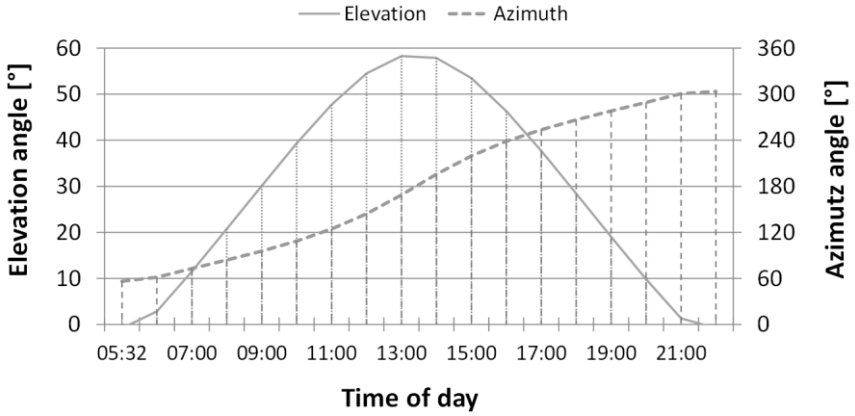

Figure 5.7: Sun azimuth and elevation angles during the day. Date: 24.07.2012, day light saving time, UTC+1h (derived from sunearthtools.com).

Irradiance E is defined as the incident radiant flux per area. It is often obtained as integrated over the PAR region of 400-700 nm. Here, the spectral irradiance is obtained for the full spectrum from blue to shortwave infrared. For the in situ measurements of incoming radiation an ASD FieldSpec3 HiRes field spectroradiometer (ANALYTICAL SPECTRAL DEVICES INC.) was used. The device has a spectral resolution of 350-2500 nm and a spectral sampling of 1.4-2 nm. By using internal interpolations, which produce bandwidths of 1 nm, it offers 2150 single channels. For measuring global spectral irradiance, a cosine receptor was attached on the fiber optics of the device (Figure 5.8). This diffuser allows the user recording the insolation or incident radiant flux, respectively, in units of watts per area and wavelength over the complete hemisphere.

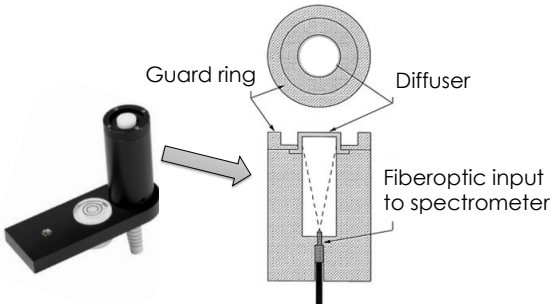

Figure 5.8: Remote cosine receptor (ASDI, 2012, modified).

In the core area the incoming light below the canopy was recorded on a 10 m grid (Figure 5.4). The survey was conducted on July 25th 2012, one day after the AISA EAGLE/HAWK fly-over. For sensor calibration the spectral irradiance measured outside the forest on a free area is assumed as above-canopy insolation and conducted just before and after the collection within the stand. Later analysis incorporates the average of the chronological different values. The spectroradiometer was calibrated using a white spectralon panel for ideal reflectance reference. This had been repeated on a nearby forest gap during the campaign whenever necessary. Each below-canopy measurement was done at 2 m height and aligned using a bubble level and consists of four single records leading to more than 660 entries. The derived curves are compared to references in the literature to check if the measured values of spectral irradiances are meaningful. It should be noticed that the following calculations only consider the spectral irradiance of the PAR region, here assumed as 400-700 nm. In order to get estimation about the intercepted light within the forest stand the ratio of below-canopy irradiance E to above-canopy irradiance E_o is calculated for every record:

$$E_r = \left(\frac{E}{E_o}\right) \quad \text{(Eq. 5.1)}$$

where the irradiance-ratio, here denoted as E_r, can actually be considered as the canopy transmission (Aubin et al., 2000). The fractional cover (fC) of the forest stand is comparable with the fraction of intercepted photosynthetically active radiation (fIPAR) and is calculated simply by (Eklundh et al., 2011; Propastin and Panferov, 2013):

$$fC = \left(\frac{E_o - E}{E_o}\right) = 1 - E_r \quad \text{(Eq. 5.2)}$$

The logarithm of the leaf area index is proportional to the logarithm of the transmission (Lang and Xiang, 1986). Hence, following the Beer-Lambert law it can be approximated by:

$$E_r = e^{-k*LAI} \quad \text{(Eq. 5.3)}$$

where k represents the extinction coefficient and LAI is the leaf area index (Daughtry and Ranson, 1986; Monsi and Saeki, 2005; Serrano and Peñuelas, 2005). The term $k * LAI$ is also named the bulk canopy optical thickness (Hardy et al., 2004). Equation 3 can furthermore be written as:

$$k = \frac{-ln(E_r)}{LAI} \quad \text{(Eq. 5.4)}$$

It should be noticed that in this study the LAI is rather associated to the plant area index (PAI) (Weiss et al., 2004) than to the projected leaf area only. The extinction coefficient k is reported for vegetation as 0.2-2.0, whereas it is ranging between 0.5 and 1 for broadleaved species (Bréda, 2003; Daughtry and Ranson, 1986; Monsi and Saeki, 2005). Although k is often set to about 0.5 (Richardson et al., 2009), this general assumption may not lead to appropriate results in some situations and needs to be adjusted for bigger trees and forest stands of different density and type (Hopkinson et al., 2013). Transmission is, similarly to reflection and absorption, depending on the spectral range, tree species and crown structure. Furthermore, sun and leaf-inclination angles are important factors for the probability that photons collide with crown parts (Bréda, 2003; Propastin and Panferov, 2013). Finally, transmission, and therefore the irradiance ratio, can be set equal to gap fraction (Martens et al., 1993). This implies that E_r and fC derived from ASD field measurements could subsequently be compared with the gap or cover fractions obtained from digital photography.

5.3 RESULTS

5.3.1 DCP

Figure 5.9 shows examples of the digital cover photographs taken at plot 16 by the RGB and NIR version of the camera. It is apparent that they differ regarding the details within the crown, but also in crown and background-sky. The NIR image is highlighting the contrast between woody parts and foliage, which is appearing by nature brighter. For direct comparison, the VIS photos have to be re-mirrored horizontally to get the real orientation

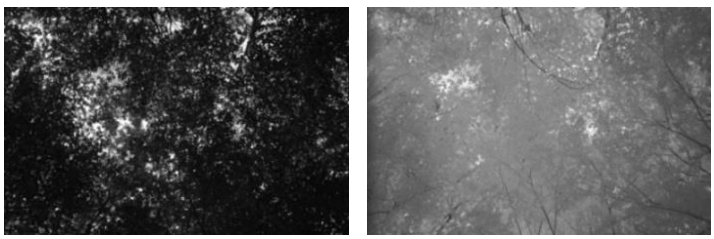

Figure 5.9: Examples of normal (left) and near infrared image (right) on DCP plot number 16.

When comparing the calculated gap fractions for dense plots both cameras lead to values in similar quantity. However, in regions of higher openness, say above 20 %, the RGB images tend to induce

lower values than the NIR photos (Figure 5.10). These remarkable differences can also be seen in the median values which are 6.2 % (VIS) and 3.1 % (NIR). For the NIR photos the standard deviation of 11.9 % is remarkably higher than the mean. Differences are clearly apparent in the distributions (Figure 5.11). However, the mean gap fractions, defined as proportion of sky in relation to the whole image, are quite similar with 7.50 % (VIS) and 7.66 % (NIR). Moreover, the averaged values for the 25 core plots yield to a Pearson correlation coefficient of about 0.85.

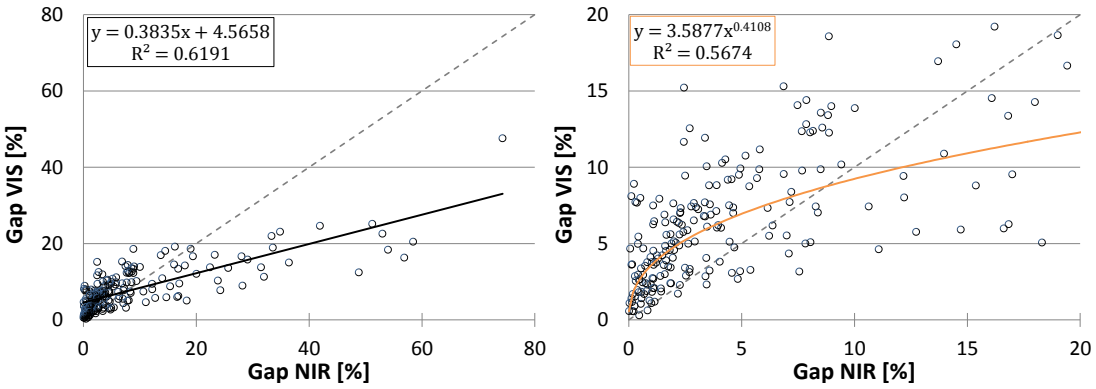

Figure 5.10: Scatterplots of crown openness derived from 225 normal (VIS) and near infrared (NIR) digital cover photographs. NIR DCP show higher values; for smaller gap proportions NIR is lower. Left: Black line is a linear regression. Right: Graph represents a potential trendline for values ≤ 20 %.

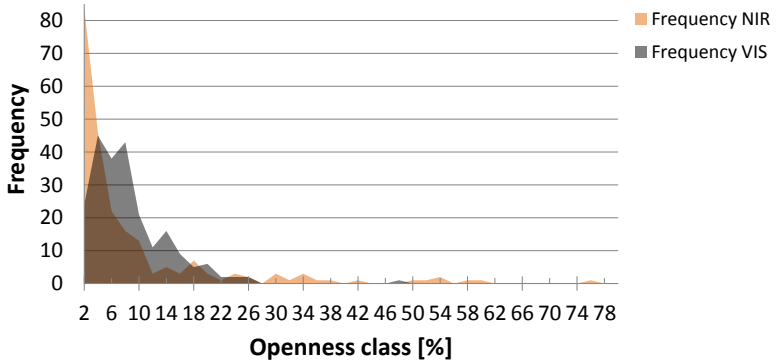

Figure 5.11: Histograms of the percentage openness derived from RGB (VIS) and near infrared (NIR) digital cover photos.

5.3.2 DHP

Figure 5.12 shows as an example the hemispherical digital photographs taken at plot 1 in normal RGB and NIR. On the upper right side the climate tower is apparent, which is almost not visible in the RGB photo. The contrast between wood and non-wooden tree parts is more pronounced in NIR.

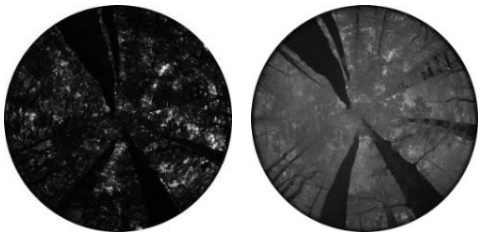

Figure 5.12: Examples of hemispherical normal (left) and near infrared image (right) on DHP plot 1 close to the tower, visible on the right side.

Overall, 81 VIS and 25 additional NIR photos could be recorded. The histograms reveal the differences in the data ranges of both methods (Figure 5.13). The VIS DHP show a much higher variation than the NIR DHP, which tend to lead to smaller openness. Table 5.4 lists the main describing statistical parameters for both data sets of the two methods DCP and DHP. Nonetheless, as the numbers of records differ considerably, conclusions might be limited from the frequency distributions (Figure 5.13). For direct comparison only the plots containing both methods are selectable. Here, no clear correlation is recognizable. When opposing DCP_{VIS} and DHP_{VIS} as averaged for each of the 25 core plots Pearson correlation coefficient r amounts only to about 0.13.

Table 5.4: Basic openness statistics of digital cover photographs (DCP) and digital hemispherical photographs (DHP) incorporating the two data sets of visible (VIS) and near infrared (NIR), values in percentage. The NIR DHP were recorded on smaller extent and cannot be compared directly.

Parameter [openness]	DCP		DHP	
	VIS	NIR	VIS	NIR
Mean	7.50	7.66	4.59	2.05
Median	6.23	3.08	4.06	1.61
Minimum	0.30	0.01	1.46	0.71
Maximum	47.59	74.29	10.73	6.15
Standard deviation	5.78	11.86	2.02	1.46

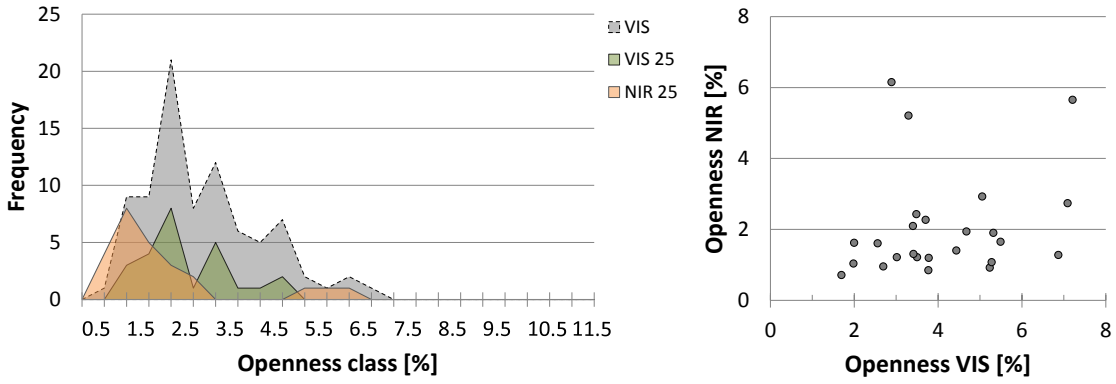

Figure 5.13: Left: Histograms of the 81 VIS and the 25 coincident VIS and NIR hemispherical photos. Right: Scatterplot of gap fractions derived from the coincident VIS and NIR DHP.

5.3.3 Ground irradiance and transmission

Hemispherical spectral irradiances are measured outside the forest stand referred as above-canopy. Below-canopy irradiance was recorded within the core area as described. In comparison to available data from literature, irradiances range in meaningful limits and show the typical pattern of incoming sun light on Earth's surface (Figure 5.14). Furthermore, it is obvious that absorption is wavelength-dependent. This stand for the radiation through the atmosphere as well as for the light transmitted through a forest canopy. Mean below-canopy irradiance extenuates heavily and reveals strong changes especially in PAR. Figure 5.14 depicts all spectral irradiances measured below the canopy during the campaign. In this dense forest stand the quantity of PAR light incidencing the forest floor is quite low. The irradiance ranges between 0.003 and 0.253 $W/m^2\,nm^{-1}$. The overall average is only about 0.018 $W/m^2\,nm^{-1}$. However, as mentioned, the amount of light reaching the lowest layer differs with the wavelength. Hence, we can split the measurements into four segments: (I) 400-700 nm, (II) 760-1100 nm, (III) 1150-1350 nm, (IV) 1500-1800 nm. Leaving out water bands and noisy regions the sections would correspond to VIS, NIR (2x) and SWIR1. SWIR2 must be disregarded due to low signal.

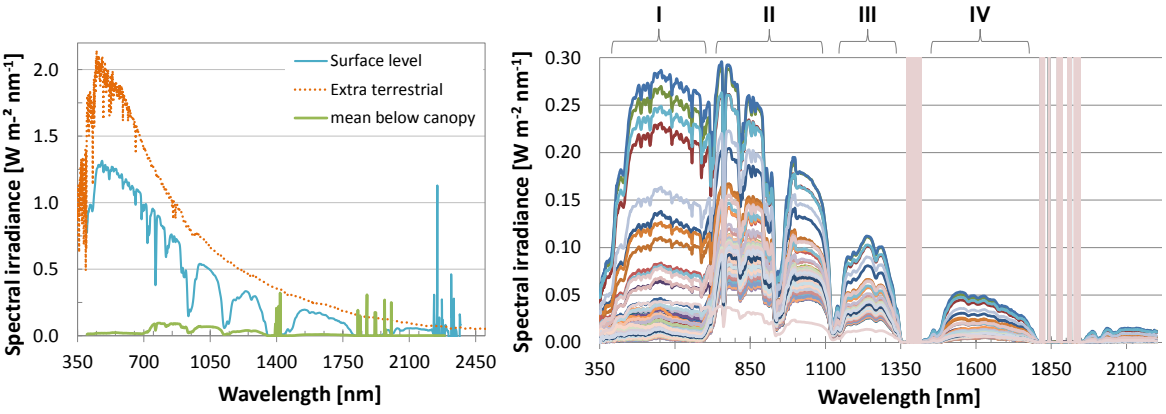

Figure 5.14: Left: Comparison of spectral irradiance at the top of atmosphere (orange dashed line) (Wehrli, 1985), measured at surface level (solid blue line) and average below-canopy (green line) at the study site on 24.07.2012. Right: All 167 measured irradiances below the forest canopy. The water absorption bands around 1400 and 1900 nm are clearly visible. Weak signals cause heavy noise.

The dependency of the intercepted light on the spectral range and the light composition itself become more understandable when plotting the above-canopy against the below-canopy irradiance (Figure 5.15). Though the transmitted radiation is decreased by about the factor 10, we can see the strongest absorption in the visible PAR region, followed by SWIR1.

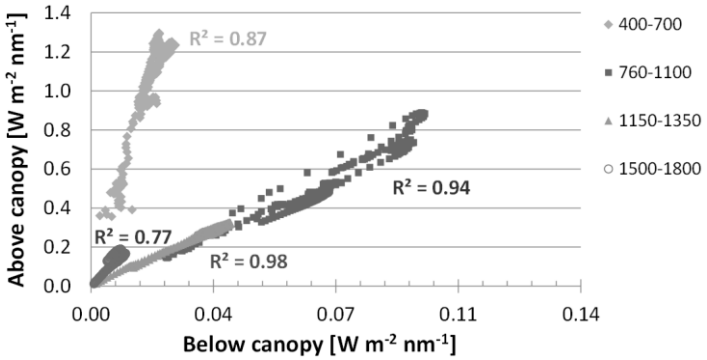

Figure 5.15: Correlations between above and mean below-canopy irradiance for four different spectral ranges. R^2 corresponds individually to the coefficient of determination.

The calculated standard deviations are in the visible spectrum larger than the mean values (Figure 5.16). This is due to the variability in the PAR region and extreme high values, respectively, and caused by a certain skewness of the data. Coefficients of variation are at maximum in red about 680 nm. Hence, this is another clear hint for the importance of VIS in terms of transmission and absorption by photosynthetic processes. One can state that the more light reaches freely the forest floor through gaps or by scattering, the higher is the proportion of short wavelength radiation.

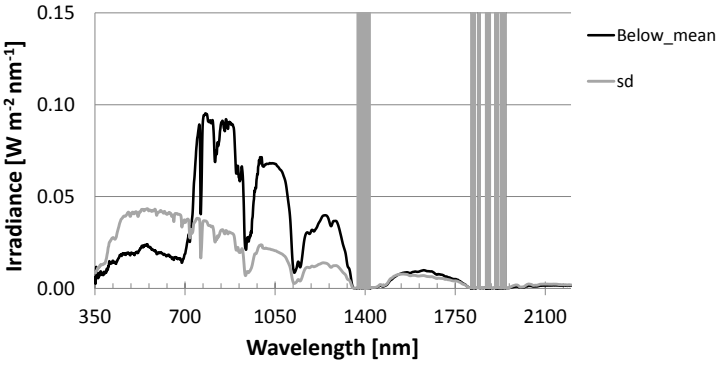

Figure 5.16: Mean below-canopy irradiance and the corresponding standard deviation (sd).

The patterns of below-canopy spectral irradiances are rather varying. In more open plots, where more sun light hits the forest floor, even the shape of solar irradiance is still recognizable. Under denser conditions we can see a pattern which is similar to transmittance curves including high absorption in the visible spectrum. This is more apparent for the light interception building the ratio $E_r = E/E_o$. In PAR only 1.6 % of the light is reaching on average the forest floor (min. 0.2 %, max. 22.4 %, sd. 3.4 %). Whereas with 13.3 % the proportion of transmitted infrared radiation – as averaged over 800-1200 nm – is higher (min. 8.7 %, max. 36.1 %, sd. 4.4 %). However, especially in the shortwave infrared above 1800 nm the ratios tend to be noisy (Figure 5.17). In addition, several peaks are apparent in NIR. From this, the next step is the approximation of the transmission. After applying the negative natural logarithm following Beer's law, the irradiance ratio becomes to a certain degree comparable with absorptance curves of the foliage (Figure 5.18).

Here, the highest values are apparent in VIS and in the water bands. Whereas values are the lowest in NIR, just in contrast to the transmission.

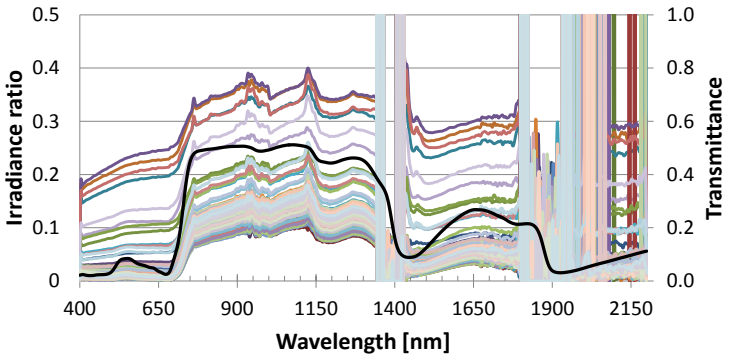

Figure 5.17: All ratios of below- above-canopy irradiances (E/Eo). A transmittance pattern of a single beech leaf (black curve) sampled in May is plotted for comparison.

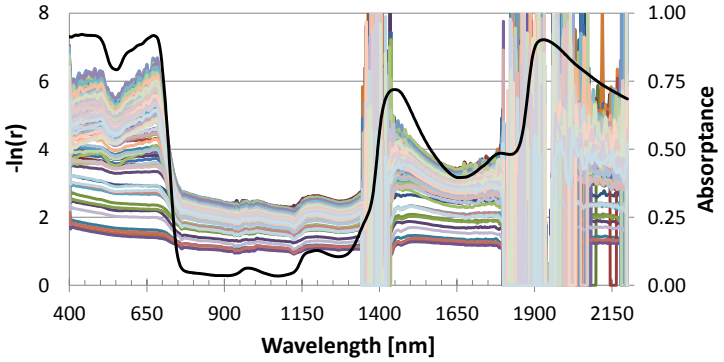

Figure 5.18: All derived negative logarithmic values from the ratio of below- and above-canopy irradiance (-ln(E_r)). An absorptance pattern of a single beech leaf (black curve) sampled in May is plotted for comparison.

Multiplying $-ln(E_r)$ with the reciprocal extinction factor $(1/k)$ one can derive an estimation for the leaf area index (Monsi and Saeki, 2005; Serrano et al., 2000), which hinges on the extinction coefficient and vice versa. This connection of the two variables makes a precise acquisition difficult. The result increases strongly with decreasing k. Whereas with smaller k not only the mean LAI increases, but also the range of values (Figure 5.19). The often used k=0.5 (Groenendijk et al., 2011; Macfarlane et al., 2007; Pekin and Macfarlane, 2009) would lead to an average LAI of 9.7. By assuming a k of 0.7-1 the ratio-derived LAI values average about 4.8-6.9, what corresponds to the LAI in this type of forests (Breuer et al., 2003; Scurlock et al., 2001). Moreover, the LAI reported for this stand of about 5 to 5.5 would imply an average extinction coefficient of 0.88-0.97. Indeed, the histogram of fC classes reveals that the coverage is most often very close to 100 %.

However, although the stand canopy appears rather dense and homogenous, there are still some variations in crown light permeability. Figure 5.20 depicts the theoretical relationship between fractional vegetation cover and the extinction coefficient for fix leaf area indices of 4 to15.

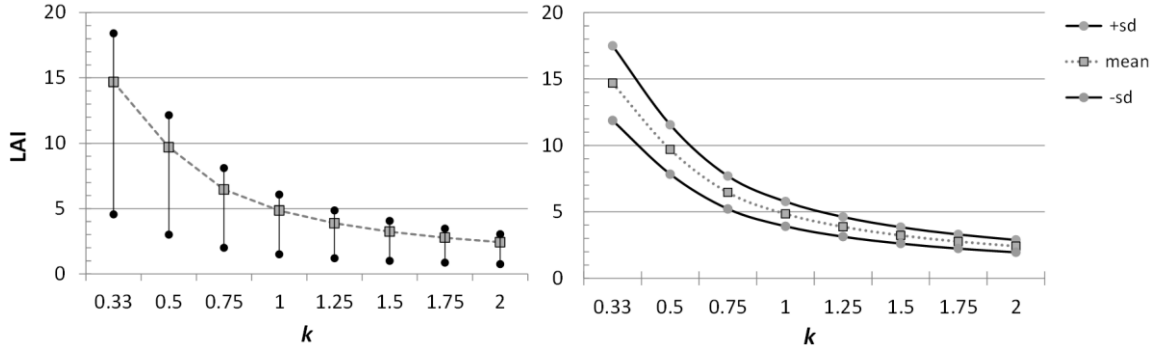

Figure 5.19: Left: Theoretical LAI (minimum, mean, maximum) in dependence of extinction coefficient. Right: Corresponding mean ± 1 standard deviation. Data bases on the in-situ irradiance ratios per plot.

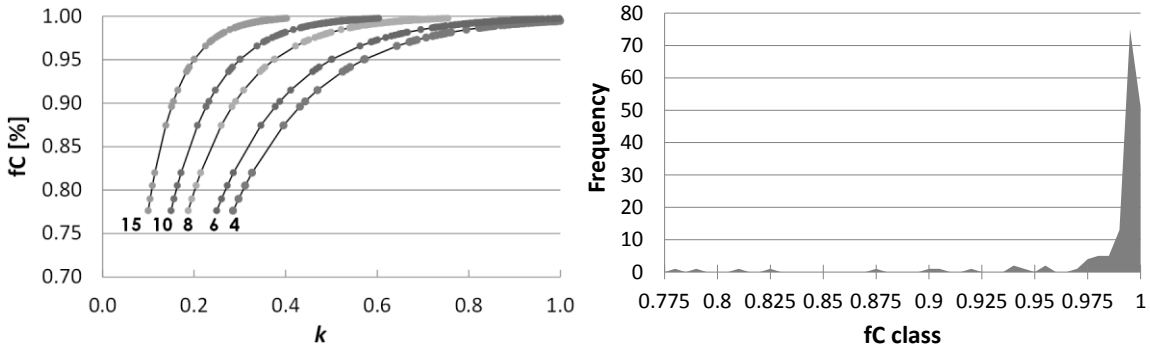

Figure 5.20: Left: Theoretical relation of fractional cover (fC) and extinction coefficient (*k*) for the measured irradiance ratios at the 25 core plots and assumed LAI of 4 to 15 (LAI of about 5.5 is reported for the study site). Right: Histogram of fC values as derived from PAR irradiance on all plots.

5.3.4 Remotely sensed data

Some example pixel values from the used AISA EAGLE and HAWK imagery show the characteristic reflectance pattern. The mean responses per core plot are emphasizing this. On average, the plot reflectances differ mainly in NIR and SWIR1 (Figure 5.21).

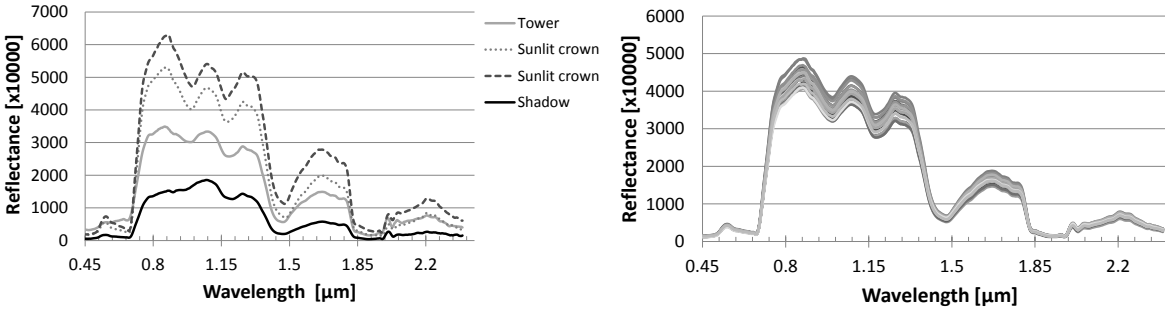

Figure 5.21: Left: Spectral responses of some arbitrarily selected pixels within the core area; tower values are clearly influenced by adjacent vegetation pixels. Right: Mean reflectances of the 25 core plots.

The reflectance imagery is basis for the calculation of the vegetation indices. Figure 5.22 shows the core area for some VI considering greenness and light use efficiency. Corresponding statistics calculated for the whole core area are listed in Table 5.5. The different appearances of the forest stand surrounding the climate tower are clearly visible for each VI. Those pixels are cut to avoid misleading mean values. Especially the NDVI shows a rather homogeneous surface compared to CRI1 or PRI which are richer in contrast. However, the images are only a hint and differences can be due to display settings. The true pixel values are considered in the paragraphs further down.

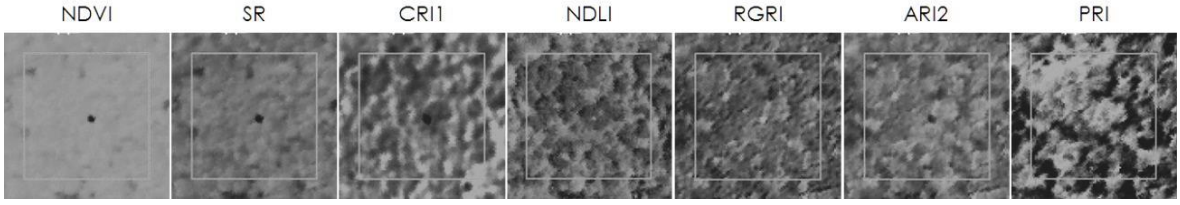

Figure 5.22: Imagery of selected vegetation indices at the core area; the inner square has a size of 150x150 m; the tower appears as spot in the middle.

Table 5.5: Resulting values of selected VI for the core area.

Metric	NDVI	SR	CRI1	ARI2	NDLI	RGRI	SIPI	PRI
Mean	0.887	16.795	28.747	5.379	0.047	1.004	1.027	-0.079
Minimum	0.639	4.543	7.145	2.549	0.027	0.850	1.012	-0.140
Maximum	0.907	20.447	79.365	9.136	0.067	1.396	1.144	0.018

5.3.5 Remote vs field methods

For intercomparison of the field and remote methods the means of each of the 25 plots are calculated and compared. Figure 5.23 shows the correlation matrix of the in-situ acquisitions and remotely sensed indices.

Here, k is chosen as the extinction coefficient for the reported LAI of 5.5. Since fC on plot number four caused an outlier in the analysis, it is omitted from the fC data set. The plot wise relationships of the variables were checked by calculating Pearson correlation coefficients. This is done for among and between the metrics k, fC and the openness values for DCP_{VIS}, DCP_{NIR} and DHP_{VIS}. Additionally, in order to include also the forest structure parameters, the sum of basal area and averaged tree height are considered. Overall, the correlations are not very distinct but rather moderate and range between -0.64 (PRI~DHP) and 0.85 (DCP_{NIR}~DCP_{VIS}). The DHP have highest r values on average. However, there is almost no correlation (r = 0.2-0.3) with the forest structure parameters, which can be excluded subsequently. Similarly, there is no high correlation between DHP and the ground-derived fractional cover (-0.21), whereas there is a moderate one with k (-0.52).

Associating the correlation coefficients of the variables with each of the AISA bands and vegetation indices allows an incorporation of the spectral reflectance information. For each plot the mean response curve is derived. However, none of the metrics has a high relation with the remotely sensed data. From the calculated vegetation indices PRI and CRI1 show the highest correlations with DCP_{NIR} and DHP. In the example of k, the single bands with high r values like for the two wavelengths 531 and 570 are also included in the vegetation index PRI. The ten variables with the highest r are listed in Table 5.6.

Figure 5.23: Part of the correlation matrix of selected features. Absolute r values ≥0.45 regarding the in-situ data are highlighted. Photography metrics DCP and DHP refer to openness.

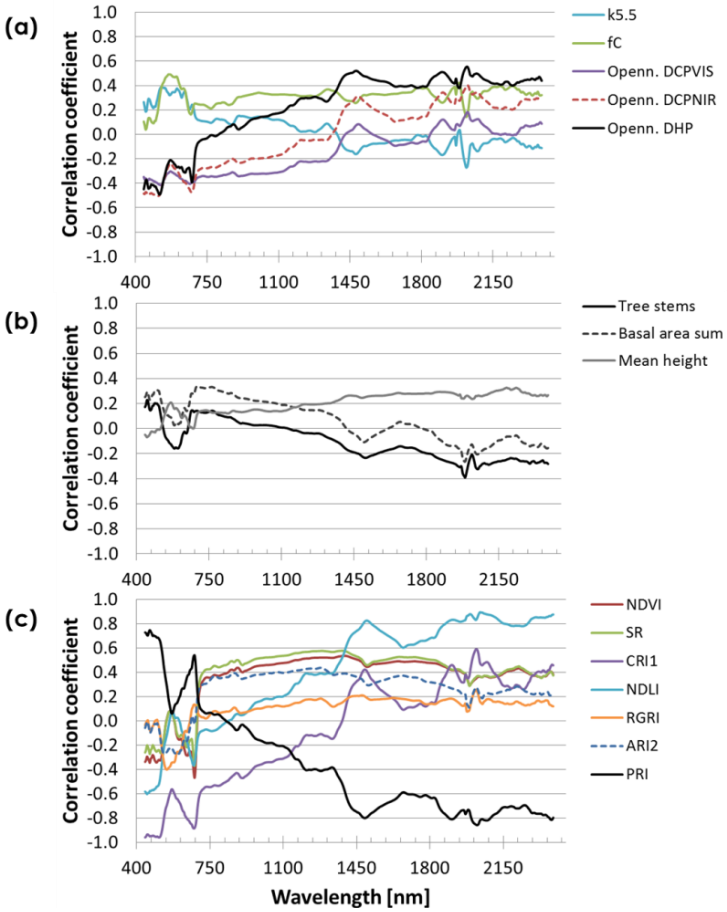

Figure 5.24: Pearson correlation coefficients between (a) in-situ metrics, (b) forest structure and, for comparison, (c) vegetation indices and the spectral reflectance.

Table 5.6: Top ten of Pearson correlation coefficients between the five main approaches, selected vegetation indices and AISA bands representing wavelengths. First row contains mostly redundancy.

$k_{5.5}$		**fC**		**DCP_{VIS}***		**DCP_{NIR}***		**DHP***	
fC	0.78	$k_{5.5}$	0.78	DCP_{NIR}	0.85	DCP_{VIS}	0.85	Plot	0.78
DHP_{VIS}	-0.52	531	0.49	525	-0.42	CRI1	0.59	PRI	-0.64
DCP_{NIR}	-0.46	571	0.49	521	-0.41	PRI	-0.56	CRI1	0.59
ARI2	-0.42	566	0.49	516	-0.41	512	-0.50	2026	0.55
RGRI	-0.42	575	0.49	512	-0.41	507	-0.50	2020	0.55
525	0.39	RGRI	-0.45	530	-0.41	516	-0.50	2013	0.54
530	0.38	ARI2	-0.40	CRI1	0.40	503	-0.50	2032	0.53
534	0.38	Stems	-0.36	NDLI	0.22	DHP_{VIS}	0.46	k5.5	-0.52
543	0.38	DCP_{NIR}	-0.23	2026	0.18	NDLI	0.41	516	-0.49
CRI1	-0.38	DCP_{VIS}	-0.21	2020	0.17	2026	0.40	521	-0.49

*openness

By plotting the most correlated wavelengths, it becomes more obvious which of the spectral bands are involved. The focus is on PAR and mainly blue-green radiation. Whereas NIR is practically

almost not represented. Only a few bands are located in the red edge area and in both SWIR regions (Figure 5.25).

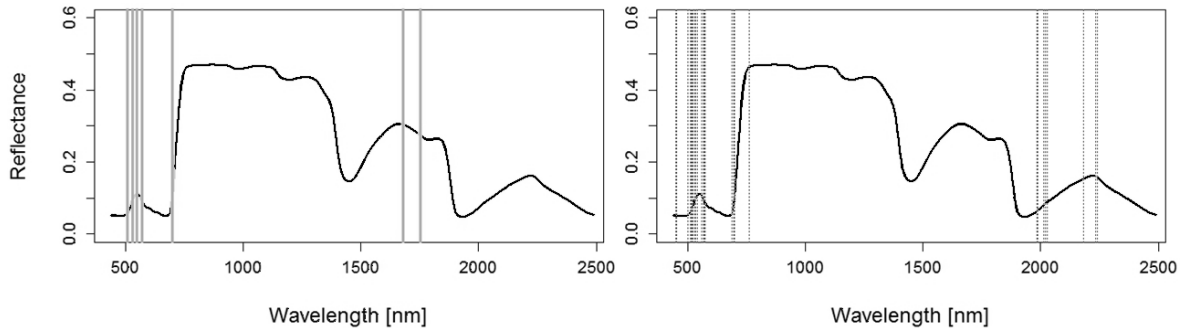

Figure 5.25: Location of the wavelengths that are most frequent in the top ten correlations. Left: Bands included in vegetation indices. Right: Single bands.

5.3.5.1 Spatial interpolation

Although the statistics did not lead to clear relations, a visual comparison reveals some pattern pointing to a connection of remotely sensed PRI and in-situ measured transmission. There are several recognizable structures coinciding with k and fC and mainly the DHP values (Figure 5.26, Figure 5.27). Interpolation is done by using ordinary kriging (Geostatistical Analyst, ArcMap 10, ESRI), the contour lines represent 12 classes by geometric intervals.

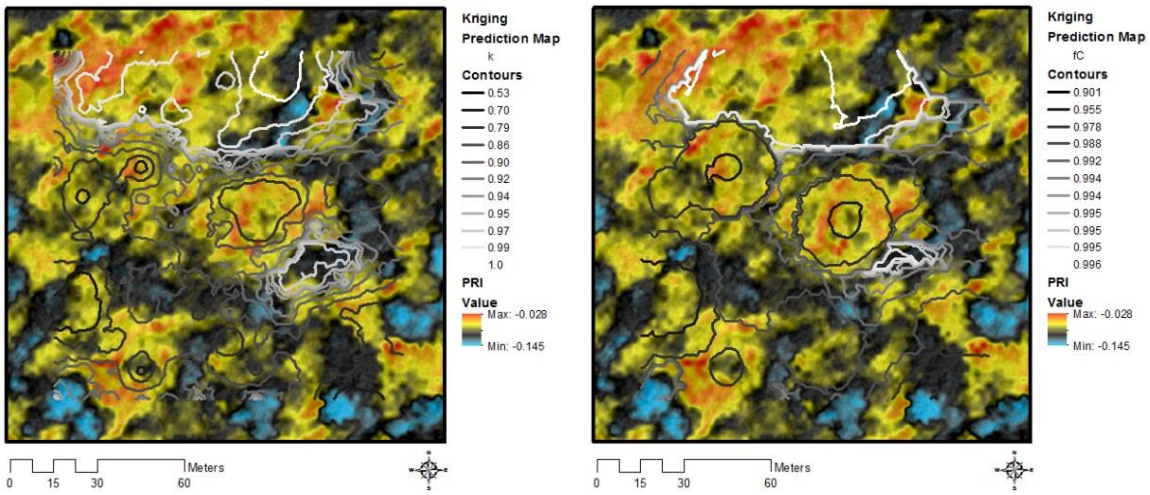

Figure 5.26: PRI image of the core area, overlaid by contour lines of ordinary kriging of mean k (left) and fC (right). There are pattern recognizable in the center and the south western part.

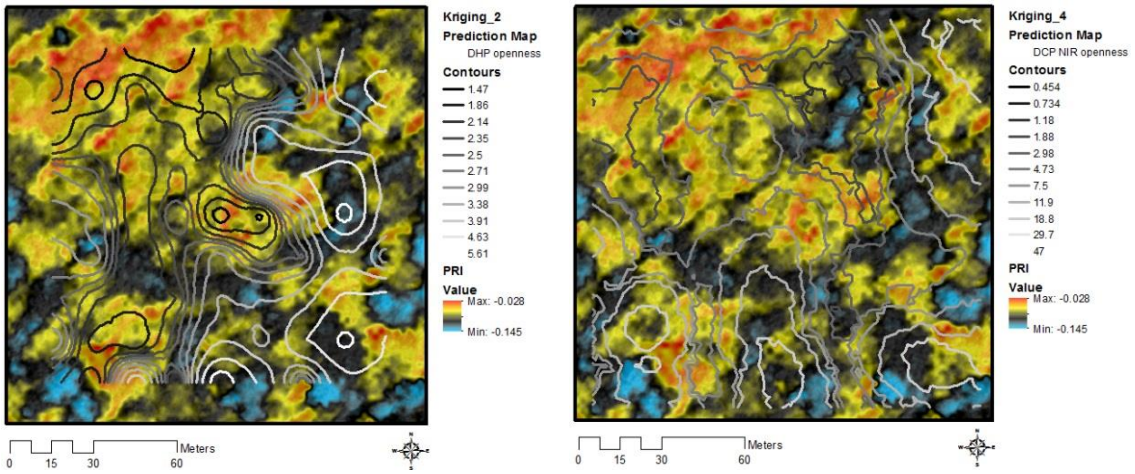

Figure 5.27: PRI image of the core area, overlaid by contour lines of ordinary kriging of openness values from DHP (left) and DCP (right).

An interpolation of *k* using a radial basis function leads to a different result, which seems to take the forest canopy structure more in account objectively (Figure 5.28). However, also here there is no clear trend in data correlation detectable.

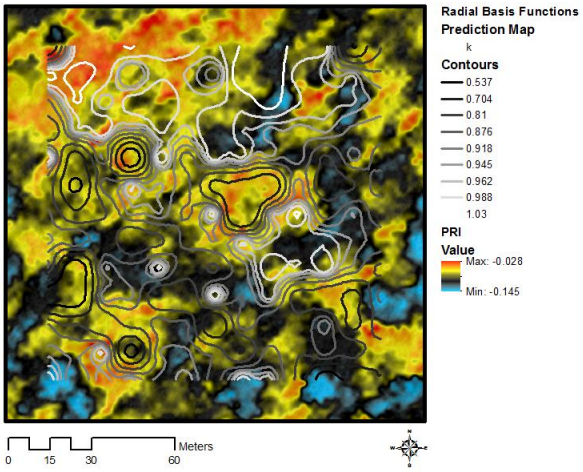

Figure 5.28: PRI image of the core area, overlaid by contour lines of a radial basis function of k values.

5.4 DISCUSSION

It was observed that the photographs are sometimes not covering the same scene to hundred percent, so that small differences between the images on the same plot can arise. Discrepancies may appear generally in repeated recordings when exact positions cannot be adhered. For DCP this was coped by using the new device combining two cameras. However, considering the digital crown photography there is a discrepancy between VIS and NIR regarding the estimation of gap fractions. DCP_{VIS} images tend to lead to smaller openness than the DCP_{NIR}. The latter seem to be more suitable in catching details within the crowns in terms of discrimination between woody parts and leaves, whereas the DCP_{VIS} appear to have higher contrast between sky and foliage. In

addition, the influence of the method of DCP is not further highlighted here. However, it is definitely an issue which could be analyzed in more details for upcoming research. Both DCP approaches differ in grey value distribution. It became clear in this study that the same binarization algorithm leads to different results for VIS and NIR imagery. Besides the threshold method for this binarization also the settings of the camera such as exposure can play a role for the resulting gap fractions or sky/non-sky proportions, respectively. This might be an issue especially in denser canopies where differences in gap fractions become relatively larger (Beckschäfer et al., 2013; Jonckheere et al., 2005; Zhang et al., 2005). The resolution of the cameras is only an issue if the pixel size is too coarse making an adequate detection of very small holes in the canopy difficult. This can be neglected in this study. This study also tested successfully the applicability of a high-resolution field spectroradiometer for measuring below-canopy radiation. However, it was observed that the acquisition of irradiance underneath a rather dense forest canopy is challenging for the ASD FieldSpec. The sensor apparently needs a certain amount of light to deliver rather good signal values without too much noise. Moreover, it did not work under overcast sky, so the measurements were done in rather sunny conditions. It could be clarified that insolation and incident energy is highly day time dependent, as the irradiance conditions are changing. During noon time conditions are somewhat stable. This is important for any field work incorporating the irradiance above the canopy or outside a forest stand. For future research repeated recordings covering several days from the beginning to the end of a growing season are suggested. On average, only less than 2 % of the sunlight in PAR region was reaching the forest floor during noon time. That matches with other published information for dense beech forests of 1-3 % (Ellenberg and Leuschner, 2010). Hence, the old-growth stand in the study area has a dense canopy, yet having some gaps and sun flecks where the insolation is higher with up to 25 % sunlight. This is also supported by the openness derived from VIS and NIR photos. Higher irradiation is possible (i) through small holes and bigger gaps in the crowns but also (ii) due to partly thinner tissue cover. In terms of reflectance and transmittance, optical properties of leaves (see chapter 3) are similar to the crown level. Nevertheless, there are several factors such as gaps, shadows, branches and woody elements providing spectral responses of canopies that differ from leaf level. Moreover, the crown architecture can differ widely with the species (Purves et al., 2007). As shown in chapter 3, leaf stacking has an immediate and high impact on the light absorption of the foliage, and hence on the transmission through the whole canopy. The more leaf layers there are, the higher is the NIR reflectance, and the lower is the NIR transmittance (Bartlett et al., 2011). This observation could also be confirmed in this study. Moreover, reflectance, transmittance and absorptance are not behaving similar when the number of leaf layers or the canopy thickness increases. Reflectance tends to saturate much earlier than transmittance and absorptance (Jacquemoud and Baret, 1990).

As the true leaf area index itself is not measurable by indirect methods in the field anyway, we only can handle with estimations while the real values stay unrevealed. What we can state at least are

limits of values in which the derived k and LAI are ranging. Moreover, measured irradiance ratios or fC and sky/non-sky proportions in terms of gap fractions are rather the only reliable variables. The obtained results are somewhat contrary to the expected relationship between k and LAI. Seemingly, there is not always a clear correlation trend of the extinction coefficient and leaf area index. Both positive and negative relationships between k and LAI are observed by Zhang et al. (2014). Here a LAI of 5.5 was assumed as average over the whole area. Since leaf area index is not a spatial invariant, for more detailed analysis additional estimations of LAI should be incorporated. This would lead to locally better adopted results of light interception. However, the here employed approach, using $-1/k * ln(E_r)$, is an adequate approximation, at least to narrow the expectable range of values. Though the stand canopy was rather homogeneous and dense, there are notable local differences in the results of the approaches but also in the spectral reflectance of crowns and crown parts as indicated by the vegetation indices. Scatterplots of the variables suggest that for a description of the relationship between remotely sensed PRI and openness values derived from digital photography a non-linear model might be more appropriate than a linear. Both Pearson's r and the interpolated openness values suggest that the DHP data is most related to remotely sensed PRI. Interestingly, the core plot number has some of the maximum r for some of the entries. That shows once more to take results with care and that further research is needed. Since DHP and the ASD measurements are covering a hemisphere, nearby gaps are included and influence the metrics. This should be taken into account when combining for example raster data such as remote sensing imagery of Lidar and a spatially distinct intersect. For more accurate results the extraction of VI values might be conducted not for the whole core plots, but rather based on an area buffering around field points. This should be done for each of the in-situ data sets separately. Similarly, remote sensing data can be split and averaged over smaller tiles in order to avoid a too strong smoothing. A spatial interpolation of point data can be an appropriate approach when the records are distributed meaningfully without too large space in-between. Kriging and other techniques should be used with care to avoid misleading results. For filling up gaps between the measuring points, all used data sets inclusive remote sensing imagery have to fit spatially to each other implying an exact georeferencing. This also requires accurate field work.

5.5 CONCLUSIONS

This study compared different methods to assess sun light interception of forest canopy. Besides digital NIR and VIS terrestrial cover and closure photos also detailed spectral information about irradiance and transmittance, respectively, were gathered. As here only an area of a certain size could be covered, one possible approach would be to derive the transmission of sunlight through the canopy of other stands over a wider area. The information of already established forest

inventory plots might be used to cover a larger area. Stands of different age and species composition including broad-leaved and conifers could then be compared to examine potential differences in terms of transmission and absorption. Additionally, canopy light transmission is also depending on the species' capacity to endure cover or water stress. On one hand, shade tolerate species tend to block more light, on the other hand, transmission increases with the drought tolerance (Niinemets and Valladares, 2006). Similar hints about the species-dependency and light interception are presented in Legner et al. (2013). Hence, for future work a more detailed tree-dependent absorption could be analyzed considering species and tree dimension. Gathered data can be used as an input for comparison in (three dimensional) models such as PROSPECT (Jacquemoud et al., 2009; Jacquemoud and Baret, 1990) and DART (Discrete anisotropic radiative transfer model) (Gastellu-Etchegorry et al., 2004). Applications of these models could be supported by acquisition of chlorophyll contents at leaf and canopy level. The derived results for canopy reflection and transmission might then be incorporated within the radiation transfer model intercomparison (RAMI) network (Pinty, 2004). PRI can have a strong relation to the light use efficiency on leaf level. However, on a short-time scale changes in cloud condition and solar radiation are also influencing PRI. Over a growing season the relation to LUE might be even weakened by structural and biochemical properties of the forest canopy (Soudani et al., 2014). The influence of canopy structure and temporal variability of PRI and LUE is discussed in Wu et al. (2015) and Merlier et al. (2015). This also impacts the utilization of remote sensing data for larger areas and the index interpretation over time. The present study data can only be used for single season analysis. For stronger evidences multitemporal data acquisition should be conducted to estimate both the seasonal trend and diurnal changes. In cases where a full spectrum is not needed, more simple and less costly PAR sensors might be preferable to achieve the desired information. LAI, biomass and fAPAR are declared as essential climate variables, according to the global climate observing system (GCOS) (Füssel et al., 2012), what underlines the importance of studies involving the analysis of those in-situ and remotely sensed variables. Moreover, the link of ground measurements and flux towers with productivity and CO_2 storage of trees is still a crucial issue (Gamon, 2015; Porcar-Castell et al., 2015). Collected field data and derived results need to be (i) related to remote sensing data and (ii) validated. For that, an operational system of high spectral resolution sensors is required. Nonetheless, combined hyperspectral field data and remotely sensed imaging spectroscopy are promising tools for detailed retrieval of the amount on intercepted light in forested areas. It could be shown that depending on time and approach we can derive rather different results on forest canopy porousness. There were no high linear correlations detectable between the used approaches. The results have to be interpreted with care and reveal the challenge and complexity of assessing canopy light interception. Besides multitemporal measurements also the inclusion of plots with more variable canopy density incorporating gradients and different forest types with variable productivity is suggested.

5.6 APPENDIX

Table 5.7: Averaged values of the used terrestrial methods and the selected remote sensing vegetation indices for the 25 core plots. Extinction coefficient *k* set for LAI=5.5, CRI1 and NDLI x100.

Plot	$k_{5.5}$	ASD fC	Open. DCP_{VIS}	Open. DCP_{NIR}	Open. DHP_{VIS}	NDVI	SR	CRI1	NDLI	RGRI	ARI2	PRI
1	0.916	0.985	7.509	4.093	1.753	0.875	15.219	0.254	-1.232	1.002	4.933	-0.065
2	0.868	0.987	5.714	1.733	2.075	0.890	17.180	0.248	-1.247	0.999	5.558	-0.065
3	0.800	0.978	6.878	7.109	2.916	0.892	17.581	0.278	-1.232	0.993	5.433	-0.077
4	0.597	0.913	9.517	12.749	2.619	0.885	16.510	0.289	-1.160	0.979	4.850	-0.084
5	0.934	0.994	10.315	14.585	2.080	0.886	16.568	0.311	-1.166	0.982	4.923	-0.093
6	0.863	0.979	6.679	4.228	2.023	0.884	16.358	0.295	-1.210	0.998	5.268	-0.072
7	0.878	0.991	7.521	4.254	2.238	0.887	16.776	0.267	-1.207	1.015	5.599	-0.079
8	0.908	0.971	7.995	4.663	2.023	0.889	16.996	0.287	-1.289	1.009	5.587	-0.068
9	0.991	0.996	5.568	3.487	1.540	0.880	15.703	0.257	-1.231	0.994	5.069	-0.059
10	0.995	0.996	6.192	3.569	1.783	0.884	16.318	0.260	-1.239	0.989	5.123	-0.065
11	0.975	0.995	4.976	3.665	2.594	0.889	17.142	0.258	-1.179	0.996	5.322	-0.078
12	0.795	0.968	7.898	6.433	2.686	0.878	16.302	0.251	-1.260	1.038	5.749	-0.067
13	0.826	0.985	10.336	13.403	2.790	0.891	17.409	0.308	-1.168	1.021	5.829	-0.088
14	0.885	0.991	12.538	18.556	3.304	0.886	16.712	0.324	-1.158	1.002	5.247	-0.092
15	0.795	0.972	6.992	8.041	4.399	0.888	16.899	0.321	-1.199	1.013	5.508	-0.087
16	0.900	0.991	7.133	3.401	3.802	0.885	16.498	0.300	-1.193	1.016	5.482	-0.081
17	0.876	0.987	6.170	1.832	3.905	0.887	16.797	0.280	-1.225	1.019	5.692	-0.077
18	0.948	0.994	5.647	1.866	3.873	0.891	17.339	0.302	-1.213	1.003	5.374	-0.085
19	1.018	0.996	5.324	3.247	3.032	0.890	17.251	0.294	-1.172	0.999	5.396	-0.083
20	0.793	0.979	12.310	20.604	4.544	0.890	17.296	0.287	-1.233	0.995	5.353	-0.081
21	0.916	0.993	9.749	14.349	4.492	0.889	17.064	0.294	-1.187	1.000	5.346	-0.081
22	0.890	0.992	4.861	7.715	4.393	0.892	17.605	0.288	-1.188	1.022	5.884	-0.090
23	0.792	0.985	5.553	7.002	4.560	0.884	16.347	0.286	-1.216	1.008	5.277	-0.085
24	0.712	0.971	8.081	17.200	5.160	0.890	17.173	0.352	-1.187	1.013	5.603	-0.087
25	0.874	0.991	6.140	3.739	2.522	0.888	16.836	0.296	-1.208	0.982	5.062	-0.077
mean	*0.870*	*0.983*	*7.504*	*7.661*	*3.084*	*0.887*	*16.795*	*0.287*	*-1.208*	*1.003*	*5.379*	*-0.079*

Chapter 6

Forest inventory & hyperspectral remote sensing

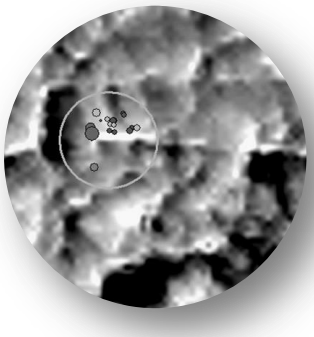

6 CHAPTER SIX - FOREST INVENTORY AND HYPERSPECTRAL REMOTE SENSING

6.1 INTRODUCTION

Forests are complex and dynamic ecosystems. They take up vital functions of economic, ecological and social aspects for local communities and people worldwide (Füssel et al., 2012; Thomas, 2012). In days of increasing environmental pressure and global carbon trading systems, forests become more important and valuable than ever. One key method to derive relevant information about forested areas is the implementation of in-situ forest inventories on regional and national level. Mainly based on systematic sampling, they can give an overview about species composition and dispersion as well as tree dimension. Obtained information can be used as a basis for decisions regarding the forest management and the corresponding strategies on national and international level for countries and organizations (Fridman et al., 2014). The importance and need can be seen in the fact that more than 80 % of the global forests have been covered by forest inventories (FAO, 2015). About one third of the country of Germany are forests, which corresponds to the global proportion of forested land (BMEL, 2015; UNEP et al., 2009).

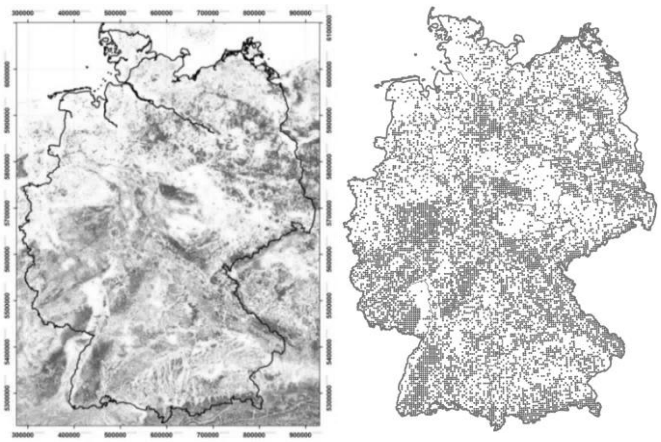

Figure 6.1: Left: spatial distribution of Germany's forests according to CORINE Land Cover Europe 2006 (Forested semi natural areas) (EEA, 2012). Right: Forest inventory plots of the third national forest inventory of Germany (BMEL, 2015).

In forest inventories, we often deal with circular nested plots with different subplot sizes. Within these plots, trees are sampled depending on their diameter at breast height. In remote sensing (RS) studies, those inventory plots are used for training data and can be used to extract the pixel values of remotely sensed data or their derivates (Foster and Townsend, 2004). Hence, the link of field based information and remotely sensed data can be an asset to extend the information and support inventories (Romijn et al., 2015). Although it is a common procedure, there is no clear and standardized rule on how users should extract RS raster values. This can be done by using the,

quasi-original, circular plots or by creating squares around a sample point. Certainly, the method highly depends on the scale and pixel resolution and can be more or less meaningful. As here hyperspectral airborne imagery with a GSD of 2.0 m is used, rather detailed extraction and analysis are possible. In this study, additional to circular plot extraction another method to obtain raster values is applied. The proposed way is the utilization of a convex hull (CH), which span modelled crowns of recorded trees on each inventory plot. This study includes following objectives: Both data sets, circular and CH plots, are compared to answer the question if there are differences in extracted pixel values. Of main interest are common forestry variables such as mean tree diameter at breast height (dbh) [cm], basal area [m^2/ha] and stand density [stems/ha] as derived from the inventory plots. As a main objective, potential relationships between inventory plot data and airborne hyperspectral remotely sensed metrics containing reflectances and selected narrow- and broadband vegetation indices shall be examined.

6.2 MATERIAL & METHODS

6.2.1 Study site

The study was conducted in the Hainich, a forested ridge at about N51.08° E10.45° and with an elevation ranging around 400 m a.s.l. The forest stands are unmanaged since decades (Knohl et al., 2003; Mund et al., 2010) and cover a large area of the Hainich national park. See chapter 3 for a detailed description about the study site. The dominating tree species is beech (*Fagus sylvatica*), followed by ash (*Fraxinus excelsior*), maples (*Acer spec.*), oaks (*Quercus spec.*), hornbeam (*Carpinus betulus*) and other broadleaved species. The few patches of coniferous trees are mostly composed of spruce (*Picea abies*).

6.2.2 Remotely sensed data

6.2.2.1 Reflectance and vegetation indices

The hyperspectral AISA sensors EAGLE and HAWK (SPECTRAL IMAGING LTD.) cover a spectral range of 400-2500 nm split into 368 bands. Figure 6.2 shows the complete mosaic of the eight flight stripes as single-band greyscale image representing reflectance at 869 nm. At each wavelength, the scenery is appearing more or less different, whereas adjacent bands tend to be redundant. The figure depicts additionally some single-channel images on the example of a spatial subset including forest and crops. Several common broad- and narrowband vegetation indices (VI) are calculated to examine the potential relationship with tree based plot variables such as mean dbh and stems per hectare. The selected VI address multiple objectives like greenness, pigments or light use efficiency (Table 6.1).

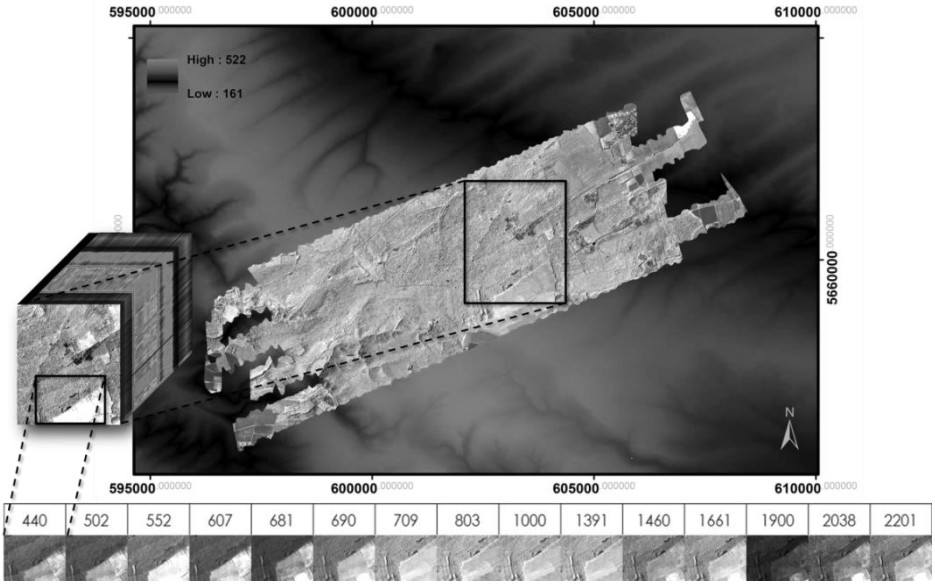

Figure 6.2: Mosaic of the eight flight stripes at 869 nm, overlaid over a digital elevation model. Selected layers of the same subset of AISA EAGLE and HAWK imagery and the corresponding wavelengths in nanometers. The scene depicts forest and neighboring grass land.

Table 6.1: Vegetation indices used in this study and the according formulas.

Objective	Index	Formula	Reference
Greenness	Normalized Difference Vegetation Index	$\mathrm{NDVI} = \frac{\rho_{\mathrm{NIR}} - \rho_{\mathrm{RED}}}{\rho_{\mathrm{NIR}} + \rho_{\mathrm{RED}}}$	(Rouse et al., 1974)
	Simple Ratio	$\mathrm{SR} = \frac{\rho_{\mathrm{NIR}}}{\rho_{\mathrm{RED}}}$	(Tucker, 1979)
Leaf pigments	Carotenoid Reflectance Index 1	$\mathrm{CRI1} = \frac{1}{\rho_{510}} - \frac{1}{\rho_{550}}$	(Gitelson et al., 2002)
	Anthocyanin Reflectance Index 2	$\mathrm{ARI2} = \rho_{800} * \left(\frac{1}{\rho_{510}} - \frac{1}{\rho_{700}}\right)$	(Gitelson et al., 2001)
Carbon	Normalized Difference Lignin Index	$\mathrm{NDLI} = \frac{\log\left(\frac{1}{\rho_{1754}}\right) - \log\left(\frac{1}{\rho_{1680}}\right)}{\log\left(\frac{1}{\rho_{1754}}\right) + \log\left(\frac{1}{\rho_{1680}}\right)}$	(Fourty et al., 1996)
Light use efficiency	Red Green Ratio Index	$\mathrm{RGRI} = \frac{\rho_{\mathrm{RED}}}{\rho_{\mathrm{GREEN}}}$	(Gamon and Surfus, 1999)
	Structure Insensitive Pigment Index	$\mathrm{SIPI} = \frac{\rho_{800} - \rho_{445}}{\rho_{800} - \rho_{680}}$	(Peñuelas et al., 1995)
	Photochemical Reflectance Index	$\mathrm{PRI} = \frac{\rho_{531} - \rho_{570}}{\rho_{531} + \rho_{570}}$	(Gamon et al., 1992)

6.2.2.2 Extraction of remote sensing raster data

Usually there is no common agreement of how raster values from an optical remote sensing image have to be derived by defined masks like vector polygons of tree crowns, inventory plots or delineated forest stands. The decision depends mainly on both the spatial resolution and characteristics of the focal raster. In heterogeneous areas like in the present study site, value extraction requires a sufficient spatial alignment of mask and base image. As mentioned, the

inventory data consist of three circular nested plots. Hence, there is no full information of the complete plot, which would be represented by the biggest circle. Actually, only the smallest and innermost subplot contains all trees. The here proposed way to extract pixel values of imagery with relatively fine spatial resolution and is the utilization of a convex hull spanning modelled crowns. The circular crown diameters depend on the dbh of the recorded trees on each inventory plot and are approximatively calculated using empiric models (Hansen and Nagel, 2014) for following species and species groups: Ash, beech, oak, hornbeam, maple/other broadleaved, spruce, Douglas fir/larch, pine. The created convex hulls differ in size from the biggest circular plots and can be larger or much smaller than the latter. Consequently, the number of selected 2 m-pixels within circles and convex hulls can differ reasonable.

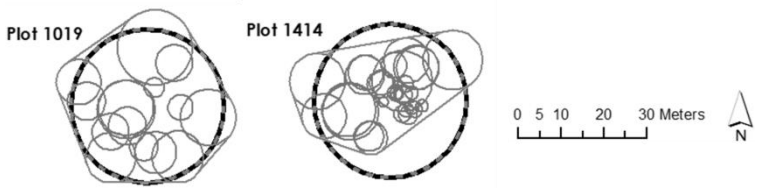

Figure 6.3: Examples of convex hulls at inventory plot 1019 and 1414 incl. modelled crowns of sampled trees, in dashed line the regular 1000 m² plot (radius=17.84 m).

6.2.3 Forest data

The data basis is a set of forest inventory plots. On a grid of 200 by 200 m, 606 plots including more than 14,000 sampled trees are considered for this study are part of a permanent control sampling gathered in 2009-2011. The plots consist of concentric nested circles with pre-defined radii of 7.68, 12.62 and 17.84 m, respectively. See chapter 2 for further information about the inventory data and the according species composition. Besides tree species, the two focus parameters are mean tree diameter at breast height (dbh) and number of stems per area. Appropriate expansion factors have to be applied to get estimations for each plot and values per hectare, respectively. In the highly mixed forest, it is almost impossible to find pure stands with only one species. Hence, the inventory database is filtered by species or species group for the extraction of plot values. The fractions of observed tree species can be expressed by both the basal area [m^2/ha] and the number of stems [n]. In any case, beech is dominating by far. However, since most of the plots contain more than one species, a specific threshold per plot is applied for each species. By this, the number of usable plots per species becomes more sufficient (Table 6.2).

The fractions of the species groups for each forest inventory plot are presented as pie charts in Figure 6.4. Here the spatial distribution of the species is already visible revealing some local trends and differences in the composition. Moreover, the assigned colors for the species are somewhat comparable with the color composite of three vegetation indices SR, PRI and SIPI.

Table 6.2: Overview of inventory plots with 'pure' species content and final number of plots per species using thresholds.

Species group	Scientific name	Species code	Pure plots [n]	Threshold per plot [%]	Thresholded plots [n]
Beech	*Fagus sylvatica*	211	72	90	119
Ash	*Fraxinus excelsior*	311	0	75	18
Oak	*Quercus spec.*	110	1	50	14
Hornbeam	*Carpinus betulus*	221	1	50	7
Sycamore maple	*Acer pseudoplatanus*	323	2	60	10
Other broadleaf	-	200	6	50	29
Spruce	*Picea abies*	511	4	70	11
Scotts pine	*Pinus sylvestris*	711	0	60	3
Other coniferous	-	800	0	50	2

Another silvicultural standard procedure is to categorize trees considering their development stage and dimension. Therefore, regarding to the diameter, common classes contain young growth (dbh ≤20 cm), young (21-35 cm), middle-aged (36-50 cm) and old timber (>50 cm). However, in this study the trees are split into seven dbh classes in steps of 10 cm as listed in Table 6.3. Additionally, considering the stand density in terms of trees per hectare, classes of a width of n=200 were created (Table 6.4). The most frequent density classes, representing about 53 % of the plots, are 201-400 and 401-600 n/ha. Only 3 % of the plots have a very high estimated density of more than 1800 n/ha.

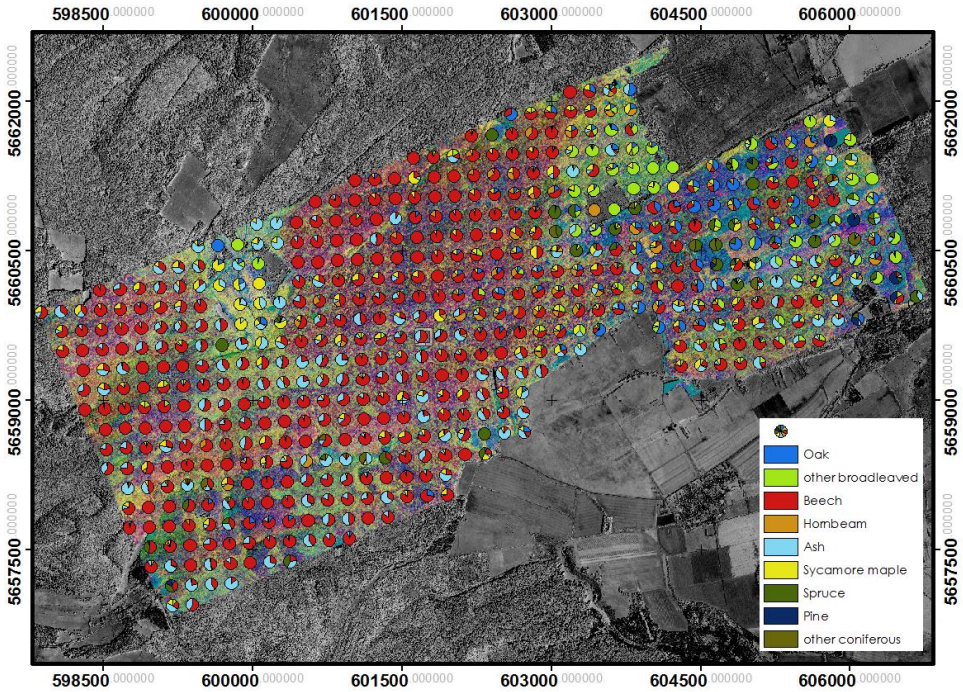

Figure 6.4: Location and species group compositions of the inventory plots. AISA VI composite: SR-PRI-SIPI covering the forested study area. Background: Greyscale aerial NIR image.

Table 6.3: Definition of the dbh classes.

Group	dbh class [cm]	Category	Plots [n]
1	≤10	*young growth*	12
2	11-20		64
3	21-30	*young and middle-aged*	105
4	31-40		190
5	41-50	*old timber*	165
6	51-60		67
7	61-70		3

Table 6.4: Definition of the stem density classes.

Group	Density [trees/ha]	Plots [n]	Group	Density [trees/ha]	Plots [n]
1	≤200	50	10	1801-2000	3
2	201-400	165	11	2001-2200	3
3	401-600	155	12	2201-2400	3
4	601-800	92	13	2401-2600	5
5	801-1000	44	14	2601-2800	0
6	1001-1200	33	15	2801-3000	3
7	1201-1400	20	16	>3001-3200	0
8	1401-1600	14	17	>3200	2
9	1601-1800	14			

Figure 6.5 shows the typical pattern between stand density and mean tree height per plot in relation to mean tree diameter at breast height. While the height increases, the number of stems per hectare decreases with dbh. The distribution of summed up basal area per plot is somewhat bimodal with maxima at the classes of 32 and 42 m^2/ha and an average of about 41 m^2/ha. Higher and lower classes are less represented (Figure 6.7).

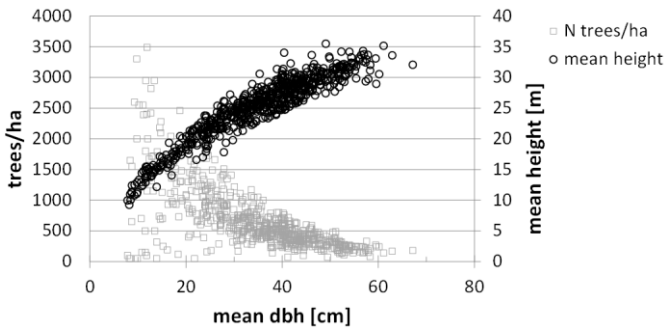

Figure 6.5: Relationship between trees per hectare, mean height, and mean dbh; values per inventory plot.

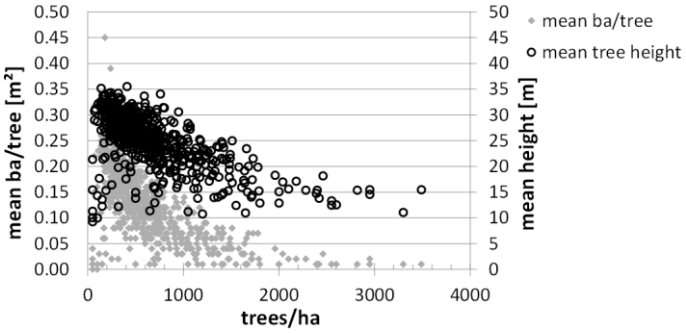

Figure 6.6: Relationship between mean basal area per tree, mean tree height and stem density; values per inventory plot.

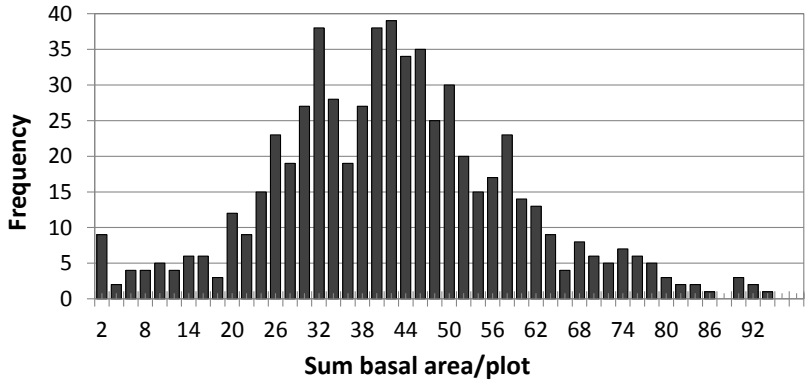

Figure 6.7: Distribution of summed basal area [m²/ha] class per inventory plot.

6.3 RESULTS

6.3.1 Plot shape effect on reflectance

There are some differences in the spectral responses of the pixels extracted by circular inventory plot and the created convex hulls spanning modelled tree crowns. As an example the reflectances of a NIR band at about 800 nm are opposed in Figure 6.8. One of the outliers at the bottom is located on an edge next to a grassland. This is a good example where in the circular plots wrongly included pixels are not considered in the convex hull.

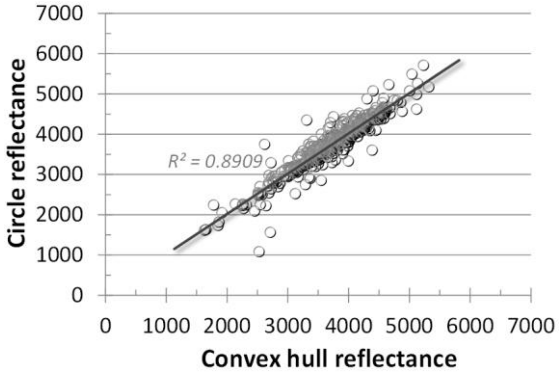

Figure 6.8: Comparison of reflectance values in NIR channel (803 nm).

Absolute differences of plot mean values are dependent on the wavelength. The reflectance values extracted from convex hulls show a smaller variation, as the difference of maximum and minimum are reduced in comparison to the values derived from circular plots. The higher variation in the circular plots can also be seen in the larger standard deviations (Figure 6.9). Most of the variability appears in NIR and SWIR1, while in VIS the differences are minor. In spite of that, the means of both approaches are almost the same, which legitimates the utilization of the approach.

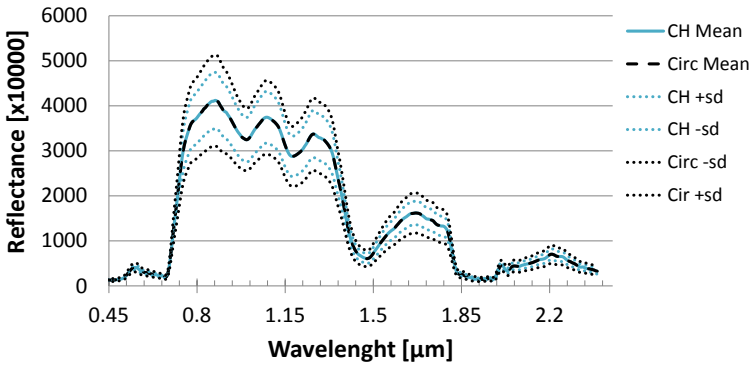

Figure 6.9: Comparison of plot-wise reflectance statistics as derived from circle-shaped (Circ) plots and convex hulls (CH). Mean values ± standard deviations (sd).

6.3.2 Tree species

The extraction of spectral response pattern from the imagery was done at inventory plots with the majority of the species classes. About 90% of the species per plot is beech. However, the derived reflectance curves of all inventory plots show the typical shape of green vegetation with the two main water absorption bands and two minor ones in the NIR plateau. The reflectances in the PAR region are decreased due to chlorophyll and other leaf pigments, but relatively low when comparing to in-situ data (see chapter 4). Besides plot averages, the calculated mean per species group is plotted in Figure 6.10. At about 2 µm, the response patterns show a strong feature, which might be an artifact due to the pre-processing steps of the imagery. Detailed graphs of the VIS region are shown in Figure 6.11.

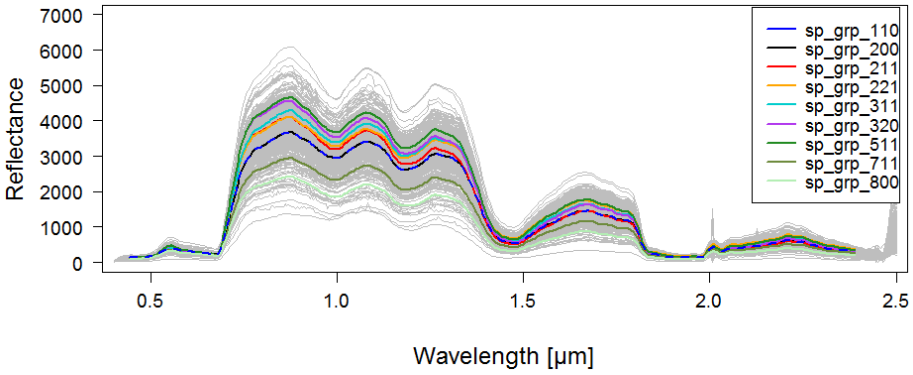

Figure 6.10: All mean spectral responses (grey) and corresponding means of the nine species groups as derived from convex hulls of the inventory plots. 110=Oak, 200=Other broadleaved, 211=Beech, 221=Hornbeam, 311=Ash, 320=Maples, 511=Spruce, 711=Douglas fir/Larch, 800=Other coniferous.

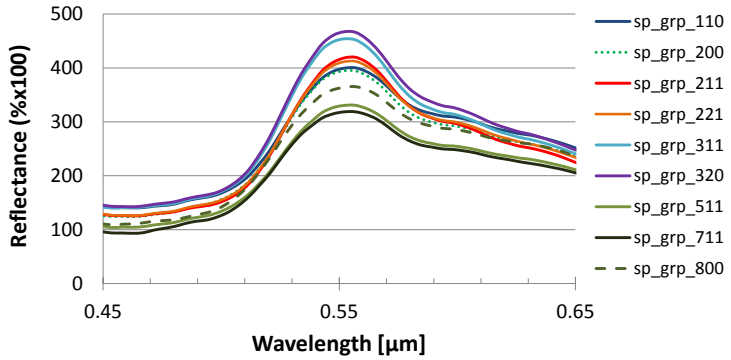

Figure 6.11: Spectral responses derived from inventory plots and averaged by species (group) for the VIS region.

By subtracting species reflectances from the one of beech, differences between species become more distinct (Figure 6.12). Hornbeam and beech are most similar over all bands. However, the differences among species are depending on the range of wavelengths. While in NIR maple plots are more similar with ash, they are rather comparable to beech in SWIR.

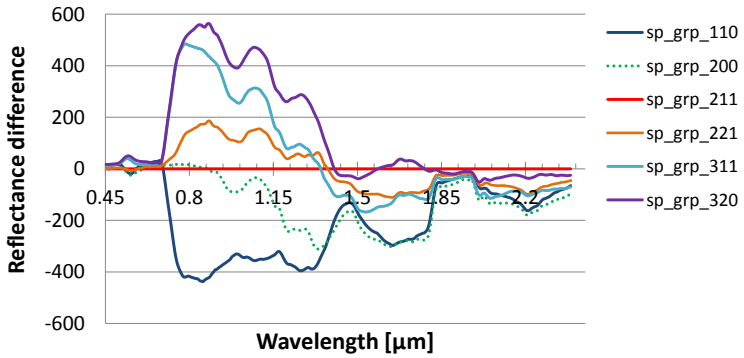

Figure 6.12: Differences in reflectance of broadleaved and beech plots as reference.

Estimated stand variables are opposed to the reflectances of the AISA images. Again, variables and pixel values are averaged per plot. There are no distinct linear relations between wavelength and basal area, mean tree height or stand density. Over all tree species, the achieved Pearson's correlation coefficients are rather small and range between -0.11 and 0.16 (Figure 6.13).

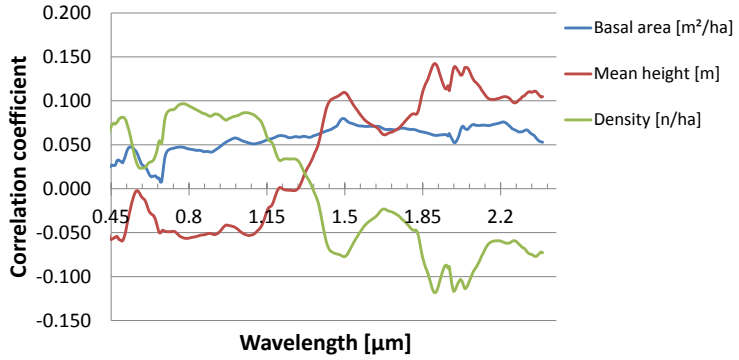

Figure 6.13: Pearson's correlation coefficients between spectral reflectance and mean forest stand attributes as derived from inventory plots.

For each inventory plot, the mean dbh was calculated. Apart from the unique average, groups of diameter classes were built and contrasted with spectral bands. Clear trends are mainly apparent in SWIR1 and SWIR2, where reflectances increase with the averaged tree dbh.

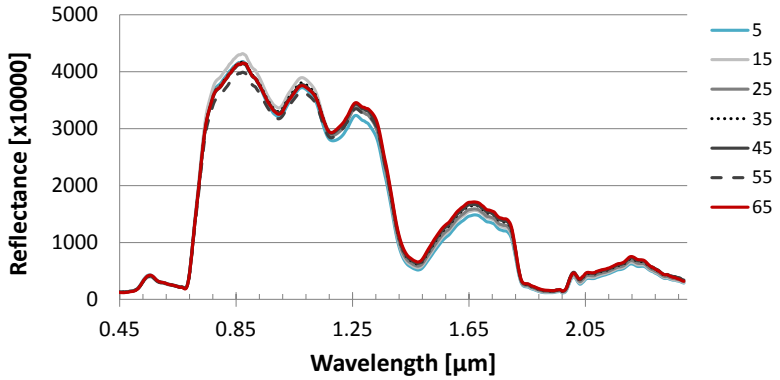

Figure 6.14: Plot-wise averaged reflectance curves for different dbh classes; numbers correspond with class means [cm].

By contrast, the relationship between stand density groups and reflectance by wavelength shows an opposite pattern. Higher densities are here associated with higher values in the near infrared but lower in the short-wave infrared reflectance (Figure 6.15).

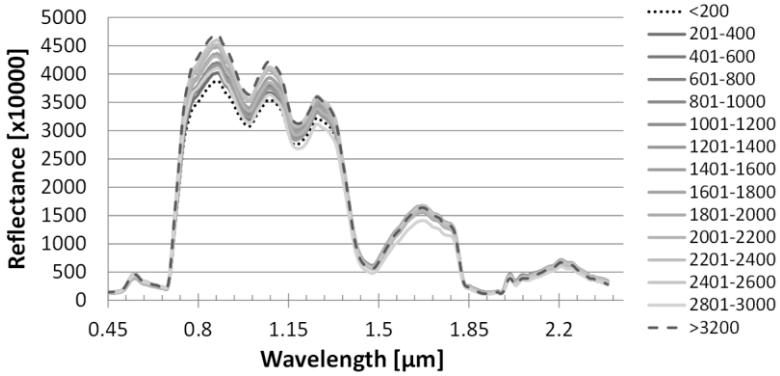

Figure 6.15: Plot-wise averaged reflectance curves for different density classes; numbers in trees per hectare as class means.

6.3.3 Vegetation indices vs. plot attributes

Additionally to the reflectance values, the calculated broad- and narrowband vegetation indices are opposed to the estimated stand variables basal area, density, mean dbh and tree height. The corresponding scatter diagrams for each inventory plot are displayed in Figure 6.16 and Figure 6.17. Potential relationships between mean VI and mean stand parameter could become visible. However, there are no clear trends at all recognizable in basal area per hectare using mean values of each variable. Similarly, mean tree height and VI are apparently without distinct correlation,

with one exception: PRI, however, has seemingly a weak negative relation with the height. In NDVI, SR, SIPI and slightly NDLI, there is some variation for mean tree heights of about 25 m, which represents the mean height of all inventory plots.

For the classified dbh and stand density data, the VI values are depicted in box plots of Figure 6.16 and Figure 6.17. In some of the VI, like RGRI and ARI2, there is a concave-like trend in the median and quantile distribution over the dbh classes, where the lowest and highest classes have minor values. Similar to the mean tree height, there is a nearly constant negative trend in PRI and dbh class. For all other VI, the distributions show rather equal median values for each class.

In contrast to the diameter classes, the first stand density classes corresponding to the sparse stands contain the most varying data. However, examining the relations between classes of trees per hectare and the VI, we can see comparable pattern to the dbh classes, albeit it is more variable due to higher number of classes. Again, in PRI there is a rather distinct trend, which is in this case positive.

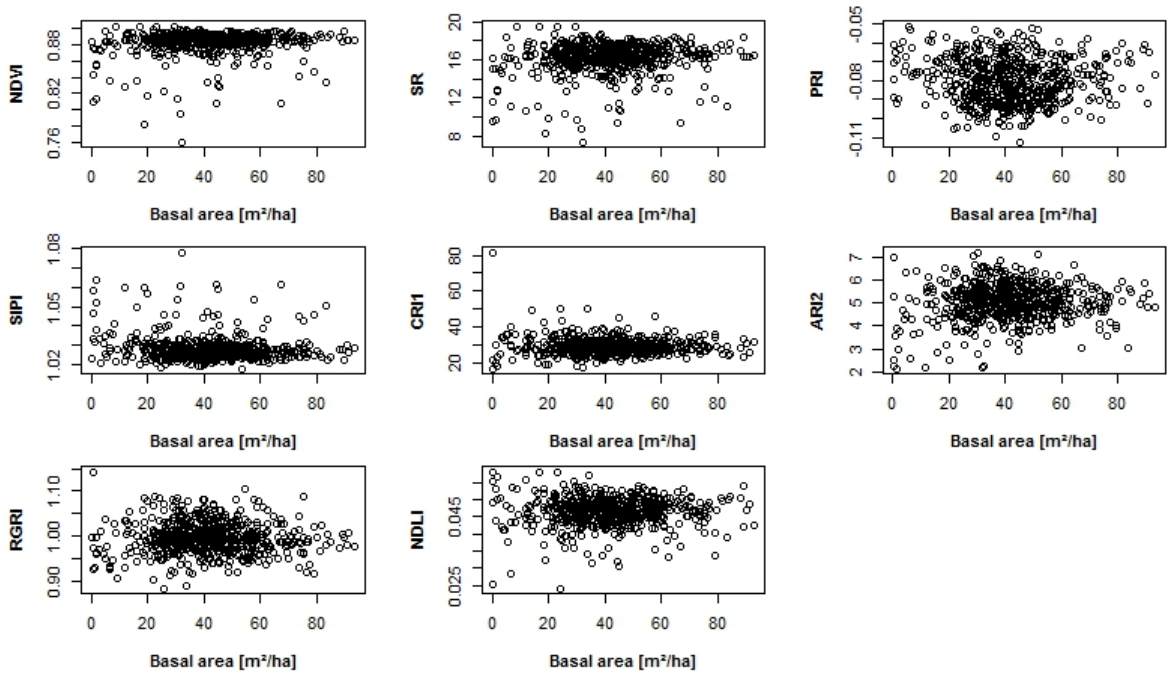

Figure 6.16: Scatter plots of plot-wise basal area per hectare and vegetation indices.

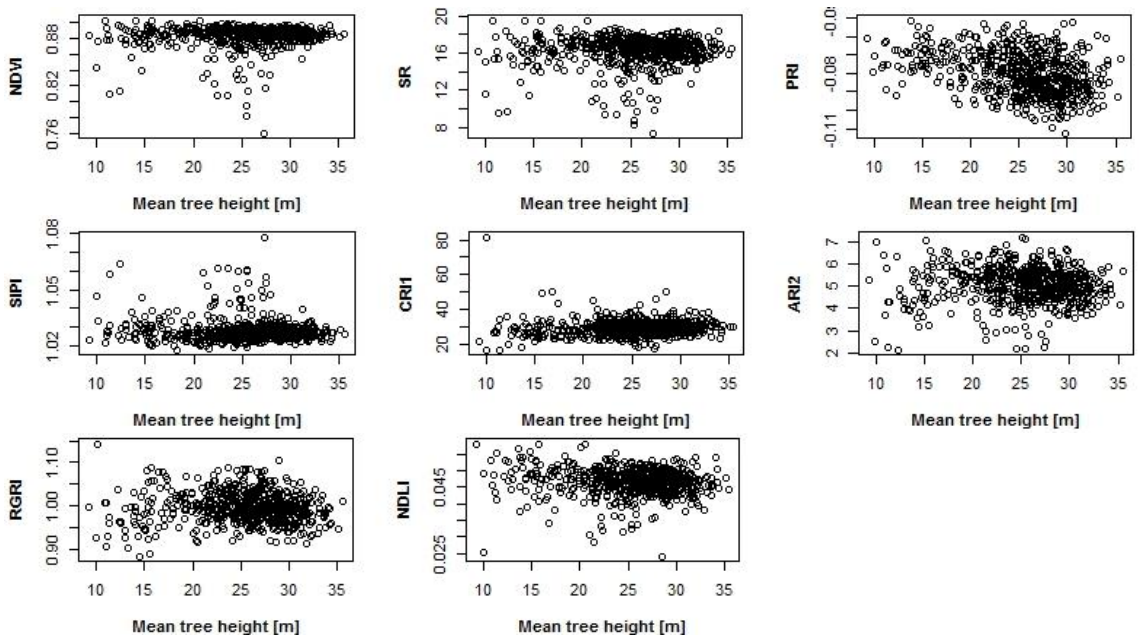

Figure 6.17: Scatter plots of plot-wise averaged tree height and vegetation indices.

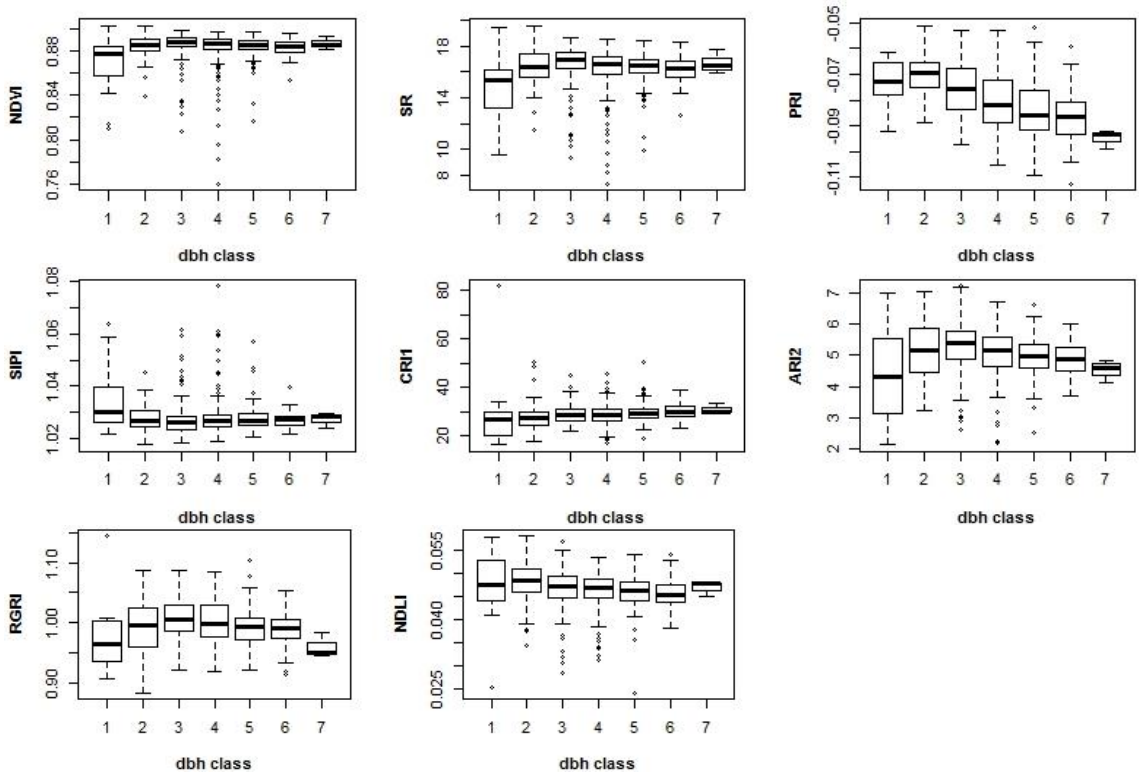

Figure 6.18: Boxplots of dbh classes for each vegetation index as derived from inventory plots.

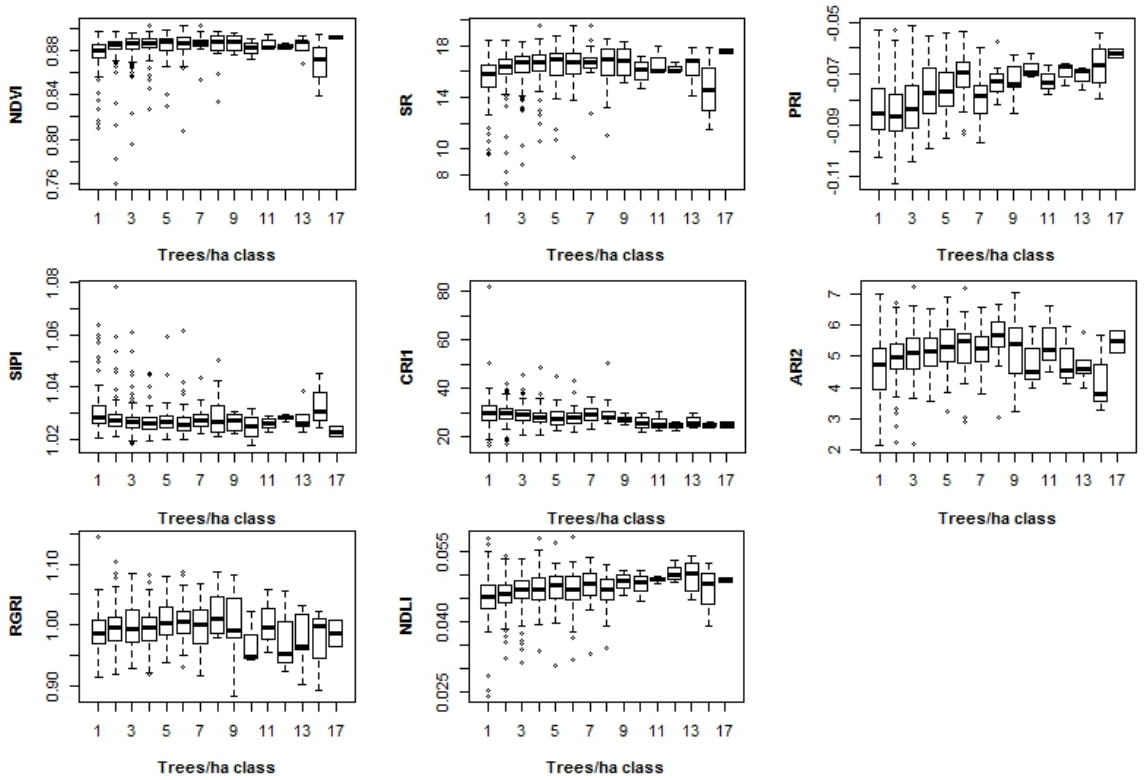

Figure 6.19: Boxplots of the trees-per-hectare classes for each vegetation index.

None of the mean VI value per inventory plot shows any correlation with basal area. It should be noticed that the dbh values are kept as mean group values, why a direct interpretation of the correlation coefficients should be done with care. However, among all VI the by far highest correlations are observable in PRI, where stand density is positively, tree height and dbh group negatively correlated.

Figure 6.20: Pearson's correlation coefficients (Spearman's correlation coefficient for dbh group) of plot-wise median VI and stand attributes as derived over all inventory plots.

6.4 DISCUSSION

Difficulties arose in the mosaicking of the RS images. Before putting them together, each flight stripe needed to be referenced again. Additionally, processing steps and polishing of the imagery

have an influence on the reflectance values and hence on a derived vegetation index. This should be kept in mind when interpreting results, comparing with other studies using another pre-processing or even different sensors. However, still the data never fit to 100 % to each other. Differences in spatial accuracy and alignment of various sources become clearer when dealing with high-resolution imagery. This can be a source of error for the extraction of pixel values and has to be taken into account in mind during analysis and interpretation. Further differences in the images due to illumination and sun-observer-angle issues, which could not fully be compensated.

This study proposed successfully an approach for extracting raster image values with vector data by using a convex hull spanning idealized modelled tree crowns. By this, it is assumed that due to that the spatial alignment is more meaningful and corresponds more to the real crowns. Comparing the convex hull approach with a common method using the biggest circle of nested inventory plots, shows that the mean pixel values per plot are almost identical. However, the variation is smaller than in the circular plots. This could be interpreted in two ways: on one hand, it is better to cover most of the variability to ensure all spectral variance of a plot. This variability can occur by shadows or other land cover types at forest edges may have an impact on the mean plot reflectance, whereas these false signals are not desired. Due to the CH, the pixel extraction is more restricted to the observed crowns leading to less noise. On the other hand, similar means of convex hulls and circular plots support and justify the use of the CH approach. However, the observed differences are smaller than expected. The unequal number of elements (plots) per dbh or height class may have an impact on the derived results when comparing class means. Hence, the observed differences in the mean class spectra might be artifacts.

However, a somewhat surprising outcome of this study is that from all calculated vegetation indices only PRI shows the highest (moderate) correlations with the examined inventory plot data. Since PRI is related to light use efficiency and productivity, the correlation with dbh, height and stand density becomes explainable. Hence, PRI has seemingly a good potential for predicting those forest stand attributes.

Canopy closure is one main driver in the spectral appearance of forest stands. The mixture of dimension, tree-to-tree distance creating gaps and shadows, and tree age influence the reflectance of forests. Younger stands, for example, which are usually denser, tend to reflect more in NIR than older ones (Nilson and Peterson, 1994). Besides the stand attributes, the tree species is surely an aspect which should be respected. When only considering plots where the majority consists of only one species like beech, the correlation coefficients might be different between the main species. The effect of species-depending reflectances could be considered when examining tree diameter and stand density, to ensure that differences are not mainly species related. For that, analysis could focus on beech at first before merging all species.

6.5 CONCLUSIONS AND OUTLOOK

It should be assessed in future for the convex hull approach if the different plot training data is affecting or even improving image classification. This could incorporate also different sensors. The approach of convex hull-based data extraction in combination with the vegetation indices can then be tested at other sites that are (i) similar and (ii) rather different in conditions. Considering the stand attributes, there are also some things to consider in subsequent analysis. Further analyses might be improved by implementing more details, for example by smaller density classes. Splitting the plots into groups with the same number of elements would overcome the unequal representations and hence maybe reduce artifact effects.

The plot reflectances already revealed that the shortwave infrared might be important for forest stand variables like mean dbh. For assessing that, vegetation indices can be a key approach in combining forest inventory data and remote sensing. Overall, the PRI showed promising results and is preferred to rather standard VI such as the NDVI. As leaf water content is one of the main drivers in SWIR reflectance, future analysis could focus on that spectral region incorporating water-related vegetation indices. A rather important issue is the estimation of aboveground biomass, which is recently often found in publications dealing with carbon sequestration and climate change mitigation analyses (Saatchi et al., 2011). Potential analyses could include species-specific allometric models to obtain detailed estimations.

Another method to be tested in the future might be ordination techniques (Feilhauer et al., 2011; Schmidtlein et al., 2007). They can be a helpful tool in describing species dissimilarities based on forest inventory plots. Similarity information could then be extended by plot-wise dimensional tree attributes such as height or diameter as well as stand characteristics like density or basal area. Moreover, site conditions and gradients are possibly to include.

The combination of forest inventories and airborne imaging spectroscopy offers a variety of possibilities of applications, not only for research but also for management purposes. However, this study showed that it is feasible, but not operational. Moreover, to cover bigger areas, hyperspectral spaceborne RS systems like the planned EnMAP are required. Apart from those technological developments, we should not lose the track of ground based forest inventories. While in Middle Europe the situation of a sustainable forest management might be different from many tropical and low-income countries, less than 40 % of low-income countries are covered by forest inventories (Sloan and Sayer, 2015). However, they are still a key method to gather information about global and regional forests. For a successful monitoring, not only researchers and decision makers, but also the local stakeholders (MacDicken et al., 2015) need to be involved.

6.6 APPENDIX

The codes for the tree species are not using the original Thuringian system, but they are rather based on the coding of the German federal state of Lower Saxony.

Table 6.5: List of tree species found within the study area and the used coding.

Code	Common name	Scientific name
110	Oak	*Quercus spec.*
112	Sessile oak	*Quercus petraea*
211	Beech	*Fagus sylvatica*
221	Hornbeam	*Carpinus betulus*
311	Ash	*Fraxinus excelsior*
321	Sycamore maple	*Acer pseudoplatanus*
322	Norway maple	*Acer platanoides*
323	Field maple	*Acer campestre*
330	Elm	*Ulmus spec.*
331	Wych elm/Scots elm	*Ulmus glabra*
340	Lime/Linden	*Tilia spec.*
341	Large-leaved linden	*Tilia platyphyllos*
342	Small-leaved linden	*Tilia cordata*
354	Wild cherry	*Prunus avium*
356	Wild pear	*Pyrus pyraster*
357	Wild service tree	*Sorbus torminalis*
410	Birch	*Betula spec.*
420	Alder	*Alnus spec.*
421	Red alder	*Alnus glutinosa*
422	Grey alder	*Alnus incana*
430	Poplar	*Populus spec.*
431	European aspen	*Populus treumula*
441	Willow	*Salix spec.*
511	Spruce	*Picea abies*
611	Douglas fir	*Pseudotsuga menziesii*
711	Scots pine	*Pinus sylvestris*
810	Larch	*Larix spec.*
811	European larch	*Larix decidua*
812	Japanese larch	*Larix kaempferi*

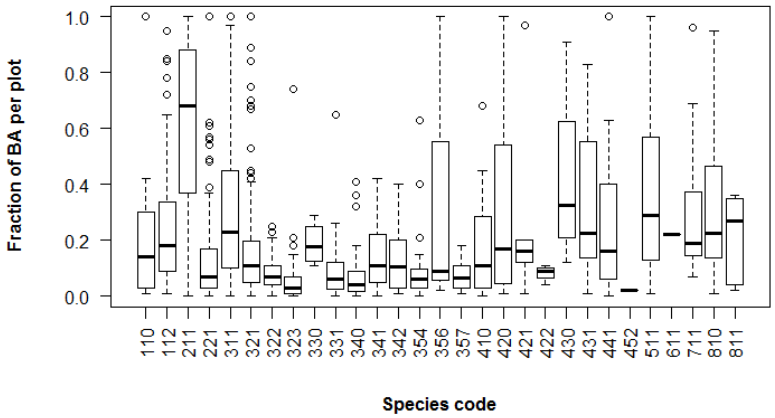

Figure 6.21: Proportions of species (groups) considering the basal area (BA) per plot.

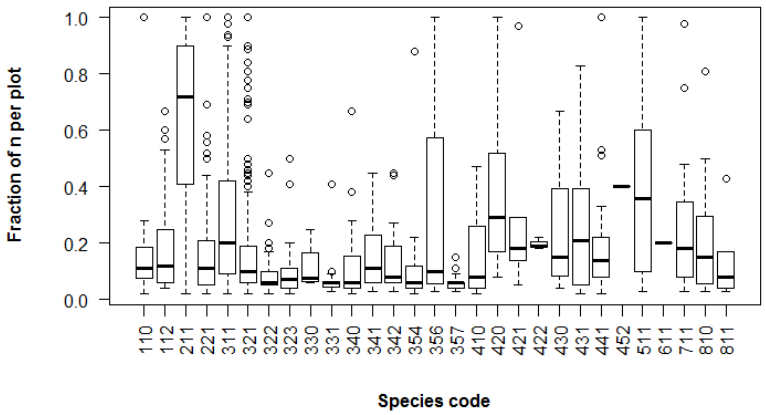

Figure 6.22: Proportions of species (groups) considering the number of trees per hectare (n) per plot

CHAPTER 7

SYNOPSIS

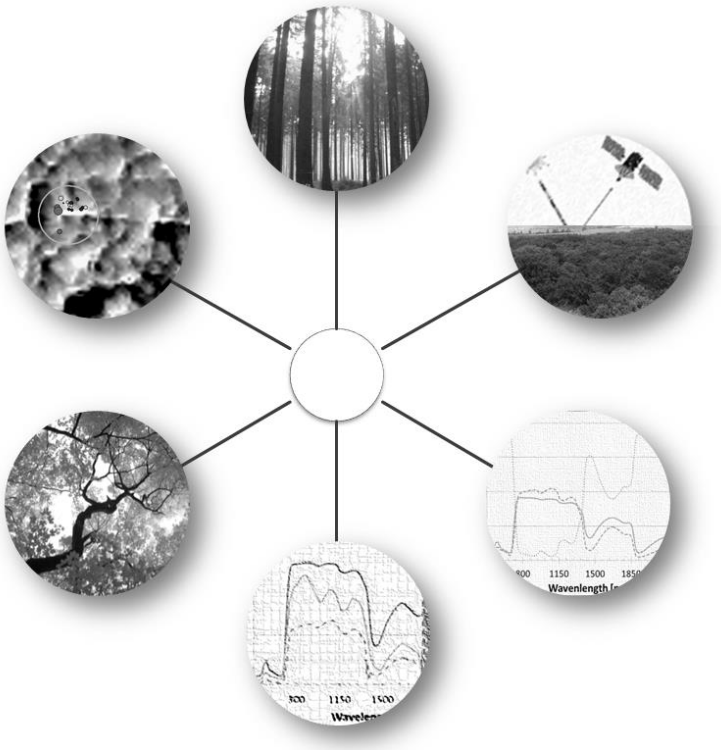

7 SYNTHESIS

7.1 INTRODUCTION

Collecting up-to-date information about our world is getting more and more important and valuable. This is not only valid for our daily life, but also counts for the commercial and non-commercial observation of land cover as basis for informed decisions in forest management and forest policy. Nowadays the monitoring of forests plays a key role within the context of climate change and carbon sequestration. The knowledge about the spatial extent of forested land and its status is essential for planning and conservation (Lui and Coomes, 2015; O'Connor et al., 2015; Turner et al., 2015). The utilization of remote sensing is one way of Earth observation from a distance. In recent years, there was a raise of awareness and accessibility of this imagery and the derived maps for the public due to faster distribution of information and the appearance of new technologies. Besides that, also scientific and non-civilian missions with improving platforms are increasing (Belward and Skøien, 2014). For monitoring purposes, there is another trend towards cheaper solutions incorporating armadas of micro- and nanosatellites. The most prominent systems having rather different intentions are from GOOGLE (Terra Bella, formerly Skybox) or PLANET LABS, which operate satellites with a size of about a shoebox.

However, it is essential for Earth observation to have a working and reliable system of both ground and remote data, and the incorporation of multiple scales within a multi-temporal monitoring has to be extended yet. By using mainly passive sensors, the amount and composition of reflected sunlight can give us detailed information about a material or vegetation on the surface. However, the acquisition of images alone is not enough. Comprehensive analyses require also in-situ information, which is often referred to as ground truth. This includes mapping of single trees or landscape composites as well as the derivation of biochemical variables or rather structure related information like the leaf area index. Many studies are conducted on minerals, agricultural crops or on other targets that are rather easy to reach (Arafat et al., 2013; Ramakrishnan et al., 2013; Schmidt and Skidmore, 2003). By contrast, the circumstances are quite different and more challenging when dealing with spectroscopy in forests. Information is composed of all parts such as soil, ground vegetation, bark and epiphytes, flowers and foliage. Each compartment causes changes in terms of reflection, absorption and transmission. Moreover, the three-dimensional structure of tree crowns is responsible for multiple scattering.

In this research study, several important aspects in field and remotely sensed spectroscopy of vegetation have been addressed. To understand the relationships and to emphasize differences, analyses were conducted on different levels from single leaves to crowns. The schematic graphic of overall study setup (Figure 7.1) illustrates the link of the concerned levels on a spatial scale. The

remote sensing of forests deals with the characterization of the most ex part, the visible canopy. On the second level, the leaves of deciduous trees are examined considering the spectral properties.

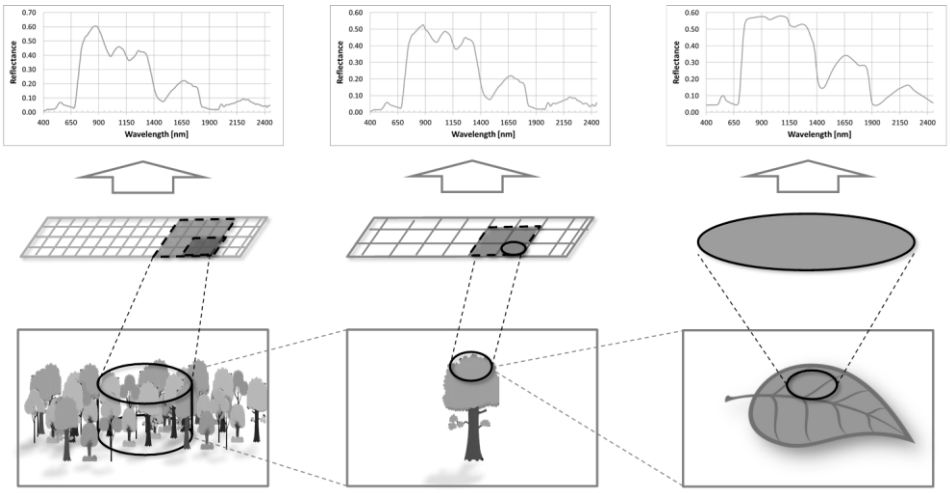

Figure 7.1: Sketch of the general study setup. From left to right: forest inventory plot as small stand level containing several trees, partial tree crown and single leaf.

Overall, this study incorporates a unique set of simultaneously recorded data but also multitemporal measurements. It is, to my knowledge, one of the very few research studies that are dealing with spectroscopy on Middle European deciduous broadleaved trees, and in an old-growth forest.

7.2 LEAF OPTICAL PROPERTIES

The most striking and exposed compartment of broadleaved crowns and canopies during the growing season is the green foliage. Information about this organ including the spectral appearance is crucial for health and development status. For that, using a field spectroradiometer is a powerful tool to obtain very detailed information about the spectral properties. In this basic research study, leaf optical properties of seven tree species representing the most relevant deciduous species in Middle European forestry are examined. The focus is on the determination of spectral reflectance curves; in addition, leaf transmittances and absorptances. It could be shown that the obtained spectral traits of the foliage depend mainly on three things: (i) the species (ii) the day of the year within a growing season and (iii) the number of stacked leaves during the measurement process. Moreover, the measurement device itself should be appropriate and might have an immense impact on the derived response pattern. The interspecific differences are not as distinct as on canopy level, and the variation of the spectral reflectances is less. Commonly, foliar reflectances base on measurements done on the upper, adaxial, side of leaves. However, for detailed analysis and future modelling, also the lower, abaxial, side could be considered. Including

both abaxial and adaxial reflectances can be important for species like ash (*Fraxinus excelsior*), that tend to show the lower sides of the leaves upwards already at little wind speeds (Figure 7.2). Knowledge about this kind of behavior needs to be checked for the species within a study site, what may improve analysis and interpretation.

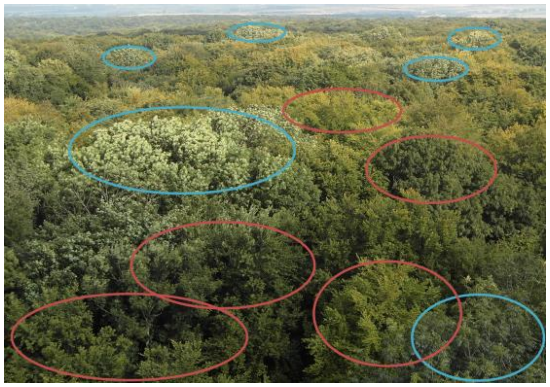

Figure 7.2: Characteristic appearances of tree crowns. Blue: ash (*Fraxinus excelsior*), red: beech (*Fagus sylvatica*). Own photograph taken from a climate tower in the Hainich forest in September 2012.

Finally, the seasonal phenology could be demonstrated well in this study by repeated measurements and the calculated vegetation indices. Comparing all VI, the NDVI slightly increases and CRI1 and ARI2 decrease over time, while PRI showed rather stable values. This matches with the relationship of daily production or carbon uptake and PRI for broadleaved forests (Gamon, 2015; Garbulsky et al., 2011). Overall, this study showed impressively the potential of detailed field spectroscopy in forestry. Future research should include additional measurements of leaf chemistry like chlorophyll, nitrogen or water content (Feilhauer et al., 2015).

7.3 SCALE DEPENDENCY OF SPECTRAL TRAITS

Scaling issues are apparent in nearly every study that is carried out using different levels of data acquisition. Examples can be found incorporating issues in temporal (Somers and Asner, 2013) and spatial scaling (Van Der Meer et al., 2001). For the utilization of flux tower approaches examining light use efficiency (LUE) and gross primary production (GPP), a correct scaling is essential for the understanding of the involved processes (Gamon, 2015). Another instance of the scaling issue give the deviating results for albedo-based nitrogen concentration on leaf and canopy level were observed by Bartlett et al. (2011). Up- and down-scaling of plant traits is still an ongoing and future topic. Functional substances such as chlorophyll and carotenoids are essential for most of the vascular plants. The concentration or content can give helpful information of the status and condition. Several absorption features of those pigments are detectable indirectly by optical sensors measuring the reflectance of vegetation. Since the features are often located at specific

wavelengths, narrowband analyses are required. Therefore, the use of hyperspectral sensors is predestinated for this task. In this study, the spectral reflectance properties of the most common broadleaved trees are examined on different levels. The first level takes the spatial scale into account, which is varying from small area on single leaves over crown parts. Here, interesting relations between the different levels were observed. With simple linear and logarithmic models leaf and RS data could be approximated. Overall, leaves reflect more than crown compartments. The second level is the temporal scale. Repeated measurements had been done during two growing seasons. This aspect is crucial for a detailed monitoring as well as for comparing results to other studies, which are conducted on varying dates. Reflectances covering the full range of 400-2500 nm were collected by field spectroradiometer and hyperspectral airborne imagery. The narrowband resolution allows the investigation of specific spectral features like the red edge position (REP). REP can be an indicator of chlorophyll content and photosynthetic performance. Two approaches of finding the REP are compared: using the maxima of second order derivatives (DV), and the calculation of the index REPI. The correlations between crown and leaf level REP are apparently higher when using REPI compared to DV (Figure 7.3). However, that does not imply that the index is per se preferable and more correct than the derivative value. The main question stays, which REP can be seen as "true". Here, the derivative could be considered as more reliable, as it is derived directly from the response curves and not calculated by formulas basing on certain assumptions.

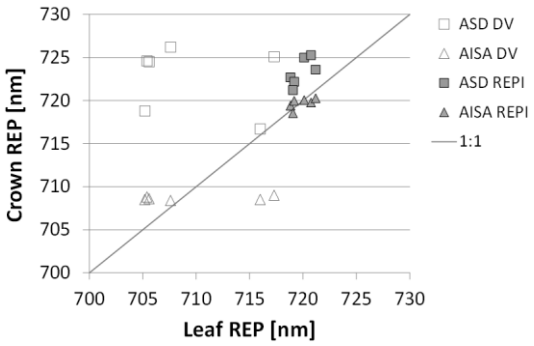

Figure 7.3: Comparisons of red edge positions (REP) as derived at crown and leaf level from derivatives (DV) and red edge position index (REPI) by ASD spectroradiometer and AISA EAGLE, respectively.

7.4 CANOPY LIGHT INTERCEPTION

The description of canopy structure and crown porosity for light interception and attenuation is an important issue for forest characteristics. The amount of intercepted PAR is linked to crown porousness and a specific extinction coefficient and can be used as an indicator for photosynthetic activity and productivity. Hence, detailed information about the absorption of sunlight within forest canopies is helpful in understanding the processes of growth and production. One variable

that is often used to characterize the canopy density and structure is the leaf area index (LAI). LAI cannot be measured with non-destructive methods, even though many authors are using this terminology. This is not only misleading but also even wrong and should be avoided. For sure, someone might call the readings of devices, such as the commonly used LAI-2000 (LICOR), measurements, but researchers should be aware of the fact that this variable is not measurable and often approximately estimated by the plant area index (PAI). However, what is derived at the most, should actually rather be seen as a proxy or index that is somehow related to the porousness of a canopy and the three-dimensional distribution of plant compartments. The main problems arise due to clumping effects. They appear in two different ways: (i) within a crown by obscured branches and leaves and (ii) within a forest stand by the arrangement of the trees and the distances in-between. Depending on the spatial collocation of the trees, the light attenuation within a forest stand can be completely different while the LAI stays the same (Binkley et al., 2013). This becomes clear when we imagine a site with a certain number of trees and a certain leaf area. By arranging them in groups, the light interception is lower in other locations than if distributed equally.

In this study, several remotely sensed broad- and narrowband vegetation indices were calculated and opposed to ground measurements including digital cover photographs (DCP) and digital hemispherical photographs (DHP). Furthermore, spectral irradiances were acquired below canopy. Field and remote values were averaged for core plots of a size of 25x25 m. As a result, it could be shown that most variables have weak linear correlations. The highest correlation is observed between DHP and Photochemical Reflectance Index (PRI) which is a promising outcome of this study. However, scatterplots of the variables indicate that non-linear approaches might be better solutions for some cases. This should be analyzed in further studies. The use of the PRI and its interpretation for LUE-related statements is an ongoing research issue (Garbulsky et al., 2011). However, the short- and long-time changes in PRI values (Soudani et al., 2014; Wong and Gamon, 2015) reveal the importance of a multi-temporal monitoring. The solar irradiance is also time-dependent. This counts for the amount and especially for the spatial allocation below a forest canopy. During a day, the radiation reaching the ground changes according to the course of the sun. Due to varying sun angles and gaps in the crowns, the diurnal radiation distribution is unlikely locally stable. As a consequent, repeated measurements are suggested to cover these variations.

Figure 7.4: Forest floor within the core area. Left: Although most of the ground is shaded rather homogeneously, several sun flecks with much higher insolation are apparent. Middle, right: effects of clouds within few minutes.

7.5 FOREST INVENTORY APPLICATIONS

This chapter addresses the applications of hyperspectral remote sensing for forest inventories and the occurring challenges coming along. One question many researchers are facing is how to extract RS data based on inventory plots. For that, a spatially correct alignment of both imagery and field data is required. Depending on the pixel size and location, a varying number of pixels will be considered for each plot. In this study, an approach is proposed to extract raster data values by a convex hull spanning modelled tree crowns. Since the number of plots is consisting of only one species is extremely small in relation to the overall number, the focus was not on species recognition. Moreover, the mainly considered variables are rather related to the stand structure: basal area [m^2/ha], stand density [trees/ha], mean tree dbh [cm] and height [m]. The latter two were split into groups. Additionally to the spectral reflectances, narrowband vegetation indices were calculated and opposed to the derived stand variables. There was none correlation between estimated basal area and any of the spectral variables. Similarly, no high linear correlation were found among all other variables. However, the highest (moderate) correlation could be observed between PRI and the plot values of dbh class, height and density. Once more, the calculation of hyperspectral VI allow a detailed way to assess the relations of forest stand characteristics and the spectral appearance, what might be an alternative approach to predict forest variables.

7.6 ADDITIONAL RESEARCH AND TESTS

7.6.1 Derivative images

Just as the spectral derivatives calculated for in-situ reflectances and some pixel values in chapter 5, any derivatives can also be obtained for whole hyperspectral images. According to the author's knowledge this function is not included by default in standard software like ENVI. Hence, a first derivative image was calculated by an own function using *R*. As it is a rather computationally intensive operation using a huge amount of RAM, it could only be applied for the small core area.

However, it is likely that there are potentials on tree species identification. Especially the discrimination of the main species ash and beech seems to be promising (Figure 7.5). Detection of ash trees are important for monitoring applications against the background of the nowadays increasing problem of the ash decline within Europe and North America (Pautasso et al., 2013; Waser et al., 2014).

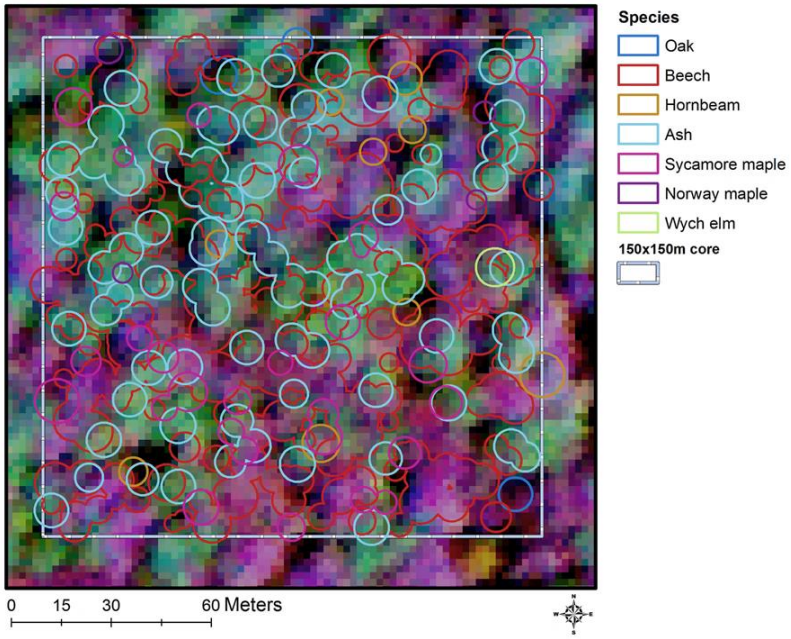

Figure 7.5: Spectral derivative image of the core area, RGB: bands 285-233-58. Overlaid modelled tree crowns are dissolved for better visibility.

7.6.2 Further vegetation indices

Another promising approach is the utilization of narrowband VI, which has been addressed often in this study. Figure 7.6 shows potential application for species detection.

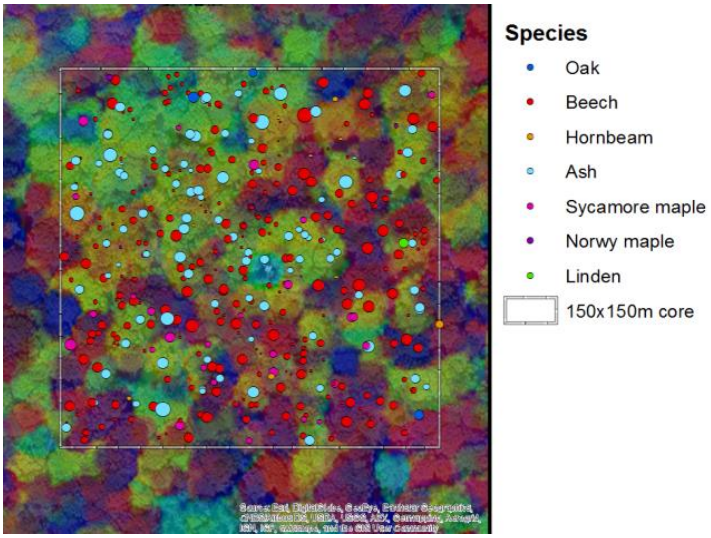

Figure 7.6: Transparent composite of the vegetation indices SR, PRI, SIPI with the sampled trees within the core area. Plot sizes are according to the tree dbh.

In this study, one focus was on some selected vegetation indices. However, there are plenty of other narrowband VI that could also be possibly investigated. Water related VI like Water Band Index (WBI), Normalized Difference Water Index (NDWI), Moisture Stress Index (MSI) and Normalized Difference Infrared Index (NDII) show in a rough test quite promising correlations with plot values derived from inventory data (Figure 7.7).

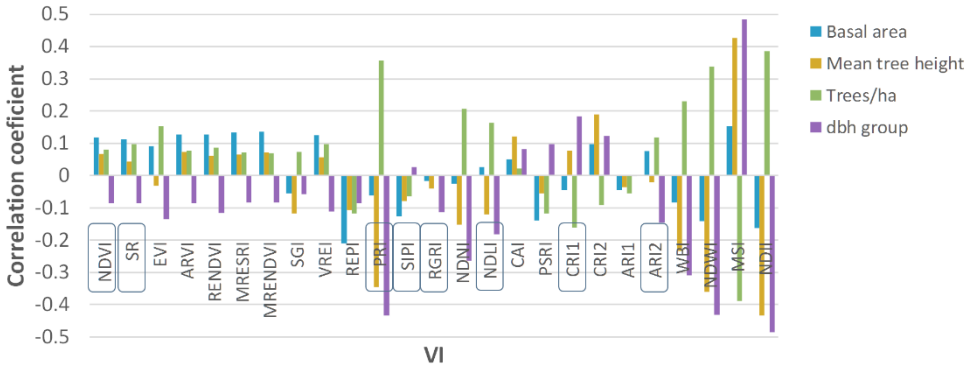

Figure 7.7: Pearson's correlation coefficients (Spearman's correlation coefficients for dbh group) of plot-wise median VI and stand attributes as derived over all inventory plots.

7.6.3 Forest stand modelling

In denser forest stands, also difficulties can emerge in the general definition of canopies and crowns. Although there is not much understory present inside the core area, there are still lower branches and leaved twigs existent that influence the radiation system. Especially the shadow tolerant beech trees show this, by what a determination of the crown basis can be challenging for field teams. Often there is no clear rule for marking vertical layers or strata within a forest (Bongers, 2001; Parker and Brown, 2000). Another definition of a canopy, which says it is the leaf-bearing part of woody plants including branches and the leaves (Sadava et al., 2011), would make it even more complicated.

For a comprehensive three-dimensional simulation of forest stands the utilization of radiative transfer models are designated. As a drawback, researchers need keen background knowledge about the radiative physics. One example of widely used models is the DART (Discrete Anisotropic Radiative Transfer) model (Gastellu-Etchegorry et al., 2004), which allows detailed three-dimensional analyses. For test purposes we imported the surveyed trees of the core area of 150x150 m into DART conform format. Further input data are the spectral properties derived from the sampled leaves and forest floor spectra. Though running the model with rather high spatial resolution is quite computational, first attempts are promising (Figure 7.8).

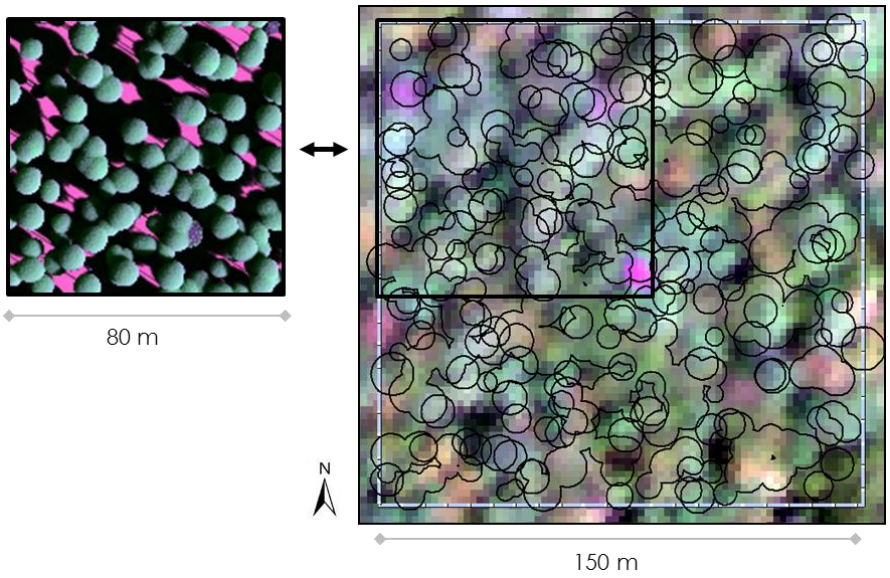

Figure 7.8: Left: Color infrared sub-scene of the core area at the climate tower, modelled with the DART model. Right: corresponding AISA EAGLE/HAWK image with overlaid modelled tree crowns based on diameters, dissolved for display. RGB: 594, 832, 480 nm.

The model permits the simulation of the following aspects:

- modelling of full hyperspectral remotely sensed scenes
- individual scenes with specific topographic and geographical properties
- simulation of sensors such as the used AISA EAGLE/HAWK or EnMAP
- viewing and sun angle for precise date

Input parameters can be varied and the model outputs can be compared with prior study results and look up tables. Spatial up- and down-scaling of radiative variables could further be implemented in spectral unmixing approaches.

7.7 CONCLUDING REMARKS

Nowadays the monitoring of forests is important more than ever, facing economic and ecological issues. Even small disturbances can influence the carbon stocks (Seidl et al., 2014), which is not only an issue for tropical rainforests but also for European forests (Lindner et al., 2010). Besides the threat of biodiversity due to the loss of species we are coping also economic loss (Hanewinkel et al., 2012). Some issues revealed by this study are common problems and can be transferred to most of the cases where we try to combine plot data, containing local in-situ information, with remote sensing data containing information covering a much larger area.

The combination of flux tower information about the carbon uptake and remote sensing approaches, which used to be separate disciplines, can be an important key for the understanding of terrestrial ecosystem processes (Gamon, 2015). Generally, a meaningful translation between the

different scales is essential in Earth observation using integrated remote sensing and ground data. Hence, the solution of up- and down-scaling issues is crucial. This can involve the link between leaves and canopies, the utilization of coarse and fine imaging and non-imaging products, or multitemporal readings. It should be noticed that in the case of forests and forested landscapes, remote sensing systems with very high spatial resolutions of some centimeters are occasionally misleading and often not appropriate to the stated problem of mapping. Moreover, the spectral resolution and spectral sampling should be examined more in the future in order to reduce the data volume and achieve operationalization. The calculation of meaningful vegetation indices, which are adapted to the specific target variables and selected spectral features, can be key approaches.

The present study site is characterized by highly mixed stand with dominant beech (*Fagus sylvatica*). Hence, the number of inventory plot with only one occurring tree species is very low. That makes a species wise analysis based on pure plots difficult or even impossible. Consequently, single-tree based analyses on small areas would be the next step. However, this would necessitate accurately referenced data and exact tree recognition. By nature, broadleaved trees are not growing as straight as spruces and firs, e.g., and the tree bases mapped in the field are often not directly underneath the crown top. It was observed that there are in some extent big discrepancies between the tree positions and the visible crowns in the remote sensing imagery. The reasons behind that can be manifold. Most likely an inaccurate application of a digital terrain model for an ortho-rectification or the use of mismatching imagery as the basis for georeferencing

The combination of data Lidar data and hyperspectral imagery (Anderson et al., 2008; Buddenbaum et al., 2013) or even future applications of hyperspectral laser technology (Hakala et al., 2012; Nevalainen et al., 2013) can provide advanced and new improvements in precise remote sensing. In contrast to multispectral data hyperspectral data is often coping the Hughes phenomenon (Hughes, 1968; Pal and Foody, 2010; Richards, 2013), which says an increasing number of features can lead to a decreasing classification accuracy. In the case of hyperspectral data, the high number of narrow and redundant bands might worsen the situation. So, incorporating more and more information, is not always the best choice and could even lower the accuracy (Onojeghuo and Blackburn, 2011).

The integration of optical measurements and carbon fluxes is still an open issue and needed for a better understanding of plant productivity and the efficiency of sunlight use (Peñuelas et al., 2013). This again includes the meaningful application of narrowband vegetation indices as we can derive from hyperspectral sensors. Since many studies deal with single sites and few species, one aim must be the comparability and intercomparison between different types of biomes and landscapes. Especially deciduous broadleaved forests are complex and highly dynamic ecosystems. This variety can be found in the spectral behavior of crowns and canopies (D'Odorico et al., 2015; Nilson et al.,

2012). In a review article (Ollinger, 2011) about the variability of tree canopies the author concludes that reflectances in the spectral region of NIR are often not easy to interpret. Multiple factors and their combination such as leaf area index (LAI) and leaf angle distribution (LAD) or leaf water and dry matter can lead to similar results.

Besides the role in LUE, photosynthetic activity and production still not all relationships are understood and not all potential applications of VI like the PRI are discovered. One key point could be in the remotely sensed monitoring of forests' emissions of volatile organic compounds (VOC) such as isoprenoids, which have an impact on the content of greenhouse gases, pollutants and secondary organic aerosols in the atmosphere (Grote, 2010; Kefauver et al., 2015; Peñuelas et al., 2013). Hence, within the framework of climate change analyses, we need knowledge of the involved processes. In this context, the link between phenology, GPP and remotely sensed vegetation indices still needs to be fully explored. Additionally, the in-situ crown data of this study reveal another possible application of non-imaging spectroradiometers. The presence of sun-induced fluorescence peaks around 760 nm show the potential of very high-resolution devices. This might lead to a better monitoring of photosynthesis rates and plant status (Meroni et al., 2009; Yang et al., 2015).

A combination of varying leaf or canopy traits such as leaf area, leaf angle or water and nitrogen content can lead to similar optical properties. Especially in radiative transfer and inverse modelling there we face these ill-posed problems (Atzberger, 2004; Combal et al., 2002). However, even today, after a rather long period of consistent technological development and enhancements of measurement devices, spectral analysis of leaf optical properties and in-situ objects covering the full-range of 400-2500 nm is still cumbersome. The elaborative field work and post-processing, the high costs for labor and equipment are the main issues that still hamper the overall progress (cf Bauerle et al., 2004). Nonetheless, in future it will be more important than ever to strengthen the link between ground-based research and information with the remotely sensed derived products (Skidmore et al., 2015).

There is still a lot of work to do when it comes to species differentiation and the observation of biodiversity and species composition. Many studies deal with only a few species and with their distinction incorporating various techniques (Ghiyamat and Shafri, 2010). However, it is barely possible to identify species only depending on a given spectrum but rather by direct comparison. Hence, spectral libraries of the tree species are needed including several development stages and sites. Sharing this information might be an asset to future analyses. Up to date, there is a lack of meaningful and especially operational hyperspectral satellite systems – also of ground reference data for validation. Existing satellites with a very high spectral resolution are still rather understood as technology demonstration missions. Nonetheless, hyperspectral remote sensing is surely about to play a key role in local and global monitoring. The Convention on Biological

Diversity includes remote sensing and the utilization of hyperspectral sensors as a measure within its defined Aichi Biodiversity Targets (O'Connor et al., 2015; Secades et al., 2014). Although the technology is not brand-new anymore and could show their potential in several studies giving new insights, the establishment of hyperspectral sensors is yet to come. The near future will show if there will be a successful integration of sensors covering different sites, biomes and research disciplines. One important step could be done with the upcoming EnMAP mission. Finally, as Secades et al. (2014) already pointed rightly, a constructive dialogue between policy makers, data providers and the Earth observation community is still needed for a serious collaboration and functional interactions coming along with mutual benefits.

REFERENCES

Aberle, H., 2014. Hyperspectral data for forest inventories, in: Kleinn, C., Kleinn, A., Fehrmann, L. (Eds.), 4th International DAAD Workshop - The Ecological and Economic Challenges of Managing Forested Landscapes in a Global Context. Cuvillier Verlag, Göttingen, pp. 145–155.

Agapiou, A., Hadjimitsis, D.G., Alexakis, D.D., 2012. Evaluation of broadband and narrowband vegetation indices for the identification of archaeological crop marks. Remote Sens. 4, 3892–3919. doi:10.3390/rs4123892

Anderson, J.E., Plourde, L.C., Martin, M.E., Braswell, B.H., Smith, M.L., Dubayah, R.O., Hofton, M. a., Blair, J.B., 2008. Integrating waveform lidar with hyperspectral imagery for inventory of a northern temperate forest. Remote Sens. Environ. 112, 1856–1870. doi:10.1016/j.rse.2007.09.009

Anderson, M.C., Norman, J.M., Meyers, T.P., Diak, G.R., 2000. An analytical model for estimating canopy transpiration and carbon assimilation uxes based on canopy light-use efficiency. Agric. For. Meteorol. 101, 265–289. doi:10.1016/S0168-1923(99)00170-7

Anthoni, P.M., Knohl, A., Rebmann, C., Freibauer, A., Mund, M., Ziegler, W., Kolle, O., Schulze, E.D., 2004. Forest and agricultural land-use-dependent CO2 exchange in Thuringia, Germany. Glob. Chang. Biol. 10, 2005–2019. doi:10.1111/j.1365-2486.2004.00863.x

Arafat, S.M., Aboelghar, M.A., Ahmed, E.F., 2013. Crop discrimination using field hyper spectral remotely sensed data. Adv. Remote Sens. 2, 63–70. doi:10.4236/ars.2013.22009

ASDI, 2012. Resource center [WWW Document]. URL asdi.com (accessed 4.29.15).

ASDI, 2008. ViewSpecPro.

Asner, G.P., 2014. Satellites and psychology for improved forest monitoring. Proc. Natl. Acad. Sci. U. S. A. 111, 567–8. doi:10.1073/pnas.1322557111

Atzberger, C., 2004. Object-based retrieval of biophysical canopy variables using artificial neural nets and radiative transfer models. Remote Sens. Environ. 93, 53–67. doi:10.1016/j.rse.2004.06.016

Aubin, I., Beaudet, M., Messier, C., 2000. Light extinction coefficients specific to the understory vegetation of the southern boreal forest, Quebec. Can. J. For. Res. 30, 168–177. doi:10.1139/x99-185

Baccini, A., Goetz, S.J., Walker, W.S., Laporte, N.T., Sun, M., Sulla-Menashe, D., Hackler, J., Beck, P.S.A., Dubayah, R., Friedl, M.A., Samanta, S., Houghton, R.A., 2012. Estimated carbon dioxide emissions from tropical deforestation improved by carbon-density maps. Nat. Clim. Chang. 2, 182–185. doi:10.1038/nclimate1354

Bannari, A., Morin, D., Bonn, F., Huete, A.R., 1995. A review of vegetation indices. Remote Sens. Rev. 13, 95–120. doi:10.1080/02757259509532298

Baranoski, G.V.G., Rokne, J.G., 2005. A practical approach for estimating the red edge position of plant leaf reflectance. Int. J. Remote Sens. 26, 503–521. doi:10.1080/01431160512331314029

Barbier, N., Couteron, P., Gastelly-Etchegorry, J.P., Proisy, C., 2012. Linking canopy images to forest structural parameters: Potential of a modeling framework. Ann. For. Sci. 69, 305–311. doi:10.1007/s13595-011-0116-9

Bartlett, M.K., Ollinger, S. V., Hollinger, D.Y., Wicklein, H.F., Richardson, A.D., 2011. Canopy-scale relationships between foliar nitrogen and albedo are not observed in leaf reflectance and transmittance within temperate deciduous tree species. Botany 89, 491–497. doi:10.1139/b11-037

Barton, C.V.M., North, P.R.J., 2001. Remote sensing of canopy light use efficiency using the photochemical reflectance index model and sensitivity analysis. Remote Sens. Environ. 78, 264–273. doi:10.1016/S0034-4257(01)00224-3

Baty, L., Christian Ritz, Charles, S., Brutsche, M., Flandrois, J.-P., Delignette-Muller, M.-L., 2015. A Toolbox for Nonlinear Regression in R: The Package nlstools. J. Stat. Softw. 66.

Bauerle, W.L., Oren, R., Way, D.A., Qian, S.S., Stoy, P.C., Thornton, P.E., Bowden, J.D., Hoffman, F.M., Reynolds, R.F., 2012. Photoperiodic regulation of the seasonal pattern of photosynthetic capacity and the implications for carbon cycling. Proc. Natl. Acad. Sci. 109, 8612–8617. doi:10.1073/pnas.1119131109

Bauerle, W.L., Weston, D.J., Bowden, J.D., Dudley, J.B., Toler, J.E., 2004. Leaf absorptance of photosynthetically active radiation in relation to chlorophyll meter estimates among woody plant species. Sci. Hortic. (Amsterdam). 101, 169–178.

Baumann, P.R., 2014. History of remote sensing, aerial photography [WWW Document]. URL http://www.oneonta.edu/faculty/baumanpr/geosat2/RS History I/RS-History-Part-1.htm (accessed 6.20.15).

Beck, R., 2003. EO-1 User Guide v. 2.3 74.

Beckschäfer, P., Fehrmann, L., Harrison, R.D., Xu, J., Kleinn, C., 2014. Mapping leaf area index in subtropical upland ecosystems using rapideye imagery and the randomforest algorithm. IForest 7, 1–11. doi:10.3832/ifor0968-006

Beckschäfer, P., Seidel, D., Kleinn, C., Xu, J., 2013. On the exposure of hemispherical photographs in forests. IForest 6, 228–237. doi:10.3832/ifor0957-006

Belward, A.S., Skøien, J.O., 2014. Who launched what, when and why; trends in global land-cover observation capacity from civilian earth observation satellites. ISPRS J. Photogramm. Remote Sens. 103, 115–128. doi:10.1016/j.isprsjprs.2014.03.009

Binkley, D., Campoe, O.C., Gspaltl, M., Forrester, D.I., 2013. Light absorption and use efficiency in forests: Why patterns differ for trees and stands. For. Ecol. Manage. 288, 5–13. doi:10.1016/j.foreco.2011.11.002

Black, T.A., Chen, J.-M., Lee, X., Sagar, R.M., 1991. Characteristics of shortwave and longwave irradiances under a Douglas-fir forest stand. Can. J. For. Res. 21, 1020–1028. doi:10.1139/x91-140

Blackburn, G.A., Ferwerda, J.G., 2008. Retrieval of chlorophyll concentration from leaf reflectance spectra using wavelet analysis. Remote Sens. Environ. 112, 1614–1632. doi:10.1016/j.rse.2007.08.005

BMEL, 2015. The Forests in Germany. Selected Results of the Third National Forest Inventory. Federal Ministry of Food and Agriculture, Bonn.

Boch, S., Prati, D., Müller, J., Socher, S., Baumbach, H., Buscot, F., Gockel, S., Hemp, A., Hessenmöller, D., Kalko, E.K. V, Linsenmair, K.E., Pfeiffer, S., Pommer, U., Schöning, I., Schulze, E.D., Seilwinder, C., Weisser, W.W., Wells, K., Fischer, M., 2013. High plant species richness indicates management-related disturbances rather than the conservation status of forests. Basic Appl. Ecol. 14, 496–505. doi:10.1016/j.baae.2013.06.001

Bohn., U., Gollub., G., Hettwer, C., Neuhäuslova, Z., Raus, T., Schlüter, H., Weber., H., 2004. Map of the Natural Vegetation of Europe.

Bolduc, E., Leach, J., Miatto, F., 2014. A“ fair sampling” perspective on an apparent violation of duality. arXiv Prepr. arXiv … 111, 1–10. doi:10.1073/pnas.1400106111

Bonan, G.B., 2008. Forests and climate change: forcings, feedbacks, and the climate benefits of forests. Science 320, 1444–1449. doi:10.1126/science.1155121

Bongers, F., 2001. Methods to assess tropical rain forest canopy structure: an overview. Plant Ecol. 153, 263–277.

Botta, A., Viovy, N., Ciais, P., Friedlingstein, P., Monfray, P., 2000. A global prognostic scheme of vegetation growth onset using satellite data. Glob. Chang. Biol. 6, 709–725.

Boyd, D.S., Danson, F.M., 2005. Satellite remote sensing of forest resources: three decades of research development. Prog. Phys. Geogr. 29, 1–26. doi:10.1191/0309133305pp432ra

Brantley, S.T., Zinnert, J.C., Young, D.R., 2011. Application of hyperspectral vegetation indices to detect variations in high leaf area index temperate shrub thicket canopies. Remote Sens. Environ. 115, 514–523. doi:10.1016/j.rse.2010.09.020

Bréda, N.J.J., 2003. Ground-based measurements of leaf area index: A review of methods, instruments and current controversies. J. Exp. Bot. 54, 2403–2417. doi:10.1093/jxb/erg263

Breuer, L., Eckhardt, K., Frede, H.G., 2003. Plant parameter values for models in temperate climates. Ecol. Modell. 169, 237–293. doi:10.1016/S0304-3800(03)00274-6

Buddenbaum, H., Seeling, S., Hill, J., 2013. Fusion of full-waveform lidar and imaging spectroscopy remote sensing data for the characterization of forest stands. Int. J. Remote Sens. 34, 4511–4524.

doi:10.1080/01431161.2013.776721

Burger, J., Gowen, A., 2011. Data handling in hyperspectral image analysis. Chemom. Intell. Lab. Syst. 108, 13–22. doi:10.1016/j.chemolab.2011.04.001

Buschmann, C., Nagel, E., Szabó, K., Kocsányi, L., 1994. Spectrometer for fast measurements of in vivo reflectance, absorptance, and fluorescence in the visible and near-infrared. Remote Sens. Environ. 48, 18–24. doi:10.1016/0034-4257(94)90110-4

Campbell, J.B., 2006. Introduction to Remote Sensing, 4th ed. Taylor & Francis, London; New York.

Canham, C.D., Finzi., A.C., Pacala., S.W., Burbank., D.H., 1993. Causes and consequences of resource heterogeneity in forests: interspecific variation in light transmission by canopy trees. Can. J. For. Res. 24, 337–349.

Carter, G.A., Knapp, A.K., 2001. Leaf optical properties in higher plants: linking spectral characteristics to stress and chlorophyll concentration. Am. J. Bot. 88, 677–684. doi:10.2307/2657068

Castro-Esau, K.L., Sánchez-Azofeifa, G.A., Rivard, B., Wright, S.J., Quesada, M., 2006. Variability in leaf optical properties of mesoamerican trees and the potential for species classification. Am. J. Bot. 93, 517–530. doi:10.3732/ajb.93.4.517

Ceccato, P., Flasse, S., Tarantola, S., Jacquemoud, S., Grégoire, J.M., 2001. Detecting vegetation leaf water content using reflectance in the optical domain. Remote Sens. Environ. 77, 22–33. doi:10.1016/S0034-4257(01)00191-2

Chang, C.-I., 2013. Hyperspectral data processing. John Wiley & Sons, Inc., Hoboken, NJ. doi:10.1002/9781118269787

Chao, S., 2012. FOREST PEOPLES: Numbers across the world, Forest People Programme. 1c Fosseway Business Centre, Moreton-in-Marsh, UK.

Cho, M.A., Skidmore, A.K., 2006. A new technique for extracting the red edge position from hyperspectral data: The linear extrapolation method. Remote Sens. Environ. 101, 181–193. doi:10.1016/j.rse.2005.12.011

Cho, M.A., Skidmore, A.K., Atzberger, C., 2008a. Towards red edge positions less sensitive to canopy biophysical parameters for leaf chlorophyll estimation using properties optique spectrales des feuilles (PROSPECT) and scattering by arbitrarily inclined leaves (SAILH) simulated data. Int. J. Remote Sens. 29, 2241–2255. doi:10.1080/01431160701395328

Cho, M.A., Sobhan, I., Skidmore, A.K., Leeuwb, J. De, 2008b. Discriminating Species Using Hyperspectral Indices At Leaf and Canopy Scales. Remote Sens. Spat. Inf. Sci. XXXVII, 369–376.

Cilia, C., Panigada, C., Rossini, M., Candiani, G., Pepe, M., Colombo, R., 2015. Mapping of Asbestos Cement Roofs and Their Weathering Status Using Hyperspectral Aerial Images. ISPRS Int. J. Geo-Information 4, 928–941. doi:10.3390/ijgi4020928

Clark, J.B., Lister, G.R., 1975. Photosynthetic Action Spectra of Trees. Plant Physiol. 55, 407–413.

Clark, M.L., Roberts, D.A., 2012. Species-level differences in hyperspectral metrics among tropical rainforest trees as determined by a tree-based classifier. Remote Sens. 4, 1820–1855. doi:10.3390/rs4061820

Clark, M.L., Roberts, D.A., Clark, D.B., 2005. Hyperspectral discrimination of tropical rain forest tree species at leaf to crown scales. Remote Sens. Environ. 96, 375–398. doi:10.1016/j.rse.2005.03.009

Cole, B., McMorrow, J., Evans, M., 2014. Spectral monitoring of moorland plant phenology to identify a temporal window for hyperspectral remote sensing of peatland. ISPRS J. Photogramm. Remote Sens. 90, 49–58. doi:10.1016/j.isprsjprs.2014.01.010

Colombo, R., Meroni, M., Marchesi, A., Busetto, L., Rossini, M., Giardino, C., Panigada, C., 2008. Estimation of leaf and canopy water content in poplar plantations by means of hyperspectral indices and inverse modeling. Remote Sens. Environ. 112, 1820–1834. doi:10.1016/j.rse.2007.09.005

Combal, B., Baret, F., Weiss, M., Trubuil, A., Macé, D., Pragn??re, A., Myneni, R., Knyazikhin, Y., Wang, L., 2002. Retrieval of canopy biophysical variables from bidirectional reflectance using prior information to solve the ill-posed inverse problem. Remote Sens. Environ. 84, 1–15. doi:10.1016/S0034-4257(02)00035-4

Cordón, G.B., Lagorio, M.G., 2007. Optical properties of the adaxial and abaxial faces of leaves. Chlorophyll fluorescence, absorption and scattering coefficients. Photochem. Photobiol. Sci. Off. J. Eur. Photochem. Assoc. Eur. Soc. Photobiol. 6, 873–882. doi:10.1039/b617685b

Crouvi, O., Ben-Dor, E., Beyth, M., Avigad, D., Amit, R., 2006. Quantitative mapping of arid alluvial fan surfaces using field spectrometer and hyperspectral remote sensing. Remote Sens. Environ. 104, 103–117. doi:10.1016/j.rse.2006.05.004

CSTR, 2005. SAMS - Spectral Analysis and Management System.

Cundill, S., van der Werff, H., van der Meijde, M., 2015. Adjusting Spectral Indices for Spectral Response Function Differences of Very High Spatial Resolution Sensors Simulated from Field Spectra. Sensors 15, 6221–6240. doi:10.3390/s150306221

Curran, P.J., 1989. Remote sensing of foliar chemistry. Remote Sens. Environ. 278, 271–278. doi:10.1016/0034-4257(89)90069-2

Curran, P.J., Windham, W.R., Gholz, H.L., 1995. Exploring the Relationship Between Reflectance Red Edge and Chlorophyll Content in Slash Pine Leaves. Tree Physiol. 3, 203–206. doi:10.1093/treephys/7.1-2-3-4.33

D'Odorico, P., Gonsamo, A., Gough, C.M., Bohrer, G., Morison, J., Wilkinson, M., Hanson, P.J., Gianelle, D., Fuentes, J.D., Buchmann, N., 2015. The match and mismatch between photosynthesis and land surface phenology of deciduous forests. Agric. For. Meteorol. 214–215, 25–38. doi:10.1016/j.agrformet.2015.07.005

D'Odorico, P., Gonsamo, A., Pinty, B., Gobron, N., Coops, N., Mendez, E., Schaepman, M.E., 2014. Intercomparison of fraction of absorbed photosynthetically active radiation products derived from satellite data over Europe. Remote Sens. Environ. 142, 141–154. doi:10.1016/j.rse.2013.12.005

Dalponte, M., Ørka, H.O., Gobakken, T., Gianelle, D., Næsset, E., 2013. Tree species classification in boreal forests with hyperspectral data. IEEE Trans. Geosci. Remote Sens. 51, 2632–2645. doi:10.1109/TGRS.2012.2216272

Das, S., Singh, T.P., 2012. Correlation analysis between biomass and spectral vegetation indices of forest ecosystem. Int. J. Eng. Res. Technol. 1, 1–13.

Daughtry, C.S.T., Ranson, K.J., 1986. Measuring and modeling biophysical and optical properties of diverse vegetative canopies, LARS Technical Reports 41. West Lafayette, Indiana.

Dawson, T.P., Curran, P., 1998. A new technique for interpolating the reflectance red edge position 19, 2133–2139. doi:10.1080/014311698214910

Dawson, T.P., Curran, P.J., North, P.R.J., Plummer, S.E., 1999. The propagation of foliar biochemical absorbtion features in forest canopy reflectance: a theoretical analysis. Remote Sens. Envirnonment 67, 147–159.

De Castro, F., 2000. Light spectral composition in a tropical forest: measurements and model. Tree Physiol. 20, 49–56. doi:10.1093/treephys/20.1.49

Demetriades-Shah, T.H., Steven, M.D., Clark, J.A., 1990. High resolution derivative spectra in remote sensing 64, 55–64. doi:10.1016/0034-4257(90)90055-Q

Dillen, S.Y., de Beeck, M.O., Hufkens, K., Buonanduci, M., Phillips, N.G., 2012. Seasonal patterns of foliar reflectance in relation to photosynthetic capacity and color index in two co-occurring tree species, Quercus rubra and Betula papyrifera. Agric. For. Meteorol. 160, 60–68. doi:10.1016/j.agrformet.2012.03.001

EC, 2015. Copernicus - Europe's eyes on Earth [WWW Document]. Eur. Comm. URL copernicus.eu (accessed 6.2.15).

EEA, 2012. Corine Land Cover 2006.

Eklundh, L., Jin, H., Schubert, P., Guzinski, R., Heliasz, M., 2011. An optical sensor network for vegetation phenology monitoring and satellite data calibration. Sensors 11, 7678–7709. doi:10.3390/s110807678

Ellenberg, H., Leuschner, C., 2010. Vegetation Mitteleuropas mit den Alpen, 6th ed. Ulmer, Stuttgart.

Endler, J.A., 1993. The Color of Light in Forests and Its Implications. Ecol. Monogr. - Ecol. Soceity Am. 63, 1–27.

Eriksson, H.M., Eklundh, L., Kuusk, A., Nilson, T., 2006. Impact of understory vegetation on forest canopy reflectance and remotely sensed LAI estimates. Remote Sens. Environ. 103, 408–418. doi:10.1016/j.rse.2006.04.005

Ershadi, A., McCabe, M.F., Evans, J.P., Chaney, N.W., Wood, E.F., 2014. Multi-site evaluation of terrestrial evaporation models using FLUXNET data. Agric. For. Meteorol. 187, 46–61. doi:10.1016/j.agrformet.2013.11.008

Exelis, 2012. Documentation Center [WWW Document]. URL http://www.exelisvis.com/docs/home.html (accessed 6.2.15).

Fagan, M., Defries, R., 2009. Measurement and Monitoring of the World's Forests: A Review and Summary of Remote Sensing Technical Capability, 2009–2015, Resources for the Future.

FAO, 2015. Global Forest Resources Assessment 2015 - How are the world's forests changing?, Change. Rome.

FAO, 2014. Global Land Cover SHARE (GLC-SHARE) database - Beta-release version 1.0 -2014. Food and Agriculture Organization of the United Nations and European Commission Joint Research Centre, Rome.

FAO, 2012. FRA 2015 - Terms and definitions, Forest Resources Assessment Working Papers Series - 180. Rome.

FAO, 2010. Global Forest Resources Assessment 2010 - Main report. FAO Forestry Paper 163. FAO United Nations Food and Agriculture Organisation, Rome.

FAO & JRC, 2012. Global forest land-use change 1990-2005. FAO Forestry Paper No. 169. Food and Agriculture Organization of the United Nations and European Commission Joint Research Centre, Rome.

FAO, UNDP, UNEP, 2011. The UN-REDD Programme Strategy. Food and Agriculture Organization of the United Nations (FAO), United Nations Development Programme (UNDP), the United Nations Environment Programme (UNEP), Chatelaine, Switzerland.

Fassnacht, K.S., Gower, S.T., Norman, J.M., McMurtrie, R.E., 1994. A comparison of optical and direct methods for estimating foliage surface area index in forests. Agric. For. Meteorol. 71, 183–207. doi:10.1016/0168-1923(94)90107-4

Feilhauer, H., Asner, G.P., Martin, R.E., 2015. Multi-method ensemble selection of spectral bands related to leaf biochemistry. Remote Sens. Environ. 164, 57–65. doi:10.1016/j.rse.2015.03.033

Feilhauer, H., Faude, U., Schmidtlein, S., 2011. Combining Isomap ordination and imaging spectroscopy to map continuous floristic gradients in a heterogeneous landscape. Remote Sens. Environ. 115, 2513–2524. doi:10.1016/j.rse.2011.05.011

Féret, J.-B., Asner, G.P., 2013. Tree Species Discrimination in Tropical Forests Using Airborne Imaging Spectroscopy. IEEE Trans. Geosci. Remote Sens. 51, 73–84. doi:10.1109/TGRS.2012.2199323

Féret, J.-B., Asner, G.P., 2011. Spectroscopic classification of tropical forest species using radiative transfer modeling. Remote Sens. Environ. 115, 2415–2422. doi:10.1016/j.rse.2011.05.004

Féret, J.B., François, C., Asner, G.P., Gitelson, A.A., Martin, R.E., Bidel, L.P.R., Ustin, S.L., le Maire, G., Jacquemoud, S., 2008. PROSPECT-4 and 5: Advances in the leaf optical properties model separating photosynthetic pigments. Remote Sens. Environ. 112, 3030–3043. doi:10.1016/j.rse.2008.02.012

Ferreira, M.P., Grondona, A.E.B., Rolim, S.B.A., Shimabukuro, Y.E., 2013. Analyzing the spectral variability of tropical tree species using hyperspectral feature selection and leaf optical modeling. J. Appl. Remote Sens. 7, 73502. doi:10.1117/1.JRS.7.073502

Filella, I., Peñuelas, J., 1994. The red edge position and shape as indicators of plant chlorophyll content, biomass and hydric status. Int. J. Remote Sens. 15, 1459–1470. doi:10.1080/01431169408954177

Fischer, M., Bossdorf, O., Gockel, S., Hänsel, F., Hemp, A., Hessenmöller, D., Korte, G., Nieschulze, J., Pfeiffer, S., Prati, D., Renner, S., Schöning, I., Schumacher, U., Wells, K., Buscot, F., Kalko, E.K. V, Linsenmair, K.E., Schulze, E.D., Weisser, W.W., 2010. Implementing large-scale and long-term functional biodiversity research: The Biodiversity Exploratories. Basic Appl. Ecol. 11, 473–485. doi:10.1016/j.baae.2010.07.009

Fisher, J.B., 2009. Canopy nitrogen and albedo from remote sensing: what exactly are we seeing? Proc. Natl. Acad. Sci. U. S. A. 106, E16; author reply E17. doi:10.1073/pnas.0813124106

Forestier, G., Inglada, J., Wemmert, C., Gançarski, P., 2013. Comparison of optical sensors discrimination ability using spectral libraries. Int. J. Remote Sens. 34, 2327–2349. doi:10.1080/01431161.2012.744488

Foster, J., Townsend, P.A., 2004. Linking hyperspectral imagery and forest inventories for forest assessment in the central Applachians, in: 14th Central Hardwood Forest Conference. pp. 76–86.

Fourty, T., Baret, F., Jacquemoud, S., Schmuck, G., Verdebout, J., 1996. Leaf optical properties with explicit description of its biochemical composition: Direct and inverse problems. Remote Sens. Environ. 56, 104–117. doi:10.1016/0034-4257(95)00234-0

Franklin, S.E., 2001. Remote Sensing for Sustainable Forest Management. Llc, C R C Press, Boca Raton.

Frazer, G., Trofynow, J., Lertzman, K., 1997. A method for estimating canopy opennes, effective leaf area index, and photosynthetically active photon flux density using hemispherical photography and computerized image analysis techniques.

Fridman, J., Holm, S., Nilsson, M., Nilsson, P., Ringvall, A.H., Ståhl, G., 2014. Adapting National Forest Inventories to changing requirements - The case of the Swedish National Forest Inventory at the turn of the 20th century. Silva Fenn. 48, 1–29. doi:10.14214/sf.1095

Füssel, H., Jol, A., Kurnik, B., Hemming, D., 2012. Climate change, impacts and vulnerability in Europe 2012: an indicator-based report., EEA Report. Copenhagen. doi:10.2800/66071

Gamon, J.A., 2015. Reviews and Syntheses: Optical sampling of the flux tower footprint. Biogeosciences 12, 4509–4523. doi:10.5194/bg-12-4509-2015

Gamon, J.A., Peñuelas, J., Field, C.B., 1992. A narrow-waveband spectral index that tracks diurnal changes in photosynthetic efficiency. Remote Sens. Environ. 41, 35–44. doi:10.1016/0034-4257(92)90059-S

Gamon, J.A., Surfus, J.S., 1999. Assessing leaf pigment content and activity with a reflectometer. New Phytol. 143, 105–117. doi:10.1046/j.1469-8137.1999.00424.x

Garbulsky, M.F., Peñuelas, J., Gamon, J., Inoue, Y., Filella, I., 2011. The photochemical reflectance index (PRI) and the remote sensing of leaf, canopy and ecosystem radiation use efficiencies. A review and meta-analysis. Remote Sens. Environ. 115, 281–297. doi:10.1016/j.rse.2010.08.023

Gastellu-Etchegorry, J.P., Martin, E., Gascon, F., 2004. DART: a 3D model for simulating satellite images and studying surface radiation budget. Int. J. Remote Sens. 25, 73–96. doi:10.1080/0143116031000115166

Gausman, H.W., 1984. Evaluation of factors causing reflectance differences between Sun and Shade Leaves. Remote Sens. Environ. 15, 177–181. doi:10.1016/0034-4257(84)90045-2

GCOS, 2010. Implementation Plan for the Global Observing System for Climate in Support of the UNFCCC (2010 Update). Global Climate Observing System, World Meteorological Organization, Geneva, Switzerland.

Getzin, S., Wiegand, K., Schöning, I., 2012. Assessing biodiversity in forests using very high-resolution images and unmanned aerial vehicles. Methods Ecol. Evol. 3, 397–404. doi:10.1111/j.2041-210X.2011.00158.x

Ghiyamat, A., Shafri, H.Z.M., 2010. A review on hyperspectral remote sensing for homogeneous and heterogeneous forest biodiversity assessment. Int. J. Remote Sens. 31, 1837–1856. doi:10.1080/01431160902926681

Ghiyamat, A., Shafri, H.Z.M., Mahdiraji, G.A., Shariff, A.R.M., Mansor, S., 2013. Hyperspectral discrimination of tree species with different classifications using single- and multiple-endmember. Int. J. Appl. Earth Obs. Geoinf. 23, 177–191. doi:10.1016/j.jag.2013.01.004

Giri, C., Pengra, B., Long, J., Loveland, T.R., 2013. Next generation of global land cover characterization, mapping, and monitoring. Int. J. Appl. Earth Obs. Geoinf. 25, 30–37. doi:10.1016/j.jag.2013.03.005

Gitelson, A.A., Gritz, Y., Merzlyak, M.N., 2003. Relationships between leaf chlorophyll content and spectral reflectance and algorithms for non-destructive chlorophyll assessment in higher plant leaves. J. Plant Physiol. 160, 271–282. doi:10.1078/0176-1617-00887

Gitelson, A.A., Merzlyak, M.N., Chivkunova, O.B., 2001. Optical properties and nondestructive estimation of

anthocyanin content in plant leaves. Photochem. Photobiol. 74, 38–45. doi:10.1562/0031-8655(2001)0740038OPANEO2.0.CO2

Gitelson, A.A., Zur, Y., Chivkunova, O.B., Merzlyak, M.N., 2002. Assessing carotenoid content in plant leaves with reflectance spectroscopy assessing carotenoid content in plant leaves with reflectance. Photochem. Photobiol. 75, 272–281. doi:10.1562/0031-8655(2002)075<0272

Glenn, E.P., Huete, A.R., Nagler, P.L., Nelson, S.G., 2008. Relationship between remotely-sensed vegetation indices, canopy attributes and plant physiological processes: What vegetation indices can and cannot tell us about the landscape. Sensors 8, 2136–2160. doi:10.3390/s8042136

Gobron, N., Pinty, B., Aussedat, O., Chen, J.M., Cohen, W.B., Fensholt, R., Gond, V., Huemmrich, K.F., Lavergne, T., Mélin, F., Privette, J.L., Sandholt, I., Taberner, M., Turner, D.P., Verstraete, M.M., Widlowski, J.L., 2006. Evaluation of fraction of absorbed photosynthetically active radiation products for different canopy radiation transfer regimes: Methodology and results using Joint Research Center products derived from SeaWiFS against ground-based estimations. J. Geophys. Res. Atmos. 111, 1–15. doi:10.1029/2005JD006511

Gobron, N., Verstraete, M.M., 2009a. Leaf Area Index, Assessment of the status of the development of the standards for the Terrestrial Essential Climate Variables. GTOS Secretariat NRL, Food and Agriculture Organization of the United Nations (FAO), Rome.

Gobron, N., Verstraete, M.M., 2009b. Fraction of Absorbed Photosynthetically Active Radiation (FAPAR), Assessment of the status of the development of the standards for the Terrestrial Essential Climate Variables. Rome.

Goetz, A.F., Vane, G., Solomon, J.E., Rock, B.N., 1985. Imaging spectrometry for Earth remote sensing. Science 228, 1147–1153. doi:10.1126/science.228.4704.1147

Goetz, A.F.H., 2009. Three decades of hyperspectral remote sensing of the Earth: A personal view. Remote Sens. Environ. 113, S5–S16. doi:10.1016/j.rse.2007.12.014

Gong, P., Pu, R., Biging, G.S., Larrieu, M.R., 2003. Estimation of forest leaf area index using vegetation indices derived from Hyperion hyperspectral data. IEEE Trans. Geosci. Remote Sens. 41, 1355–1362. doi:10.1109/TGRS.2003.812910

Gonsamo, A., Chen, J.M., David, T.P., Kurz, W. a., Wu, C., 2012. Land surface phenology from optical satellite measurement and CO 2 eddy covariance technique. J. Geophys. Res. Biogeosciences 117, 1–18. doi:10.1029/2012JG002070

Gonsamo, A., D'odorico, P., Pellikka, P., 2013. Measuring fractional forest canopy element cover and openness - definitions and methodologies revisited. Oikos 122, 1283–1291. doi:10.1111/j.1600-0706.2013.00369.x

Gonsamo, A., Pellikka, P., 2009. The computation of foliage clumping index using hemispherical photography. Agric. For. Meteorol. 149, 1781–1787. doi:10.1016/j.agrformet.2009.06.001

Goodenough, A.E., Goodenough, A.S., 2012. Development of a Rapid and Precise Method of Digital Image Analysis to Quantify Canopy Density and Structural Complexity. ISRN Ecol. doi:10.5402/2012/619842

Gowen, A.A., O'Donnell, C.P., Cullen, P.J., Downey, G., Frias, J.M., 2007. Hyperspectral imaging - an emerging process analytical tool for food quality and safety control. Trends Food Sci. Technol. 18, 590–598. doi:10.1016/j.tifs.2007.06.001

Gower, S.T., Normann, J.M., 1991. Rapid estimation of leaf area index in conifer and broad-leaf plantations. Ecology 72, 1896–1900.

Goyal, G., Bansal, A.K., Singhal, M., 2013. Review Paper on Various Filtering Techniques and Future Scope to Apply These on TEM Images. Int. J. Sci. Res. Publ. 3, 1–11.

Granshaw, S.I., 2015. First World War Aerial Photography: 1915. Photogramm. Rec. 30, 330–338. doi:10.1111/phor.12131

Green, R.O., Eastwood, M.L., Sarture, C.M., Chrien, T.G., Aronsson, M., Chippendale, B.J., Faust, J. a, Pavri, B.E., Chovit, C.J., Solis, M., Olah, M.R., Williams, O., 1998. Imaging Spectroscopy and the Airborne Visible / Infrared Imaging Spectrometer (AVIRIS). Remote Sens. Environ. 65, 227–248.

Gregoire, T.G., Ståhl, G., Næsset, E., Gobakken, T., Nelson, R., Holm, S., 2011. Model-assisted estimation of

biomass in a LiDAR sample survey in Hedmark County, NorwayThis article is one of a selection of papers from Extending Forest Inventory and Monitoring over Space and Time. Can. J. For. Res. 41, 83–95. doi:10.1139/X10-195

Groenendijk, M., Dolman, A.J., Ammann, C., Arneth, A., Cescatti, A., Dragoni, D., Gash, J.H.C., Gianelle, D., Gioli, B., Kiely, G., Knohl, A., Law, B.E., Lund, M., Marcolla, B., van der Molen, M.K., Montagnani, L., Moors, E., Richardson, A.D., Roupsard, O., Verbeeck, H., Wohlfahrt, G., 2011. Seasonal variation of photosynthetic model parameters and leaf area index from global Fluxnet eddy covariance data. J. Geophys. Res. 116, G04027. doi:10.1029/2011JG001742

Groeneveld, D.P., Baugh, W.M., Silverman, J.., Barz, D.D., 2006. Non-imaging Airborne Spectroscopy for Calibrating Satellite Imagery.

Grosjean, M., Amann, B., Butz, C., Rein, B., Tylmann, W., 2014. Hyperspectral imaging: a novel , non-destructive method for investigating sub- annual sediment structures and composition. Pages Mag. 22, 10–11.

Grote, R., 2010. Welche Rolle spielen Kohlenwasserstoff-Emissionen aus Wäldern für die Forstwirtschaft der Zukunft? Algemeine Forst- und Jagdzeitung 181, 77–81.

Gschwantner, T., Schadauer, K., Vidal, C., Lanz, A., Tomppo, E., Di Cosmo, L., Robert, N., Duursma, D.E., Lawrence, M., 2009. Common tree definitions for national forest inventories in Europe. Silva Fenn. 43, 303–321. doi:10.14214/sf.463

Guanter, L., Kaufmann, H., Segl, K., Foerster, S., Rogass, C., Chabrillat, S., Kuester, T., Hollstein, A., Rossner, G., Chlebek, C., Straif, C., Fischer, S., Schrader, S., Storch, T., Heiden, U., Mueller, A., Bachmann, M., Mühle, H., Müller, R., Habermeyer, M., Ohndorf, A., Hill, J., Buddenbaum, H., Hostert, P., van der Linden, S., Leitão, P., Rabe, A., Doerffer, R., Krasemann, H., Xi, H., Mauser, W., Hank, T., Locherer, M., Rast, M., Staenz, K., Sang, B., 2015. The EnMAP Spaceborne Imaging Spectroscopy Mission for Earth Observation. Remote Sens. 7, 8830–8857. doi:10.3390/rs70708830

Guckland, A., Flessa, H., Prenzel, J., 2009. Controls of temporal and spatial variability of methane uptake in soils of a temperate deciduous forest with different abundance of European beech (Fagus sylvatica L.). Soil Biol. Biochem. 41, 1659–1667. doi:10.1016/j.soilbio.2009.05.006

Guyot, G., Baret, F., Guyot, G., & Baret, F., 1988. Utilisation de la haute résolution spectrale pour suivre l'état des couverts végétaux, in: Proceedings of the 4th International Colloquium on Spectral Signatures of Objects in Remote Sensing. p. 279–286. doi:10.1007/s13398-014-0173-7.2

Guyot, G., Baret, F., Jacquemoud, S., 1992. Imaging spectroscopy for vegetation studies, in: Toselli, F., Bodechtel, J. (Eds.), Imaging Spectroscopy: Fundamentals and Prospective Applications. ECSC, EEC, EAEC, pp. 145–165.

Haboudane, D., Miller, J.R., Pattey, E., Zarco-Tejada, P.J., Strachan, I.B., 2004. Hyperspectral vegetation indices and novel algorithms for predicting green LAI of crop canopies: Modeling and validation in the context of precision agriculture. Remote Sens. Environ. 90, 337–352. doi:10.1016/j.rse.2003.12.013

Hakala, T., Suomalainen, J., Kaasalainen, S., Chen, Y., 2012. Full waveform hyperspectral LiDAR for terrestrial laser scanning. Opt. Express 20, 7119. doi:10.1364/OE.20.007119

Hale, S.E., Edwards, C., 2002. Comparison of film and digital hemispherical photography across a wide range of canopy densities. Agric. For. Meteorol. 112, 51–56. doi:10.1016/S0168-1923(02)00042-4

Hanewinkel, M., Cullmann, D.A., Schelhaas, M.-J., Nabuurs, G.-J., Zimmermann, N.E., 2012. Climate change may cause severe loss in the economic value of European forest land. Nat. Clim. Chang. 3, 203–207. doi:10.1038/nclimate1687

Hansen, J., Nagel, J., 2014. Waldwachstumskundliche Softwaresysteme auf Basis von TreeGrOSS – Anwendung und theoretische Grundlagen, Beiträge aus der Nordwestdeutschen Forstlichen Versuchsanstalt Band 11. Universitätsverlag Göttingen, Göttingen.

Hansen, M., Potapov, P., Margono, B., Stehman, S., Turubanova, S., Tyukavina, A., 2014. Response to comment on "High-resolution global maps of 21st-century forest cover change". Science 344, 981. doi:10.1126/science.1248817

Hansen, M., Potapov, P. V, Moore, R., Hancher, M., Turubanova, S.A., Tyukavina, A., 2013. High-resolution global maps of 21st-century forest cover change. Science 342, 850–853. doi:10.1126/science.1244693

Hansen, M.C., Roy, D.P., Lindquist, E., Adusei, B., Justice, C.O., Altstatt, A., 2008. A method for integrating MODIS and Landsat data for systematic monitoring of forest cover and change in the Congo Basin. Remote Sens. Environ. 112, 2495–2513. doi:10.1016/j.rse.2007.11.012

Hardy, J.P., Melloh, R., Koenig, G., Marks, D., Winstral, A., Pomeroy, J.W., Link, T., 2004. Solar radiation transmission through conifer canopies. Agric. For. Meteorol. 126, 257–270. doi:10.1016/j.agrformet.2004.06.012

Heiden, U., Heldens, W., Roessner, S., Segl, K., Esch, T., Mueller, A., 2012. Urban structure type characterization using hyperspectral remote sensing and height information. Landsc. Urban Plan. 105, 361–375. doi:10.1016/j.landurbplan.2012.01.001

Henrich, V., Krauss, G., Götze, C., Sandow, C., 2012. Index DataBase - A database for remote sensing indices [WWW Document]. IDB - Entwicklung einer Datenbank für Fernerkundungsindizes. URL www.indexdatabase.de

Herold, N., Schöning, I., Michalzik, B., Trumbore, S., Schrumpf, M., 2014. Controls on soil carbon storage and turnover in German landscapes. Biogeochemistry 119, 435–451. doi:10.1007/s10533-014-9978-x

Holmgren, P., Thuresson, T., 1998. Satellite remote sensing for forestry planning - A review. Scand. J. For. Res. 13, 90–110. doi:10.1080/02827589809382966

Homolová, L., Malenovský, Z., Clevers, J.G.P.W., García-Santos, G., Schaepman, M.E., 2013. Review of optical-based remote sensing for plant trait mapping. Ecol. Complex. 15, 1–16. doi:10.1016/j.ecocom.2013.06.003

Hopkinson, C., Lovell, J., Chasmer, L., Jupp, D., Kljun, N., van Gorsel, E., 2013. Integrating terrestrial and airborne lidar to calibrate a 3D canopy model of effective leaf area index. Remote Sens. Environ. 136, 301–314. doi:10.1016/j.rse.2013.05.012

Huang, D., Knyazikhin, Y., Dickinson, R.E., Rautiainen, M., Stenberg, P., Disney, M., Lewis, P., Cescatti, A., Tian, Y., Verhoef, W., Martonchik, J. V., Myneni, R.B., 2007. Canopy spectral invariants for remote sensing and model applications. Remote Sens. Environ. 106, 106–122. doi:10.1016/j.rse.2006.08.001

Huang, H., Liu, L., Ngadi, M.O., 2014. Recent developments in hyperspectral imaging for assessment of food quality and safety. Sensors (Basel). 14, 7248–76. doi:10.3390/s140407248

Huang, L.-K., Wang, M.-J.J., 1995. Image thresholding by minimizing the measures of fuzziness. Pattern Recognit. 28, 41–51.

Huete, A., Didan, K., Miura, T., Rodriguez, E.P., Gao, X., Ferreira, L.G., 2002. Overview of the radiometric and biophysical performance of the MODIS vegetation indices. Remote Sens. Environ. 83, 195–213. doi:10.1016/S0034-4257(02)00096-2

Huete, A.R., Liu, H.Q., Batchily, K., Van Leeuwen, W., 1997. A comparison of vegetation indices over a global set of TM images for EOS-MODIS. Remote Sens. Environ. 59, 440–451. doi:10.1016/S0034-4257(96)00112-5

Hughes, G., 1968. On the mean accuracy of statistical pattern recognizers. IEEE Trans. Inf. Theory 14. doi:10.1109/TIT.1968.1054102

Hughes, N.M., Vogelmann, T.C., Smith, W.K., 2008. Optical effects of abaxial anthocyanin on absorption of red wavelengths by understorey species: Revisiting the back-scatter hypothesis. J. Exp. Bot. 59, 3435–3442. doi:10.1093/jxb/ern193

IPCC, 2013. Summary for Policymakers, in: Stocker, T.F., Qin, D., Plattner, G.-K., Tignor, M., Allen, S.K., Boschung, J., Nauels, A., Xia, Y., Bex, V., Midgley, P.M. (Eds.), Climate Change 2013: The Physical Science Basis. Contribution of Working Group I to the Fifth Assessment Report of the Intergovernmental Panel on Climate Change. Cambridge University Press, Cambridge, United Kingdom and New York, NY, USA.

IPCC, 2003. Good Practice Guidance for Land Use , Land-Use Change and Forestry. Institute for Global Environmental Strategies (IGES), for the The Intergovernmental Panel on Climate Change (IPCC), Hayama, Kanagawa, Japan.

IPCC, 2000. Land Use, Land-Use Change and Forestry. Cambridge University Press, Geneva, Switzerland.

Jackson, R.D., Huete, A.R., 1991. Interpreting vegetation indices. Prev. Vet. Med. doi:10.1016/S0167-5877(05)80004-2

Jacquemoud, S., Baret, F., 1990. PROSPECT: A model of leaf optical properties spectra. Remote Sens. Environ. 34, 75–91. doi:10.1016/0034-4257(90)90100-Z

Jacquemoud, S., Verhoef, W., Baret, F., Bacour, C., Zarco-Tejada, P.J., Asner, G.P., François, C., Ustin, S.L., 2009. PROSPECT + SAIL models: A review of use for vegetation characterization. Remote Sens. Environ. 113, S56–S66. doi:10.1016/j.rse.2008.01.026

Jennings, S.B., Brown, N.D., Sheil, D., 1999. Assessing forest canopies and understorey illumination : canopy closure , canopy cover and other measures. Forestry 72, 59–73. doi:10.1093/forestry/72.1.59

Jensen, J.R., 2007. Remote sensing of the environment: an earth resource perspective, 2nd ed. Prentice Hall Inc., Upper Saddle, NJ.

Jonckheere, I., Fleck, S., Nackaerts, K., Muys, B., Coppin, P., Weiss, M., Baret, F., 2004. Review of methods for in situ leaf area index determination Part I. Theories, sensors and hemispherical photography. Agric. For. Meteorol. 121, 19–35. doi:10.1016/j.agrformet.2003.08.027

Jonckheere, I., Nackaerts, K., Muys, B., Coppin, P., 2005. Assessment of automatic gap fraction estimation of forests from digital hemispherical photography. Agric. For. Meteorol. 132, 96–114. doi:10.1016/j.agrformet.2005.06.003

Jones, H.G., Vaughn, R.A., 2010. Remote Sensing of Vegetation. Principles, techniques and applications., 1st ed. Oxford University Press Inc., New York.

Jordan, C.F., 1969. Derivation of leaf area index from quality of light on the floor. Ecology 50, 663–666.

Kalacska, M., Bohlman, S., Sánchez-Azofeifa, G.A., Castro-Esau, K., Caelli, T., 2007. Hyperspectral discrimination of tropical dry forest lianas and trees: Comparative data reduction approaches at the leaf and canopy levels. Remote Sens. Environ. 109, 406–415. doi:10.1016/j.rse.2007.01.012

Kaufmann, H., Doerffer, R., Hill, J., Hostert, P., 2014. Preparing to Exploit the Science Potentials The EnMAP Space Mission. EnMAP Science Advisory Group, Großbeeren.

Kaufmann, H., Förster, S., Wulf, H., Segl, K., Guanter, L., Bochow, M., Heiden, U., Müller, A., Heldens, W., Schneiderhan, T., Leitão, P.J., Linden, S. van der, Hostert, P., Hill, J., Buddenbaum, H., Mauser, W., Hank, T., Krasemann, H., Röttgers, R., Oppelt, N., Heim, B., 2012. Science Plan of the Environmental Mapping and Analysis Program (EnMAP). Potsdam.

Kefauver, S.C., Filella, I., Zhang, C., Peñuelas, J., Unit, G.E., Vallès, C., Vallès, C., 2015. Linking OMI HCHO and MODIS PRI satellite data with BVOCs emissions in NE Spain. Geosci. Remote Sens. Symp. 2661–2664.

Keith, H., Mackey, B.G., Lindenmayer, D.B., 2009. Re-evaluation of forest biomass carbon stocks and lessons from the world's most carbon-dense forests. Proc. Natl. Acad. Sci. U. S. A. 106, 11635–11640. doi:10.1073/pnas.0901970106

Keshava, N., 2003. A Survey of Spectral Unmixing Algorithms. LINCOLN Lab. J. 14, 55–78.

Kim, D., Sexton, J.O., Noojipady, P., Huang, C., Anand, A., Channan, S., Feng, M., Townshend, J.R., 2014. Remote Sensing of Environment Global , Landsat-based forest-cover change from 1990 to 2000. Remote Sens. Environ. 155, 178–193. doi:10.1016/j.rse.2014.08.017

Kleinn, C., 2015. Lecture Notes for the Module Monitoring of Forest Resources. Göttingen.

Kleinn, C., 2002. New technologies and methodologies for national forest inventories. Unasylva 53, 10–15. doi:10.1353/sho.2002.0073

Kleinn, C., Corrales, L., Morales, D., 2002. Forest area in Costa Rica: A comparative study of tropical forest cover estimates over time. Environ. Monit. Assess. 73, 17–40. doi:10.1023/A:1012659129083

Knapp, A.K., Carter, G.A., 1998. Variability in leaf optical properties among 26 species from a broad range of habitats. Am. J. Bot. 85, 940–946. doi:10.2307/2446360

Knipling, E.B., 1970. Physical and physiological basis for the reflectance of visible and near-infrared radiation from vegetation. Remote Sens. Environ. 1, 155–159. doi:10.1016/S0034-4257(70)80021-9

Knohl, A., Schulze, E.D., Kolle, O., Buchmann, N., 2003. Large carbon uptake by an unmanaged 250-year-old deciduous forest in Central Germany. Agric. For. Meteorol. 118, 151–167. doi:10.1016/S0168-1923(03)00115-1

Knohl, A., Søe, A.R.B., Kutsch, W.L., Göckede, M., Buchmann, N., 2008. Representative estimates of soil and ecosystem respiration in an old beech forest. Plant Soil 302, 189–202. doi:10.1007/s11104-007-9467-2

Knyazikhin, Y., Lewis, P., Disney, M.I., Stenberg, P., Mõttus, M., Rautiainen, M., Kaufmann, R.K., Marshak, A., Schull, M.A., Carmona, P.L., Vanderbilt, V., Davis, A.B., Baret, F., Stéphane Jacquemoud, A., Myneni, R.B., 2013a. Reply toTownsend et al.: Decoupling contributions from canopy structure and leaf optics is critical for remote sensing leaf biochemistry. Proc. … 2–3. doi:10.1073/pnas.1301247110

Knyazikhin, Y., Schull, M.A., Stenberg, P., Mõttus, M., Rautiainen, M., Yang, Y., Marshak, A., Latorre Carmona, P., Kaufmann, R.K., Lewis, P., Disney, M.I., Vanderbilt, V., Davis, A.B., Baret, F., Jacquemoud, S., Lyapustin, A., Myneni, R.B., 2013b. Hyperspectral remote sensing of foliar nitrogen content. Proc. Natl. Acad. Sci. U. S. A. 110, E185-92. doi:10.1073/pnas.1210196109

Korhonen, L., Korhonen, K., Rautiainen, M., Stenberg, P., 2006. Estimation of forest canopy cover: a comparison of field measurement techniques. Silva Fenn. 40, 577–588. doi:citeulike-article-id:7886289

Kumar, L., Skidmore, A., Mutanga, O., 2010. Leaf level experiments to discriminate between eucalyptus species using high spectral resolution reflectance data: use of derivatives, ratios and vegetation indices. Geocarto Int. 37–41. doi:10.1080/10106040903505996

Kutsch, W.L., Kolle, O., Rebmann, C., Knohl, A., Ziegler, W., Schulze, E.D., 2008. Advection and resulting CO2 exchange uncertainty in a tall forest in central Germany. Ecol. Appl. 18, 1391–1405.

Kutsch, W.L., Persson, T., Schrumpf, M., Moyano, F.E., Mund, M., Andersson, S., Schulze, E.D., 2010. Heterotrophic soil respiration and soil carbon dynamics in the deciduous Hainich forest obtained by three approaches. Biogeochemistry 100, 167–183. doi:10.1007/s10533-010-9414-9

Lambert, J., Edwards, A., 2013. Electromagnetic Spectrum [WWW Document]. Energy Driv. Clim. URL http://www.ces.fau.edu/nasa/module-2/radiation-sun.php (accessed 4.29.15).

Landgrebe, D.A., 2003. Signal theory methods in multispectral remote sensing, Wiley. John Wiley & Sons, Inc., Hoboken, NJ.

Lang, A.R.G., Xiang, Y., 1986. Estimation of leaf area index from transmission of direct sunlight in discontinuos canopies. Agric. For. Meteorol. 37, 229–243.

Lausch, A., Heurich, M., Gordalla, D., Dobner, H.J., Gwillym-Margianto, S., Salbach, C., 2013a. Forecasting potential bark beetle outbreaks based on spruce forest vitality using hyperspectral remote-sensing techniques at different scales. For. Ecol. Manage. 308, 76–89. doi:10.1016/j.foreco.2013.07.043

Lausch, A., Pause, M., Merbach, I., Zacharias, S., Doktor, D., Volk, M., Seppelt, R., 2013b. A new multiscale approach for monitoring vegetation using remote sensing-based indicators in laboratory, field, and landscape. Environ. Monit. Assess. 185, 1215–1235. doi:10.1007/s10661-012-2627-8

Le Maire, G., François, C., Dufrêne, E., 2004. Towards universal broad leaf chlorophyll indices using PROSPECT simulated database and hyperspectral reflectance measurements. Remote Sens. Environ. 89, 1–28. doi:10.1016/j.rse.2003.09.004

Leblanc, S.G., Chen, J.M., Fernandes, R., Deering, D.W., Conley, A., 2005. Methodology comparison for canopy structure parameters extraction from digital hemispherical photography in boreal forests. Agric. For. Meteorol. 129, 187–207. doi:10.1016/j.agrformet.2004.09.006

Legner, N., Fleck, S., Leuschner, C., 2013. Low light acclimation in five temperate broad-leaved tree species of different successional status: the significance of a shade canopy. Ann. For. Sci. 70, 557–570. doi:10.1007/s13595-013-0298-4

Lehnert, L.W., Bässler, C., Brandl, R., Burton, P.J., Müller, J., 2013. Conservation value of forests attacked by bark beetles: Highest number of indicator species is found in early successional stages. J. Nat. Conserv. 21, 97–104. doi:10.1016/j.jnc.2012.11.003

Lehnert, L.W., Meyer, H., Bendix, J., 2015. hsdar: Manage, analyse and simulate hyperspectral data in R.

Leuning, R., Hughes, D., Daniel, P., Coops, N., Newnham, G., 2006. A multi-angle spectrometer for automatic measurement of plant canopy reflectance spectra. Remote Sens. Environ. 103, 236–245. doi:10.1016/j.rse.2005.06.016

Li, L., Ustin, S.L., Lay, M., 2005. Application of AVIRIS data in detection of oil-induced vegetation stress and

cover change at Jornada, New Mexico. Remote Sens. Environ. 94, 1–16. doi:10.1016/j.rse.2004.08.010

Liang, S., 2004. Quantitative remote sensing of land surfaces. John Wiley & Sons, Inc., Hoboken, NJ.

Lichtenthaler, H.K., Ač, A., Marek, M. V., Kalina, J., Urban, O., 2007. Differences in pigment composition, photosynthetic rates and chlorophyll fluorescence images of sun and shade leaves of four tree species. Plant Physiol. Biochem. 45, 577–588. doi:10.1016/j.plaphy.2007.04.006

Lichtenthaler, H.K., Buschmann, C., 2001. Chlorophylls and Carotenoids : Measurement and Characterization by UV-VIS. Curr. Protoc. Food Anal. Chem. F4.3.1-F4., 1–8. doi:10.1002/0471142913

Lillesaeter, O., 1982. Spectral reflectance of partly transmitting leaves: Laboratory measurements and mathematical modeling. Remote Sens. Environ. 12, 247–254. doi:10.1016/0034-4257(82)90057-8

Lillesand, T.M., Kiefer, R.W., Chipman, J.W., 2008. Remote sensing and image interpretation, 6th ed. Wiley-Blackwell, John Wiley & Sons, Hoboken, NJ.

Lindner, M., Maroschek, M., Netherer, S., Kremer, A., Barbati, A., Garcia-Gonzalo, J., Seidl, R., Delzon, S., Corona, P., Kolström, M., Lexer, M.J., Marchetti, M., 2010. Climate change impacts, adaptive capacity, and vulnerability of European forest ecosystems. For. Ecol. Manage. 259, 698–709. doi:10.1016/j.foreco.2009.09.023

Lu, S., 2013. Effects of Leaf Surface Wax on Leaf Spectrum and Hyperspectral Vegetation Indices, in: IEEE International Geoscience and Remote Sensing Symposium. IEEE, Melbourne, pp. 453–456. doi:http://dx.doi.org/10.1109/IGARSS.2013.6721190

Lui, G., Coomes, D., 2015. A Comparison of Novel Optical Remote Sensing-Based Technologies for Forest-Cover/Change Monitoring. Remote Sens. 7, 2781–2807. doi:10.3390/rs70302781

Luyssaert, S., Schulze, E.-D., Börner, A., Knohl, A., Hessenmöller, D., Law, B.E., Ciais, P., Grace, J., 2008. Old-growth forests as global carbon sinks. Nature 455, 213–215. doi:10.1038/nature07276

MacDicken, K.G., Sola, P., Hall, J.E., Sabogal, C., Tadoum, M., de Wasseige, C., 2015. Global progress toward sustainable forest management. For. Ecol. Manage. 352, 47–56. doi:10.1016/j.foreco.2015.02.005

Macfarlane, C., Hoffman, M., Eamus, D., Kerp, N., Higginson, S., McMurtrie, R., Adams, M., 2007. Estimation of leaf area index in eucalypt forest using digital photography. Agric. For. Meteorol. 143, 176–188. doi:10.1016/j.agrformet.2006.10.013

Malenovský, Z., Bartholomeus, H.M., Acerbi-Junior, F.W., Schopfer, J.T., Painter, T.H., Epema, G.F., Bregt, A.K., 2007. Scaling dimensions in spectroscopy of soil and vegetation. Int. J. Appl. Earth Obs. Geoinf. 9, 137–164. doi:10.1016/j.jag.2006.08.003

Manakos, I., Manevski, K., Petropoulos, G.P., 2010. Development of a spectral library for mediterranean land cover types. Proc. 30th EARSeL Symp. Remote Sens. Sci. Educ. Nat. Cult. Herit. 663–668.

Mansour, K., Mutanga, O., Everson, T., Adam, E., 2012. Discriminating indicator grass species for rangeland degradation assessment using hyperspectral data resampled to AISA Eagle resolution. ISPRS J. Photogramm. Remote Sens. 70, 56–65. doi:10.1016/j.isprsjprs.2012.03.006

Marchi, A., Paletto, A., 2010. Relationship between forest canopy and natural regeneration in the subalpine spruce-larch forest (north-east Italy). Folia For. Pol. Ser. A 52, 3–12.

Martens, S.N., Ustin, S.L., Rousseau, R.A., 1993. Estimation of tree canopy leaf area index by gap fraction analysis. For. Ecol. Manage. 61, 91–108. doi:10.1016/0378-1127(93)90192-P

Mather, P.M., Koch, M., 2011. Computer Processing of Remotel-Sensed Images: An Introduction, 4th ed. Wiley-Blackwell, John Wiley & Sons.

McDowell, N.G., Coops, N.C., Beck, P.S.A., Chambers, J.Q., Gangodagamage, C., Hicke, J.A., Huang, C., Kennedy, R., Krofcheck, D.J., Litvak, M., Meddens, A.J.H., Muss, J., Negrón-Juarez, R., Peng, C., Schwantes, A.M., Swenson, J.J., Vernon, L.J., Williams, A.P., Xu, C., Zhao, M., Running, S.W., Allen, C.D., 2015. Global satellite monitoring of climate-induced vegetation disturbances. Trends Plant Sci. 20, 114–123. doi:10.1016/j.tplants.2014.10.008

McRoberts, R.E., Tomppo, E.O., 2007. Remote sensing support for national forest inventories. Remote Sens. Environ. 110, 412–419. doi:10.1016/j.rse.2006.09.034

Medina, J.M., Pereira, L.M., Correia, H.T., Nascimento, S.M.C., 2011. Hyperspectral optical imaging of human

iris in vivo: characteristics of reflectance spectra. J. Biomed. Opt. 16, 76001. doi:10.1117/1.3595710

Menzel, R., Puhlmann, D., Heuer, A., Schleich, W.P., 2012. Wave-particle dualism and complementarity unraveled by a different mode. Proc. Natl. Acad. Sci. 109, 9314–9319. doi:10.1073/pnas.1201271109

Merlier, E., Hmimina, G., Dufrêne, E., Soudani, K., 2015. Explaining the variability of the photochemical reflectance index (PRI) at the canopy-scale: Disentangling the effects of phenological and physiological changes. J. Photochem. Photobiol. B Biol. 151, 161–171. doi:10.1016/j.jphotobiol.2015.08.006

Meroni, M., Rossini, M., Guanter, L., Alonso, L., Rascher, U., Colombo, R., Moreno, J., 2009. Remote sensing of solar-induced chlorophyll fluorescence: Review of methods and applications. Remote Sens. Environ. 113, 2037–2051. doi:10.1016/j.rse.2009.05.003

Microsoft, 2010. Microsoft Excel.

Miller, J.R., Wu, J., Boyer, M.G., Belanger, M., Hare, E.W., 1991. Seasonal patterns in leaf reflectance red-edge characteristics. Int. J. Remote Sens. 12, 1509–1523. doi:10.1080/01431169108955186

Milton, E.J., Blackburn, G.A., Rollin, E.M., Danson, F.M., 1994. Measurement of the spectral directional reflectance of forest canopies: a review of methods and a practical application. doi:10.1080/02757259409532251

Milton, E.J., Schaepman, M.E., Anderson, K., Kneubühler, M., Fox, N.P., Schaepman, M.E., 2009. Progress in field spectroscopy. Remote Sens. Envirnonment 113, S92–S109. doi:10.1016/j.rse.2007.08.001

Mölder, A., Bernhardt-Römermann, M., 2009. Zur Bedeutung der Winterlinde (Tilia cordata Mill.) in mittel- und nordwestdeutschen Eichen-Hainbuchen-Wäldern. Tuexenia 9–23.

Mölder, A., Bernhardt-Römermann, M., Schmidt, W., 2008. Herb-layer diversity in deciduous forests: Raised by tree richness or beaten by beech? For. Ecol. Manage. 256, 272–281. doi:10.1016/j.foreco.2008.04.012

Monsi, M., Saeki, T., 2005. On the factor light in plant communities and its importance for matter production. Ann. Bot. 95, 549–567. doi:10.1093/aob/mci052

Morisette, J.T., Baret, F., Privette, J.L., Myneni, R.B., Nickeson, J.E., Garrigues, S., Shabanov, N. V., Weiss, M., Fernandes, R. a., Leblanc, S.G., Kalacska, M., Sánchez-Azofeifa, G.A., Chubey, M., Rivard, B., Stenberg, P., Rautiainen, M., Voipio, P., Manninen, T., Pilant, A.N., Lewis, T.E., Iiames, J.S., Colombo, R., Meroni, M., Busetto, L., Cohen, W.B., Turner, D.P., Warner, E.D., Petersen, G.W., Seufert, G., Cook, R., 2006. Validation of global moderate-resolution LAI products: A framework proposed within the CEOS land product validation subgroup. IEEE Trans. Geosci. Remote Sens. 44, 1804–1814. doi:10.1109/TGRS.2006.872529

Mund, M., Kutsch, W.L., Wirth, C., Kahl, T., Knohl, A., Skomarkova, M. V., Schulze, E.D., 2010. The influence of climate and fructification on the inter-annual variability of stem growth and net primary productivity in an old-growth, mixed beech forest. Tree Physiol. 30, 689–704. doi:10.1093/treephys/tpq027

Nackaerts, K., Coppin, P., Muys, B., Hermy, M., 2000. Sampling methodology for LAI measurements with LAI-2000 in small forest stands. Agric. For. Meteorol. 101, 247–250. doi:10.1016/S0168-1923(00)00090-3

Nagel, J., 2009. Waldwachstumssimulation mit dem Java Software Paket TreeGrOSS.

Nationalparkverwaltung-Hainich, 2012. UNESCO-Weltnaturerbe. [WWW Document]. URL http://www.nationalpark-hainich.de/einsteigen/unesco-weltnaturerbe.html 1 (accessed 9.20.12).

Nationalparkverwaltung-Hainich, 2011. Kontrollstichprobe im Gebiet des Nationalparks Hainich 2009-2011.

Nevalainen, O., Hakala, T., Suomalainen, J., Kaasalainen, S., 2013. Nitrogen concentration estimation with hyperspectral LiDAR. ISPRS Ann. Photogramm. Remote Sens. Spat. Inf. Sci. II-5/W2, 205–210. doi:10.5194/isprsannals-II-5-W2-205-2013

Nicodemus, F.E., Richmond, J.C., Hsia, J.J., 1977. Geometrical considerations and nomenclature for reflectance. Sci. Technol. 60, 1–52. doi:10.1109/LPT.2009.2020494

Niinemets, Ü., Valladares, F., 2006. Tolerance to shade, drought, and waterlogging of temperate northern hemisphere trees and shrubs. Ecol. Monogr. 76, 521–547. doi:10.1890/0012-9615(2006)076[0521:TTSDAW]2.0.CO;2

Nilson, T., Peterson, U., 1994. Age dependence of forest reflectance: Analysis of main driving factors. Remote

Sens. Environ. 48, 319–331. doi:10.1016/0034-4257(94)90006-X

Nilson, T., Rautiainen, M., Pisek, J., Peterson, U., 2012. Seasonal reflectance courses of forests. New Adv. Contrib. to For. Res. 33–58.

Nölke, N., Beckschäfer, P., Kleinn, C., 2015. Thermal canopy photography in forestry - an alternative to optical cover photography. iForest - Biogeosciences For. 8, 1–5. doi:10.3832/ifor1129-007

O'Connor, B., Secades, C., Penner, J., Sonnenschein, R., Skidmore, A., Burgess, N.D., Hutton, J.M., 2015. Earth observation as a tool for tracking progress towards the Aichi Biodiversity Targets. Remote Sens. Ecol. Conserv. 1, 19–28. doi:10.1002/rse2.4

Olander, L.P., Gibbs, H.K., Steininger, M., Swenson, J.J., Murray, B.C., 2008. Reference scenarios for deforestation and forest degradation in support of REDD: a review of data and methods. Environ. Res. Lett. 3, 25011.

Ollinger, S. V., 2011. Sources of variability in canopy reflectance and the convergent properties of plants. New Phytol. 189, 375–394. doi:10.1111/j.1469-8137.2010.03536.x

Ollinger, S. V., Richardson, A.D., Martin, M.E., Hollinger, D.Y., Frolking, S.E., Reich, P.B., Plourde, L.C., Katul, G.G., Munger, J.W., Oren, R., Smith, M.-L., Paw U, K.T., Bolstad, P. V, Cook, B.D., Day, M.C., Martin, T.A., Monson, R.K., Schmid, H.P., 2008. Canopy nitrogen, carbon assimilation, and albedo in temperate and boreal forests: Functional relations and potential climate feedbacks. Proc. Natl. Acad. Sci. U. S. A. 105, 19336–19341. doi:10.1073/pnas.0810021105

Omar, H., 2010. Digital Globe 8 - Bands Research Challenge Commercial Timber Tree Species Identification Using Multispectral Worldview - 2 Data. 52109 Kepong, Selangor MALAYSIA.

Onojeghuo, A.O., Blackburn, G.A., 2011. Optimising the use of hyperspectral and LiDAR data for mapping reedbed habitats. Remote Sens. Environ. 115, 2025–2034. doi:10.1016/j.rse.2011.04.004

Pacheco-Labrador, J., González-Cascón, R., Pilar Martín, M., Riaño, D., 2014. Understanding the optical responses of leaf nitrogen in mediterranean holm oak (Quercus ilex) using field spectroscopy. Int. J. Appl. Earth Obs. Geoinf. 26, 105–118. doi:10.1016/j.jag.2013.05.013

Pal, M., Foody, G.M., 2010. Feature selection for classification of hyperspectral data by SVM. IEEE Trans. Geosci. Remote Sens. 48, 2297–2307. doi:10.1109/TGRS.2009.2039484

Paletto, A., Tosi, V., 2009. Forest canopy cover and canopy closure: Comparison of assessment techniques. Eur. J. For. Res. 128, 265–272. doi:10.1007/s10342-009-0262-x

Pan, Y., Birdsey, R.A., Fang, J., Houghton, R., Kauppi, P.E., Kurz, W.A., Phillips, O.L., Shvidenko, A., Lewis, S.L., Canadell, J.G., Ciais, P., Jackson, R.B., Pacala, S.W., McGuire, A.D., Piao, S., Rautiainen, A., Sitch, S., Hayes, D., 2011. A large and persistent carbon sink in the world's forests. Science 333, 988–993. doi:10.1126/science.1201609

Panferov, O., Knyazikhin, Y., Myneni, R.B., Szarzynski, J., Engwald, S., Schnitzler, K.G., Gravenhorst, G., 2001. The role of canopy structure in the spectral variation of transmission and absorption of solar radiation in vegetation canopies. IEEE Trans. Geosci. Remote Sens. 39, 241–253. doi:10.1109/36.905232

Panigrahy, S., Kumar, T., Manjunath, K.R., 2012. Hyperspectral leaf signature as an added dimension for species discrimination: Case study of four tropical mangroves. Wetl. Ecol. Manag. 20, 101–110. doi:10.1007/s11273-011-9245-z

Parker, G.G., Brown, M.J., 2000. Forest canopy stratification - Is it useful? Am. Nat. 155, 473–484. doi:10.1086/303340

Parrotta, J.A., Wildburger, C., Mansourian, S., 2012. Understanding relationships between biodiversity, carbon, forests and people: the key to achieving REDD+ objectives. A global assessment report prepared by the Global Forest Expert Panel on Biodiversity, Forest Management and REDD+, IUFRO World Series. doi:1016-3263

Pautasso, M., Aas, G., Queloz, V., Holdenrieder, O., 2013. European ash (Fraxinus excelsior) dieback - A conservation biology challenge. Biol. Conserv. 158, 37–49. doi:10.1016/j.biocon.2012.08.026

Pekin, B., Macfarlane, C., 2009. Measurement of crown cover and leaf area index using digital cover photography and its application to remote sensing. Remote Sens. 1, 1298–1320. doi:10.3390/rs1041298

Peng, C., Ma, Z., Lei, X., Zhu, Q., Chen, H., Wang, W., Liu, S., Li, W., Fang, X., Zhou, X., 2011. A drought-induced pervasive increase in tree mortality across Canada's boreal forests. Nat. Clim. Chang. 1, 467–471. doi:10.1038/nclimate1293

Peñuelas, J., Baret, F., Filella, I., 1995. Semi-empirical indices to assess carotenoids/chlorophyll a ratio from leaf spectral reflectance. Photosynthetica 31, 221–230.

Peñuelas, J., Marino, G., Llusia, J., Morfopoulos, C., Farré-Armengol, G., Filella, I., 2013. Photochemical reflectance index as an indirect estimator of foliar isoprenoid emissions at the ecosystem level. Nat. Commun. 4, 2604. doi:10.1038/ncomms3604

Petterson, H., 1955. Yield of coniferous forests. Medd. fran Statens Skogsforsoksanst, Sweden 45.

Pfitzner, K., Bollhöfer, A., Carr, G., 2006. A standard design for collecting vegetation reference spectra: Implementation and implications for data sharing. J. Spat. Sci. doi:10.1080/14498596.2006.9635083

Pinty, B., 2004. Radiation Transfer Model Intercomparison (RAMI) exercise: Results from the second phase. J. Geophys. Res. 109, 1–19. doi:10.1029/2003JD004252

Pinty, B., Clerici, M., Andredakis, I., Kaminski, T., Taberner, M., Verstraete, M.M., Gobron, N., Plummer, S., Widlowski, J.-L., 2011a. Exploiting the MODIS albedos with the Two-stream Inversion Package (JRC-TIP): 2. Fractions of transmitted and absorbed fluxes in the vegetation and soil layers. J. Geophys. Res. 116, 1–15. doi:10.1029/2010JD015373

Pinty, B., Jung, M., Kaminski, T., Lavergne, T., Mund, M., Plummer, S., Thomas, E., Widlowski, J.L., 2011b. Evaluation of the JRC-TIP 0.01° products over a mid-latitude deciduous forest site. Remote Sens. Environ. 115, 3567–3581. doi:10.1016/j.rse.2011.08.018

Porcar-Castell, A., Mac Arthur, A., Rossini, M., Eklundh, L., Pacheco-Labrador, J., Anderson, K., Balzarolo, M., Martín, M.P., Jin, H., Tomelleri, E., Cerasoli, S., Sakowska, K., Hueni, A., Julitta, T., Nichol, C.J., Vescovo, L., 2015. EUROSPEC: At the interface between remote-sensing and ecosystem CO2 flux measurements in Europe. Biogeosciences 12, 6103–6124. doi:10.5194/bg-12-6103-2015

Prewitt, J.M.S., Mendelsohn, M.L., 1966. The analysis of cell images. Ann. N. Y. Acad. Sci. 128, 1035–1053. doi:10.1111/j.1749-6632.1965.tb11715.x

Propastin, P., Panferov, O., 2013. Retrieval of remotely sensed LAI using Landsat ETM+ data and ground measurements of solar radiation and vegetation structure: Implication of leaf inclination angle. Int. J. Appl. Earth Obs. Geoinf. 25, 38–46. doi:10.1016/j.jag.2013.02.006

Prospere, K., Mclaren, K., Wilson, B., 2014. Plant Species Discrimination in a Tropical Wetland Using In Situ Hyperspectral Data. Remote Sens. 6, 8494–8523. doi:10.3390/rs6098494

Pu, R., 2009. Broadleaf species recognition with in situ hyperspectral data. Int. J. Remote Sens. 30, 2759–2779. doi:10.1080/01431160802555820

Pu, R., Gong, P., 2004. Wavelet transform applied to EO-1 hyperspectral data for forest LAI and crown closure mapping. Remote Sens. Environ. 91, 212–224. doi:10.1016/j.rse.2004.03.006

Pulla, P., Schuck, A., Verkerk, P.J., Lasserre, B., Marchetti, M., Green, T., 2013. Mapping the distribution of forest ownership in Europe - Annex 1: Forest definitions. EFI Tech. Rep. 88, 5.

Purves, D.W., Lichstein, J.W., Pacala, S.W., 2007. Crown plasticity and competition for canopy space: A new spatially implicit model parameterized for 250 North American tree species. PLoS One 2. doi:10.1371/journal.pone.0000870

Qi, J., Inoue, Y., Wiangwang, N., 2012. Hyperspectral remote sensing in global change studies, in: Thenkabail, P.S., Lyon, J.G., Huete, A. (Eds.), Hyperspectral Remote Sensing of Vegetation. CRC Press, Taylor & Francis Group, Boca Raton, p. 705.

R Core Team, 2012. R: A language and environment for statistical computing.

Ramakrishnan, D., Nithya, M., Singh, K.D., Bharti, R., 2013. A field technique for rapid lithological discrimination and ore mineral identification: Results from Mamandur Polymetal Deposit, India. J. Earth Syst. Sci. 122, 93–106. doi:http://dx.doi.org/10.1007/s12040-012-0255-x

Rasband, W.S., 2014. ImageJ.

Rautiainen, M., Stenberg, P., Nilson, T., 2005. Estimating canopy cover in scots pine stands. Silva Fenn. 39,

137–142.

Raychaudhuri, B., 2012. Remote sensing of solar-induced chlorophyll fluorescence at atmospheric oxygen absorption band around 760 nm and simulation of that absorption in laboratory. IEEE Trans. Geosci. Remote Sens. 50, 3908–3914. doi:10.1109/TGRS.2012.2185503

Rich, P.M., 1990. Characterizing plant canopies with hemispherical photographs. Remote Sens. Rev. doi:10.1080/02757259009532119

Richards, J.A., 2013. Remote Sensing Digital Image Analysis: An Introduction, 5th ed. Springer, Berlin / Heidelberg.

Richardson, J.J., Moskal, L.M., Kim, S.H., 2009. Modeling approaches to estimate effective leaf area index from aerial discrete-return LIDAR. Agric. For. Meteorol. 149, 1152–1160. doi:10.1016/j.agrformet.2009.02.007

Richter, K., Atzberger, C., Vuolo, F., D'Urso, G., 2011. Evaluation of Sentinel-2 Spectral Sampling for Radiative Transfer Model Based LAI Estimation of Wheat, Sugar Beet, and Maize. Sel. Top. Appl. Earth Obs. Remote Sensing, IEEE J. 4, 458–464. doi:10.1109/JSTARS.2010.2091492

Roberts, D.A., Nelson, B.W., Adams, J.B., Palmer, F., 1998. Spectral changes with leaf aging in Amazon caatinga. Trees - Struct. Funct. 12, 315–325. doi:10.1007/s004680050157

Romijn, E., Lantican, C.B., Herold, M., Lindquist, E., Ochieng, R., Wijaya, A., Murdiyarso, D., Verchot, L., 2015. Assessing change in national forest monitoring capacities of 99 tropical countries. For. Ecol. Manage. 352, 109–123. doi:10.1016/j.foreco.2015.06.003

Rouse, J.W., Haas, R.H., Scheel, J.A., Deering, D.W., 1974. Monitoring Vegetation Systems in the Great Plains with ERTS, in: Earth Resources Technology Satellite-1 Symposium- Volume I: Technical Presentations. pp. 309–317.

RStudio Team, 2015. RStudio: Integrated Development for R.

Rueda, C.A., Wrona, A.F., 2003. SAMS - Spectral Analysis and Management System. User's Man. - Version 2.0.

Rühle, W., Wild, A., 1979. The intensification of absorbance changes in leaves by light-dispersion - Differences between high-light and low-light leaves. Planta 146, 551–557. doi:10.1007/BF00388831

Russell, G., Marshall, B., Jarvis, P.G., 1989. Plant canopies: Their growth, form and fuction. Cambridge University Press, Cambridge.

Ryan, P.T., 1997. Modern regression methods. Wiley, New York.

Saatchi, S.S., Harris, N.L., Brown, S., Lefsky, M., Mitchard, E.T.A., Salas, W., Zutta, B.R., Buermann, W., Lewis, S.L., Hagen, S., Petrova, S., White, L., Silman, M., More, A., 2011. Benchmark map of forest carbon stocks in tropical regions across three continents. Proc. Natl. Acad. Sci. 108, 72. doi:10.1073/pnas.1019576108

Sadava, D., Hillis, D.M., Heller, H.C., Berenbaum, M.R., 2011. Life: The Science of Biology, 9th ed. Sinauer Associates and W. H. Freeman.

Saldaña, E., Siche, R., Lujan, M., Quevedo, R., 2013. Review : computer vision applied to the inspection and quality control of fruits and vegetables. Revisão : visão computacional aplicada à inspeção e ao controle da qualidade de frutas e verduras. Brazilian J. Food Technol. Campinas 16, 254–272.

Savitzky, A., Golay, M.J.E., 1964. Smoothing and differentiation by simplied least squares procedures. Anal. Chem. 36, 1627–1639.

Schaepman-Strub, G., Schaepman, M.E., Painter, T.H., Dangel, S., Martonchik, J. V., 2006. Reflectance quantities in optical remote sensing-definitions and case studies. Remote Sens. Environ. 103, 27–42. doi:10.1016/j.rse.2006.03.002

Schaepman, M.E., 2009. Earth system science related imaging spectroscopy. Present. Remote Sens. Environ. doi:10.1016/j.rse.2009.03.001

Schaepman, M.E., Kneubühler, M., Bartholomeus, H., Zbynek, M., Damm, A., 2010. Scaling Spectroscopic Approaches – from Leaf Albedo to Ecosystems Mapping. Art, Sci. Appl. Reflectance Spectrosc. Symp. 1–19.

Schafer, R.W., 2011. What is a savitzky-golay filter? IEEE Signal Process. Mag. 28, 111–117. doi:10.1109/MSP.2011.941097

Schlerf, M., Atzberger, C., 2006. Inversion of a forest reflectance model to estimate structural canopy variables from hyperspectral remote sensing data. Remote Sens. Environ. 100, 281–294. doi:10.1016/j.rse.2005.10.006

Schlerf, M., Atzberger, C., Hill, J., 2005. Remote sensing of forest biophysical variables using HyMap imaging spectrometer data. Remote Sens. Environ. 95, 177–194. doi:10.1016/j.rse.2004.12.016

Schmidt, A., 1968. Der rechnerische Ausgleich von Bestandeshöhenkurven. Forstwissenschaftliches Cent. 86, 370–382.

Schmidt, K.S., Skidmore, A.K., 2003. Spectral discrimination of vegetation types in a coastal wetland. Remote Sens. Environ. 85, 92–108. doi:10.1016/S0034-4257(02)00196-7

Schmidtlein, S., Zimmermann, P., Schupferling, R., Weiss, C., 2007. Mapping the floristic continuum: Ordination space position estimated from imaging spectroscopy. J. Veg. Sci. 18, 131–140. doi:10.1111/j.1654-1103.2007.tb02523.x

Scurlock, J.M.O., Asner, G.P., Gower, S.T., 2001. Worldwide Historical Estimates and Bibliography of Leaf Area Index, 1932-2000. ORNL Tech. Memo. TM-2001/268 27.

Secades, C., O'Connor, B., Brown, C., Walpole, M., 2014. Earth Observation for Biodiversity Monitoring: A review of current approaches and future opportunities for tracking progress towards the Aichi Biodiversity Targets, Technical Series. Secretariat of the Convention on Biological Diversity, Montréal, Canada.

Segl, K., Guanter, L., Gascon, F., Kuester, T., Rogass, C., Mielke, C., 2015. S2eteS : An End-to-End Modeling Tool for the Simulation of Sentinel-2 Image Products. IEEE Trans. Geosci. Remote Sens. 53, 5560–5571.

Segl, K., Guanter, L., Rogass, C., Kuester, T., Roessner, S., Kaufmann, H., Sang, B., Mogulsky, V., Hofer, S., 2012. EeteS — The EnMAP End-to-End Simulation Tool. IEEE J. Sel. Top. Appl. Earth Obs. Remote Sens. 5, 522–530.

Seidl, R., Schelhaas, M., Rammer, W., Verkerk, P.J., 2014. Increasing forest disturbances in Europe and their impact on carbon storage. Nat. Clim. Chang. 4, 1–6. doi:10.1038/nclimate2318

Sellers, P.J., 1985. Canopy reflectance, photosynthesis and transpiration. Int. J. Remote Sens. 6, 1335–1372. doi:10.1080/01431168508948283

Sellers, P.J., Berry, J.A., Collatz, G.J., Field, C.B., Hall, F.G., 1992. Canopy reflectance, photosynthesis, and transpiration. III - A reanalysis using improved leaf models and a new canopy integration scheme. Remote Sens. Envirnonment 42, 187–216. doi:10.1016/0034-4257(92)90102-P

Serbin, S.P., Dillaway, D.N., Kruger, E.L., Townsend, P. a., 2012. Leaf optical properties reflect variation in photosynthetic metabolism and its sensitivity to temperature. J. Exp. Bot. 63, 489–502. doi:10.1093/jxb/err294

Serrano, L., Gamon, J.A., Peñuelas, J., 2000. Estimation of canopy photosynthetic and nonphotosynthetic components from spectral transmittance. Ecology 81, 3149–3162.

Serrano, L., Peñuelas, J., 2005. Assessing forest structure and function from spectral transmittance measurements: a case study in a Mediterranean holm oak forest. Tree Physiol. 25, 67–74. doi:10.1093/treephys/25.1.67

Shahshahani, B.M., Landgrebe, D.A., 1994. The effect of unlabeled samples in reducing the small sample size problem and mitigating the Hughes phenomenon. Geosci. Remote Sensing, IEEE Trans. 32, 1087–1095. doi:10.1109/36.312897

Sims, D.A., Gamon, J.A., 2002. Relationships between leaf pigment content and spectral reflectance across a wide range of species, leaf structures and developmental stages. Remote Sens. Envirnonment 81, 337–354.

Skidmore, A., Pettorelli, N., C., N.C., Geller, G.N., Hansen, M., Lucas, R., Mücher, C.A., O'Connor, B., Paganini, M., Pereira, H.M., Schaepman, M.E., Turner, W., Wang, T., Wegmann, M., 2015. Agree on biodiversity metrics to track from space. Nature 523, 403–405.

Slaton, M.R., Raymond Hunt Jr., E., Smith, W.K., 2001. Estimating near-infrared leaf reflectance from leaf

structural characteristics. Am. J. Bot. 88, 278–284.

Sloan, S., Sayer, J.A., 2015. Forest Resources Assessment of 2015 shows positive global trends but forest loss and degradation persist in poor tropical countries. For. Ecol. Manage. 352, 134–145. doi:10.1016/j.foreco.2015.06.013

Smith, G.M., Milton, E.J., 1999. The use of the empirical line method to calibrate remotely sensed data to reflectance. Int. J. Remote Sens. 20, 2653–2662. doi:10.1080/014311699211994

Smith, J.A., Lin, T.L., Ranson, K.J., 1980. The Lambertian assumption and Landsat data. Eng. Remote Sens 46, 1183–1189. doi:10.1017/CBO9781107415324.004

Soffer, B.H., Lynch, D., 1999. Some paradoxes, errors, and resolutions concerning the spectral optimization of human vision. Am. J. Phys. 67, 946–953. doi:http://dx.doi.org/10.1119/1.19170

Somers, B., Asner, G.P., 2013. Multi-temporal hyperspectral mixture analysis and feature selection for invasive species mapping in rainforests. Remote Sens. Environ. 136, 14–27. doi:10.1016/j.rse.2013.04.006

Soudani, K., François, C., le Maire, G., Le Dantec, V., Dufrêne, E., 2006. Comparative analysis of IKONOS, SPOT, and ETM+ data for leaf area index estimation in temperate coniferous and deciduous forest stands. Remote Sens. Environ. 102, 161–175. doi:10.1016/j.rse.2006.02.004

Soudani, K., Hmimina, G., Dufrêne, E., Berveiller, D., Delpierre, N., Ourcival, J.M., Rambal, S., Joffre, R., 2014. Relationships between photochemical reflectance index and light-use efficiency in deciduous and evergreen broadleaf forests. Remote Sens. Environ. 144, 73–84. doi:10.1016/j.rse.2014.01.017

SSP, 2015. How to rewire the eye [WWW Document]. Sci. – Mag. Soc. Sci. Public. URL https://www.sciencenews.org/article/how-rewire- (accessed 6.2.15).

Staenz, K., Held, A., 2012. Summary of current and future terrestrial civilian hyperspectral spaceborne systems, in: Geoscience and Remote Sensing Symposium (IGARSS), 2012 IEEE International. IEEE, Munich, pp. 123–126. doi:10.1109/IGARSS.2012.6351621

Steiner, D., Gutermann, T., 1966. Russian data on spectral reflectance of vegetation, soil and rock types, Final Technical Report. Zürich.

Stoy, P.C., Trowbridge, A.M., Bauerle, W.L., 2014. Controls on seasonal patterns of maximum ecosystem carbon uptake and canopy-scale photosynthetic light response: Contributions from both temperature and photoperiod. Photosynth. Res. 119, 49–64. doi:10.1007/s11120-013-9799-0

Thenkabail, P.S., Smith, R.B., De Pauw, E., 2000. Hyperspectral vegetation indices and their relationships with agricultural crop characteristics. Remote Sens. Environ. 71, 158–182. doi:10.1016/S0034-4257(99)00067-X

Thimonier, A., Sedivy, I., Schleppi, P., 2010. Estimating leaf area index in different types of mature forest stands in Switzerland: A comparison of methods. Eur. J. For. Res. 129, 543–562. doi:10.1007/s10342-009-0353-8

Thomas, V., 2012. Hyperspectral remote sensing for forest management, in: Thenkabail, P., Lyon, J.G., Huete, A. (Eds.), Hyperspectral Remote Sensing of Vegetation. CRC Press, Taylor & Francis Group, Boca Raton, p. 705.

Townsend, P.A., Serbin, S.P., Kruger, E.L., Gamon, J.A., 2013. Disentangling the contribution of biological and physical properties of leaves and canopies in imaging spectroscopy data. Proc. Natl. Acad. Sci. U. S. A. 110, E1074. doi:10.1073/pnas.1300952110

Townshend, J.R.G., Justice, C.O., 1988. Selecting the spatial resolution of satellite sensors required for global monitoring of land transformations. Int. J. Remote Sens. 9, 187–236.

Treitz, P.M., Howarth, P.J., 1999. Hyperspectral remote sensing for estimating biophysical parameters of forest ecosystems. Prog. Phys. Geogr. 23, 359–390. doi:10.1177/030913339902300303

Trenberth, K.E., Fasullo, J.T., Kiehl, J., 2009. Earth's global energy budget. Bull. Am. Meteorol. Soc. 90, 311–323. doi:10.1175/2008BAMS2634.1

Trishchenko, A.P., Cihlar, J., Li, Z., 2002. Effects of spectral response function on surface reflectance and NDVI measured with moderate resolution satellite sensors. Remote Sens. Environ. 81, 1–18. doi:10.1016/S0034-4257(01)00328-5

Tropek, R., Beck, J., Keil, P., Musilová, Z., Irena, Š., Storch, D., 2014. Comment on " High-resolution global maps of 21st-century forest cover change ." Science 344, 981.

Tsai, F., Philpot, W., 1998. Derivative analysis of hyperspectral data. Remote Sens. Environ. 66, 41–51. doi:10.1016/S0034-4257(98)00032-7

Tuanmu, M.N., Jetz, W., 2014. A global 1-km consensus land-cover product for biodiversity and ecosystem modelling. Glob. Ecol. Biogeogr. 23, 1031–1045. doi:10.1111/geb.12182

Tucker, C.J., 1979. Red and photographic infrared linear combinations for monitoring vegetation. Remote Sens. Envirnonment 8, 127–150. doi:10.1016/0034-4257(79)90013-0

Turner, W., Rondinini, C., Pettorelli, N., Mora, B., Leidner, A.K., Szantoi, Z., Buchanan, G., Dech, S., Dwyer, J., Herold, M., Koh, L.P., Leimgruber, P., Taubenboeck, H., Wegmann, M., Wikelski, M., Woodcock, C., 2015. Free and open-access satellite data are key to biodiversity conservation. Biol. Conserv. 182, 173–176. doi:10.1016/j.biocon.2014.11.048

UGA, 2013. Light and Matter [WWW Document]. Univ. Georg. USA, Dr. Robin Shelton. Astron. Lect. Mater. URL http://www.physast.uga.edu/~rls/astro1020/ch4/ovhd.html (accessed 6.2.15).

UNEP, 2014. New Collaboration Launched to Restore the World's Forests [WWW Document]. UNEP News Cent. URL http://www.unep.org/newscentre/Default.aspx?DocumentID=2796&ArticleID=10974 (accessed 6.2.15).

UNEP, FAO, UNFF, 2009. Vital Forest Graphics. United Nations Environment Programmme (UNEP), United Nations Food and Agriculture Organisation (FAO), United Nations Food and Agriculture Organisation (UNFF), United Nations Forum on Forests, Nairobi.

UNESCO, 2014. World Heritage List. Primeval Beech Forests of the Carpathians and the Ancient Beech Forests of Germany [WWW Document]. URL http://whc.unesco.org/en/list/1133 (accessed 10.13.14).

Ustin, S.L., Gitelson, A.A., Jacquemoud, S., Schaepman, M., Asner, G.P., Gamon, J.A., Zarco-Tejada, P., 2009. Retrieval of foliar information about plant pigment systems from high resolution spectroscopy. Remote Sens. Environ. 113, S67–S77. doi:10.1016/j.rse.2008.10.019

Vahtmäe, E., Kutser, T., Martin, G., Kotta, J., 2006. Feasibility of hyperspectral remote sensing for mapping benthic macroalgal cover in turbid coastal waters - A Baltic Sea case study. Remote Sens. Environ. 101, 342–351. doi:10.1016/j.rse.2006.01.009

Vaiphasa, C., 2006. Consideration of smoothing techniques for hyperspectral remote sensing. ISPRS J. Photogramm. Remote Sens. 60, 91–99. doi:10.1016/j.isprsjprs.2005.11.002

van der Linden, S., Hostert, P., 2009. The influence of urban structures on impervious surface maps from airborne hyperspectral data. Remote Sens. Environ. 113, 2298–2305. doi:10.1016/j.rse.2009.06.004

Van Der Meer, F., Bakker, W., Scholte, K., Skidmore, A., De Jong, S., Clevers, J., Addink, E., Epema, G., 2001. Spatial scale variations in vegetation indices and above-ground biomass estimates: Implications for MERIS. Int. J. Remote Sens. 22, 3381–3396. doi:10.1080/01431160152609227

van der Werf, G.R., Morton, D.C., DeFries, R.S., Olivier, J.G.J., Kasibhatla, P.S., Jackson, R.B., Collatz, G.J., Randerson, J.T., 2009. CO2 emissions from forest loss. Nat. Geosci. 2, 9–11. doi:10.1038/ngeo671

Van Gardingen, P.R., Jackson, G.E., Hernandez-Daumas, S., Russell, G., Sharp, L., 1999. Leaf area index estimates obtained for clumped canopies using hemispherical photography. Agric. For. Meteorol. 94, 243–257. doi:10.1016/S0168-1923(99)00018-0

Verburg, P.H., Neumann, K., Nol, L., 2011. Challenges in using land use and land cover data for global change studies. Glob. Chang. Biol. 17, 974–989. doi:10.1111/j.1365-2486.2010.02307.x

Villafranca, A.G., Corbera, J., Martín, F., Marchán, J.F., 2012. Limitations of Hyperspectral Earth Observation on Small Satellites. J. Small Satell. 1, 19–29.

Vogelmann, J.E., Rock, B.N., Moss, D.M., 1993. Red edge spectral measurements from sugar maple leaves. Int. J. Remote Sens. 14, 1563–1575. doi:10.1080/01431169308953986

Vorovencii, I., 2009. The hyperspectral sensors used in satellite and aerial remote sensing. Bull. Transilv. Univ. Braşov 2, 51–56.

Wagner, S., 1998. Calibration of grey values of hemispherical photographs for image analysis. Agric. For.

Meteorol. 90, 103–117. doi:10.1016/S0168-1923(97)00073-7

Walter-Shea, E.A., Biehl, L.L., 1990. Measuring vegetation spectral properties. Remote Sens. Rev. Spec. Issue Instrum. Stud. Veg. canopies Remote Sens. Opt. Therm. infrared Reg. 5, 179–205. doi:10.1080/02757259009532128

Walter, J.M.N., Fournier, R.A., Soudani, K., Meyer, E., 2003. Integrating clumping effects in forest canopy structure: An assessment through hemispherical photographs. Can. J. Remote Sens. 29, 388–410. doi:10.5589/m03-011

Wang, Y., Buermann, W., Stenberg, P., Smolander, H., Häme, T., Tian, Y., Hu, J., Knyazikhin, Y., Myneni, R.B., 2003. A new parameterization of canopy spectral response to incident solar radiation: Case study with hyperspectral data from pine dominant forest. Remote Sens. Environ. 85, 304–315. doi:10.1016/S0034-4257(03)00009-9

Wang, Y.S., Miller, D.R., Welles, J.M., Heisler, G.M., 1992. Spatial Variability of Canopy Foliage in an Oak Forest Estimated with Fisheye Sensors. For. Sci. 38, 854–865. doi:S

Waser, L.T., Küchler, M., Jütte, K., Stampfer, T., 2014. Evaluating the potential of worldview-2 data to classify tree species and different levels of ash mortality. Remote Sens. 6, 4515–4545. doi:10.3390/rs6054515

Wehrli, C., 1985. Extraterrestrial Solar Spectrum. Phys. Obs. + World Radiat. Cent. 615.

Weiss, M., Baret, F., Smith, G.J., Jonckheere, I., Coppin, P., 2004. Review of methods for in situ leaf area index (LAI) determination Part II. Estimation of LAI, errors and sampling. Agric. For. Meteorol. 121, 37–53. doi:10.1016/j.agrformet.2003.08.001

Wertz-Kanounnikoff, S., 2008. Monitoring forest emissions: a review of methods. CIFOR Work. Pap. 24.

White, D., Williams, M., Barr, S., 2008. Detecting sub-surface soil disturbance using hyperspectral first derivative band rations of associated vegetation stress. … . Photogramm. Remote Sens. Spat. Inf. Sci 1980, 243–248.

White, M.A., Beurs, K.M. de, Didan, K., Inouye, D.W., Richardson, A.D., Jensen, O.P., O'Keefe, J., Zhang, G., Nemani, R., Leeuwen, W.J.D. van, Brown, J.F., Wit, A. de, Schaepman, M.E., X. Lin, M.D., Bailey, A.S., Kimball, J., Schwartz, M.D., Baldocchi, D.D., Lee, J.T., Lauenroth, W.K., 2009. Intercomparison, interpretation, and assessment of spring phenology in North America estimated from remote sensing for 1982-2006. Glob. Chang. Biol. 15, 2335–2359. doi:10.1111/j.1365-2486.2009.01910.x

Wilson, K.B., Baldocchi, D.D., Hanson, P.J., 2001. Leaf age affects the seasonal pattern of photosynthetic capacity and net ecosystem exchange of carbon in a deciduous forest. Plant, Cell Environ. 24, 571–583. doi:10.1046/j.0016-8025.2001.00706.x

Wong, C.Y.S., Gamon, J.A., 2015. Three causes of variation in the photochemical reflectance index (PRI) in evergreen conifers. New Phytol. 187–195. doi:10.1111/nph.13159

Woolley, J.T., 1971. Reflectance and transmittance of light by leaves. Plant Physiol. 47, 656–662. doi:10.1104/pp.47.5.656

Wu, C., Huang, W., Yang, Q., Xie, Q., 2015. Improved estimation of light use efficiency by removal of canopy structural effect from the photochemical reflectance index (PRI). Agric. Ecosyst. Environ. 199, 333–338. doi:10.1016/j.agee.2014.10.017

Wu, C., Niu, Z., Tang, Q., Huang, W., 2008. Estimating chlorophyll content from hyperspectral vegetation indices: Modeling and validation. Agric. For. Meteorol. 148, 1230–1241. doi:10.1016/j.agrformet.2008.03.005

Wu, H., Li, Z.L., 2009. Scale issues in remote sensing: A review on analysis, processing and modeling. Sensors 9, 1768–1793. doi:10.3390/s90301768

Yang, X., Tang, J., Mustard, J.F., Lee, J.-E., Rossini, M., Joiner, J., Munger, J.W., 2015. Solar-induced chlorophyll fluorescence that correlates with canopy photosynthesis on diurnal and seasonal scales in a temperate deciduous forest. Geophys. Res. Lett. 42, 2977–2987. doi:10.1002/2015GL063201

Zarco-Tejada, P.J., Berjón, A., López-Lozano, R., Miller, J.R., Martín, P., Cachorro, V., González, M.R., De Frutos, A., 2005. Assessing vineyard condition with hyperspectral indices: Leaf and canopy reflectance simulation in a row-structured discontinuous canopy. Remote Sens. Environ. 99, 271–287. doi:10.1016/j.rse.2005.09.002

Zarco-Tejada, P.J., Pushnik, J.C., Dobrowski, S., Ustin, S.L., 2003. Steady-state chlorophyll a fluorescence detection from canopy derivative reflectance and double-peak red-edge effects. Remote Sens. Environ. 84, 283–294. doi:10.1016/S0034-4257(02)00113-X

Zhang, C., Kovacs, J.M., Liu, Y., Flores-verdugo, F., Flores-de-santiago, F., 2014. Separating Mangrove Species and Conditions Using Laboratory Hyperspectral Data: A Case Study of a Degraded Mangrove Forest of the Mexican Pacific. Remote Sens. 6, 11673–11688. doi:10.3390/rs61211673

Zhang, J., Rivard, B., Sánchez-Azofeifa, A., Castro-Esau, K., 2006. Intra- and inter-class spectral variability of tropical tree species at La Selva, Costa Rica: Implications for species identification using HYDICE imagery. Remote Sens. Environ. 105, 129–141. doi:10.1016/j.rse.2006.06.010

Zhang, L., Hu, Z., Fan, J., Zhou, D., Tang, F., 2014. A meta-analysis of the canopy light extinction coefficient in terrestrial ecosystems. Front. Earth Sci. 8, 599–609. doi:10.1007/s11707-014-0446-7

Zhang, Y., Chen, J.M., Miller, J.R., 2005. Determining digital hemispherical photograph exposure for leaf area index estimation. Agric. For. Meteorol. 133, 166–181. doi:10.1016/j.agrformet.2005.09.009

Zheng, G., Moskal, L.M., 2009. Retrieving Leaf Area Index (LAI) Using Remote Sensing: Theories, Methods and Sensors. Sensors 9, 2719–2745. doi:10.3390/s90402719

Zigmantas, D., Hiller, R.G., Sundstrom, V., Polivka, T., 2002. Carotenoid to chlorophyll energy transfer in the peridinin-chlorophyll-a-protein complex involves an intramolecular charge transfer state. Proc. Natl. Acad. Sci. U. S. A. 99, 16760–16765. doi:10.1073/pnas.262537599